3D simulations of the interactions between crack and dislocations

Elena Jover Carrasco

Communauté
UNIVERSITÉ Grenoble Alpes

THÈSE

Pour obtenir le grade de

DOCTEUR DE LA COMMUNAUTÉ UNIVERSITÉ GRENOBLE ALPES

Spécialité : **Sciences pour l'Ingénieur**

Arrêtée ministériel : 25 mai 2016

Présentée par

Jover Carrasco, Elena

Thèse dirigée par **Fivel, Marc**

préparée au sein du **Laboratoire SIMaP : Science et Ingénierie des Matériaux et Procédés**
dans **l'École Doctorale I-MEP2 : Ingénierie - Matériaux, Mécanique, Environnement,Énergétique, Procédés, Production**

Simulation 3D des interactions entre fissure et dislocations

3D simulations of the interactions between crack and dislocations

Thèse soutenue publiquement le **2 mars 2022**,
devant le jury composé de :

M. Rémy DENDIEVEL
Professeur des Universités, Univ. Grenoble Alpes, SIMaP, Président

M. Christian ROBERTSON
Ingénieur CEA Saclay, Rapporteur

M. Stéphane BERBENNI
Directeur de Recherche CNRS, LEM3, Rapporteur

M. Thomas PARDOEN
Professeur à l'Université Catholique de Louvain, Examinateur

M. Vincent CHIARUTTINI
Ingénieur Onera Chatillon, Examinateur

M. Marc FIVEL
Directeur de Recherche CNRS, SIMaP, Directeur de thèse

M. Erik BITZEK
Docteur Ingénieur, Max-Planck-Institut für Eisenforschung, Düsseldorf, Invité

Abstracts

3D simulations of the interactions between crack and dislocations

Fracture toughness of materials is not only controlled by macroscopic parameters like the geometry of the studied sample but also by the microstructure. The defects of the crystalline structure such as voids, inclusions or dislocations can also greatly impact toughness. To better understand this, 3D simulations of a crack front interacting with dislocations will be carried out. These simulations aim at measuring the variations of the stress intensity factors caused by the presence of dislocations. To carry out these simulations, two preexisting models will be combined : Extended Finite Elements Method (XFEM) and Discrete Dislocation Dynamics (DDD). XFEM is an evolution of the Finite Elements Methods that allows the study of a propagating crack without needing to remesh, it will control the studied volume, the applied loading and the crack position while DDD controls the dislocations, their movement, and their multiplication. The accuracy of the created model is tested by comparisons with atomistic simulations. To test the effect of dislocations on toughness, several dislocations on different slip systems were studied. Other parameters such as dislocation crack distance, line direction, and applied load were also studied. To compare the studied model with existing simulation results, two crack orientations were selected. The studied dislocations have different behaviors depending on their slip system. The results show dislocations creating shielding, antishielding or a combination of both. These effects are only dependent of the dislocation orientation, and do not change if the dislocation is farther from the crack, though the intensity of the effect does change given these circumstances. Since the presence of dislocations is associated to a shear stress in their glide planes, it is found that they have more effect on K_{II} than on K_I. K_{II} also controls the crack propagation angle, which means that the dislocations are one of the main sources of crack deviation.

Simulation 3D des intéractions entre fissure et dislocations

La ténacité à la rupture est contrôlée non seulement par les paramètres macroscopiques comme la géométrie de l'échantillon étudié mais aussi par la microstructure. Les défauts de la structure cristalline comme les lacunes, les inclusions ou les dislocations peuvent aussi grandement impacter la ténacité. Pour mieux comprendre ce phénomène, on mènera des simulations 3D d'un front de fissure interagissant avec des dislocations. Ces simulations visent à mesurer les variations des facteurs d'intensité des contraintes créées par la présence de dislocations. Pour cela, on combinera deux modèles préexistants : la méthode des éléments finis étendus (XFEM) et la dynamique des dislocations discrètes (DDD). XFEM est une évolution de la méthode des éléments fini qui permet l'étude d'une fissure qui se propage sans avoir besoin de remaillage, elle contrôlera le volume étudié, le chargement appliqué et la position de la fissure tandis que tant que la DDD contrôlera les dislocations, leur mouvement et leur multiplication. La précision du modèle crée sera testée en le comparant avec des résultats de simulations atomistiques. Pour mesurer qualitativement les effets des dislocations sur la ténacité, plusieurs dislocations avec des différents systèmes de glissement seront étudiées. D'autres paramètres comme la distance entre la fissure et la dislocation, la direction de la fissure, et le chargement appliqué seront aussi étudiées. Pour comparer le modèle étudié avec des résultats provenant d'autres simulations, deux orientations de fissure seront simulées. Les dislocations étudiées ont des effets sur la fissure différents en fonction de leur système de glissement. Les résultats montrent des dislocations créant soit de l'écrantage, doit de l'anti-écrantage

soit une combinaison des deux. Ces effets sont uniquement dépendants de l'orientation de la dislocation et ne changent pas quand la dislocation est plus éloignée de la fissure, même si l'intensité de l'effet change. De plus, les dislocations étant associées à un état de cisaillement local, elles affectent plus fortement K_{II} que K_I. K_{II} contrôle aussi l'angle de propagation de la fissure, ce qui implique que les dislocations sont une des principales sources des déviations des fissures.

Résumé de thèse

La fracture est un des problèmes en science des matériaux le plus étudié. Même les fractures macroscopiques sont contrôlées par la microstructure du matériau, en particulier les défauts, qui sont des sites préférentiels de nucléation de fissure et peuvent aussi influencer la direction de propagation de la fissure. Les dislocations, qui sont des défauts linéaires, sont la force conductrice derrière la plasticité dans les structures cristallines. Elles ont été observées interagissant avec des fissures. Les fissures sont aussi des sites de nucléation des dislocations. Ainsi, l'étude des interactions de dislocations avec des fissure est de grande importance pour comprendre le comportement des fissures.

Ils existent des travaux sur des simulations des interactions entre fissure et dislocations. La majorité de ces travaux sont réalisés en utilisant des simulations atomistiques, ce qui limite grandement la taille du volume qui peut être étudié. D'autres travaux utilisent de la dynamique discrète des dislocations avec une fissure statique. Il y a un manque de travaux concernant des volumes mésoscopiques avec une fissure qui peut se propager.

Pour arriver à créer une simulation tridimensionnelle d'une fissure quasistatique avec une ou plusieurs dislocations, deux méthodes existantes seront couplées. Pour la fissure, on utilisera la méthode des éléments finis étendus qui permet une approche précise et indirecte d'une fissure qui se propage. Le volume de la simulation sera défini en utilisant cette méthode. Pour les dislocations, on utilisera de la dynamique discrète des dislocations, spécifiquement, la méthode de superposition. Cette méthode a été utilisé précédemment en couplage avec la méthode des éléments finis. L'objectif de cette thèse et de créer un couplage fonctionnel entre les deux méthodes mentionnées et vérifier les résultats obtenus en les comparant avec des résultats préexistants.

Cette thèse fait partie du projet MicroKIC, dirigé par le professeur Bitzek qui a pour but d'investiguer les origines microscopiques de la ténacité à la fracture. Ce projet cherche à comprendre les procès microscopiques de la pointe de fissure pendant la fracture et d'étudier ses interactions avec plusieurs éléments microstructurels. C'est pour ceci que notre étude se centre sur les interactions fissure dislocations. Pour valider notre modèle, on comparera nos résultats avec ceux obtenus avec des simulations atomistiques.

Les dislocations peuvent interagir avec une fissure de plusieurs façons. D'abord, elles peuvent écranter la fissure. L'écrantage est le phénomène par lequel la présence de dislocations ralentira l'avancée d'une fissure. Les dislocations peuvent même arrêter la propagation de la fissure.

De l'autre côté, les dislocations peuvent produire l'effet contraire, l'anti-écrantage. Cela est plus rare, mais les dislocations peuvent aussi accélérer dans certains cas la propagation de la fissure.

Quand les dislocations croisent une surface libre, celles-ci créent des marches sur les surfaces.

Ce phénomène peut aussi provoquer l'émoussement des pointes de fissure ce qui ralenti aussi la propagation. Ce phénomène n'est pas discuté ici car la représentation que l'on fait de la fissure ne permet pas de modifier la géométrie de la pointe de fissure.

Les dislocations peuvent aussi nucléer en pointe de fissure, en particulier si les contraintes locales sont suffisamment élevées. Cette nucléation homogène peut aussi se produire ailleurs dans le volume si les conditions de contrainte sont atteintes. La nucléation homogène reste un phénomène plutôt théorique puisqu'un cristal réel sans défauts préexistants est presque impossible d'obtenir.

La méthode des éléments finis étendus (XFEM) est une méthode de simulation basée sur la méthode des éléments finis qui permet la simulation de la propagation d'une fissure. Au lieu d'utiliser un remaillage pour créer la fissure, les éléments finis étendus ajoute des fonctions qui représentent la fissure sur les éléments qui sont fissurés.

Pour suivre la fissure, cette méthode utilise les fonctions de niveau. Les fonctions de niveau sont des fonctions dont la valeur dépend de la distance entre le point où elle est calculée et une surface. Pour une fissure tridimensionnelle, deux fonctions de niveau ϕ et ψ sont nécessaires pour repérer la fissure. Le front de fissure est défini par ϕ et ψ étant nuls.

Puisqu'il n'y a pas de remaillage, la fissure est définie par des enrichissements aux nœuds des éléments que la fissure croise. Ces éléments sont séparés en deux catégories, ceux qui contiennent le front de fissure et ceux qui ont été traversés par la fissure. Les éléments traversés par la fissure sont enrichis avec une fonction de saut qui représente l'ouverture de la fissure alors que les éléments contenant le front de la fissure sont enrichis avec une fonction représentant le champ asymptotique en pointe de fissure.

La propagation de la fissure est définie par l'énergie en front de fissure. Les points du front de la fissure avanceront proportionnellement à leur énergie. L'angle de propagation est calculé avec les valeurs de K_I et K_{II}. En particulier, c'est K_{II} qui est responsable de la déviation de la direction de propagation de la fissure.

La dynamique discrète des dislocations est une méthode de simulation qui permet de créer un volume mésoscopique avec une densité de dislocations qui peut évoluer. Les dislocations sont la majorité du temps des dislocations mixtes. Ces dislocations sont discrétisées par le logiciel en des segments coins et des segments vis qui conforment la dislocation complète.

Une fois les dislocations discrétisées, cette méthode permet d'appliquer au volume un état de déformation ou contrainte. La vitesse des segments de dislocation sera ensuite calculée pour déplacer ces dislocations à $t + dt$. Une fois la nouvelle position des dislocations est calculée celles-ci sont déplacées et leur nouveau champ de contraintes est calculé.

L'état des contraintes ainsi que la géométrie du volume initial peut être définie sur le logiciel de simulation d'éléments finis Cast3M. C'est sur ce logiciel où on fera le couplage entre la méthode des éléments finis étendus et la dynamique discrète des dislocations.

Le couplage a pour but de créer une simulation où une fissure qui peut se propager interagit avec une ou plusieurs dislocations. Pour que ce couplage fonctionne correctement, il faut que les deux codes utilisés travaillent ensemble et communiquent les données nécessaires aux simulations. Cast3M est le logiciel qui contrôle l'avancement de la fissure. C'est aussi où la déformation au volume initial est appliquée. C'est pour cela que Cast3M doit transmettre à TriDis l'état de contraintes du volume.

Pour TriDis, une fois l'état des contraintes connu et appliqué aux dislocations, TriDis transmet à Cast3M l'aire balayée par les dislocations pour vérifier si les dislocations ont arrivé à une configuration stable. Le champ des contraintes crées par les dislocations est aussi transmis à Cast3M qui l'utilisera pour être appliquée à la fissure et ainsi dévier sa propagation.

Un autre point important pour le couplage est les forces images. Les forces images corres-

pondent à des dislocations virtuelles que les dislocations voient de l'autre côté des surfaces libres qui sont l'opposé des dislocations réelles. Ainsi, le champ de contrainte des dislocations est projeté sur les surfaces libres du volume, c'est-à-dire les surfaces de la fissure ainsi que la surface fissurée, et inversé pour créer les forces images. Ces forces sont à leur tour transmises à TriDis et impactent donc les dislocations.

Pour faire avancer la fissure, deux valeurs sont nécessaires, la direction de propagation ainsi que la valeur de cette propagation. Pour calculer la norme du vecteur de propagation, on utilisera les facteurs d'intensité de contraintes calculés à chaque point de la fissure. Le calcul des facteurs d'intensité de contraintes ce fait par la méthode G-θ. Cette méthode permet de calculer l'énergie à chaque point du front de fissure en utilisant une vision Lagrangienne de la propagation de la fissure. À partir de cette valeur, les facteurs d'intensité de contraintes peuvent aussi être calculés. Avec les valeurs de K_I et K_{II} on peut calculer le vecteur de propagation de la fissure et ainsi la faire avancer.

Ce calcul énergétique, extrêmement important, utilise le champ de contraintes autour du front de la fissure. Pour mesurer l'impact des dislocations, et des forces images, on calcule ces énergies deux fois ; la première en tenant en compte de tous les champs de contraintes présents et la deuxième en prenant pas en compte ni les champs des dislocations ni les forces images pour ainsi pouvoir isoler l'effet des dislocations sur les facteurs d'intensité de contraintes.

Une fois le couplage fonctionnel, les premières simulations réalisés quantifient l'impact des paramètres du maillage sur les facteurs d'intensité de contrainte de la fissure. Ces simulations ont permis aussi d'ajuster les paramètres des simulations ainsi que le maillage. Le maillage est composé d'éléments CUB8, qui correspondent à des cubes. La taille d'élément a été choisie telle qu'elle discrétise le volume assez finement pour avoir des résultats précis mais qui n'handicape pas le temps de calcul. La fissure doit être placé au milieu d'un élément pour éviter des problèmes de calcul.

Une fois les paramètres de maille établis, les simulations réalisées visent à comprendre les effets de plusieurs paramètres sur leurs effets sur les facteurs d'intensité de contraintes du front de fissure. Le fait qu'on cherche à comparer nos résultats avec des simulations similaires provenant soit de simulations atomistiques soit de simulations en dynamique discrète des dislocations nous amène à utiliser deux orientations différentes de fissure pour reproduire ces résultats.

La première orientation étudiée correspond à l'orientation utilisée pour les simulations atomistiques d'une fissure qui interagit avec une dislocation. La première simulation menée utilisait les mêmes paramètres que ceux de la simulation atomistique pour en pouvoir comparer les résultats. Les résultats en question montrent un comportement très similaire des dislocations même si le procès de stabilisation est différent. Les contraintes sur les différents systèmes de glissement ont été aussi calculées pour être comparées. La distribution des contraintes permet de séparer les différents systèmes de glissement en catégories en fonction de leurs symétries. Ceci permet de séparer les douze systèmes de glissement en trois catégories. Les effets des dislocations appartenant à la même catégorie ont été comparés pour vérifier si le comportement des dislocations de la même catégorie est similaire. Ces similitudes ont été précédemment observées. Nos résultats montrent une tendance similaire, seule l'intensité de l'effet des dislocations sur l'énergie de la fissure change d'une dislocation à l'autre de la même catégorie. Dans la même catégorie, la nature de l'effet de la dislocation reste inchangée.

Pour compléter ces résultats, une simulation réalisée en atomistique est reproduite avec le couplage DDD et XFEM. Cette simulation consiste en une seule dislocation se déplaçant devant une fissure. Les résultats sont globalement comparables même si le procès de stabilisation de la dislocation n'est évidemment pas le même.

Les catégories mentionnées sont nommées Classe I, Class II et Classe III. Pour les dislocations de la Classe I, on observe un fort effet d'écrantage. Il existe aussi un effet mineur d'anti-écrantage pour ses dislocations. Ceci résulte en une fissure qui est ralentie devant la dislocation mais qui essaye de la contourner en accélérant au tour de la dislocation.

Pour les dislocations de Classe II, on observe le comportement contraire, leur effet est majoritairement d'anti-écrantage avec des zones d'écrantage. La fissure essaye de se propager ver la dislocation le plus vite possible. En observant les courbes énergétiques, il y a une légère baisse d'énergie au point le plus proche entre la fissure et la dislocation. Ainsi, même si globalement, la présence de dislocations de Classe II accélère la propagation, la dislocation en soit la freine légèrement.

Finalement, pour les dislocations de Classe III on observe un mélange des deux comportements sans que l'écrantage ou l'anti-écrantage sont plus prédominant que l'autre. Il faut, cependant, tenir en compte que l'une des dislocations étudiées ici est coplanaire avec la fissure ce qui la rend très proche du front de fissure au point de le croiser. Ceci a sûrement un effet sur l'intensité de l'effet plus que sur sa nature.

Après les études préliminaires, plusieurs paramètres concernant les dislocations sont étudiés pour qualifier leurs effets sur les facteurs d'intensité de contraintes du front de fissure. Les observations réalisées concluent que la nature du système de glissement de la dislocation contrôle la nature de l'effet de la dislocation de la fissure. Cet effet peut être de l'écrantage, de l'anti-écrantage ou un mélange des deux. Chaque catégorie de dislocation a un type d'effet différent sur la fissure comme décrit ci-dessus.

Les simulations sont étudiées à deux moments différents, d'abord avant la propagation des dislocations et aussi une fois les dislocations sont stables. En sachant que la stabilisation des dislocations est atteinte quand l'aire balayait par les dislocations varie moins de cinq pourcents en dix itérations des dislocations, cela implique que chaque configuration aura un temps de stabilisation différent. C'est pour cela que les résultats pré-stabilisation sont considérés aussi.

L'intensité des effets crées par les dislocations est cependant influencée par un nombre d'autres paramètres comme la distance entre la fissure et la dislocation ou le sens de la dislocation. Le premier paramètre étudié était la déformation imposée initiale. En effet, on a étudié une déformation qui correspond à la moitié de la déformation utilisée. Les résultats observés sont cohérents puisque les facteurs d'intensité des contraintes sont divisés en deux entre les deux configurations. La stabilisation des dislocations se fait différemment aussi. En effet, la déformation étant plus faible, la dislocation étudiée ne change pas de configuration puisque la déformation est trop faible pour initier la propagation de la dislocation.

Un autre paramètre important étudié est la direction de la ligne de la dislocation. Deux dislocations ayant le même vecteur de Burgers et le même plan de glissement peuvent se propager dans des directions opposées. La question ici était si la nature de l'effet d'une dislocation sur l'énergie du front de fissure dépendait de ci celle-ci avançait vers la fissure ou pas. Ainsi, les résultats obtenus montrent que seule l'intensité de l'effet de la dislocation est modifiée et pas ça nature. Ceci est aussi cohérent avec les résultats obtenus sur l'effet de la distance entre dislocations et fissure.

Plusieurs dislocations situées à différentes distances du front de fissure ont été étudiées. À plus de 16 nm de la fissure, celle-ci ne perçoit plus le champ de contraintes de la dislocation. Ainsi, plus les dislocations sont proches de la fissure, plus elles en influencent l'énergie.

Le nombre de dislocations a été aussi considéré. Il semble que l'effet des dislocations soit amplifié par le nombre de dislocations présentes. Cette augmentation de l'effet des dislocations est plus importante que la simple addition des effets individuels des dislocations.

Pour mieux comprendre l'effet du nombre de dislocations sur l'énergie du front de fissure trois configurations sont étudiées pour chaque catégorie de dislocation ; 1, 3 et 5 dislocations seront étudiés. Les dislocations ici étudiées sont placées devant la fissure telles que leur centre est à 8 nm de la fissure selon la direction de propagation et équidistantes les unes des autres. L'effet

des dislocations s'additionne, mais pour le cas de cinq dislocations, l'effet et légèrement plus important que celui des cinq dislocations individuelles.

Mis à part l'effet direct sur les valeurs de l'énergie de la fissure, on regarde aussi la longueur de front de fissure qui a été affectée par les dislocations. Chaque dislocation semble influencer une zone de longueur différente, certaines dislocations arrivent à influencer toute la longueur de la fissure.

La deuxième orientation de fissure étudiée correspond à une des orientations étudiées avec de la dynamique discrète des dislocations et une fissure statique. La comparaison des résultats ne peut être que qualitative puisque notre volume et plusieurs ordres de grandeur plus petit puisque la géométrie des simulations atomistiques a été conservée. La géométrie n'a pas été changée pour pouvoir comparer les résultats obtenus entre eux. Le comportement des dislocations reste le même entre nos simulations et les simulations de référence.

Les dislocations qu'on a étudiées précédemment sont aussi étudiées pour cette orientation. Pour la première orientation, on a pu séparer les résultats en fonction des champs de contraintes des différents systèmes de glissement et de leurs symétries. L'orientation de la fissure étant différente, il n'y a plus les symétries qu'on avait observé sur la première orientation. C'est pour cela que les comportements observés ne peuvent pas être généralisés. Chaque dislocation étudiée a un effet différent sur les facteurs d'intensité de contraintes. Et comme observée, plus il y a de dislocations, plus l'effet de celles-ci est magnifié au-delà d'une addition des effets indépendants.

Même si les catégories de dislocations ne sont pas applicables ici, on utilisera les mêmes nomenclatures par soucis de simplicité. Les dislocations de Classe I ont un clair effet d'anti-écrantage sur la fissure. Les résultats pour la simulation contenant trois dislocations ne semblent pas cohérente avec les autres résultats. Ceci est surement dû à une différence de propagation entre les simulations.

Pour les dislocations de Classe II, leur effet sur l'énergie du front de fissure est symétrique à celui des dislocations de Classe I. Connaissant les systèmes de glissement des dislocations en question ainsi que la position de la fissure par rapport à ceux-ci, ces résultats semblent cohérents. Ainsi, les dislocations de Classe II ont aussi un effet d'anti-écrantage sur la fissure, augmentant son énergie.

Quant aux dislocations de Classe III, elles écrantent l'énergie du front de la fissure. Ces résultats montrent que c'est l'orientation de la dislocation ainsi que celle de la fissure qui contrôlent la nature de leurs effets sur la fissure.

En conclusion, on a créé un couplage qui permet la simulation d'interactions entre une fissure qui se propage et une densité de dislocations dans un environnement tridimensionnel. Pour vérifier nos résultats on les a comparés à des simulations faites par d'autres méthodes en utilisant des paramètres similaires voir identiques. On a pu aussi étudier l'effet de plusieurs paramètres des dislocations sur les facteurs d'intensité des contraintes.

Remerciements

J'aimerai tout d'abord remercier le SIMaP et en particulier le groupe GPM2 pour m'avoir accueilli et soutenu pendant ma thèse ainsi qu'à l'ERC pour le financement au projet MicroKIC sans lequel ce travail n'aurait pas pu être réalisé. Un grand merci à mon directeur de thèse Marc Fivel dont le soutient et l'optimisme m'ont aidé à poursuivre la thèse. Merci à Erik Bitzek pour son aide et conseils sur le traitement et présentation des résultats. Je tiens à remercier également Christophe Martin pour son aide lors de la rédaction du manuscrit.

Je remercie également les doctorants du GPM2, Pauline et Alexis pour leur conseils, Fabien pour son aide avec TriDis, Cast3M et les dislocations en général, Jessica pour les après-midis au tour d'une tasse de thé, Brayan, Corentin, Tristan, Loïcia, Mathilde pour leur amitié pendant la thèse. Un grand merci à Benedikt et à Erik pour leur aide et travail sur les simulations atomistiques que ce travail référence et utilise ainsi que pour leurs relectures de mon manuscrit.

Je remercie également l'ensemble des membres du jury de thèse pour leur retour sur mon manuscrit ainsi que pour l'échange scientifique lors de ma soutenance. Je remercie Rémy Dendievel pour avoir accepté de présider le jury de ma thèse, Christian Robertson et Stéphane Berbenni pour avoir rapporté mon manuscrit ainsi qu'à Thomas Pardoen et Vincent Chiaruttini pour avoir évalué mon travail de thèse.

Merci à Gaël, Erwan, Nicolas, Gautier et Maxime pour les parties de jeux de rôle hebdomadaires et les discussions sur la vie de thésard. Merci à Marie-Anne pour être toujours à l'écoute et pour égayer mes journées quand on discutait de tout et de rien. Merci à Lee, Nate, Ashley, Ryan, Jasmine et Kyra pour leur soutient quand j'en avais le plus besoin et à tous ceux qui m'ont aussi accompagné, du moins moralement, pendant ces années.

Je veux remercier enfin mon beau-père, mes oncles, mes tantes et mes cousins pour leur soutient pendant les moments difficiles, pour me pousser à donner le meilleur de moi-même et m'écouter pendant que je radotais sur les dislocations. Le plus grand des mercis à ma mère, sans qui je ne serais pas où je suis aujourd'hui.

À ma grand-mère

Table of Contents

General Introduction

Fracture is one of the most studied problems in materials science and yet plenty remains to be discovered. Even at a macroscopic level, fracture is controlled by the microstructure of the material. Defects in the material are preferential sites of crack nucleation [71] and can also define the crack propagation path [22,28]. Dislocations are the main plasticity carrier in crystalline structures and have been observed interacting with cracks [54,98] as well as nucleating from them [114]. As such, the study of dislocation interactions with cracks is of great importance to understand crack behavior.

There are existing works simulating the interactions between cracks and dislocations. Most of these works use atomistic simulations [17, 129] which limits the size of the studied volume. There exists a study at a mesoscale which used 3D discrete dislocation dynamics to investigate dislocation/crack interactions [70]. However, this work was restricted to the case of a static crack. The aim of this thesis is to use 3D discrete dislocation dynamics with a mobile crack and to investigate the complex dislocation/crack interaction mechanisms during crack advance.

In order to achieve a three dimensional simulation of a moving crack interacting with one or several dislocations we will be coupling two existing methods. For the crack, we will be using eXtended Finite Element Method that allows a precise and indirect approach to crack propagation [126]. The simulation volume will be defined using this method. As for the dislocations, we will be using Discrete Dislocations Dynamics,with the help of the superposition method [137]. This method has already been used successfully with the Finite Element Method before [45]. The objective of this work is therefore to build a new model coupling the two presented methods and verify the results obtained.

This thesis is part of the MicroKIC project funded by European Research Council (ERC-2016-CoG number 725483) and led by Prof. E. Bitzek which aims at investigating the microscopic origins of fracture toughness. This project aims to understand the microscopic crack-tip process during fracture and study its interactions with various microstructural elements. This thesis work will concentrate on crack-tip dislocations interactions. To verify our model, we will compare our results with results obtained using atomistic simulations.

This manuscript is divided into five chapters :

Chapter One starts with an introduction to fracture mechanics and dislocations. It will also review the existing theory, experiments and simulations on crack dislocation interactions.

Chapter Two will introduce various methods for the simulation of a crack. It will also describe the extended finite element method theory, as well as its implementation in code.

Chapter Three will introduce dislocation dynamics simulation methods as well as our implementation of the coupling for the simulations of the interactions between crack and dislocations. The main simulation parameters including the meshed geometry of the simulated volume will also be described and their effects on the results will be analyzed.

Chapter Four will present the accuracy of the model. A study of several individual dislocations to compare their effects between each other will be here presented. A simulation carried out with our model will also be compared to an atomistic simulation carried out using the same parameters.

Chapter Five consists of a case study of the effect of different dislocation parameters on the crack front energy for a given crack orientation. This study aims at a better understanding of the effect of each individual parameter on the crack front energy and how dislocations influence it.

Chapter Six consists of a case study with a different crack orientation. This second orientation was chosen because it allowed our results to be qualitatively compared to previous studies of the interactions between a crack front and dislocations.

This thesis will end with the conclusions and the perspectives for future studies.

1

Bibliographic study of crack-dislocation interactions

Contents

1.1 Introduction

This chapter is a literature survey of fracture mechanics, dislocations and crack - dislocation interactions. While not exhaustive, this chapter aims at establishing the bases on which this thesis stands on.

If the reader wishes more information on this topics, the following publications are available. Regarding dislocations, Hulls and Bacon book *Introduction to dislocations* [64] offers extensive information on dislocations and their dynamics. For fracture mechanics, Zehnder's book titled *Fracture mechanics* [147] includes an ample coverage on the basics as well as more advanced concepts on this subject.

Atomistic simulation is not the topic of this manuscript, but since some of our results will be compared to atomistic simulations, it is still important to understand the method. More information on Molecular Dynamics (MD) simulations can be found in Frenkel and Smit book *Understanding molecular simulation : from algorithms to applications* [52].

1.2 Fracture mechanics

Fracture mechanics is essential in the study of crack propagation. It is specially important in material science, as crack propagation usually precedes catastrophic failure of a material. Macroscopic failure of a material is linked to the microscopic and crystallographic defects existing in said material. Since defects are such a prominent part of fracture study, the understanding of how defects influence crack propagation is primordial to accurately predict material failure.

Crack stress field

A sharp crack creates a stress field in the volume defined in the elastic case as [127] :

$$\sigma_{ij} = \frac{K_I}{\sqrt{2\pi r}} f_{ij}(\theta) + \frac{K_{II}}{\sqrt{2\pi r}} g_{ij}(\theta) + \frac{K_{III}}{\sqrt{2\pi r}} h_{ij}(\theta) \tag{1.1}$$

with r and θ the studied point coordinates and K the stress intensity factor for the corresponding mode. This definition corresponds to Irwin's analytical expression.

This stress field tends to infinity when close to the crack. This is due to the fact that the crack is considered sharp, which creates this discontinuity even if a crack is actually never sharp at the atomic scale. A way to correct this, is accounting for the plastic zone at the crack tip. As illustrated in Figure 1.1, the stress at the plastic zone is considered constant.

Stress intensity factors

Stress intensity factors were established by Irwin [65] and are used as a way to predict the stress state at the crack tip. The stress intensity factors, noted as K, which unit is MPa.m$^{0.5}$, are dependent on the sample geometry, crack length and the loading applied. Since K is related to the crack growth, it can be used to establish failure criteria usually noted as K_C.

As K can also be related to the strain energy release rate G, it will be used on this work for two main purposes. First, to determine both the velocity and then direction of the crack propagation and second to quantify the effect of dislocations on the crack front as we will compare the values of K with and without the effect of dislocations.

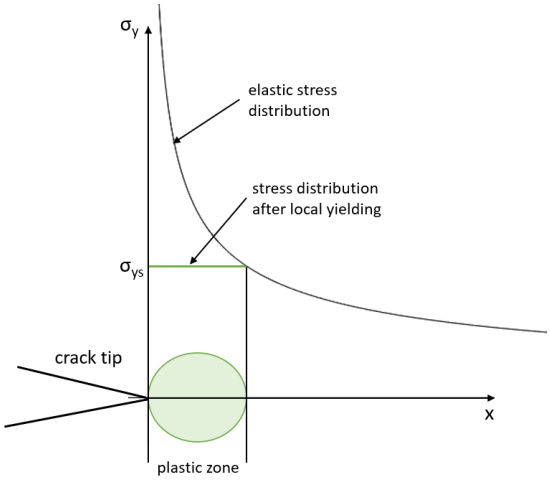

FIGURE 1.1 – *Elastic stress field created by a crack tip. If the plastic zone of the crack tip is taken into account, the stress field of that zone will correspond to the yield stress σ_{ys} (green line)*

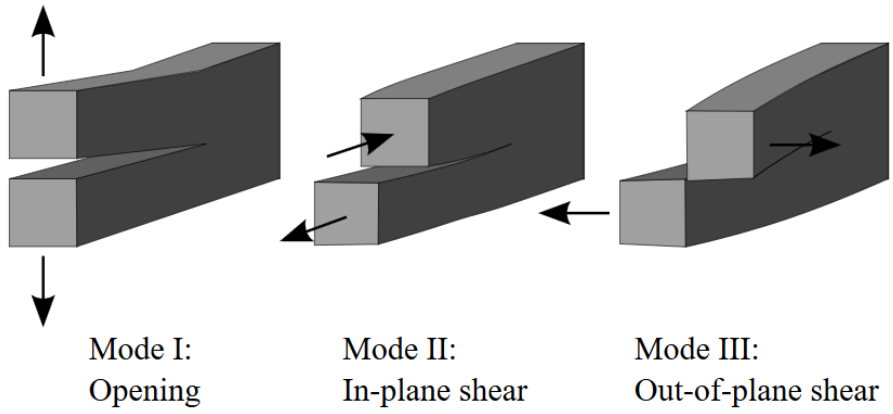

FIGURE 1.2 – *Elementary loading modes for a three dimensional crack [143]*

Loading modes for a crack

There are three main modes of loading for a crack as illustrated in Figure 1.2.

— Mode I : Opening mode

— Mode II : In-plane shear mode

— Mode III : Out-of-plane shear mode

Mode I corresponds to a tensile stress normal to the crack plane, mode II to a shear stress parallel to the crack plane and perpendicular to its front and mode III to a shear stress parallel to both the crack plane and front. To each of these modes is associated a corresponding value K called the stress intensity factor. There is a second value, K_C which corresponds to critical stress intensity factor on the crack beyond which the crack advances. Usually, mode I cracks are the ones considered for study, with their corresponding values K_I and K_{IC}.

Plane stress and plane strain conditions

In the case of 2D modeling, the system can be defined either in terms of plane strain or plane stress modes. In the case of plane stress, the stress vector associated to the third dimension is equal to zero. For plane strain, the strain along the third direction is equal to zero. Plane strain

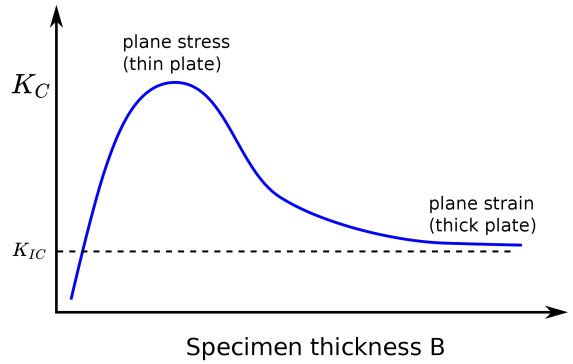

FIGURE 1.3 – *Impact of the thickness of the studied sample on the fracture toughness [144]*

like conditions can be achieved if one dimension of the specimen studied is much greater than the other two dimensions.

Plane stress conditions are used to test the fracture toughness K_C of a material since, as Figure 1.3 shows, K_C can be obtained at plane stress conditions. As for plane strain conditions, they are commonly used to conduct fracture toughness analysis as the crack growth observed occurs on a cycle-by-cycle basis [8].

Energy release rate (Griffith's theory)

In order to propagate, a crack needs a certain amount of energy. This energy is given by the external forces applied to the volume and corresponds to the thermodynamic driving force of the crack advance also known as energy release rate G. G corresponds to the energy available in the solid for the crack to advance. There are some energy criteria that are used to determine the propagation of a crack and if the crack can propagate. The first energy criteria was used for brittle materials and was discussed by Griffith [56]. This criteria was reworked by Irwin [65] to take into account ductile materials for small scale yielding and is defined as :

$$G = 2\gamma + G_p \tag{1.2}$$

With γ the surface energy and G_p the plastic dissipation per unit area of crack advance. Griffith's original equation [56] did not include a term for dissipation resulting in unphysical high surface energy values for ductile materials. In ductile materials, dislocations create a plastic zone around the crack tip which accounts for the higher energy needed for the crack to propagate.

This criteria can also be defined using the stress intensity factor, for example in the case of mode I in the framework of isotropic elasticity :

$$G_I = \begin{cases} \frac{K_I^2}{E} & \text{plane stress} \\ \frac{(1-\nu^2)K_I^2}{E} & \text{plane strain} \end{cases} \tag{1.3}$$

With E Young modulus and ν Poisson coefficient. Equation 1.3 allows an easier way to calculate G for a mode I crack as a dissipation term, that not only includes plastic dissipation but any dissipatory term. It requires an extensive knowledge of the exact structure of the studied material.

1.3 Introduction to dislocations

No real crystalline material is free of defects, which exist in several forms. For example, point defects like vacancies and interstitial atoms or planar defects like stacking faults. In this work, we will be studying particularly dislocations which are linear defects.

Definition of dislocations

The energy required to break a fragile material was described by Griffith [56] as depending on the surface energy of the material. But for ductile materials, the stress actually needed to cause the fracture is several orders of magnitude lower than the stress needed to break the atomic bonds. This was explained by the presence of crack-like defects in the material as the theoretical shear stress was higher than the real yield stress.

Ductile materials are also known for their plasticity. To explain this phenomenon, it was proposed [101] that dislocation movement was at the origin of plastic deformation. It is important to note that at that time, dislocations had not been observed yet but had been theoretically formulated since 1907 [138].

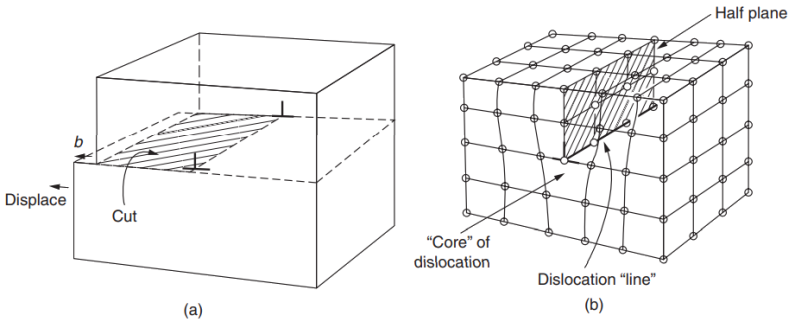

FIGURE 1.4 – *Illustration of an edge dislocation for the continuum view (a) and showing the atoms of the material.(b)* ***b*** *corresponds to the Burgers vector of the dislocation [6]*

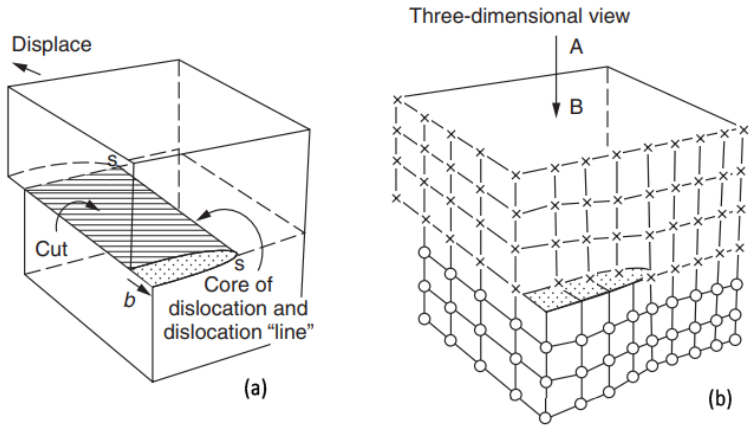

FIGURE 1.5 – *Illustration of a screw dislocation for the continuum view (a) and showing the atoms of the material. (b)* ***b*** *correspond to the Burgers vector of the dislocation [6]*

Dislocations are linear defects present in crystalline structures, they correspond to a sudden change in atomic arrangement. Any dislocation can be decomposed in elementary segment characters named edge, illustrated in Figure 1.4 and screw, illustrated in Figure 1.5 dislocations. In practice, dislocations in materials are usually a mix of these two dislocation types [64].

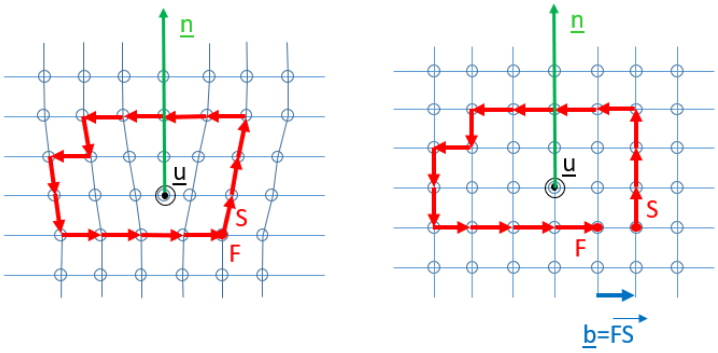

FIGURE 1.6 – *Line vector and Burgers vector illustrated for an edge dislocation. The red arrows represents the Burgers circuit of the dislocation following the RHFS rule [48]*

The Burgers vector defines the magnitude and direction of the lattice distortions created by a dislocation in a crystal, so it can be used to describe a dislocation. This vector, denoted as $\boldsymbol{b}$, can be defined from a Burgers circuit using the Right Hand Finish to Start rule. A Burgers circuit is an atom to atom closed path defined in a deformed crystal containing dislocations as illustrated by the red rectangle in Figure 1.6. When a dislocation is present inside this loop, the same loop defined in the undeformed perfect crystal will be no longer closed. The vector needed to close the loop in the perfect crystal is the Burgers vector $\mathbf{b} = \mathbf{FS}$. The Burgers vector of an edge dislocation is normal to the line vector of the dislocation while the Burgers vector of a screw dislocation is parallel to the line vector.

System	*BC(d)*	*BC(a)*	*DB(a)*	*DB(c)*	*AB(d)*	*AB(c)*
Burgers vector	$[\bar{1}01]$	$[\bar{1}01]$	$[011]$	$[011]$	$[1\bar{1}0]$	$[1\bar{1}0]$
Slip plane	(111)	$(\bar{1}1\bar{1})$	$(\bar{1}1\bar{1})$	$(\bar{1}\bar{1}1)$	(111)	$(\bar{1}\bar{1}1)$
Schmid-Boas notation	B4	D4	D1	C1	B5	C5

System	*DC(a)*	*DC(b)*	*AC(b)*	*AC(d)*	*AD(c)*	*AD(b)*
Burgers vector	$[\bar{1}\bar{1}0]$	$[\bar{1}\bar{1}0]$	$[0\bar{1}1]$	$[0\bar{1}1]$	$[101]$	$[101]$
Slip plane	$(\bar{1}1\bar{1})$	$(1\bar{1}\bar{1})$	$(1\bar{1}\bar{1})$	(111)	$(\bar{1}\bar{1}1)$	$(1\bar{1}\bar{1})$
Schmid-Boas notation	D6	A6	A2	B2	C3	A3

TABLE 1.1 – *Slip systems for face centered cubic crystals*

Slip is defined by the displacement of a part of a crystal relative to the other part along crystallographic planes caused by the passage of a dislocation. In their glide plane, dislocations are shearing the crystal along a given slip direction which is the Burgers vector. The combination of a slip plane and a slip direction is called a slip system. There are four slip planes and six slip directions creating a total of twelve slip systems in face centered cubic crystals (FCC) which is the crystal system that will be used in this thesis. These slip systems are listed in Table 1.1.

Another way to illustrate slip systems is using the Thompson tetrahedron in Figure 1.7. Each face of the tetrahedron corresponds to a slip plane while the edges correspond to the Burgers vectors of perfect dislocations.

Dislocation movement are the carrier of plasticity in materials. It is worth noting that dislocation density is usually between 10^{10} m^{-2} and 10^{12} m^{-2} but it rapidly increases with plastic deformation reaching values of 5×10^{15} m^{-2}. Thermal treatment of the crystal can also lower the

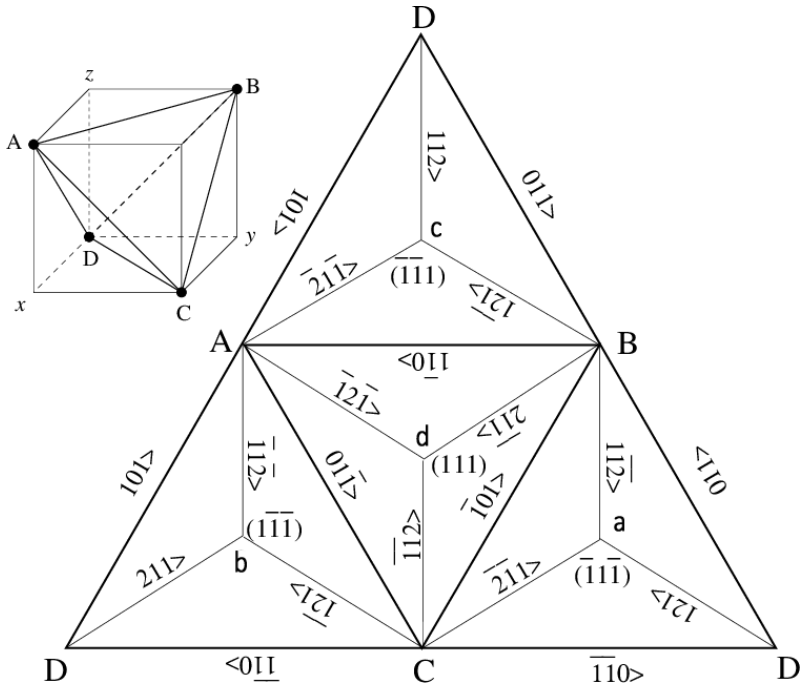

FIGURE 1.7 – *Thompson tetrahedron illustrating the glide planes ((a),(b),(c),(d)) as well as the dislocations Burgers vectors (edges of the tetrahedron) [24]*

dislocation density to a density as low as 10^6 m^{-2} [64].

Stresses created by dislocations

Stress field of a single dislocation

In order to calculate the stress field created by a dislocation, an equivalent elastic distortion can be used [68].

Screw dislocation For an infinite screw dislocation lying on the z-axis, the equivalent elastic distortion is shown in Figure 1.8. As a cylinder of isotropic material is used, the equivalent stress field is easily calculated from the displacement induced by the dislocation :

$$\boldsymbol{U}(r,\theta) = \frac{\mathbf{b}.\theta}{2\pi}. \tag{1.4}$$

It is worth noting that using cylindrical coordinates facilitates these calculations.
Using the equivalent distortion we obtain the following stress for a screw dislocation :

$$\begin{cases} \tau_{\theta z} = \tau_{z\theta} = \frac{Gb}{2\pi r} \\ \sigma_r = \sigma_\theta = \sigma_z = \tau_{\theta r} = \tau_{r\theta} = \tau_{rz} = \tau_{zr} = 0 \end{cases} \tag{1.5}$$

With G the shear modulus and b the magnitude of Burgers vector. Since there are only displacements in the z direction, this field is purely shear. In Cartesian coordinates the stress fields corresponds to :

$$\begin{cases} \tau_{xz} = \tau_{zx} = -\frac{Gb}{2\pi}\frac{y}{x^2+y^2} \\ \tau_{yz} = \tau_{zy} = \frac{Gb}{2\pi}\frac{y}{x^2+y^2} \\ \sigma_x = \sigma_y = \sigma_z = \tau_{xy} = \tau_{yx} = 0 \end{cases} \tag{1.6}$$

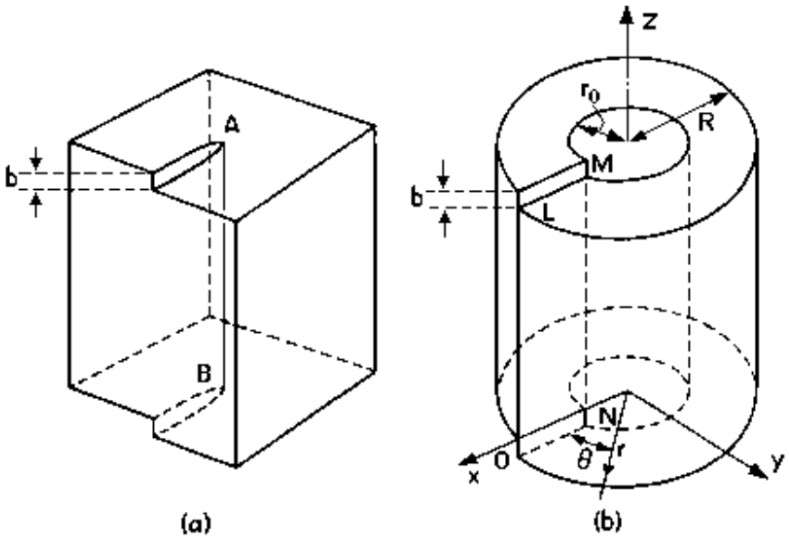

FIGURE 1.8 – *(a) Screw dislocation in a crystal. (b) Cylinder subjected to an elastic distortion equivalent of the dislocation caused by the infinite screw dislocation presented in (a) [64]*

Edge dislocation The same approach can be used on edge dislocations though it leads to a more complex expression of the stress field. The distortion of an infinite edge dislocation can again be assimilated to the distortion created on a cylinder as illustrated in Figure 1.9.

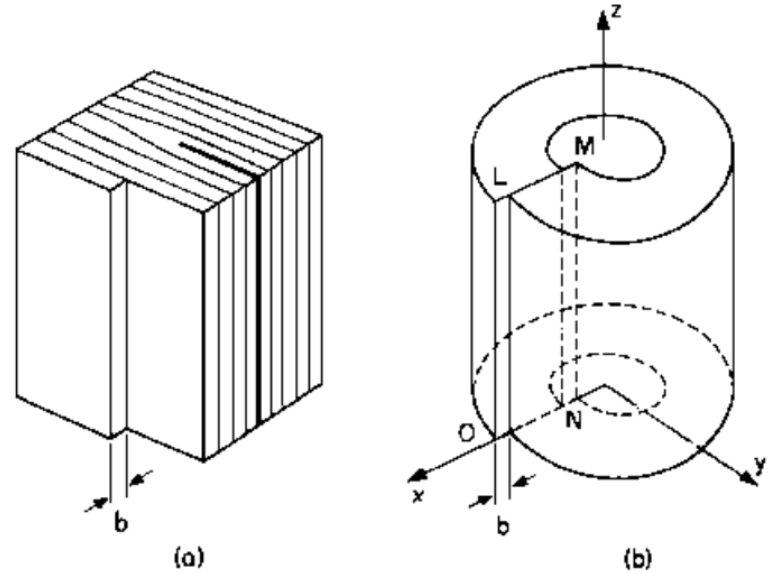

FIGURE 1.9 – *(a) Edge dislocation in a crystal. (b) Cylinder subjected to an infinite elastic distortion equivalent of the dislocation caused by the edge dislocation presented in (a) [64]*

In cylindrical coordinates, the stress field of an infinite edge dislocation lying on the z-axis is :

$$\begin{cases} \sigma_r = \sigma_\theta = -\frac{Gb}{2\pi(1-\nu)}\frac{\sin\theta}{r} \\ \tau_{\theta r} = \tau_{r\theta} = \frac{Gb}{2\pi(1-\nu)}\frac{\cos\theta}{r} \\ \sigma_z = \nu(\sigma_r + \sigma_\theta) \\ \tau_{\theta z} = \tau_{z\theta} = \tau_{rz} = \tau_{zr} = 0 \end{cases} \tag{1.7}$$

With G the shear modulus, b the Burgers vector magnitude and ν the Poisson's ratio. This field can be converted to Cartesian coordinates to obtain the following results :

$$\begin{cases} \sigma_x = -\frac{Gb}{2\pi(1-\nu)} y \frac{(3x^2+y^2)}{(x^2+y^2)^2} \\ \sigma_y = \frac{Gb}{2\pi(1-\nu)} y \frac{(x^2-y^2)}{(x^2+y^2)^2} \\ \tau_{xy} = \tau_{yx} = \frac{Gb}{2\pi(1-\nu)} x \frac{(x^2-y^2)}{(x^2+y^2)^2} \\ \sigma_z = \nu(\sigma_x + \sigma_y) \\ \tau_{xz} = \tau_{zx} = \tau_{yz} = \tau_{zy} = 0 \end{cases} \tag{1.8}$$

About the dislocation core It is worth noting that the equations above are all based on an equivalent elastic distortion within a cylinder. While broadly used for the study of dislocations, these fields tend to infinite stresses when r tends to zero since the stress varies inversely with the distance to the center of the dislocation. There is a limiting radius of $r_0 = 5 \sim 10$ Å below which the above elastic solution does not apply. The core of the dislocation is not a continuum, for an accurate result the forces between individual atoms must be considered.

Dislocations interactions

Two dislocations can interact with each other. As seen above, the stress field of a dislocation inversely varies with the distance to the center of the dislocation. Two dislocations of same Burgers vector and same line direction will exert a repulsive force on each other. On the other hand, two dislocations of opposite Burgers vector or opposite line orientation will attract each other and may combine.

Peach Koehler force

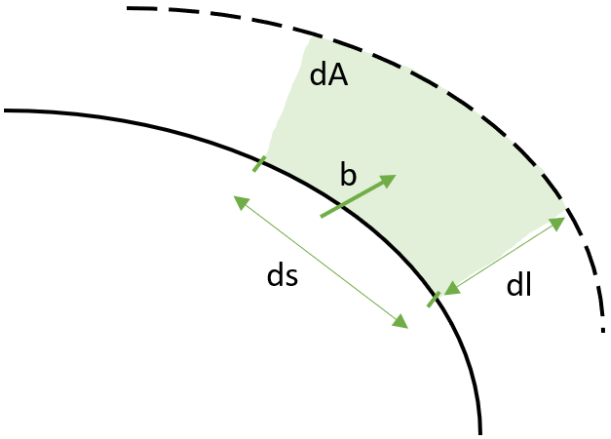

FIGURE 1.10 – *Movement of a dislocation of Burgers vector* $\boldsymbol{b}$*. The dislocation of length* ds *moving over a distance* dl *swipes an area* $dA = ds.dl$

When a force is applied to a crystal containing dislocations, this force will act on the dislocations. If the dislocation moves and sweeps and area dA (see Figure 1.10), it will lead to an increment of the plastic shear strain accumulated in the material equals to :

$$d\Gamma = \frac{b.dA}{V} \tag{1.9}$$

The magnitude of force F acting on a dislocation is defined from the work (dW) done when a unit length of dislocation (ds) moves a unit distance (dl) as illustrated in Figure 1.10 :

$$F = \frac{dW}{dsdl} = \frac{dW}{dA} = \tau b \tag{1.10}$$

τ corresponds to the effective shear stress felt by the dislocation. This shear stress is resolved on the dislocation glide system and is induced by the applied load and all the other dislocations contained in the crystal.

Image forces

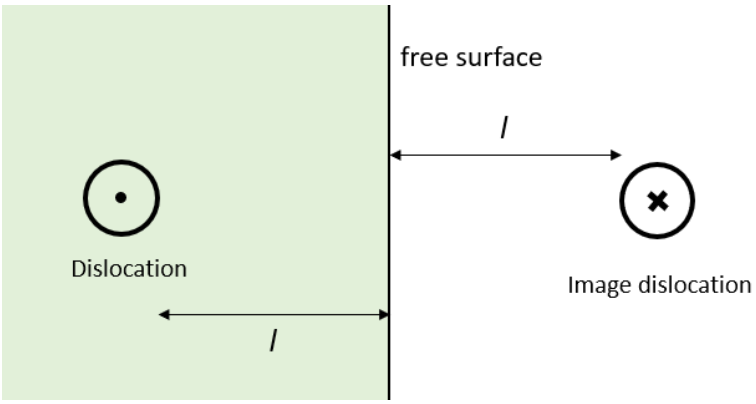

FIGURE 1.11 – *Image force created by a free surface on a dislocation. Both the dislocation and the image dislocation are equidistant from the free surface. This example is illustrated for an infinite screw dislocation*

Dislocations generate stresses on free surfaces but since these are traction free surfaces, the boundary conditions induces image forces on the dislocation [64]. In the elementary case of an infinite screw dislocation parallel to the free surface, this image force corresponds to the one induced by a mirrored dislocation of opposite sign located outside the crystal. This gave the name of image forces to the back forces exerted on dislocations induced by the presence of free surfaces. These image forces are illustrated in Figure 1.11.

In the general case of dislocations with any possible line orientation and random Burgers vector, the mirroring analysis is not valid any more. Nevertheless, the free surface will exert forces on the dislocation which are still called image forces. As seen later in this thesis, the image forces can be estimated by solving a boundary value problem where the traction free condition is enforced at the surface, for example using an FEM calculation.

Dislocation movement

Dislocations move in two basic types of movement. Conservative motion, or glide, corresponds to the movement where the dislocations move in the plane defined by their line and Burgers vectors. Non-conservative motion, or climb corresponds to the movement where a dislocation moves out of its glide surface. In the following, only conservative motion will be taken into account since non-conservative motion is not relevant to our case studies.

Dislocation mobility

Dislocation mobility is a fundamental property of crystals impacting its plasticity. A dislocation velocity v can be defined as [78] :

$$v = \frac{\tau.b}{B} \tag{1.11}$$

with τ the shear stress, B a viscosity coefficient corresponding to the dislocation-phonon interaction and b the magnitude of the Burgers vector.

Cross slip

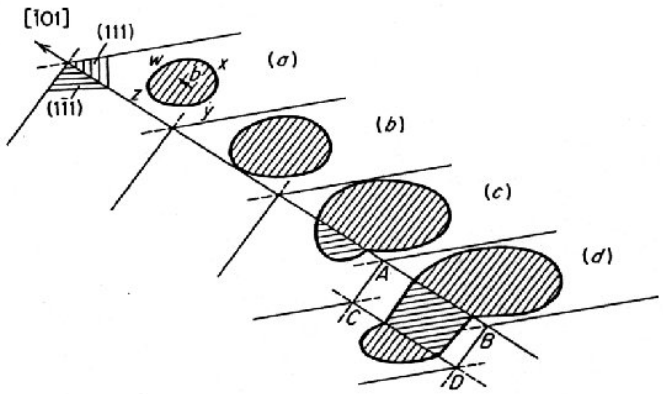

FIGURE 1.12 – *Cross slip mechanism A dislocation loop in the* (111) *slip plane (a) is moved due to the stress applied on the* $(1\bar{1}1)$ *plane (b). Since the z part of the dislocation is pure screw, it is free to expand on the other plane (c). The dislocation can cross slip again to the original slip plane in what is called doucle cross slip (d) [64]*

In face-centered cubic metals, screw dislocations are able to switch from one $\{111\}$ type plane to another $\{111\}$ type plane. As described above, dislocations can move in the plane defined by its line and Burgers vector. These vectors are co-linear for pure screw dislocations allowing them to move on more than one plane. In the case of FCC, there exists two slip planes sharing a given Burgers vector as shown on the Thompson tetrahedron 1.7. The cross slip mechanism is illustrated in Figure 1.12 and it is thermally activated.

Dislocation nucleation

There are several dislocation nucleation mechanisms. Here, two of them will be presented in detail, but it worth noting that other mechanisms exists including multiplication by climb, from prismatic loops or by multiple cross glide. For more details on these mechanisms, the reader can refer to Hulls *Introduction to dislocations* [64].

Frank-Read sources

Frank-Read sources, as illustrated in Figure 1.13, are dislocations pinned in the volume either by other dislocations, precipitates or other obstacles in the volume. When a stress is applied, these dislocations will bow out and loop around creating a new dislocation loop.

Nucleation at stress concentrations

Aside from the Frank-Read sources, there are other dislocation multiplication mechanisms. Dislocation nucleation occurs when a dislocation is created in a zone of the crystal free of any defects. This nucleation, also named homogeneous nucleation, can only occur under extreme conditions which can be estimated [36] :

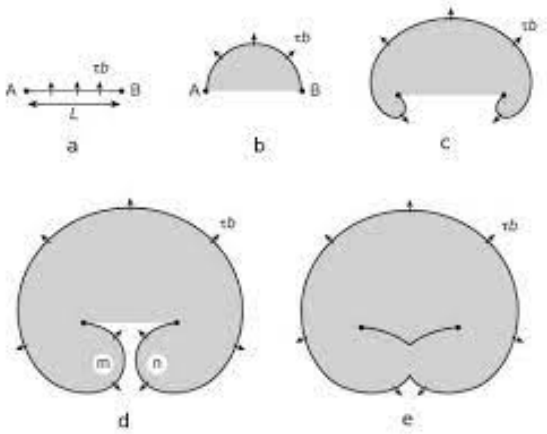

FIGURE 1.13 – *Frank-Read source mechanism. Shaded area corresponds to the zone where slip occurred. [108]*

$$\tau_N \simeq \frac{G}{30}, \tag{1.12}$$

with τ_N the stress required for the nucleation to occur and G the shear modulus. In practice, the stress τ_N is much higher than the stress at which plasticity starts. It is highly unlikely such stresses are reached everywhere in the volume, though it could be reached locally. Therefore, on stress concentration zones, such as the stress caused by an inclusion on the crystal or by the presence of cracks, dislocations can nucleate.

1.4 Crack - dislocations interactions

Since dislocations create the plastic zones developped near the crack tip, their presence is inherently tied to crack propagation, or lack thereof. Aside from the plastic zone, dislocations also directly interact with the crack. These interactions can be observed, but the observation methods cannot cut out all the possible parameters that affect dislocations and crack. Therefore, simulations not only allow to study more specific and controlled cases but also to measure variables in a more precise manner.

Theory of dislocation - crack interactions

Dislocations can interact in several ways with a crack which could mainly be decomposed into shielding and antishielding effets. Shielding is defined when the presence of a dislocation is lowering locally the stress intensity factors of a crack, it also affects the nucleation of dislocation on the crack front. The concept of shielding was first proposed by Thompson and Weertman [131, 141]. Antishielding corresponds to a local increase in the local stress intensity factors of a crack created by the presence of a dislocation.

Interactions between dislocations and cracks can be divided in two categories. First, the dislocations nucleated from the crack itself and second the dislocations already present in the bulk of the cracked material. Dislocations nucleated from the crack have usually a shielding effect since they were generated in order to accommodate the crack advance. On the other hand, pre-existing dislocations can have both effects. In this work, we will focus on the effect of a pre-existing dislocation population on the crack.

Between the crack tip and the plastic zone, there is evidence of a Dislocation-Free Zone (DFZ) [15, 83]. This zone has been shown to be a consequence of the presence of a barrier to dislocation emission from the crack tip. Dislocations are still able to enter this zone and interact directly with the crack. This zone limit corresponds to the equilibrium between the crack force and the lattice friction force [99].

The effect of the dislocations on the crack can be quantified by their effect on the stress intensity factors. The method of conformal mapping [82] can be used to determine the shear stress, τ, acting along the crack propagation direction at a distance x from a crack tip due to a screw dislocation located at a distance r on a coplanar slip plane :

$$\tau = -\frac{\mu b}{2\pi}\sqrt{\frac{r}{x}}\frac{1}{r-x} \tag{1.13}$$

This configuration is specially useful for estimating the effect of dislocations emitted from the crack. For a point at the vicinity of the crack tip ($x \to 0$), the stress field reduces the stress intensity factor k by a magnitude of [73] :

$$k^D = \lim_{x\to 0}\sqrt{2\pi x}\tau = -\frac{\mu b}{\sqrt{2\pi x}} \tag{1.14}$$

Denoting K the applied stress intensity factor, the local intensity factor k is equal to :

$$k = K + k^D \tag{1.15}$$

Therefore, if k^D is negative, the stress intensity factor will decrease locally creating a shielding effect. On the other hand, for a positive k^D, the presence of the dislocation will create an antishielding effect on the crack.

Another mechanism observed between dislocations and crack is the blunting of the crack tip by dislocations [142]. One of the theorized ways for this blunting is described by the emission of dislocations at the crack tip. This emission can therefore blunt the crack tip by the formation of the plastic steps on the crack surfaces. This will slow down its propagation as the stress is reduced when the tip is not infinitely sharp.

Experimental observations

There are several methods that have been used to observe dislocation crack interaction such as, etch pit studies [33], X-ray topography [61, 91], in situ TEM [62, 100] or AFM [115].

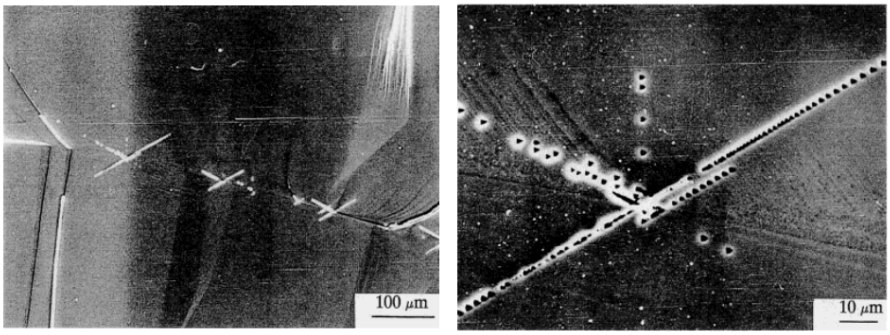

FIGURE 1.14 – *SEM observation of dislocation emission from direct sources along the crack front on silicon. Crack plane :* $\{\bar{1}10\}$*, propagation direction :* $\{\overline{111}\}$*, T = 885K, brittle fracture at* $K = 1.11K_{IC}$*. Etch pattern of the crack surface. [115]*

One of these studies, [115], is based on the AFM technique and focuses on Silicon samples since it is a material often used as reference. In this study, several phenomena were observed using

SEM (scanning electron microscope) like the dislocation emission from various sources on the crack front, as illustrated in Figure 1.14. This emission is inhomogeneous and may use ledges on the crack as nucleation sites. There is no evidence of spontaneous emission of dislocations which is corroborated by what is known so far about spontaneous emission. As for the plastic zone, it seems that it is mostly formed by either preexisting dislocations or dislocations emitted from remote sources rather than being created by the crack front itself.

Simulations

The direct observation of dislocation crack interactions is extremely difficult and can be further complicated by the lack of control over the dislocations and the exact geometry of the crack. Simulations allow a complete control over the studied parameters as well as an ease to individually test each parameter.

Atomistic simulations

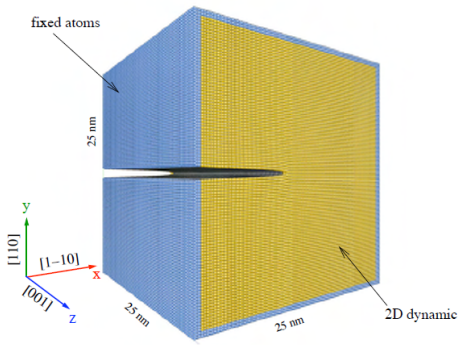

FIGURE 1.15 – *Example of a 3D arrangement of atoms with a crack used for atomistic simulations [16]*

Molecular dynamics is a simulation method consisting on solving numerically Newtons equation of motion for a system of interacting atoms using a discrete time step. This method is used in several domains like chemistry [81], microbiology [51] or material science [60].

A 3D arrangement of atoms such as the one in Figure 1.15 can be used to study the interactions between a crack and a dislocation. In the example of Figure 1.16, a dislocation loop is emitted from the crack front after another dislocation interacts with it. As DDD simulations can be run using a nanometric volume, we will be able to compare our results with what has been done in atomistic simulations.

The limitation constraint of this method is the size of the simulation box. As all the atoms are simulated, the simulations are usually of nanometric scale, which, while extremely accurate, limits what can be simulated. Moreover the simulated time is limited to a few nanoseconds, the time step being of the order of 10^{-15} s.

Discrete Continous Model

Discrete-Continous Model(DCM) has been used to simulate the effect of dislocations on a crack front [70]. These simulations are carried out with a static crack in a micrometric volume containing a large population of dislocations belonging to any of the twelve possible dislocation systems of FCCC crystals.

Figure 1.17 corresponds to the final stage for a DCM simulation containing a crack. As the crack was explicitly introduced in the simulated volume, the code had to be modified to be able to

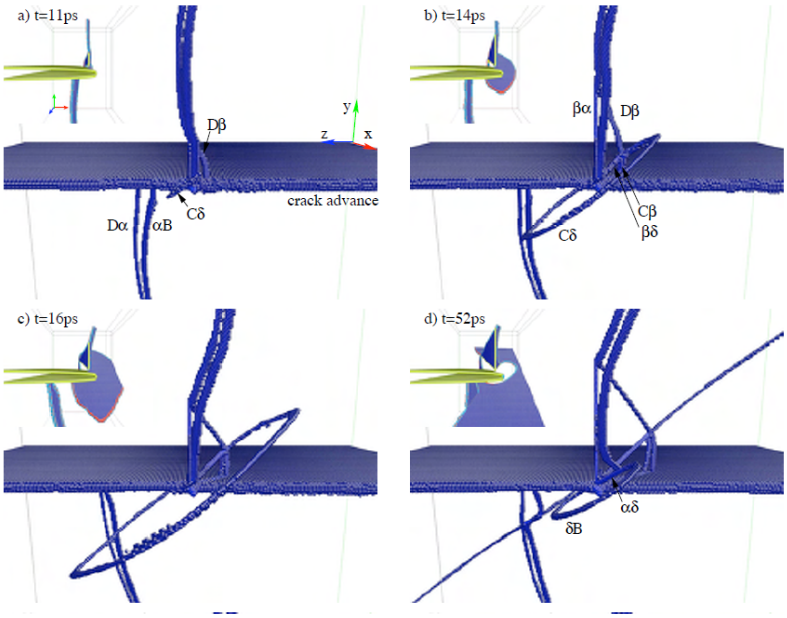

FIGURE 1.16 – *Example of an atomistic simulation containing a crack and a dislocation and their following interactions [16] : A 60° dislocation of Burgers vector DB(a) creating a stimulated emission of a dislocation loop*

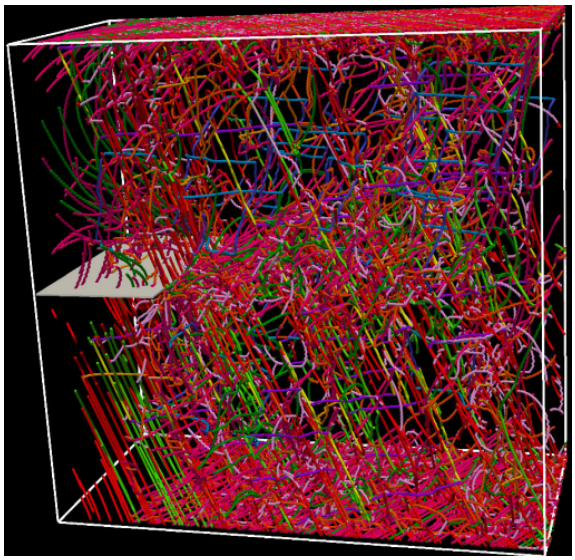

FIGURE 1.17 – *Configuration of a DCM simulation containing a crack and a dislocation microstructure (color lines). Each color represents a different dislocation slip system [70]*

accommodate a concave surface. Comparisons with Crystal Plasticity were carried out to validate the model.

These simulations were able to separate the different contribution factors to the total strain as illustrated in Figure 1.18 as well as to measure the stability of a crack though they do not consider the individual contribution of dislocations nor they could study the case of a propagating crack as the studied crack was static.

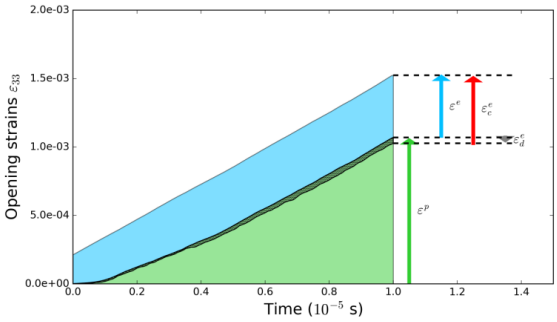

FIGURE 1.18 – *Relative contributions to the total opening strain field ε_{33} in the DCM simulations : ε_p the plastic strain in green, ε^e_c the elastic strain associated with the crack, ε^e_d the elastic strain associated with the dislocation microstructure, ε^e the total elastic strain [70]*

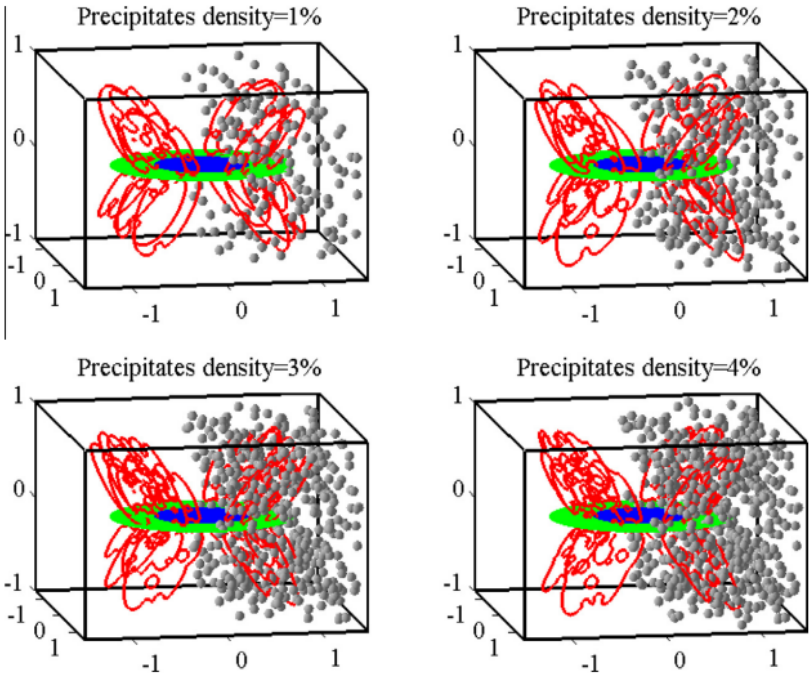

FIGURE 1.19 – *3D presentation of Frank-Read sources (red lines) interacting with different precipitate densities (grey spheres). The blue disk represents the crack in XFEM and the surrounding green zone its propagation area [69]*

Extended Finite Element Method and Dislocation Dynamics

A study by Keyhani et al. [69] has been carried out combining both eXtended Finite Element Method and Dislocation Dynamics to represent plasticity both at a macro scale with a propagating crack and at a micro scale with the dislocations as illustrated in Figure 1.19. This method combination was used to study the effects of precipitates on a crack propagation. This methodology is similar to what has been done in this study but in our case, the crack opening takes into account the dislocations fields and advances accordingly. Additionally, we concentrate in the crack front stress intensity factors instead of the dislocation propagation.

1.5 Conclusion

In this chapter the principles of fracture mechanics that will be used in this work were introduced. Especially what concerns crack stress fields and their local stress intensity factors. Dislocations were also introduced in this chapter as, alongside cracks, dislocations are the main focus of this work. Dislocation movement and forces created by them were also reviewed.

Interactions between dislocations and crack were discussed, introducing their theoretical aspects and what has been observed experimentally and on various simulations.

2

Extended finite element method

Contents

2.1 Introduction

There are several methodologies able to simulate crack propagation. In this chapter we will review the main existing methods, and, in particular the eXtended Finite Element Method which is the method used in this work. If the reader wishes more details on crack propagation simulations they can refer to the French book from Pommier et al. titled *La simulation numérique de la propagation des fissures en milieux tridimensionnels, fonctions de niveau, éléments finis étendus et critères énergétiques* [106] which contains a practical and substantial explanation of three dimensional crack simulations.

2.2 Continuum simulations methods for the study of crack propagation

Simulation for crack advancement has always been a complicated topic. Crack propagation implies a change in the geometry of the studied volume, creating new surfaces as the crack propagates. These new surfaces are numerically a problem since energy conservation is hard to achieve using traditional simulations methods such as finite elements (FEM). There are nonetheless a variety of methods used to simulate crack propagation, some of which are presented here.

Introduction to FEM

The bases of the finite element method was first developed during the fifties [5, 133], but its name was coined later by Clough [34]. This method was created to numerically solve partial differential equations problems.

The first step of this method is the discretisation. It consists in dividing the entirety of the studied volume into elements that do not overlap and are connected by nodal points. These elements usually are elemental geometry shapes like cubes or tetrahedra for the three dimensional cases. Each element and its displacement is described by the positions of the nodal points. This method consists on using an algorithm to determine an approximate result of the partial differential equations that define the volume's equilibrium state. In FEM, the unknown is the displacement of the mesh nodes. In each element, the displacement is interpolated from the nodal values using shape functions. In the case of 8 node-elements as shown in Figure 2.1, the shape functions consists of second order polynomials. In the case of linear elasticity, once introduced in the weak form of the partial differential equation, it leads to a linear system to solve :

$$\boldsymbol{K}.\boldsymbol{U} = \boldsymbol{F}, \tag{2.1}$$

where **U** is the nodal displacement field.

When the global boundary conditions are known, the elastic problem can be solved and the solution is unique.

Finite element method is used in a wide range of domains due to its ability to deal with complex shapes, like the one illustrated in Figure 2.1. This method has been used in domains such as heat transfer fluid dynamics [109], structure design [58] or even biology [104].

Node release scheme in FEM

The node release scheme was first developed by Newman [96]. This 2D method, illustrated in Figure 2.2, consists in releasing the node delimitating the crack tip to represent its advancement. At each release, the load is also adjusted since the resting area it is reduced [120]. This method

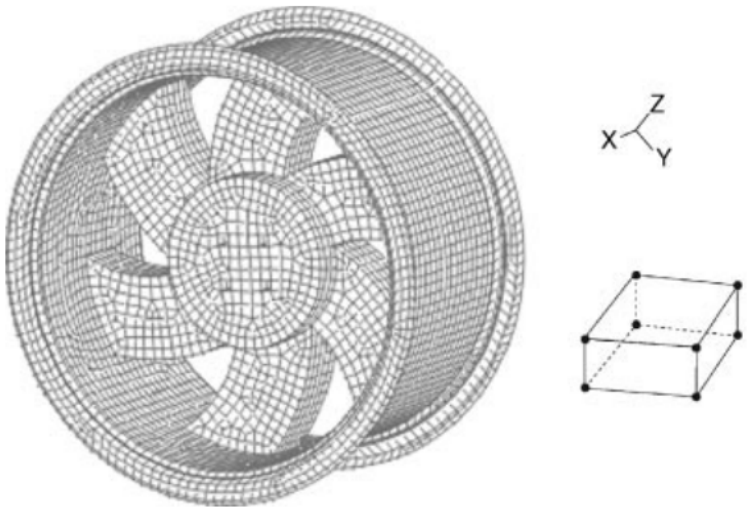

FIGURE 2.1 – *Example of a wheel meshed created with 8-node elements for a finite element simulation [10]*

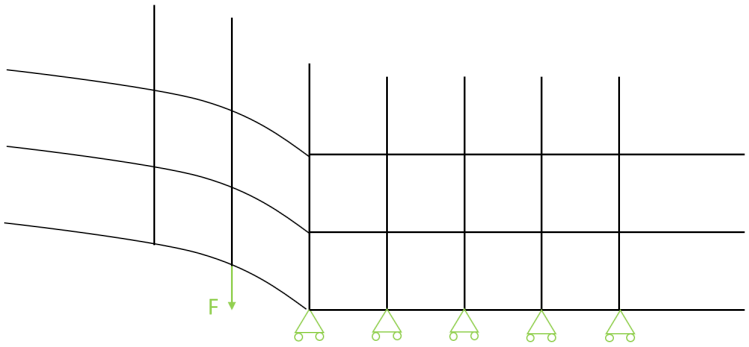

FIGURE 2.2 – *Node release scheme. The nodes of the mesh will be released to represent the crack advancement*

imposes *a priori* knowing the path the crack will take beforehand and forces the crack tip to always be situated on a node.

While this method easily allows representing a crack in 2D, a 3D representation is more complex, especially if the crack is not straight. The crack advancement per iteration is determined by the mesh size, which is a parameter chosen by numerical needs, not using a material parameter. In this model, the crack growth rate is an average, making the advancement in this scheme arbitrary [86, 87].

This method has been mainly used to study fatigue cracks [112, 113, 121].

Remeshing methods

These methods, illustrated in Figure 2.3, consist in remeshing the volume near the crack tip when it advances in the volume. This allows an accurate representation of the fields near the crack tip. The algorithms used for these methods are often very complex since it requires to transfer the state variables of the former mesh to the new one. Remeshing is mainly implemented in two dimensional simulations and has been used to simulate interactions between cracks and inclusions for either brittle or ductile materials [19, 20, 118].

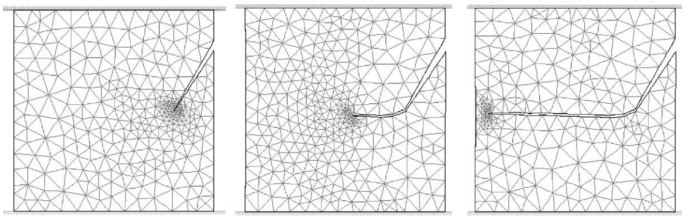

FIGURE 2.3 – *Example of a crack trajectory obtained with a remeshing method [20]*

There are two main error sources in these methods. First, once the remeshing is done, the solution of the previous step needs to be projected on the new mesh. Being a finite element method, the solution is not only discrete but the new mesh does not have the same nodes as the previous one making it impossible to do a simple projection and still have balanced fields. A rebalancing step is then added, but it does not guarantee there will be mechanical energy conservation during the projection. The second error source is simply the fact that new surfaces are created at each step. The discrete systems energy is heavily modified during the projections leading to a number of numerical errors on the crack propagation itself if not done properly [110].

There are some other methods close to the remeshing method like the moving element method [97], which consist in moving the nodes belonging to elements near the crack tip to take into account the new crack position or the use of space-time finite elements, for which time schemes can be treated with Galerkin type formulation for example [1, 63].

Element deletion method

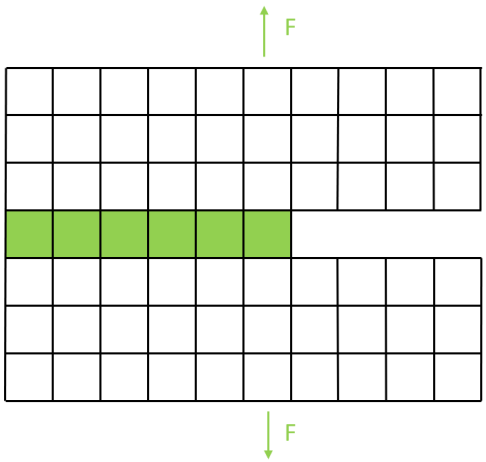

FIGURE 2.4 – *Element deletion method : The green elements will be removed to represent the crack advancement*

This method illustrated in Figure 2.4 consists in taking the elements that have reached a breaking criteria and setting their Young's modulus to zero, thus deleting the element in question. In some cases, the mass of the element is deleted too. This method is largely used in industrial settings, but it can be very inaccurate [21, 75].

If the crack path does not coincide with the mesh, the crack path is more inaccurate. It has been found that this method constantly underestimates the speed of cracks, making it unreliable. It is also heavily dependent on the mesh size since it is the removal of the elements that creates the crack [122].

Cohesive elements method

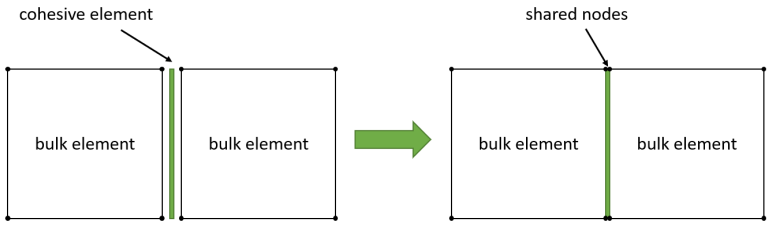

FIGURE 2.5 – *Cohesive elements method. An element (green) with no thickness is introduced between the two starting elements*

This method, based on the Dugdale-Barenblatt model [130], consists in introducing two dimensional elements between the elements that compose the studied mesh as illustrated in Figure 2.5. These surfaces have a behavior law that normally includes the link between the crack displacement and the opening stress. These introduced elements modify the rigidity of the whole mesh as they possess their own rigidity even if their thickness is equal to zero.

The main problem with this model is that it is heavily mesh dependent. Since cracks can only propagate on interfaces, its geometry will be totally dependent on the mesh [146]. To avoid some dependence, some works have used the cohesive elements to represent grain boundaries and study intergranular fracture [145]. Despite this major issue, this method is still often used for crack propagation in rocks [67, 145] and composite laminates [80].

There have been adaptations of the cohesive element method. For example in [25,37,103,148], cohesive elements are only added to the mesh once the elements reach a certain stress near the crack tip.

2.3 Extended finite element method (XFEM)

XFEM is based on the Finite Element method and uses the partition of unity presented bellow to take into account the deformation produced by the crack [4,59,92,124]. Contrary to the remesh methods, in XFEM the mesh remains the same during the entire simulation, but the elements that contain the crack are harshly distorted [11, 149]. The crack position is tracked by the level set method [102] and the propagation is determined from the estimation of the energy at the crack front calculated by the G-θ method [111].

The partition of unity

This method was first used by Benzley [14], and was further formalized by Babuska and Melenk [7, 88]. It has been used in a multitude of fields, aside fracture mechanics, such as fluid mechanics [30, 31, 139, 140], phase transition [32, 90] or the modeling of inclusions [125]. The partition of unity allows enriching the classic finite element method to represent a given function on a given domain. The finite element interpolation of the displacement field at any point $\boldsymbol{x}$ is as follows within an element Ω_e :

$$\boldsymbol{u}(\boldsymbol{x}) \mid_{\Omega_e} = \sum_{i \in N_n} \sum_{\alpha} \boldsymbol{d}_i^{\alpha} \phi_i^{\alpha}(\boldsymbol{x}), \tag{2.2}$$

with N_n the set of nodes on the element Ω_e, $\boldsymbol{d}_i^{\alpha}$ the displacement of node i in the α direction and ϕ_i^{α} the corresponding shape function.

Since the degrees of freedom of a node are the same for all the elements connected on said node, the interpolations in each element can be combined to give the global interpolation that will be valid for every point $\boldsymbol{x}$ of the domain :

$$\boldsymbol{u}(\boldsymbol{x}) = \sum_{i \in N_n(x)} \sum_{\alpha} \boldsymbol{d}_i^{\alpha} \phi_i^{\alpha}(\boldsymbol{x}), \tag{2.3}$$

with $N_n(\boldsymbol{x})$ the set of nodes of the element including $\boldsymbol{x}$. It is possible to enrich the finite element approximation of the displacement field the following way :

$$\boldsymbol{u}(\boldsymbol{x}) = \sum_{i \in N_n(x)} \sum_{\alpha} \boldsymbol{d}_i^{\alpha} \phi_i^{\alpha}(\boldsymbol{x}) + \sum_{i \in N_n(x) \cap N_F} \sum_{\alpha} \boldsymbol{d}_i^{\alpha} \phi_i^{\alpha}(\boldsymbol{x}) F(\boldsymbol{x}), \tag{2.4}$$

with $F(\boldsymbol{x})$ the enrichment functions on the Ω_F domain and N_F the nodes for which their supports intersect with the Ω_F domain.

In order to account for the discontinuities a crack creates, two sets of enrichment functions are added to the corresponding nodes [46] : the first function $\mathscr{H}$, also known as Heaviside function, corresponding to the discontinuity created by the crack on the volume, the second set of functions $\mathscr{F}_j$ for $j = \{1...4\}$ corresponding to the crack tip enrichment.

This enrichment is defined in a cylindrical framework with r the distance to the crack tip and θ the angle between the crack propagation direction and the concerned point. The functions are defined as follows :

$$\mathscr{H}(x,y) = \begin{cases} -1 & \text{for } y < 0 \\ +1 & \text{for } y > 0, \end{cases} \tag{2.5}$$

$$\mathscr{F}_j(\boldsymbol{x}) = \sqrt{r}\{\sin(\frac{\theta}{2}), \cos(\frac{\theta}{2}), \sin(\frac{\theta}{2})\sin(\theta), \cos(\frac{\theta}{2})\sin(\theta)\}. \tag{2.6}$$

These enrichments are the ones used by Moës et al. [93] on the first development of this method. They were generalized to three dimensions by Sukumar [125]. The generalization remains very close to the two dimensional version, replacing the crack tip, previously a point, by a curve, the crack, previously a curve, by a surface and using a volume as element support. These functions are applied to different elements depending on where the crack is located in the mesh. It is worth mentioning that the first of the four $\mathscr{F}_j$ functions is discontinuous at the crack as it represents the discontinuity induced by the crack tip. The functions defined by $\mathscr{F}_j$ are derived from linear elasticity and correspond to an approximation of the stress field created by the crack tip [50].

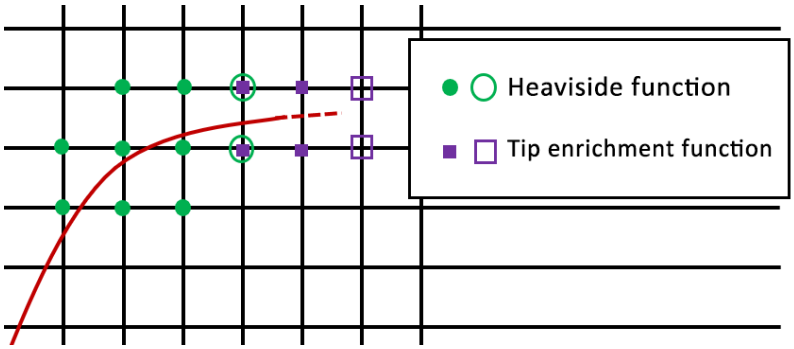

FIGURE 2.6 – *Node enrichment for a two dimensional crack at time t (full symbols) and at time $t + \delta t$ (hollow symbols). The crack advancement between the two times corresponds to the doted line*

As illustrated in Figure 2.6, the element containing the crack front will be enriched with the $\mathscr{F}$ functions while the elements containing the surfaces of the crack are enriched with the Heavi-

side function $\mathscr{H}$. When the crack advances, the elements are once again enriched. The previous enrichments are not removed since it would impact the energy equilibrium of the volume.

Level set method

The partition of unity method was used here to modify the interpolation inside the elements intersected by the crack. Thus the crack needs to be tracked in order to accordingly enrich the intersected elements. In order to track this interface, some methods use an explicit approach which leads to the remeshing of the volume as the crack advances. Other methods, like the volume of fluid method, allows the tracking of the interface by assigning a value at each element representing what fraction of the element is in the interior of the established boundary. Instead of trying to define the interface in an explicit way, the level set method, first developed by Osher and Sethian [102], consists in using an Eulerian approach for the definition of the interface.

Method generalities

The level set method has been implemented in many fields [128] such as image processing [84] or crystal growth and germination modeling [117]. Level set functions are used to model interfaces [23, 29, 116]. An interface is modeled by a continuum function defined at every point of the studied space and that results in the distance between said point and the interface. The interface being oriented, the function will be signed depending on what side of the interface the studied point is situated as illustrated in Figure 2.7.

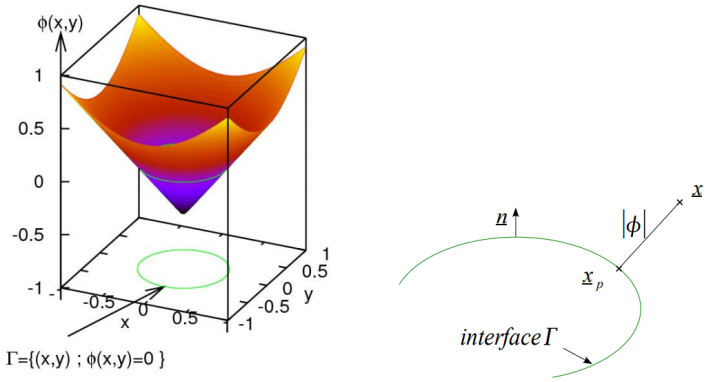

FIGURE 2.7 – *Definition of an interface using a level set function [107]*

Application of the level set method to cracks

Representing a crack using level sets functions was first done by Stolarska [123] in 2D and by Moës [94] in 3D. In a finite element mesh, the level set function is interpolated between the nodes by the classic finite element functions, creating a field inside the mesh [12, 136]. In a 3D environment, a crack is represented by a surface. In order to track a surface, two level set functions are used, ψ and ϕ that are as illustrated in Figure 2.8. ψ separates the space in two, following the crack surface while ϕ follows the crack front.

In order to track a moving crack, the level set methods need to be updated after each propagation step.

Algorithm

There are several algorithms that can be used to update the level set functions [89]. Several of these algorithms were compared in a study by Duflot [44], where it was concluded that the easiest

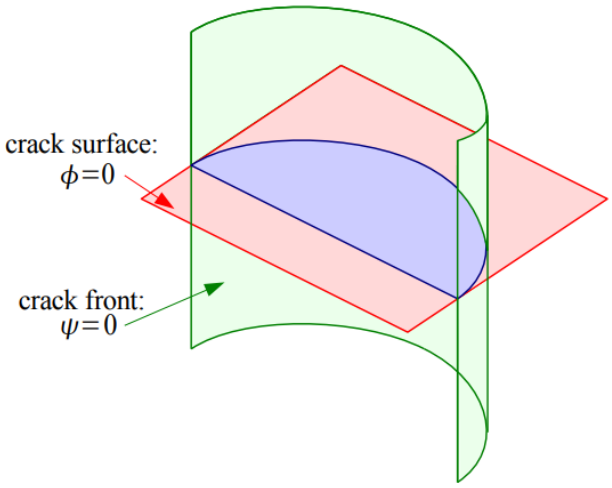

FIGURE 2.8 – *Definition of a crack surface and front using two level set functions [107]*

and most efficient algorithms are the ones using Hamilton-Jacobi type equations. The algorithm that was introduced in Cast3M was developed by Gravouil et al. [55] and is as follows :

1. Calculation of the propagation speed and angle using the mechanical model
2. Extension of these quantities to the whole domain
3. Crack plane speed modification
4. Update and re-initialization of the crack plane
5. Update of the crack front
6. Orthogonalization and re-initialization of the crack plane

In order to calculate the propagation speed and angle, the stress intensity factors for the crack need to be calculated.

Stress intensity factors measure : G - θ method

The $G-\theta$ method, first developed by Destuynder et al. [39], is a calculation method that allows to calculate G, the thermodynamic force of the crack progress also known as energy release rate, on the crack tip. This method consists in analyzing the dissipation of energy during an irreversible process and in characterizing the contributions to the dissipation. The value of this energy allows to ascertain the crack advancement. Thus, G can be used to measure dislocations effects on the crack front by comparing the energies with and without dislocations on said front.

To achieve this calculation, a virtual kinematics of the crack tip named $\boldsymbol{\theta}$ will be used.

Introduction to G

The studied volume is a solid S which includes a crack with a length of l. $\Omega(l)$ is defined as the open set occupied by the solid, and $\mathbf{C}$ as the stiffness tensor. For the sake of simplicity, the solid is supposed two-dimensional. In 2D, the applied forces are represented by $\mathbf{f} = (f_1, f_2)$ while the displacements are represented by $\mathbf{u} = (u_1, u_2)$. The associated deformations to these displacements are :

$$\varepsilon_{ij}(\boldsymbol{u}) = \frac{1}{2}(\partial_i u_j + \partial_j u_i) \text{ for } i, j \in \{1,2\}. \tag{2.7}$$

W is defined as the potential energy of the system and the applied load as :

$$W = \frac{1}{2}\int_{\Omega(l)} Tr(\boldsymbol{C\varepsilon}(\boldsymbol{u})\boldsymbol{\varepsilon}(\boldsymbol{u})) - \mathbf{fu}. \tag{2.8}$$

Thus W is dependent on the crack length l and the load $\boldsymbol{f}$. This energy is available in the solid for the crack to advance.

Therefore, G, the energy release rate, can be defined as :

$$G = \frac{-\partial W}{\partial l} \tag{2.9}$$

Principle of virtual work

The principle of virtual [3] work states that for $\mathbf{v}$ a virtual kinematically admissible displacement field :

$$\int_{\Omega(l)} Tr(\boldsymbol{C\varepsilon}(\boldsymbol{v})\boldsymbol{\varepsilon}(\boldsymbol{v})) = \mathbf{fv} \tag{2.10}$$

Since the displacement u is a solution of 2.10, it can be deduced from 2.8 that :

$$W = -\frac{1}{2}\int_{\Omega(l)} Tr(\boldsymbol{C\varepsilon}(\boldsymbol{u})\boldsymbol{\varepsilon}(\boldsymbol{u})) \tag{2.11}$$

Introduction to theta

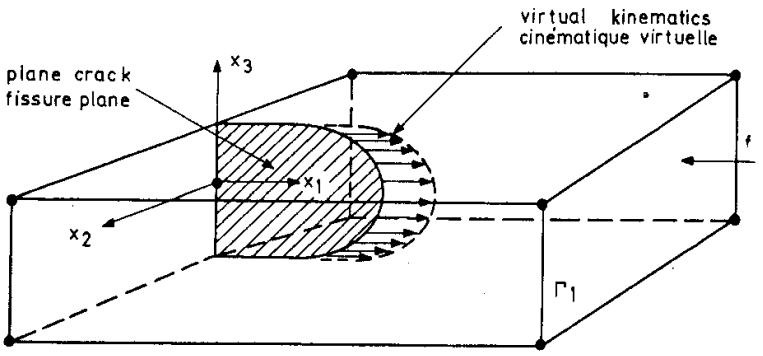

FIGURE 2.9 – *Crack in a volume with its vitual kinematics [39]*

A series of open sets indexed with the scalar parameter $\varepsilon > 0$ is used as a series of configurations during the virtual crack advance. The virtual crack advance field at any point of the crack front is named $\boldsymbol{\theta}(\boldsymbol{M})$. This open sets are such as :

$$\Omega^{\varepsilon} = F^{\varepsilon}(\Omega) \tag{2.12}$$

With F^{ε} a map of $\mathbb{R}^3$ in $\mathbb{R}^3$ such as :

$$\forall \boldsymbol{M} \in \Omega, \boldsymbol{M}^{\varepsilon} = F^{\varepsilon}(\boldsymbol{M}) = \boldsymbol{M} + \varepsilon\boldsymbol{\theta}(\boldsymbol{M}) \tag{2.13}$$

With $\boldsymbol{M}$ being a point in the open set Ω and $\boldsymbol{\theta}$ a vector field defined on Ω verifying the following hypothesis [39] :

— $\boldsymbol{\theta}$ parallel to the crack plan

— $F^{\varepsilon}(\boldsymbol{M}) \subset \Omega$

— $\boldsymbol{\theta}$ support is limited to the surroundings of the crack where no force is applied

— the vector element are at least Lipschitz continuous

— the area created is unitary corresponding to an infinitesimal movement

$\boldsymbol{\theta}$ is the virtual kinematics of the crack tip illustrated in Figure 2.9. These hypothesis allow an easier problem resolution. The admissible propagation mechanisms, in other words the $\boldsymbol{\theta}$ fields verifying these hypothesis, cannot lead to crack branching. The $\boldsymbol{\theta}$ field is a mathematical artifact, only its restriction to the crack tip has a mechanical sense; this field matches the advancement speed of the crack.

Elasticity problem

For every open set Ω^ε there is a corresponding elasticity problem defined by the following equations for all $\boldsymbol{\tau}$ virtual stress field and for all $\boldsymbol{v}$ kinematically admissible displacement field [39] :

$$\begin{cases} \forall \boldsymbol{\tau} \text{ virtual stress field}, & \displaystyle\int_{\Omega^\varepsilon} Tr(\boldsymbol{C}^{-1}\boldsymbol{\sigma}^\varepsilon\boldsymbol{\tau}) = \int_{\Omega^\varepsilon} Tr\left(\boldsymbol{\tau}\frac{\partial \boldsymbol{u}^\varepsilon}{\partial \boldsymbol{M}^\varepsilon}\right) \\ \forall \boldsymbol{v} \text{ admissible kinetic}, & \displaystyle\int_{\Omega^\varepsilon} Tr\left(\boldsymbol{\sigma}^\varepsilon\frac{\partial \boldsymbol{v}}{\partial \boldsymbol{M}^\varepsilon}\right) = \int_{\Gamma_1} \boldsymbol{f}\boldsymbol{v} \end{cases} \tag{2.14}$$

With $\boldsymbol{C}$ the elasticity tensor, $\boldsymbol{M}^\varepsilon$ a generic point of Ω^ε, $(\boldsymbol{\sigma}^\varepsilon, \boldsymbol{u}^\varepsilon)$ the stress and the displacement fields, and Γ_1 the boundary fraction where the force $\boldsymbol{f}$ is applied. For sake of simplicity, it is supposed that no force is applied on the variable part of Ω^ε. $\boldsymbol{\sigma}^*, \boldsymbol{u}^*$ are the Lagrangian variables defined on Ω and associated to $\boldsymbol{\sigma}^\varepsilon, \boldsymbol{u}^\varepsilon$ such as :

$$\begin{cases} \boldsymbol{\sigma}^* = \boldsymbol{\sigma}^\varepsilon \circ \boldsymbol{F}^\varepsilon \\ \boldsymbol{u}^* = \boldsymbol{u}^\varepsilon \circ \boldsymbol{F}^\varepsilon \end{cases} \tag{2.15}$$

Equation 2.14 can then be rewritten as :

$$\begin{cases} \displaystyle\int_\Omega Tr(\boldsymbol{C}^{-1}\boldsymbol{\sigma}^*\boldsymbol{\tau}) = \int_\Omega Tr\left(\boldsymbol{\tau}\frac{\partial \boldsymbol{u}^*}{\partial \boldsymbol{M}}\left(\boldsymbol{I} + \varepsilon\frac{\partial \boldsymbol{\theta}}{\partial \boldsymbol{M}}\right) - \boldsymbol{1}\right) \\ \displaystyle\int_\Omega Tr\left(\boldsymbol{\sigma}^*\frac{\partial \boldsymbol{v}}{\partial \boldsymbol{M}}\left(\boldsymbol{I} + \varepsilon\frac{\partial \boldsymbol{\theta}}{\partial \boldsymbol{M}}\right)^{-1} det\left(\boldsymbol{I} + \varepsilon\frac{\partial \boldsymbol{\theta}}{\partial \boldsymbol{M}}\right)\right) = \int_{\Gamma_1} \boldsymbol{f}\boldsymbol{v} \end{cases} \tag{2.16}$$

for all τ and for all v kinematic admissible displacement fields on Ω, with I the identity matrix.

Implicit functions theorem

For $f(x,y) = 0$, $(x,y) \in \mathbb{R}$ if f is smooth enough in the neighborhood of a point belonging to the curve, $\exists \phi : \mathbb{R} \to \mathbb{R}$ at least as smooth as f for which locally the curve and the graph of ϕ are combined. In other words, if (x_0, y_0) verifies the equation, if f is a smooth function and if its partial derivative in respect to y at (x_0, y_0) is not zero then there is a neighborhood of (x_0, y_0) in which the zone identifies itself to ϕ graph.

This condition is respected by θ since it is components are at least smooth [39]. Then :

$$(\boldsymbol{\sigma}^*, \boldsymbol{u}^*) = (\boldsymbol{\sigma}^0, \boldsymbol{u}^0) + \varepsilon(\boldsymbol{\sigma}^1, \boldsymbol{u}^1) + \varepsilon^2(\boldsymbol{\sigma}^2, \boldsymbol{u}^2) + \varepsilon^2 O(\varepsilon) \text{ where } \lim_{\varepsilon \to 0} O(\varepsilon) = 0 \tag{2.17}$$

With $(\boldsymbol{\sigma}^p, \boldsymbol{u}^p)$ defined such as : $(\boldsymbol{\sigma}^0, \boldsymbol{u}^0)$ is the solution of the elasticity problem on Ω that verifies (kadf : kinematically admissible displacement field). The stress tensor is a statically admissible stress field. :

$$\begin{cases} \forall \boldsymbol{\tau}, & \displaystyle\int_\Omega Tr\left(\boldsymbol{C}^{-1}\boldsymbol{\sigma}^0\boldsymbol{\tau}\right) - \int_\Omega Tr\left(\boldsymbol{\tau}\frac{\partial \boldsymbol{u}^0}{\partial \boldsymbol{M}}\right) = 0 \\ \forall \boldsymbol{v} \text{ kadf}, & \displaystyle\int_\Omega Tr\left(\boldsymbol{\sigma}^0\frac{\partial \boldsymbol{v}}{\partial \boldsymbol{M}}\right) = \int_{\Gamma_1} \boldsymbol{f}\boldsymbol{v} \end{cases} \tag{2.18}$$

$(\boldsymbol{\sigma}^1, \boldsymbol{u}^1)$ such as it is solution of :

$$\begin{cases} \forall \boldsymbol{\tau}, & \int_\Omega Tr\left(\boldsymbol{C}^{-1}\boldsymbol{\sigma}^1\boldsymbol{\tau}\right) - \int_\Omega Tr\left(\boldsymbol{\tau}\dfrac{\partial \boldsymbol{u}^1}{\partial \boldsymbol{M}}\right) = -\int_\Omega Tr\left(\boldsymbol{\tau}\dfrac{\partial \boldsymbol{u}^0}{\partial \boldsymbol{M}}\dfrac{\partial \boldsymbol{\theta}}{\partial \boldsymbol{M}}\right) \\ \forall \boldsymbol{\nu} \text{ kadf}, & \int_\Omega Tr\left(\boldsymbol{\sigma}^1\dfrac{\partial \boldsymbol{\nu}}{\partial \boldsymbol{M}}\right) = -\int_\Omega Tr\left(\boldsymbol{\sigma}^0\dfrac{\partial \boldsymbol{\nu}}{\partial \boldsymbol{M}}\right) div\boldsymbol{\theta} + \int_\Omega Tr\left(\boldsymbol{\sigma}^0\dfrac{\partial \boldsymbol{\nu}}{\partial \boldsymbol{M}}\dfrac{\partial \boldsymbol{\theta}}{\partial \boldsymbol{M}}\right) \end{cases} \tag{2.19}$$

$(\boldsymbol{\sigma}^2, \boldsymbol{u}^2)$ such as it is solution of :

$$\begin{cases} \forall \boldsymbol{\tau}, & \int_\Omega Tr\left(\boldsymbol{C}^{-1}\boldsymbol{\sigma}^2\boldsymbol{\tau}\right) - \int_\Omega Tr\left(\boldsymbol{\tau}\dfrac{\partial \boldsymbol{u}^2}{\partial \boldsymbol{M}}\right) = \int_\Omega Tr\left(\boldsymbol{\sigma}^0\dfrac{\partial \boldsymbol{u}^0}{\partial \boldsymbol{M}}\left(\dfrac{\partial \boldsymbol{\theta}}{\partial \boldsymbol{M}}\right)^2\right) - \int_\Omega Tr\left(\boldsymbol{\tau}\dfrac{\partial \boldsymbol{u}^1}{\partial \boldsymbol{M}}\dfrac{\partial \boldsymbol{\theta}}{\partial \boldsymbol{M}}\right) \\ \forall \boldsymbol{\nu} \text{ kadf}, & \int_\Omega Tr\left(\boldsymbol{\sigma}^2\dfrac{\partial \boldsymbol{\nu}}{\partial \boldsymbol{M}}\right) = -\int_\Omega Tr\left(\boldsymbol{\sigma}^0\dfrac{\partial \boldsymbol{\nu}}{\partial \boldsymbol{M}}\left(\dfrac{\partial \boldsymbol{\theta}}{\partial \boldsymbol{M}}\right)^2\right)^2 + \int_\Omega Tr\left(\boldsymbol{\sigma}^0\dfrac{\partial \boldsymbol{\nu}}{\partial \boldsymbol{M}}\dfrac{\partial \boldsymbol{\theta}}{\partial \boldsymbol{M}}\right) div\boldsymbol{\theta} + \\ & \int_\Omega Tr\left(\boldsymbol{\sigma}^1\dfrac{\partial \boldsymbol{\nu}}{\partial \boldsymbol{M}}\dfrac{\partial \boldsymbol{\theta}}{\partial \boldsymbol{M}}\right) - \int_\Omega Tr\left(\boldsymbol{\sigma}^1\dfrac{\partial \boldsymbol{\nu}}{\partial \boldsymbol{M}}\right) div\boldsymbol{\theta} - \int_\Omega Tr\left(\boldsymbol{\sigma}^0\dfrac{\partial \boldsymbol{\nu}}{\partial \boldsymbol{M}}\right) Adj\left(\dfrac{\partial \boldsymbol{\theta}}{\partial \boldsymbol{M}}\right) \end{cases} \tag{2.20}$$

With $Adj(\partial\boldsymbol{\theta}/\partial\boldsymbol{M})$ the second invariant of $(\partial\boldsymbol{\theta}/\partial\boldsymbol{M})$.

Calculation of the potential energy derivatives

The potential energy of the system is defined such as :

$$W = -\frac{1}{2}\int_{\Gamma_1} \boldsymbol{f}\boldsymbol{u}^\varepsilon \tag{2.21}$$

In order to access the energy release rate G the potential energy derivatives are calculated. W derivatives in relation to the domain Ω in a virtual kinetic $\boldsymbol{\theta}$ are defined with :

$$\begin{cases} \dfrac{\partial W}{\partial \Omega}(\boldsymbol{\theta}) = \lim \varepsilon \to 0 \dfrac{W(\Omega^\varepsilon) - W(\Omega)}{\varepsilon} \\ \dfrac{\partial^2 W}{\partial \Omega^2}(\boldsymbol{\theta}, \boldsymbol{\theta}) = \lim \varepsilon \to 0 \dfrac{(\partial W(\Omega^\varepsilon)/\partial\Omega)(\boldsymbol{\theta}) - (\partial W(\Omega)/\partial\Omega)(\boldsymbol{\theta})}{\varepsilon} \end{cases} \tag{2.22}$$

Taking (2.17) into account leads to :

$$\begin{cases} \dfrac{\partial W}{\partial \Omega}(\Omega)(\boldsymbol{\theta}) = -\dfrac{1}{2}\displaystyle\int_{\Gamma_1} \boldsymbol{f}\boldsymbol{u}^1 \\ \dfrac{\partial^2 W}{\partial \Omega^2}(\Omega)(\boldsymbol{\theta}, \boldsymbol{\theta}) = -\dfrac{1}{2}\displaystyle\int_{\Gamma_1} \boldsymbol{f}\boldsymbol{u}^2, \text{ etc.} \end{cases} \tag{2.23}$$

Combining equations(2.19), (2.20), (2.22) and (2.23) the following expressions for the potential energy derivatives are found :

$$\frac{\partial W}{\partial \Omega}(\Omega)(\boldsymbol{\theta}) = \frac{1}{2}\int_\Omega Tr\left(\boldsymbol{\sigma}^0\frac{\partial \boldsymbol{u}^0}{\partial \boldsymbol{M}}\right) div\boldsymbol{\theta} - \int_\Omega Tr\left(\boldsymbol{\sigma}^0\frac{\partial \boldsymbol{u}^0}{\partial \boldsymbol{M}}\frac{\partial \boldsymbol{\theta}}{\partial \boldsymbol{M}}\right) \tag{2.24}$$

$$\begin{cases} \dfrac{\partial^2 W}{\partial \Omega^2}(\Omega)(\boldsymbol{\theta}, \boldsymbol{\theta}) = \displaystyle\int_\Omega Tr\left(\boldsymbol{\sigma}^0\frac{\partial \boldsymbol{u}^0}{\partial \boldsymbol{M}}\frac{\partial \boldsymbol{\theta}}{\partial \boldsymbol{M}}\frac{\partial \boldsymbol{\theta}}{\partial \boldsymbol{M}}\right) + \frac{1}{2}\int_\Omega Tr\left(\boldsymbol{\sigma}^0\frac{\partial \boldsymbol{u}^0}{\partial \boldsymbol{M}}\right) Adj\frac{\partial \boldsymbol{\theta}}{\partial \boldsymbol{M}} \\ -\dfrac{1}{2}\displaystyle\int_\Omega Tr\left(\boldsymbol{\sigma}^0\frac{\partial \boldsymbol{u}^0}{\partial \boldsymbol{M}}\frac{\partial \boldsymbol{\theta}}{\partial \boldsymbol{M}}\right) div\boldsymbol{\theta} - \frac{1}{2}\int_\Omega Tr\left(\boldsymbol{\sigma}^0\frac{\partial \boldsymbol{u}^1}{\partial \boldsymbol{M}}\frac{\partial \boldsymbol{\theta}}{\partial \boldsymbol{M}}\right) \\ -\dfrac{1}{2}\displaystyle\int_\Omega Tr\left(\boldsymbol{\sigma}^1\frac{\partial \boldsymbol{u}^0}{\partial \boldsymbol{M}}\frac{\partial \boldsymbol{\theta}}{\partial \boldsymbol{M}}\right) + \frac{1}{2}\int_\Omega Tr\left(\boldsymbol{\sigma}^1\frac{\partial \boldsymbol{u}^0}{\partial \boldsymbol{M}}\right) div\boldsymbol{\theta} \end{cases} \tag{2.25}$$

Equations (2.24) and (2.25) remain valid in two and three dimensions.

Link between energy derivatives and the stress intensity factors

In the three-dimensional case, the exact solution of the displacement field around the crack tip is unknown. On the other hand, the behavior of the solution near the crack tip is well known in the two-dimensional case. Equations (2.24) and (2.25) are used to estimate the energy release rate, which is a vectorial value.

Following equation is valid for the two-dimensional case :

$$\boldsymbol{u}^0 = K_1^0\sqrt{r}\boldsymbol{S}_1(\varphi) + K_2^0\sqrt{r}\boldsymbol{S}_2(\varphi) + \boldsymbol{u}^{0,R} \tag{2.26}$$

With $\boldsymbol{u}^0$ the displacement field solution of the 2D elasticity problem (2.16), (r,φ) the polar coordinates around the crack tip as illustrated in Figure 2.10, $\boldsymbol{S}_1(\varphi)$ and $\boldsymbol{S}_2(\varphi)$ two vectors which the components are two functions of the angle φ and the regular displacement $\boldsymbol{u}^{0,R}$, i.e. at least of C^1 class in the neighborhood of the crack tip.

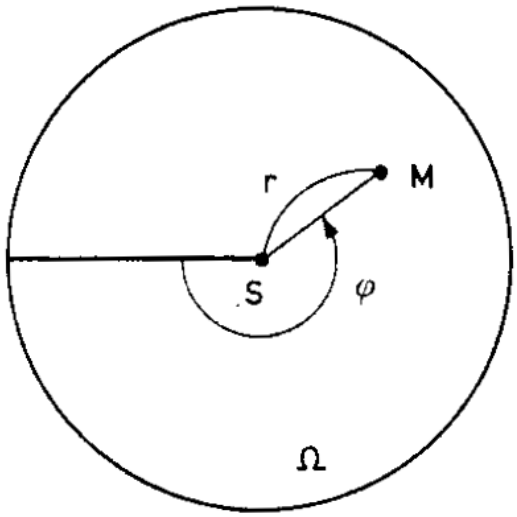

FIGURE 2.10 – *Bidimensional crack [39]*

For an homogeneous isotropic material with E the Young modulus and ν the Poisson coefficient :

$$\frac{\partial W}{\partial \Omega}(\Omega)(\boldsymbol{\theta}) = \begin{cases} -\dfrac{1}{E}\left[(K_1^0)^2 + (K_2^0)^2\right] & \text{plane stress} \\ -\dfrac{1-\nu^2}{E}\left[(K_1^0)^2 + (K_2^0)^2\right] & \text{plane strain} \end{cases} \tag{2.27}$$

Link between the Rice integral and the energy release rate

Using the Stoke theorem another expression of the energy release rate is given using a contour integral, the Rice integral [96].

The following energy release rate expression is therefore obtained :

$$\frac{\partial W}{\partial \Omega}(\Omega)(\boldsymbol{\theta}) = \frac{1}{2}\int_C Tr\left(\boldsymbol{\sigma}^0\frac{\partial \boldsymbol{u}^0}{\partial \boldsymbol{M}}\right)\boldsymbol{\theta}.\boldsymbol{n} - \int_C \boldsymbol{n}\boldsymbol{\sigma}^0\frac{\partial \boldsymbol{u}^0}{\partial \boldsymbol{M}}\boldsymbol{\theta} \tag{2.28}$$

With n the inward-pointing normal unit vector of the curve C which surrounds the crack tip. Figure 2.11 illustrates the contour C which is inside a neighborhood v of the crack tip where θ is constant.

Therefore :

$$\boldsymbol{\theta} = \begin{pmatrix} 1 \\ 0 \end{pmatrix} \tag{2.29}$$

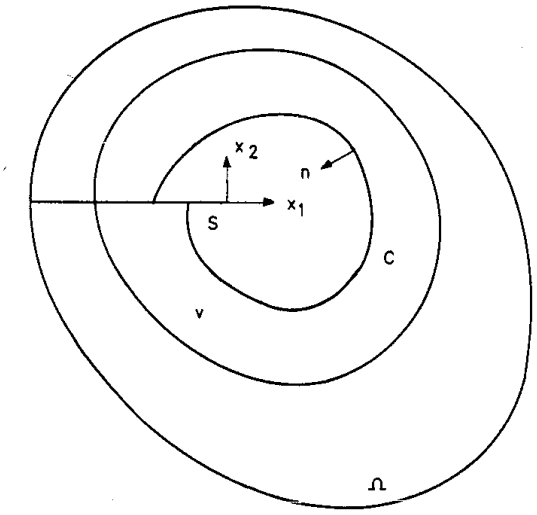

FIGURE 2.11 – *Rice integral contour for a crack tip [39]*

The equation (2.28) is independent of $\boldsymbol{\theta}$ as long as $\boldsymbol{\theta}$ complies with the hypothesis described in 2.3.

Expression and independence of G

Hence :

$$\frac{\partial W}{\partial \Omega}(\Omega)(\boldsymbol{\theta}) = \frac{1}{2}\int_C Tr\left(\boldsymbol{\sigma}^0 \frac{\partial \boldsymbol{u}^0}{\partial \boldsymbol{M}}\right) n_1 - \int n_1 \boldsymbol{\sigma}_{1j} \partial_1 \boldsymbol{u}_j^0 \tag{2.30}$$

G independence regarding $\boldsymbol{\theta}$ and the contour $\boldsymbol{C}$ results from the previous equation as well as (2.27) where $\boldsymbol{C}$ and $\boldsymbol{\theta}$ do not intervene.

Energy release rate calculations is based on a virtual kinetic $\boldsymbol{\theta}$ defined to facilitate the calculation of G. By proving G independence not only towards $\boldsymbol{\theta}$ but towards $\boldsymbol{C}$ too an easily calculable expression is achieved.

On the second derivative of W

The second derivative of the potential energy equation (2.25) shows that it not only depends on the stress state of the cracked structure but also on the strain variations during the cracks evolution, i.e. $(\boldsymbol{\sigma}^1, \boldsymbol{u}^1)$. The crack stability can then be defined by the positivity of the second derivative of the energy.

Implementation of this method in Cast3M

The G-θ method is implemented in Cast3M using three procedures. This method was adapted in Cast3M by Prabel [107] for the development of the XFEM on Cast3M. A procedure in Cast3M is a function created using the gibiane language meaning that it does not need to be compiled with the code. These three procedures consist in a general procedure called by the user, a procedure that calculates the θ field and a third procedure that calculates the stress intensity factors. These procedures allow non linear cases, but since those do not concern our work we will not mention them further.

The procedure inputs include a list of parameters that describe the calculation parameters, the volume mesh, the strain fields on said mesh, the level functions ϕ and ψ as well as the crack front. Once these variables are input in the code and verified, the $\boldsymbol{\theta}$ field is calculated.

Calculation of the $\boldsymbol{\theta}$ field

$\boldsymbol{\theta}$, which is the kinematically admissible virtual displacement of the crack, needs to be calculated to be able to determine the stress intensity factors. The first step of this process consists on selecting all the elements of the volume that contain the crack front. The easiest way to do this is to select the elements for which both ϕ and ψ are equal to zero. Additional element layers can be selected, by which the code will select the elements in contact with this first layer of elements. This volume selected here corresponds to the integral volume previously defined.

For each point of the crack, a local coordinate system is defined using the level set functions. The gradients of both ϕ and ψ are calculated and used to calculate the vector $\boldsymbol{\tau}$ defined as :

$$\boldsymbol{\tau} = \boldsymbol{grad}\psi \wedge \boldsymbol{grad}\phi \tag{2.31}$$

Which is then used to calculate θ using :

$$\boldsymbol{\theta} = \boldsymbol{grad}\phi \wedge \boldsymbol{\tau} \tag{2.32}$$

$\boldsymbol{\theta}$ is perpendicular to $\boldsymbol{grad}\phi$ and in the same directions as $\boldsymbol{grad}\psi$. Once calculated in the volume, $\boldsymbol{\theta}$ is extrapolated on the crack front and then normalized to comply with the hypothesis defined in Section 2.3.

Calculation of the stress intensity factors

In order to determine the stress intensity factors, the displacement of the crack front is locked so the different modes can be isolated. The local coordinate system of the crack front is then calculated for both Cartesian and cylindrical coordinates. The local strain field on the crack front is then created from the gradient of the displacement field solution of the boundary value problem.

First, the derivatives of the cylindrical coordinate system in relation to the global coordinate system are calculated. These values are used to calculate the displacement in the local coordinate system. Both the stress and displacement gradient are calculated on the local coordinate system which are then used to calculate K_I, K_{II}, K_{III} for each point of the crack front.

Crack propagation simulation

The energy calculation method defined above is of capital importance for the calculation of the crack advancement. The propagation is discrete and can also allow the crack propagation direction to change according to the crack energy.

Crack advancement

Since the XFEM enriches the elements containing the crack surface as well as the crack front, when advancing, the crack front needs to move at least to the next element. This is due to the enrichment functions, particularly the ones concerning the crack front that create the crack front stress field discontinuity. For them to work properly, the enrichment at $t + dt$ needs to be done on a different element. In order to do so, we impose that the crack front will move of at least $1.4 \times x_1$ with x_1 being the element size. To take into account the energy difference at every crack front point, the point with the lowest energy will move over a distance of $1.4 \times x_1$ and the rest of the crack front will move proportionally to it depending on their energy values.

The crack front will eventually change its motion direction (i.e. crack plane) depending on the local values of the stress intensity factors, especially K_{II}. The angle will be calculated using the following equation [107] :

$$\beta_c = 2\arctan\left(\frac{1}{4}\left[\frac{K_I}{K_{II}} - \text{sign}\left(K_{II}\right)\sqrt{8+\left(\frac{K_I}{K_{II}}\right)^2}\right]\right) \tag{2.33}$$

This equation is based on linear rupture mechanics for the stress corresponding to the maximal opening.

Since the crack propagation direction and intensity might lead to some points of the crack front to move outside the volume, the code will ensure that new points belonging to the crack front are created on the intersection between the crack front and the outer surface of the volume. To achieve this, it will be first checked if the points are inside the volume, in the case they are not, these points will be eliminated and a new point in the intersection between the outer surface of the volume and the crack front will be created.

Crack arrest

Crack arrest can naturally happen when the crack front energy becomes too low to create the new crack surfaces. The crack can also partially get arrested.

In this work, only a total crack arrest was implemented. In order to carry out this arrest, the code compares the average energy of the crack to a critical energy value. If the crack's energy is higher than the critical value, the crack will be able to advance. Since we lacked the critical energy value of the crack as well as the fact that this study is centered specifically on the dislocation impact rather than the actual energy values, we only verified that the crack energy was positive before propagation. The critical value can be modified as needed though.

As for partial crack arrest, it was not implemented in this code due to the functioning of the XFEM. As explained above, the crack needs to change of element for the XFEM to work properly. If one or more points of the crack where to not move, it will create a zone of very high energy as the surrounding points of the crack would advance normally. This will results on the arrested points to brutally advance on the next step of the simulation.

Regarding crack closure, the nature of XFEM makes it quite difficult to implement as it is not designed for it.

2.4 Conclusion

In this chapter we introduced several crack propagation simulation methods, including the eXtended Finite Element Method. This method consists on implementing the crack implicitly via enrichments on the nodes the of the elements containing the crack. XFEM has been implemented in the code Cast3M which will be used in this work for the simulation of the crack front presented in the following Chapter.

3

Discrete dislocation dynamics

Contents

3.1 Introduction

As said before, plasticity in metals is caused by dislocation movement under stress. Dislocation behavior is well known and has been documented in many textbooks [2, 53, 64]. This knowledge should allow the study of plasticity based on the movement of dislocations instead of studying plasticity empirically. This would require not only knowing the position of every dislocation inside the material at any given time but to also know their behavior with respect to defects and obstacles, like other dislocations or grain boundaries, and in function of the stress applied to the material. To do this for a macroscopic sample would be impossible as it would require too much computation power, but the computational means available today allows these calculations to be done at the microscopic scale.

The first dislocations dynamics codes able to simulate plasticity by calculating dislocation interactions where developed at the end of the 90s. These codes were first developed to study cyclic loading in two dimensions [38] or in three dimensions [41]. The evolution of the computation technology allows nowadays for larger simulated volumes with more entities simulated. Several codes exists including, aNumodis [27], ParaDis [72], µMEGAS [35] or TriDis [119].

In this Chapter, we will review the main existing DDD methods as well as explain in depth the method behind TriDis which we will be using. Furthermore, we will expand on the coupling of XFEM and DDD used for this work as well as the fixed parameters for the simulations carried out.

3.2 Other existing DDD models

Most dislocation dynamics methods, including the one used for this work, are based on the following principle. First, the space and the dislocations are discretized. Then the following algorithm is applied : at time t, for every dislocation, the velocity is calculated, and then explicitly integrated on the δt time step. The dislocation segments are then displaced to obtain the $t + \delta t$ configuration. There exist several way to enforce the boundary conditions such as the presence of cracks, in DD simulations, namely the superposition method or the DCM method.

The Discrete-Continuous Model

This model is based on the idea that dislocations can be assimilated to inclusions with uniform plastic strain fields. This eigen strain representation of dislocation loops was first defined by Mura [95], and a DDD model was implemented by Lemarchand [76], Groh [57], Vattré [135] and Jamond [66] among others to become what we today know as the Discrete-Continuous Model. These plastic strains belong to a group of nonelastic strains named eigenstrain. Eigenstrains are mechanical deformations not caused by any external mechanical stress such as thermal expansion.

In the Discrete-Continuous Model simulations, only short range dislocation - dislocation interactions are analytically treated. All other interactions such as external loads and long-range dislocations stresses are numerically calculated by the finite elements method. An example of a DCM code is µMEGAS [35].

XFEM inspired method

There is a dislocation dynamics method inspired of the eXtended Finite Element Method that has been recently developed [79] to study dislocation dynamics. In order to represent the dislocation effects in the volume, enrichment functions are added to the volume mesh representing not

a crack as in the case for XFEM but a dislocation. This method is illustrated in Figure 3.1. Two enrichment functions are created, defining the function $\Psi^{\alpha}(x)$:

— $\Psi_H^{\alpha}(x)$: Step enrichment function

— $\Psi_C^{\alpha}(x)$: Dislocation core enrichment function

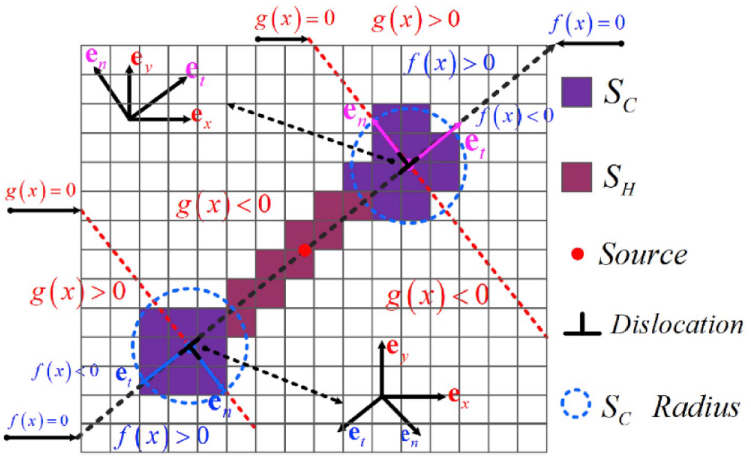

FIGURE 3.1 – *Enrichment subdomains (S_C and S_H) and level sets (g(x) and f(x)) [79]*

The step enrichment function is used to describe the displacement discontinuity across the slip planes. This discontinuity is placed far from dislocation cores. On the other hand, the dislocation core enrichment function represents the local singularity in the vicinity of a dislocation core. In this 2D model, all dislocations are pure edge, which corresponds to the following enrichment functions :

$$\Psi^{\alpha}(x) = \begin{cases} \Psi_H^{\alpha}(x) = N_I(x)(H(f(x)) - H(f(x_I)) & x \in S_H \\ \Psi_C^{\alpha}(x) = N_I(\psi_C^{\alpha}(x) - \psi_C^{\alpha}(x_I)) & x \in S_C \\ 0 & \text{else} \end{cases} \tag{3.1}$$

With $f(x)$ and $g(x)$ the level set functions used to describe the surface discontinuities induced by the dislocation gliding, $H(z)$ the Heaviside function, N_I a general shape function and ψ_C^{α} the dislocation core enrichment function. ψ_C^{α} is derived from the analytical solution of a dislocation stress field in an infinite solid. As illustrated in Figure 3.1, $f(x) = 0 \cup g(x) = 0$ denotes the dislocation core, and $f(x) = 0 \cup g(x) < 0$ denotes the plane where the dislocation glided and created a discontinuity.

In order to model the dislocation nucleation at the crack tip, the Rice-Thomson model [132] is used. Emitted dislocations are introduced as Frank-Read sources which correspond in 2D as a set of two opposed sign edge dislocations that move away from the source. When the loop is large enough, a dislocation is emitted while the other one is absorbed by the crack. In order to emit a dislocation, the strain at the source needs to be large enough following :

$$f_K \geq -(f_{image} + f_{step}) \tag{3.2}$$

With f_K the stress at the source, f_{image} the image force arising from the crack free surface the crack free surface and f_{step} the force produced by the absorption of the edge dislocation by the crack surface. These variables are depending on the dislocation emission critical stress intensity factor which can be obtained by molecular dynamics simulations.

The crack is modeled using the cohesive zone method presented in 2.2 and advances when the traction perpendicular to the cohesive surface reaches a predetermined critical value.

This method was used with a single crystal and ignores grain boundaries interactions with the dislocations as well as other dislocation sources. Being simulated in 2D, screw dislocations can't be added to the simulation, limiting the results.

3.3 The DDD code TriDis

The code used in our simulations corresponds to a DDD code. Specifically, the code we use here is called TriDis [49]. It controls the dislocation movement as well as their interactions with the simulated volume and with each other.

Discretization

In FCC materials, atoms are placed in a lattice like the one illustrated in Figure 3.2. In order to simulate this space, a similar 3D lattice of points is created, upon which points the dislocations will be attached. The discretization unit corresponds to the parameter *xl* of Figure 3.2.

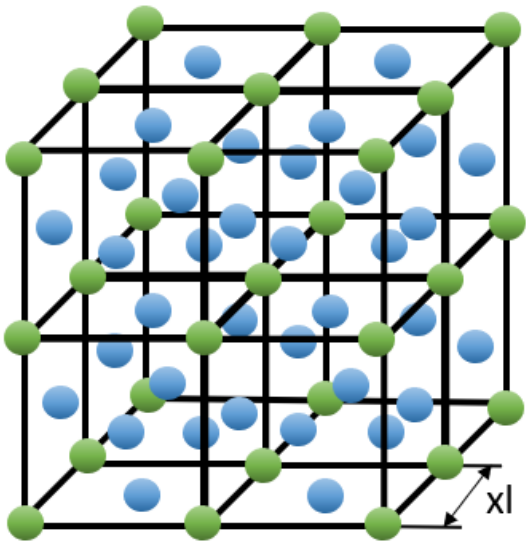

FIGURE 3.2 – *FCC atomic lattice with green atoms representing the atoms on the corners while the blue ones represent the atoms on the face centers*

xl also represents the minimal distance between two dislocation segments which means it needs to be small enough to describe accurately plasticity while large enough to lessen computation time. The value for *xl* is often chosen to be the minimal distance for two dislocations of opposite sign to annihilate which corresponds to around $10b$ [47], which means that $xl = 10b$ with b the Burgers vector norm. This means that the dislocations will be moving in a large FCC-like lattice. This discretization is used for micrometric volumes. If the studied simulation box is of a nanometric scale, $xl = 0.1b$ can be used. While it might seem illogical for a dislocation to move of less than an interatomic distance, it has been proven that this discretization is accurate with dislocation behavior [43, 85].

Edge and screw segments an be defined as shown in Figure 3.3. This allows for any dislocation loop to be divided in screw segments and edge segments [40] as illustrated in Figure 3.4. Every dislocation segment is then individually considered for the following calculations, which is why this model lends itself to parallelization.

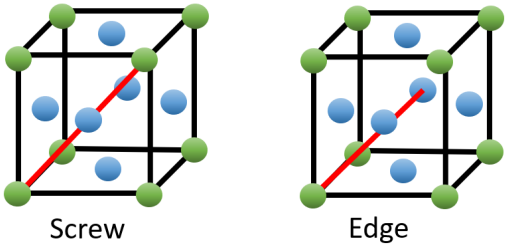

FIGURE 3.3 – *Example of the placement of a* $[011]$ *Screw segment and a* $[0\bar{1}1]$ *Edge segment (red line) in a discretization unit. The line direction of the Edge segment is* $[211]$

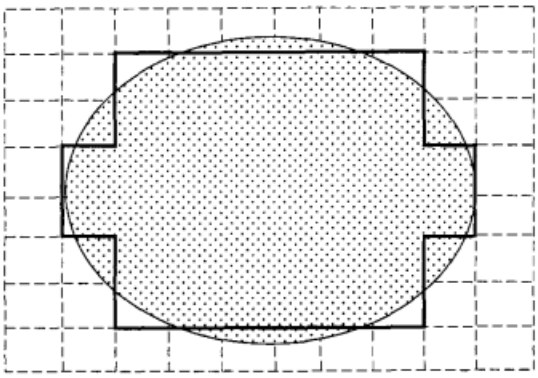

FIGURE 3.4 – *Representation of a dislocation loop (shadowed) and its discretization (full thick lines) [40]*

Dislocation stress fields

The stress field created by a dislocation can be calculated using the isotropic elasticity theory. For a dislocation following the **z** axis with a Burgers vector **b** (b_x, b_y, b_z) and limited by the points $r_1(0,0,z_1)$ and $r_2(0,0,z_2)$ as illustrated in Figure 3.5, the stress it generates on a point $r(x,y,z)$ can be defined as [77] :

$$\boldsymbol{\sigma}(\mathbf{r}-\mathbf{r_1}) - \boldsymbol{\sigma}(\mathbf{r}-\mathbf{r_2}), \tag{3.3}$$

with $\boldsymbol{\sigma}(\mathbf{r})$ defined as :

$$\begin{cases} \sigma_{xx}(\mathbf{r}) = \frac{-b_x y - b_y x}{r(r-z)} - \frac{x^2(b_x y - b_y x)(2r-z)}{r^3(r-z)^2} \\ \sigma_{yy}(\mathbf{r}) = \frac{b_x y + b_y x}{r(r-z)} - \frac{y^2(b_x y - b_y x)(2r-z)}{r^3(r-z)^2} \\ \sigma_{zz}(\mathbf{r}) = \frac{z(b_x y - b_y x)}{r^3} - \frac{2\nu(b_x y - b_y x)}{r(r-z)} \\ \sigma_{yz}(\mathbf{r}) = \frac{y(b_x y - b_y x)}{r^3} - \frac{\nu b_x}{r} + \frac{(1-\nu)b_z x}{r(r-z)} \\ \sigma_{zx}(\mathbf{r}) = \frac{x(b_x y - b_y x)}{r^3} + \frac{\nu b_y}{r} - \frac{(1-\nu)b_z y}{r(r-z)} \\ \sigma_{xy}(\mathbf{r}) = \frac{b_x x - b_y y}{r(r-z)} - \frac{xy(b_x y - b_y x)(2r-z)}{r^3(r-z)^2} \end{cases}, \tag{3.4}$$

with ν the Poisson coefficient, and r the norm of **r** illustrated in Figure 3.5 (a).

Figure 3.5 (b) and (c) show an example of the stress created by an edge and a screw dislocation around themselves. The sum of the stress created by all the dislocation segments creates the internal stress in the volume $\boldsymbol{\sigma}_{int}$.

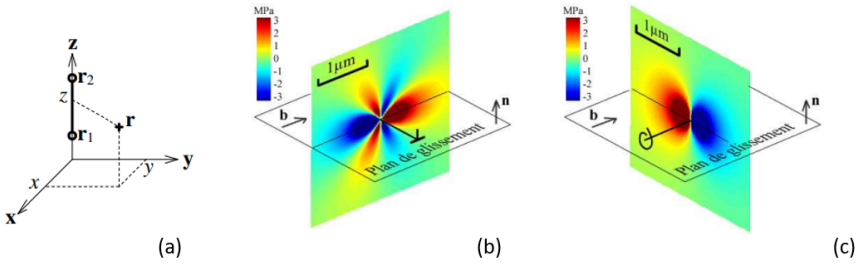

FIGURE 3.5 – *(a) notations for the above dislocation stress calculation, (b) σ_{nb} component around an edge dislocation, (c) σ_{nb} component around a screw dislocation [42]*

Dislocation velocity

While a transition regime exists during which dislocations accelerate, this regime can be overlooked [105]. Effectively, the dislocation speed depends on the effective shear τ^*, that needs to be higher than the friction stress of the volume τ_{fr}, b the norm of the Burgers vector of the moving segment i and B a viscosity coefficient corresponding to the dislocation-phonon interaction. This speed v^i is calculated with :

$$v^i = \frac{\tau^* b}{B}, \tag{3.5}$$

with τ^* defined with :

$$\tau* = \tau^{**} - sign(\tau^{**}).\tau_{fr}, \tag{3.6}$$

$$\tau^{**} = \{\left[\frac{1}{b}(\boldsymbol{\sigma}_{app} + \boldsymbol{\sigma}_{int} + \boldsymbol{\sigma}_{image})\boldsymbol{b}\right] \times \mathbf{l}\}.\mathbf{g} + \tau_{lt} \tag{3.7}$$

with **b** the Burgers vector, **l** the dislocation segment line vector, **g** its movement direction. The contributions to the effective shear stress are :

— $\boldsymbol{\sigma}_{app}$ the macroscopic stress field applied

— $\boldsymbol{\sigma}_{int}$ the internal stress created by other dislocations

— $\boldsymbol{\sigma}_{image}$ the stress created by the image forces

— τ_{lt} the line tension of the studied dislocation

On the time step

The algorithm used for the calculations is an explicit one which means that the time step used is highly important as a too long time step may cause the dislocations to move past zones in the volume where the stresses would modify the dislocation velocity. On the other hand, a too short time step will highly increase the computation times but also cause problems with the discretization of the volume as the time step needs to be at least large enough for the dislocation to move over a few units of the discretization space. The temporal integration is carried out using an Euler integration algorithm modified which is an implicit method. The time step used for nanometric volumes is of 10^{-12} s.

Cross slip

Dislocation cross slip is determined by a parameter which describes the probability of a dislocation to cross slip [18]. This parameter can artificially be set to zero. Otherwise, this parameter is

determined by a stochastic procedure where at each time step, a cross slip probability is calculated for each screw segment i as :

$$P_i = \beta \frac{l}{l_0} \frac{\delta t}{t_0} exp\left(\frac{\tau_{dev} - \tau_{III}}{kT} V_{act}\right), \tag{3.8}$$

with β a normalization coefficient such as $P_i \in [0;1]$, $\frac{l}{l_0}$ the screw segment length over a base length ($l_0 = 1$ µm), $\frac{\delta t}{t_0}$ the time step over a base time ($t_0 = 1$s), $(\tau_{dev} - \tau_{III})$ compares the resolved shear on the slip plane, (τ_{dev}) with a reference stress (τ_{III}), k the Boltzman constant, T the temperature and V_{act} the activation volume. Using this expression, the cross slip of every screw segment is determined at each time step.

Displacement field of a dislocation loop

The fundamental of the calculation of the displacement field created by a dislocation will be presented here. While not directly used in this work, some of the concepts exposed here will be used to describe dislocation stability.

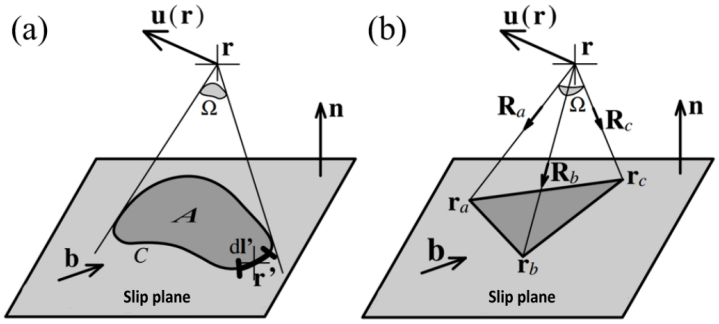

FIGURE 3.6 – *Illustration of a dislocation loop used in the calculation of a dislocation loop displacement field.* ***(a)*** *An arbitrarily shaped loop* ***(b)*** *A triangular loop [42]*

The following equation [68] gives the displacement $\boldsymbol{u}$ at $\boldsymbol{r}$ created by a dislocation loop of surface A :

$$u_m(\boldsymbol{r}) = -\int_A b_i c_{ijkl} \frac{\partial}{\partial x'_l} g_{mk}(\boldsymbol{r}' - \boldsymbol{r}) dA_j, \tag{3.9}$$

with $\boldsymbol{b}$ the Burgers vector, c_{ijkl} the elastic module tensor and g_{mk} the Green tensor. Figure 3.6(a) illustrates the other used notations. With a surface integration of 3.9, the displacement of an arbitrary dislocation loop at any point located in an infinite medium results in :

$$\boldsymbol{u}(\boldsymbol{r}) = -\frac{\boldsymbol{b}}{4\pi}\Omega - \frac{1}{4\pi}\oint_C \frac{\boldsymbol{b}\times d\boldsymbol{l}'}{R} - \frac{1}{8\pi(1-\nu)}\nabla \oint_C \frac{\boldsymbol{b}\times \boldsymbol{R}}{R}.d\boldsymbol{l}', \tag{3.10}$$

which is known as the Burgers equation. Ω represents the solid angle, $\boldsymbol{R} = \boldsymbol{r}' - \boldsymbol{r}$ and $R = \|\boldsymbol{R}\|$. The first term corresponds to the discontinuity on displacement when crossing the slip plane while the two other terms of the equation are continuous.

This calculation can be very complicated for complex loop geometry. A solution proposed in [9] is to decompose the loops in triangles, which results in :

$$\boldsymbol{u}(\boldsymbol{r}) = -\frac{\boldsymbol{b}}{4\pi}\Omega + \boldsymbol{F}_{ab} + \boldsymbol{F}_{bc} + \boldsymbol{F}_{ca} \tag{3.11}$$

using the parameters given in Figure 3.6 (b). This decomposition is particularly well adapted for the edge-screw discretisation used in this model. Further clarifications on these displacement calculations can be found in [42].

While the displacement is not used here, the area swept by a dislocation loop is of uttermost importance.

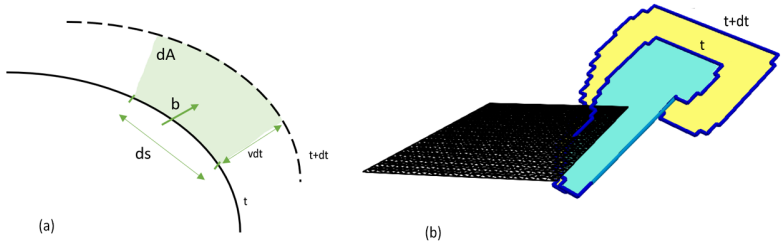

FIGURE 3.7 – ***(a)*** *representation of a dislocation advancement and the variation of its swept area* dA *corresponding to* γ ***(b)*** γ *at time* t *is represented by the blue area while at time* $t+dt$ *it is represented by the addition of the blue and yellow areas*

In order to define this equilibrium state, let γ be the area swept by the dislocations. An illustration of the swept areas is provided in Figure 3.7. After ten DDD steps, γ is calculated. Following Equation 3.12, if the relative variation of the area swept by the dislocations during these last 10 steps is inferior to 5%, we consider the dislocations to have reached a relaxed state. These values were arbitrarily chosen.

$$\frac{|\gamma_t - \gamma_{t-1}|}{|\gamma_{t-1}|} < 0.05 \tag{3.12}$$

Studied results will be considered both for the unrelaxed and relaxed configurations.

Boundary conditions

In order to account for complex boundary conditions, the superposition method [134] is used. This method uses the linear elasticity to divide complex problems in simpler ones that can be solved individually. For example, in Figure 3.8, a problem with an applied force and a dislocation is solved by considering the applied force individually and then the dislocation in an infinite space.

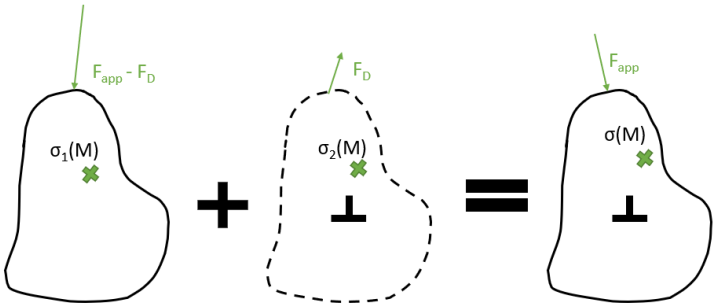

FIGURE 3.8 – *Superposition method; in order to obtain the global strain* $\boldsymbol{\sigma}$ *on M, the applied forces and the dislocations forces are considered individually*

This method has also been used for the following coupling of XFEM and DDD as explained in the following Section.

3.4 Coupling XFEM and DDD

In order to combine XFEM and DDD, we have to combine two different codes, Cast3M and TriDis. Cast3M [26] was chosen because its source code is open, allowing to program supplementary functions for the coupling. We aim at using both codes to have both a crack controlled by Cast3M and a dislocation distribution controlled by TriDis. This coupling will be using the isotropic elasticity model.

From XFEM to DDD

The two used softwares have to communicate between each other in order to carry out the simulations. First, we will discuss the data transferred by the XFEM software to the DDD one.

Volume information

Before the crack starts moving in the studied volume, this volume needs to be sent to TriDis. The main issue here is that the volume, or to be precise, the surfaces that separate the inside from the outside of the sample are initialized in TriDis when it is launched. In order to send this information, we created a file containing the volume coordinates. This file is then processed with a Python script to create the input files of the volume required by TriDis. As long as we are studying the same orientation and geometry, the same input files can be used as the volume does not change.

The crack surfaces are not send to TriDis. As said before, due to the nature of XFEM, the two surfaces of the crack are represented by a single surface in Cast3M. This surface evolves with the crack propagation and TriDis does not include a way to modify the starting volume during the simulation. Furthermore, when the crack advances, the new surface created might cross some of the existing dislocations, demanding an adjustment of said dislocations.

Initial dislocations information

Dislocations can be nucleated by either TriDis or Cast3M. In this context, nucleation means the addition of new dislocation segments in the volume. These dislocations can either be manually input, placed along a line ahead of the crack front or placed on points with the highest stresses. Since dislocations are often placed using the crack front as reference, we used Cast3M to nucleate them. The dislocation creation method included information such as : position, direction, orientation and nature. The spawned dislocations can either be Frank-Read sources or be artificially fixed. Once created, it is up to TriDis to control them.

Applied stress field

The studied volume is subjected to an external stress used to open the crack in mode I. Other modes or mixed modes are also possible, but our efforts will concentrate in mode I. This applied stress alongside the stress of the crack calculated by the XFEM is used by TriDis to move the dislocations. The stress field remains unchanged until the crack propagates, meaning that the stress field remains the same for the dislocations while they stabilize.

From DDD to XFEM

The same way Cast3M shares data with TriDis, TriDis also shares data back. This data transfer happens whenever the dislocation stability is verified, which is typically every ten DDD steps.

Dislocation stress field

The first information sent to Cast3M is the stress field created by the dislocations at specified FEM nodes. This field is calculated by the DDD software and is also used for the dislocations themselves as their stress field influence each other. This field will be used to calculate the image forces created by the surfaces as well as for the calculation of the stress intensity factors.

Image force

As presented in section 1.3, image forces are the forces a dislocation experiences in the presence of a free surface that drives it towards said free surface.

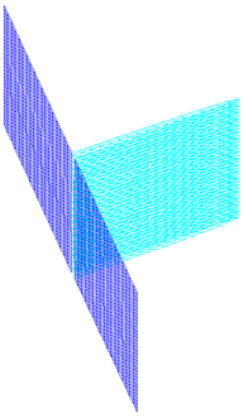

FIGURE 3.9 – *Surfaces used for the image force calculation. Crack surfaces (light blue) and volume free surface (dark blue)*

This force is calculated on the free surfaces of the volume represented in Figure 3.9. The calculation only happens before the stability of the dislocations is tested in order to save on computation time. It is calculated using the dislocation stress fields applied on the free surfaces. Once the calculation done, it is send to the DDD software as the stress fields $\boldsymbol{\sigma}_{app} + \boldsymbol{\sigma}_{image}$ so it can influence on the dislocation movement. The image forces are also included on the calculation of the crack energy following the superposition principle on Equation 2.30.

Dislocation swept area

At every step, TriDis calculate the value of the area that has been swept by the dislocations in order to compute the cumulated plastic strain (see Section 3.3). We use this value to verify the dislocation stability. Once every ten DDD iterations, the dislocation swept area is sent to Cast3M. This value is then compared to the previous area value, and if the variation is inferior to 5%, the dislocation configuration is deemed stable so the simulation can move on to crack energy calculation as well as crack advancement.

Stress intensity factor calculation

In order to calculate the effect of the dislocations on the local stress intensity factors, the dislocations stress field as well as the image forces need to be included on the stress intensity factor calculation in Equation 2.30. As described in Section 2.3, the stress field of the volume is used to calculate the stress intensity factors. Instead of only using the field generated by the applied force and the crack opening, left field in Figure 3.10, we added to it the dislocations stress field, center field in Figure 3.10, as well as the image forces stress field, right field in Figure 3.10.

In the following sections, the stress intensity factors without the dislocations effect will always be calculated as a reference.

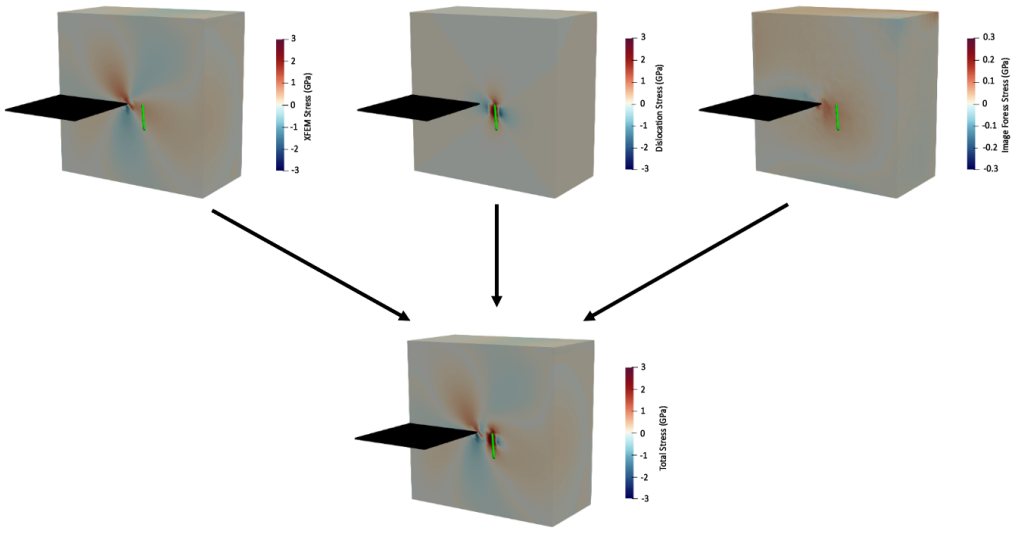

FIGURE 3.10 – *Individual stress fields used for the stress intensity factors calculations.* ***(left)*** *crack stress field* ***(center)*** *dislocation stress field* ***(right)*** *image forces stress field*

Limits of the implementation

The main limit of this implementation is the impossibility to account for crack closure. While observed in atomistic simulations, our code is unable to replicate them due to the nature of XFEM as well as the way the propagation of the crack is formulated. The new crack area created when the crack advances is added to the previous crack surface. This means that it is not possible to add a negative advancement of the crack front as it just adds a surface on top of the preexisting surface.

3.5 Simulation parameters

In the following section we will discuss on the general parameters used for the simulations. These parameters are the non variable ones ; some parameters, such as the number of dislocations or the type and value of the crack opening force will be modified as needed and presented with the corresponding simulations.

Material parameters

The MicroKIC project was set to be done with BCC materials. For sake of simplicity, we decided to start with FCC materials which removes the difficulties induced by using a thermally activated velocity law for the screw dislocation segments. The first simulations were carried out using austenitic 316L stainless steel parameters gathered in Table 3.1.

While stainless steel was useful as there was available data on it, it could not be used to compare results with atomistic simulations. Their material of choice was nickel as it is what they use for FCC simulations. The parameters used for nickel simulations are listed in Table 3.2.

Both materials are considered isotropic.

Parameter	Value	Unit
b	0.254	nm
E	210.6	GPa
ν	0.3	
μ	81	GPa

TABLE 3.1 – *Parameters for austenitic 316L stainless steel*

Parameter	Value	Unit
b	0.249	nm
E	207	GPa
ν	0.31	
μ	82	GPa

TABLE 3.2 – *Parameters for nickel*

Mesh parameters

In order to accurately model the interactions between a crack and dislocations, the mesh used for the volume needs to be properly chosen. The crack will be placed inside an element to avoid the crack front being in between two elements which can cause computation problems. The following simulations have been all carried out using stainless steel parameters. Two meshes were created for this purpose.

The first one is a nanometric sized mesh. As one of the objectives of this work is to compare DDD and atomistic simulations, we seek to reproduce said atomistic simulations in DDD. To do so, we use the volume illustrated in Figure 3.11a. As atomistic simulations simulate all the atoms present in a volume, their studied volumes are of nanometric size. DDD usually uses micrometric volumes, but the simulation parameters can be adjusted to simulate smaller volumes. More information on DDD parameters can be found in 3.5.

For future reference, another mesh was also created represented in 3.11b. This mesh aims at reproducing experimental results from a Cantilever experiment. Unfortunately, we were not able to use this mesh to compare it with any results, but the work has been prepared for future investigations when the comparison with experiments will be available.

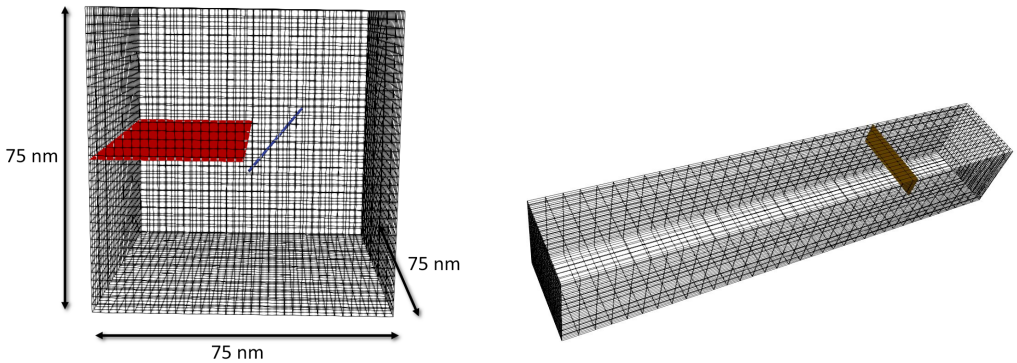

(a) Basic mesh *(b) Cantilever mesh*

FIGURE 3.11 – *Meshes created for the simulations*

Discretisation of the mesh

Element size is one of the main parameters for these simulations since the time step is dependent on the mesh size. In order for the calculations to be precise, the crack needs to advance through at least one element. This changes the element containing the crack tip and therefore allows the enrichments to be made on previously non enriched elements, preserving the calculus precision.

Since the volume does not change size, instead of referring to the discretization of the mesh by the element size, we will use the number of elements there are in the y direction to simplify the notation used.

Element size impacts also the calculation times as the more elements there are the longer the simulation will run. Since element size is tied to the time step, the smaller the elements are, the longer it will take to the simulation to completely break the mesh. In order to determine the impact of the mesh size, different parameters are studied.

As for the boundary conditions, we enforce Dirichlet boundary conditions for the bottom nodes where the three degrees of freedom are set to zero.

Crack front profile

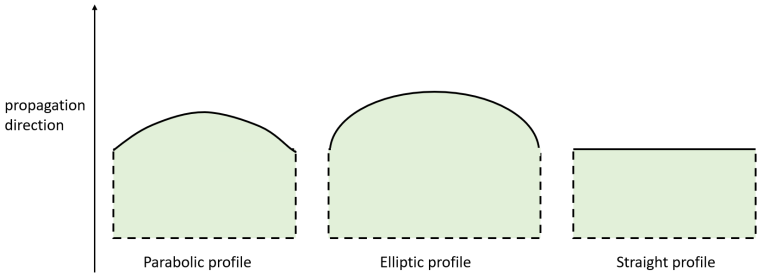

FIGURE 3.12 – *Different crack front profiles considered*

Three profiles where considered initially for the crack, an elliptic, a parabolic and a straight profile as illustrated in Figure 3.12. We aim to see if there is any important difference between the three profiles in order to chose the ones that suits us the most. First, the energy at the crack tip is studied for all the profiles. We seek to verify the consistency of the results for the same profile.

The following simulations were carried out on a cubic volume of $20 \times 20 \times 10$ µm of size without dislocations present. The material used for them was austenitic 316L stainless steel. The loading used in this case consisted in an applied negative pressure on both the top and the bottom surface of the volume of 100 MPa. Aside from comparing the profiles tested between them, these simulations were carried out for different element size as to also verify its effects.

Parabolic profile The first tested profile corresponds to a parabolic profile (see Figure 3.12 left). As can be observed in Figure 3.13 there is no consistence of the stress intensity profile along the crack front nor when the mesh size is changed. There is some tendencies that can be observed, such as a lower energy on the deeper point of the crack, but there is no regularity neither in continuity of the derivative nor on the values found thus dismissing this profile for further use. Overall, a variation of around 7% on K_I is observed which is an acceptable error.

Elliptic profile In the case of an elliptic profile (see Figure 3.12 middle), the energy in Figure 3.14, the energy at the center of the crack front, corresponding to the deeper part of the crack, is lower than at the outer parts of the crack as it is the most advanced point hence the one that

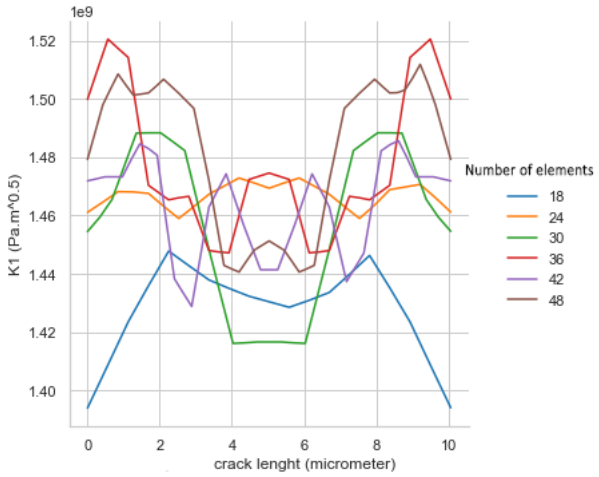

FIGURE 3.13 – *K_I for parabolic crack profiles with variable element sizes*

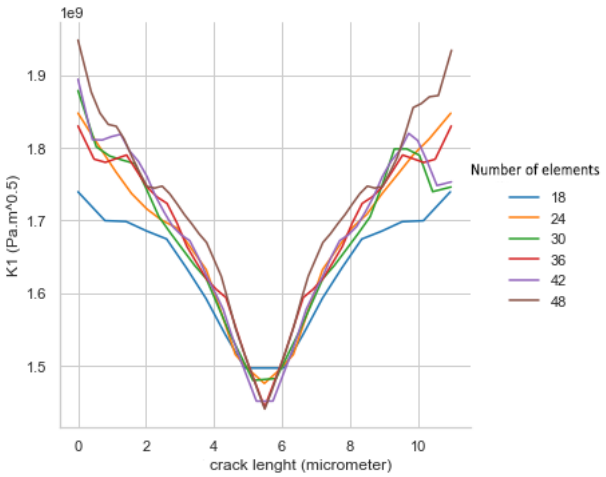

FIGURE 3.14 – *K_I for elliptic crack profiles with variable element sizes*

will advance the least on the next crack propagation step. There is some variation on the energy between the different element size, at its maximum, for the edges of the volume, this variation is around 9% which, while higher than the variation on the parabolic profile it is still acceptable.

Straight profile The last studied profile is the straight one (see Figure 3.12 right). As observed in Figure 3.15 the shape of the curve remains unchanged for different element sizes. The actual value on the other hand does vary with the element size, but does so with no apparent correlation between the variations and the element size. The maximum of the fluctuations is 5% which is an acceptable error. The element size effect will be further studied in 3.5. In most of the experimental investigation of crack propagation, the starting crack front is usually straight as it is easier to machine the samples with this geometry. This profile is the most suitable to be used on the following simulations.

Crack profile comparison Finally we compare the three studied profiles to see if the obtained values are consistent. As shown in Figure 3.16, it can be observed that K_I of the elliptic profile is much higher than the other profiles. This is mostly due to the fact that the crack sides are less advanced than the center in a more pronounced way than the parabolic one. The parabolic profile is the most unstable of the tested ones, both in shape and in value. The differences observed could

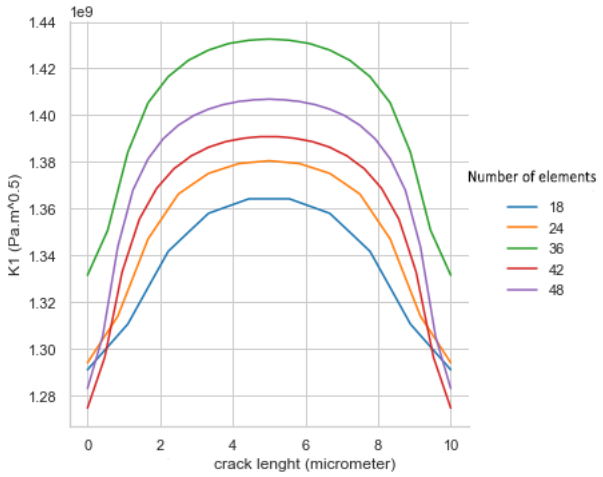

FIGURE 3.15 – *K_I for straight crack profiles with variable element sizes*

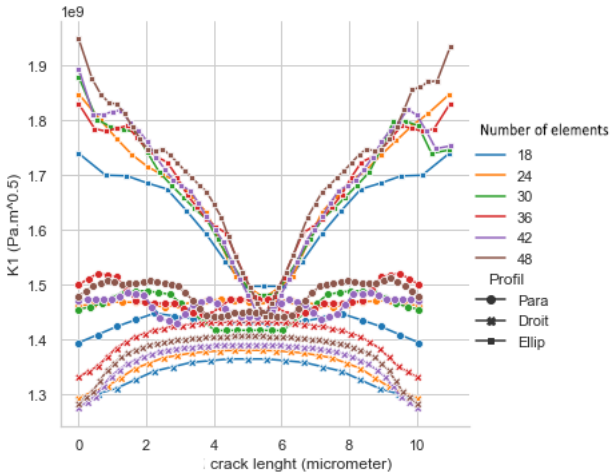

FIGURE 3.16 – *K_I plotted along the three studied profiles for several element sizes*

also be created by the fact that some configurations are closer to the stable configuration than others.

From the study of the three profiles, it is conlcuded that the profile that is the more suitable for the simulations is the straight profile. Nonetheless the element size has an impact on these values. Even if it is less regular than the straight profile, the elliptic profile is still more regular than the parabolic profile which makes it also eventually suitable for simulations if a non linear crack front is needed. The straight profile will therefore be the one used for the initial configuration unless stated otherwise.

Study of the equivalent Von Mises stress In order to compare the effect of the mesh size on the Von Mises equivalent stress, several simulations with different element sizes were carried out without dislocations and with a constant load opening the crack in mode I with a negative pressure applied to the top surface of 100 MPa. It is worth noting that the element size and number of elements are used as equivalents in here to simplify the notations. The smaller the element size is, the more elements there will be, so the number of elements along the length of the volume is used here. Since the crack speed depends on the element size, this comparison is made before the crack advances. In Figure 3.17 the equivalent Von Mises stress is compared for six different element sizes.

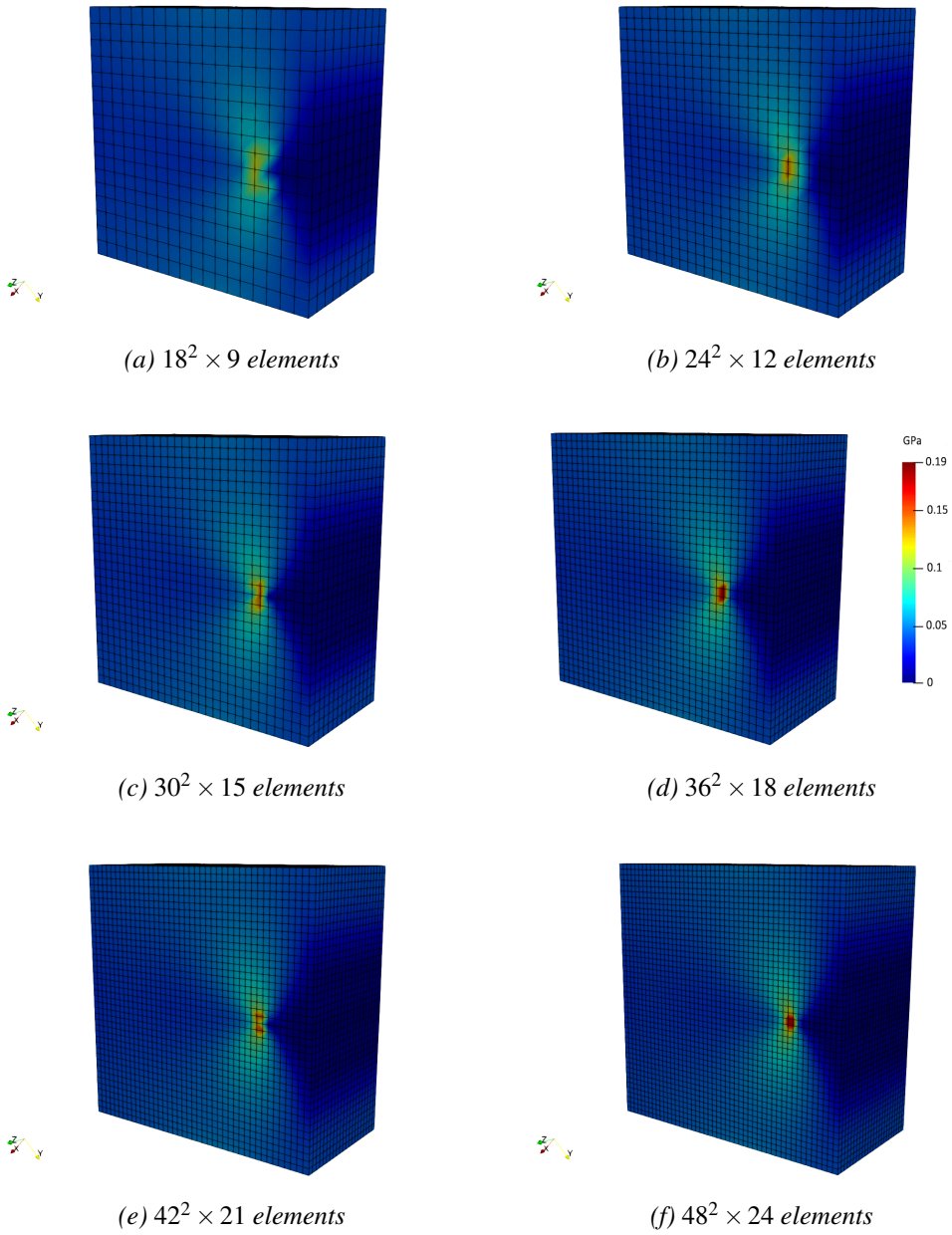

(a) $18^2 \times 9$ *elements*

(b) $24^2 \times 12$ *elements*

(c) $30^2 \times 15$ *elements*

(d) $36^2 \times 18$ *elements*

(e) $42^2 \times 21$ *elements*

(f) $48^2 \times 24$ *elements*

FIGURE 3.17 – *Von Mises equivalent stress for different element sizes. Case of a* $20 \times 20 \times 10$ *µm simulated volume with no dislocations and a mode I constant loading applied*

For all the cases, the stress distribution within the volume is equivalent as expected. But, the maximum stress on the crack tip changes. The finer the mesh is, the higher the stress on the crack tip is. Since the stress near the crack tip rapidly increases the closer to the crack tip you are, the larger the elements are, the lower the stress would be as it takes into account a bigger area to calculate the stress. A finer mesh is therefore preferred to have more accurate results. The asymmetry is caused by the crack position, it not being in the exact center of the volume but slightly displace upward.

Effect of element size on the crack front stress intensity factors In section 3.5, we illustrated not only the effect of the crack geometry but also the effect of the element size. Since we will work on straight profiles, we use Figure 3.15 to observe the element size effect on the energy values.

The element size variation results on a variation of K_I of around 5%. This variation, while not negligible is not unexpected as it is one of the main issues in finite element method [13]. As we are not comparing these results to experimental ones nor we compare simulations with different element size to each other we decide to use 36^3 elements for the future simulations with cubic simulation volumes. This element size is a compromise between accuracy and calculation time.

Volume rotation

While for XFEM the orientation of the volume is inconsequential, for the DDD simulation, the volume orientation defines the orientation of the crystal hence how the dislocations are oriented in the volume compared to the crack. The chosen orientations are listed in Table 3.3. The crack front is aligned with the x axis, the propagation direction is towards the y direction and the crack plane normal corresponds to the z direction. The Cantilever mesh had a crack of the Atomistic orientation presented in Table 3.3 as it was the orientation used in the experimental works.

The two orientations described in Table 3.3 were chosen because of existing works and results that can be used to verify our results. The first mentioned orientation noted as *Atomistic* is the one used in atomistic simulations carried out by Erik Bitzek and his team. Although atomistic simulations can only simulate nanometric volumes, if the results between DDD and atomistic simulations are similar, then it could be expected that the DDD simulations can be used accurately to simulate micrometric volumes.

The second studied orientation is called *Dense* as the crack plane is situated on a dense plane of the crystalline structure. It was also used in a study of the interactions between a static crack and dislocations in DDD. These simulations were carried out using the discrete continuous method [70]. Since we use a similar method, we thought that comparing both could lead to pertinent results.

Name	x	y	z
Atomistic	$[001]$	$[1\bar{1}0]$	$[110]$
Dense	$[\bar{1}21]$	$[\bar{1}0\bar{1}]$	$[\bar{1}\bar{1}1]$

TABLE 3.3 – *Studied volume orientations*

In order to achieve the chosen orientations, the transformation is divided in two rotations. It is worth noting that these rotations can potentially lead to a malfunction of the code. The way Cast3M works, when the rotations are carried out, the coordinates of every node of the mesh are modified instead of modifying the frame. If one of the rotation needs said coordinates to be multiplied by an irrational number, such as $\sqrt{2}$ this might lead to small misalignment of the mesh. These misalignments can cause problems in the $G-\theta$ method presented in 2.3. When the code tries to select all the elements where the crack front is located, some elements will be selected twice, so that the total number of elements is higher than it really is. When the code proceeds to calculate the stress intensity factors on each element where the crack front is, it believes that there are more elements than there actually are. The code then tries to calculate on elements that do not exist thus failing and crashing the code.

This problem can be attenuated if the crack is inserted inside an element instead of between two elements. Since the problem lies in the $G-\theta$ code, it needs to be corrected by modifying the element selection section part of the code to avoid duplicating elements.

Aside from the code malfunction, we decide to verify if the rotation has an impact on the value of K_I calculated. Since dislocations are orientation dependent, these simulations are carried out without them. The simulated volume is similar to the one plotten in Figure 3.11a but with a size of $20 \times 20 \times 10$ µm. Three cases are studied here, no rotation, a rotation around the z axis of $\frac{\pi}{4}$ (also noted as partial rotation) and a rotation that brings the crack plane to the (111) plane (also

noted as total rotation). To compare the results, K_I is calculated for the three cases at the crack front.

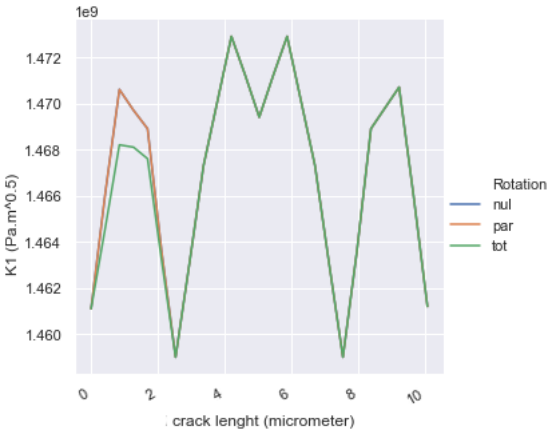

FIGURE 3.18 – *K_I for three different mesh rotations,* ***(nul)*** *no rotation* ***(par)*** *partial rotation* ***(tot)*** *total rotation*

As shown in Figure 3.18 the only difference that appears is for the (111) rotation (total rotation case). This error stems from the same error that causes the $G-\theta$ bug, the mesh misalignment. The difference between the values with and without rotation is less than 0.2% and thus should not heavily impact on the results. Although it is still necessary to acknowledge this error for the forthcoming simulations, we conclude that we can be confident that the effect of rotations is correctly taken into account in the Cast3M X-FEM calculations.

Layers used in the G-θ calculation

As described above, the G-θ method needs an envelope around the crack front in order to calculate the energy of said crack front. The way Cast3M and other finite element software achieve this is by selecting the elements containing the crack front for one layer, and then the elements surrounding these elements for the next layer and so on.

It is known that the number of layers used can affect the energy calculated with this method. In order to free the results from this variable, we performed several simulations with different number of layers to quantify the effect it has on the energy estimations. To accurately compare these results, we will compare the average K_I on the crack before it starts propagating. It is worth mentioning that the more layers we use, the longer the calculation time is.

In Figure 3.19 we observe that a minimum number of layers are needed in order to get to a stable energy value. In the forthcoming simulations, we arbitrarily decided to use four layers to have a more accurate K_I value while not penalizing the calculation time too much.

DDD parameters

TriDis not only uses the material parameters presented in 3.5 but also other parameters concerning the behavior of dislocations as explained in Section 3.3. Two sets of parameters have been used depending on the size of the studied volume. In order to reproduce atomistic simulations, the scale of the studied volume needs to be nanometric as opposed to the regular studied volume that is micrometric. Because of this, DDD parameters need to be also modified accordingly.

While not as explicitly seen as in XFEM, DDD also relies on a discretization of the space. The DDD space discretization depends on the *xl* parameter presented in Figure 3.2, which defines the mesoscale FCC lattice on which each dislocation segment is attached. This parameter is usually chosen as : $xl = 10b = 25.98$ Å with b the Burgers vector. For a nanometric volume, *xl* should be

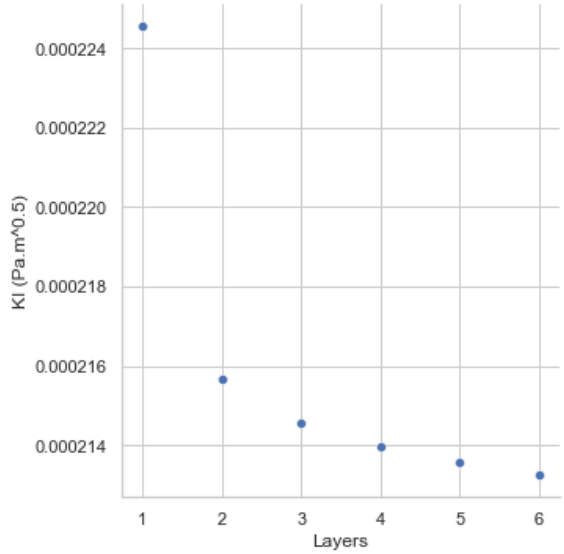

FIGURE 3.19 – *K_I evolution for a variable envelope size used in the G-θ method*

reduced to a size smaller than the actual distance between two atoms in a crystal, in our case, we choose $xl = 2.598 \times 10^{-2}$Å. Note that we could think that elasticity theory should not be used at distance smaller than the atomistic distance. However, prior simulations have proven that it is the case [43, 85]. One could conclude that elasticity framework is robust down to the atomic scale.

There is also a discretisation size for the dislocation segments that is depending on xl. This size is usually around 100 times xl.

In order for the simulation to run in a stable manner, it is important to also adapt the time step. The smaller the discretization length is, the shorter the time step should be. For the nanometric volume size, the time step is as small as 10^{-12} s.

Parameter	Value	Unit
T	300	K
τ_{III}	0.056	GPa
V_{act}	1800	b^3

TABLE 3.4 – *Cross-slip parameters*

Cross slip can also be controlled but since it is not the main topic here, and we will just recall the parameters given in Table 3.4 for the Equation 3.8.

Computation times

The simulations last between thirty minutes up to two hours. The calculation that requires the most time is the dislocation movement as it usually requires up to one hundred more steps than the crack propagation. The more dislocations are present in the volume, the longer the DDD calculation times are, which translates into an increase of the step calculation times. There is no parallelization in the coupled scheme except the internal stress calculation in the DDD part and in the linear solver for the FEM calculations.

3.6 Conclusion

This Chapter reviewed the main DDD models and explained in depth the model used in this work. In this Chapter we also introduced the code we worked on that couples XFEM and DDD. The XFEM method and its implementation in Cast3M was described alongside the theory and application of the stress intensity factor calculation method. The coupling of the two methods require for them to communicate and send each other the needed information like, for example, the stress fields corresponding to the crack opening or the dislocations. Finally, the fixed parameters that will be used for the future simulations have also been described.

4

Comparison between atomistic simulations results and discrete dislocations simulations

Contents

4.1 Introduction

This chapter aims at verifying the accuracy of the model presented in Chapter 3. In order to do this we will compare our results with results obtained with atomistic simulation as well as some experimental results.

Firstly, the different dislocation types selected for the simulations will be categorized into Classes which are defined by the symmetry of the stress seen by the dislocations. The different dislocation Classes will be studied by analyzing the values of the stress intensity factors. Lastly, a detailed comparison between an atomistic simulation and a discrete dislocation simulation will be carried out.

4.2 Dislocation classes

Definition

I	$AC(b) \equiv BD(a)$	$BC(a) \equiv AD(b)$
II	$AC(d) \equiv BD(c)$	$BC(d) \equiv AD(c)$
III	$AB(d) \equiv DC(a)$	$AB(c) \equiv DC(b)$

TABLE 4.1 – *Symmetries for the different dislocation classes*

Dislocations for a (110) crack orientation can be classified on three classes listed in Table 4.1. Dislocations belonging to the same class will have the same behavior as they will experience the same forces. This class definition has been used for atomistic simulations in the case of a (110) crack plane $[001]$ crack front loaded in mode I [17] and here we seek to verify if the dislocation behavior of two dislocations belonging to the same class is indeed equivalent, for an equivalent dislocation position in regards of the crack, and if the forces they experience are similar.

Simulations parameters

Mesh orientation

The studied volume, of 75 nm of size, is oriented following Figure 4.1. This orientation was chosen to be the same as the one studied in [17] : the crack plane is (110) and the crack front is $[001]$. Mesh parameters are the same as the ones described in Chapter 3

Loading and boundary conditions

In order to verify the accuracy of our simulations, they will be carried out by imposing a displacement on the upper surface nodes which will induce a tensile strain on the upper surface of the volume following the z direction, opening the crack in mode I. This displacement, once imposed, will remain the same throughout the entire simulation. For a sharp crack, we note ε_G the critical strain above which the crack becomes unstable in atomistic simulations. We use the strain values calculated in [16] and referred in Equation 4.1 as the critical applied strain ε_G. Our loading will be of $\varepsilon = 0.998\varepsilon_G$ that is to say that the applied load is just a 0.2% below the critical value so that the crack is still stable. The set of loading application is illustrated in Figure 4.2.

$$\varepsilon_G = 0.01896 \Rightarrow \varepsilon = 0.998\varepsilon_G \Rightarrow \varepsilon = 0.01892208 \tag{4.1}$$

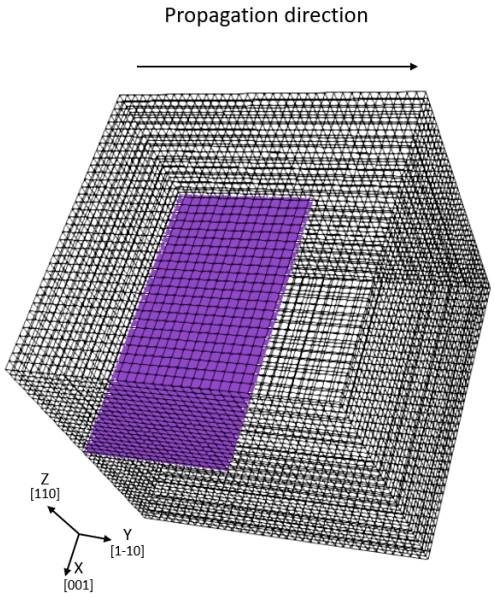

FIGURE 4.1 – *Orientation of the studied volume*

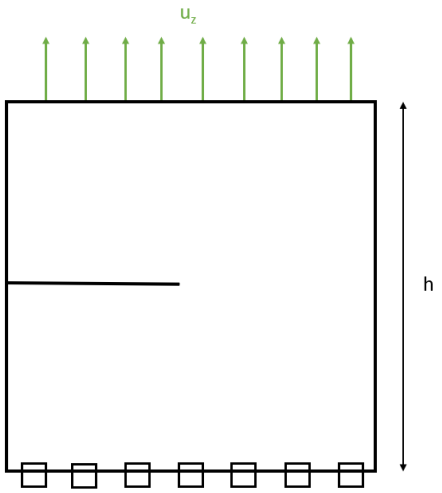

FIGURE 4.2 – *Boundary conditions used for the DDD calculations. The bottom nodes are all fixed and a vertical displacement of magnitude* $u_k = h \times \varepsilon$ *is applied to the top nodes*

This strain will allow the dislocations to move freely while being in theory too low for the crack to propagate. There is no crack propagation as in order to have comparable results the geometry of the crack front needs to remain the same between simulations.

As for the boundary conditions, the bottom surface is blocked, as illustrated in Figure 4.2 and the loading is applied on the top surface. None of the surfaces are free surfaces for the dislocations and they cannot interact directly with the crack surfaces.

Dislocations

In order to study the different dislocation classes, two dislocations of each class will be studied. The orientation of these dislocations is described in Table 4.2. All dislocations will be screw dislocations of length $l = 30$ nm. The line direction is taken as the same as the Burgers vector (positive screw segments). Dislocations will be placed such as the center of the dislocation is

Class	Class I		Class II		Class III	
System	*BC(a)*	*AD(b)*	*BC(d)*	*AD(c)*	*AB(d)*	*DC(a)*
Burgers vector	$[\bar{1}01]$	$[101]$	$[\bar{1}01]$	$[101]$	$[1\bar{1}0]$	$[\bar{1}\bar{1}0]$
Slip plane	$(\bar{1}1\bar{1})$	$(1\bar{1}\bar{1})$	(111)	$(\bar{1}\bar{1}1)$	(111)	$(\bar{1}1\bar{1})$

TABLE 4.2 – *Description of the studied dislocations including Burgers vectors and slip planes*

placed at $\Delta d = 8$ nm from the center of the crack front in the crack propagation direction $y = [1\bar{1}0]$.

Class I

Stress maps

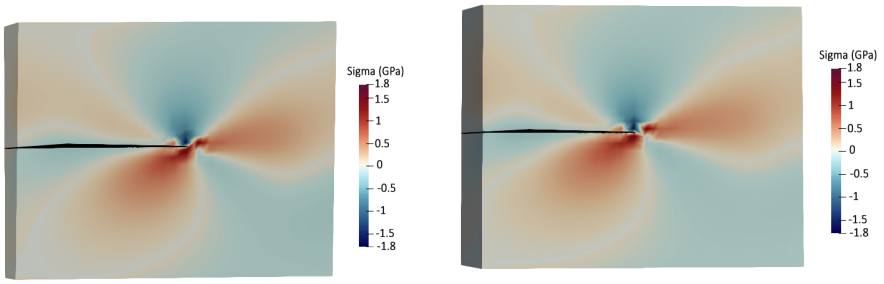

(a) BC(a) *(b) AD(b)*

FIGURE 4.3 – *Shear stress map induced by the solely presence of the crack and resolved on different slip systems of Class I dislocations. Stresses are plotted in sections for the simulated volume corresponding to the respective dislocation slip planes*

Figure 4.3 show how the studied dislocations perceive the same resolved shear stress from the crack and the applied loading only, without the effect of the dislocation. The stresses are plotted in a section plane corresponding to the dislocation slip plane. The stress patterns show an heterogeneous resolved shear stress with change of signs.

As the resolved shear stress fields are equivalent, we will be using the calculated values of the Stress Intensity Factors to further verify if these two dislocation orientations are equivalent.

Dislocation symmetry

Setting In order to study Class I dislocations, we will be comparing the effect of a *BC(a)* dislocation and an *AD(b)* dislocation on the stress intensity factors. The starting dislocations are illustrated in Figure 4.4. Both dislocations are oriented similarly in regards of the crack front while still placed on their respective glide planes.

Once the dislocations move towards their respective relaxed configuration, illustrated in Figure 4.5, we observe that both are stable on a configuration very similar to the starting one. It is also worth noting that the dislocations do not cross the crack front.

Unrelaxed configuration We consider first the effect of these dislocations on K_I and K_{II}, illustrated in Figure 4.6. Both dislocations have a shielding effect in average on the crack front as they lower its energy. The effect created by the *BC(a)* dislocation is more than twice as high as the one created by the *AD(b)* dislocation. Both dislocation have the same size of the affected zone on the crack front energy.

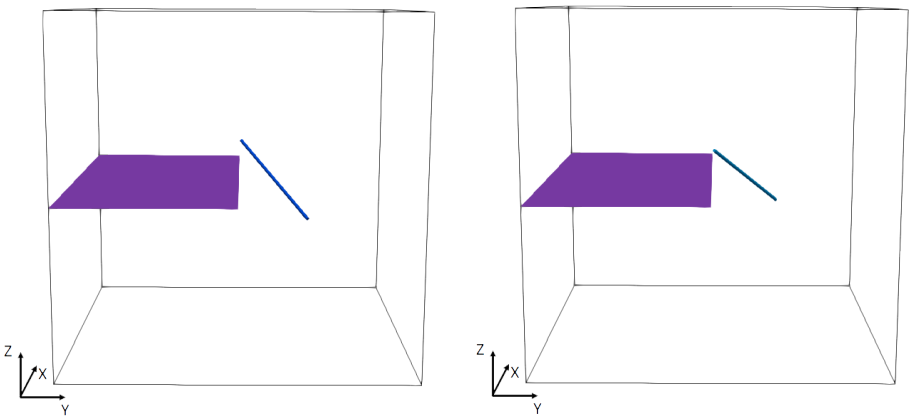

(a) BC(a) *(b) AD(b)*

FIGURE 4.4 – *Initial configuration of the two studied Class I dislocations*

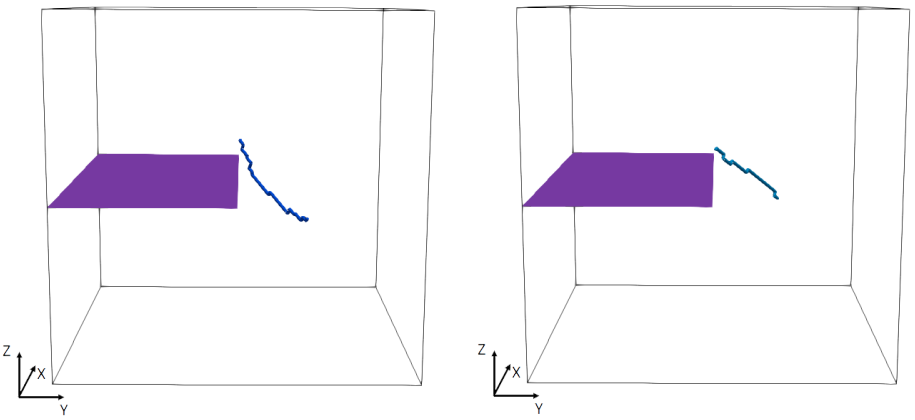

(a) BC(a) *(b) AD(b)*

FIGURE 4.5 – *Relaxed configuration of the two studied Class I dislocations*

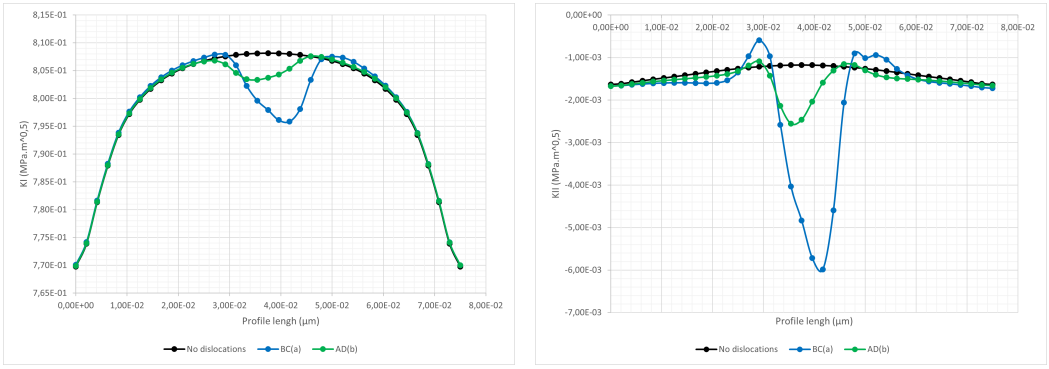

(a) Values of K_I along the crack front for Class I dislocations on the unrelaxed configuration *(b) Values of K_{II} along the crack front for Class I dislocations on the unrelaxed configuration*

FIGURE 4.6 – *Stress intensity factors for the studied Class I dislocations on the unrelaxed configuration*

Relaxed configuration After the dislocations reach a relaxed configuration, the stress intensity factors of their respective cracks are illustrated in Figure 4.7. Overall, both dislocations still provide shielding to the crack front, but *BC(a)* has a local antishielding effect, making the crack try

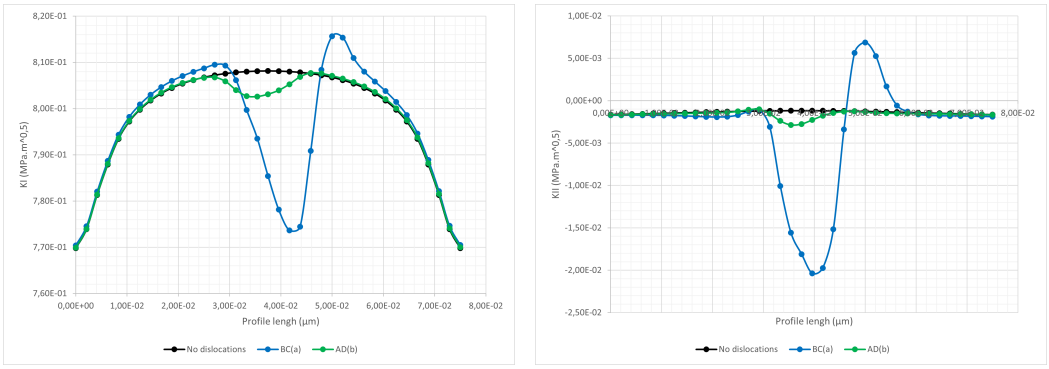

(a) Values of K_I along the crack front for Class I dislocations on the relaxed configuration

(b) Values of K_{II} along the crack front for Class I dislocations on the relaxed configuration

FIGURE 4.7 – *Stress intensity factors for the studied Class I dislocations on the relaxed configuration*

to surround the dislocation instead of being attracted to it. The *AD(b)* dislocation effect has not changed between configuration, which is due to the similarity between both configurations for this dislocation.

Conclusion

Globally, the studied Class I dislocations provide a shielding effect on the crack. The dislocation effect is enhanced by its propagation as shown by the relaxed configuration results. The *BC(a)* dislocation develops a small antishielding effect around the shielding effect, making the crack go around the dislocation. As for *AD(b)* the effect remains unchanged and the dislocation stabilizes without propagation.

Class II

Stress maps

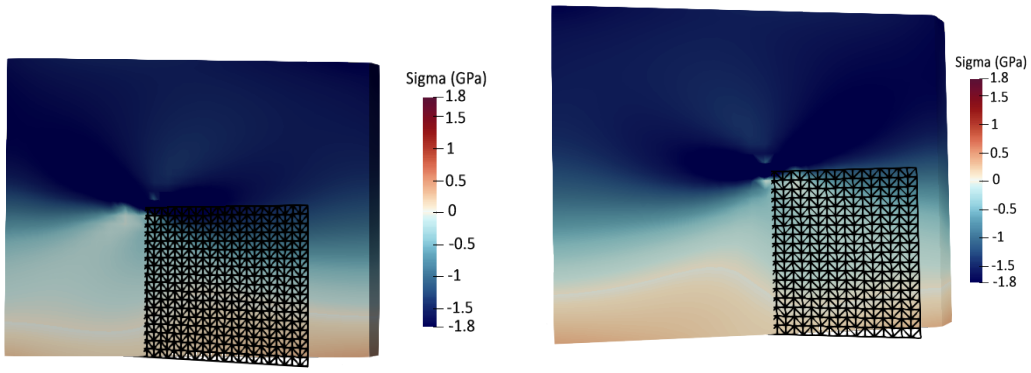

(a) BC(d)

(b) AD(c)

FIGURE 4.8 – *Shear stress map induced by the solely presence of the crack and resolved on different slip systems of Class II dislocations. Stresses are plotted in sections for the simulated volume corresponding to the respective dislocation slip planes*

For Class II dislocations, their perceived stress is illustrated on Figure 4.8. For this case, the perceived stress relative values are high compared to the previous studied case, particularly in front

of the crack. This leads us to believe that for the dislocations to reach their stable configuration, they will need to propagate more than the previous studied case.

Dislocation symmetry study

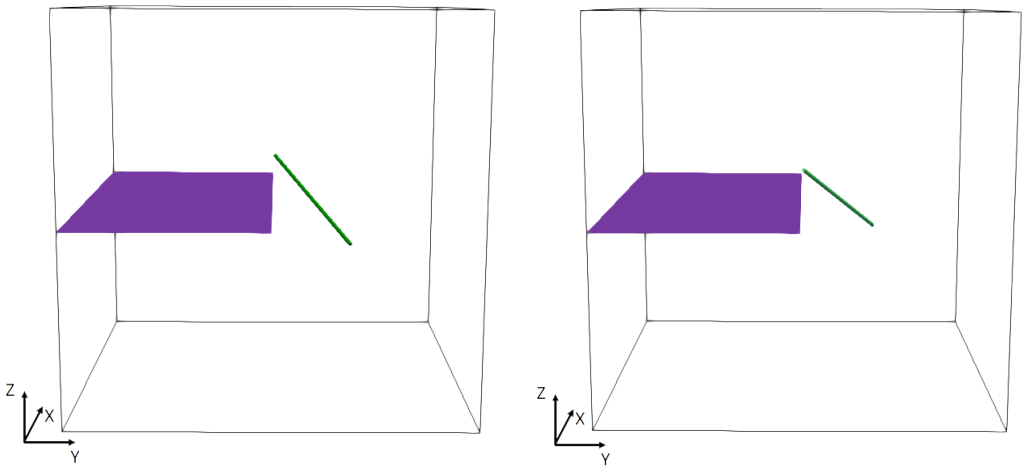

(a) BC(d) *(b) AD(c)*

FIGURE 4.9 – *Starting configuration of the two studied Class II dislocations*

Setting Two Class II dislocations will be studied here. These dislocations, illustrated in Figure 4.9, are screw dislocations of orientations *BC(d)* and *AD(c)*.

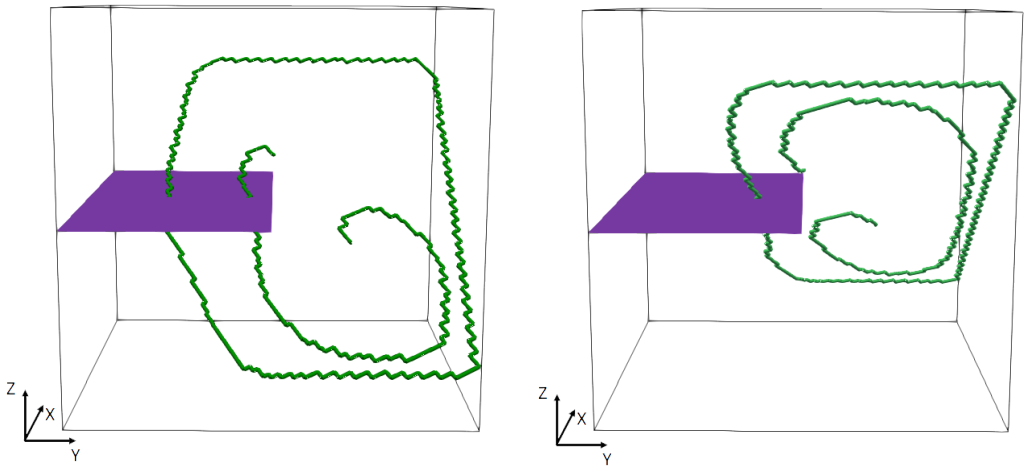

(a) BC(d) *(b) AD(c)*

FIGURE 4.10 – *Relaxed configuration of the two studied Class II dislocations*

The dislocation relaxed configuration can be found in Figure 4.10. Both dislocations create at least one dislocation loop before stabilizing. Both loops cross the crack front and a part of the crack surface.

Unrelaxed configuration The results in Figure 4.11 correspond to the unrelaxed configuration. Globally, the dislocations cause an antishielding effect on the crack. It is worth noting the symmetry on the K_I curve. This symmetry exists because the starting dislocations are also symmetric.

This symmetry is not quite as clear for K_{II}, which could be caused by its values being too low for such an effect to appear.

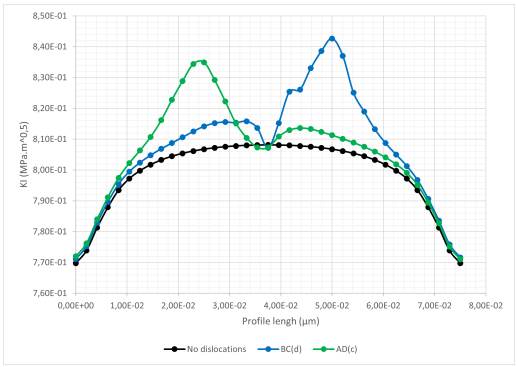

(a) Values of K_I along the crack front for Class II dislocations on the unrelaxed configuration

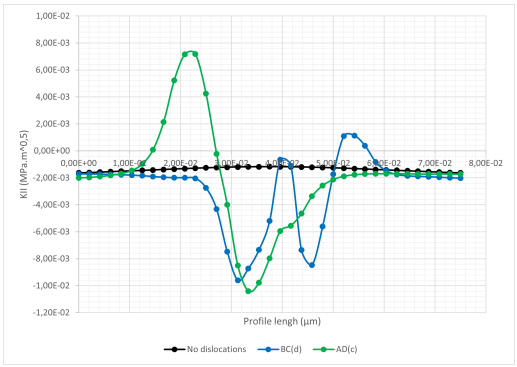

(b) Values of K_{II} along the crack front for Class II dislocations on the unrelaxed configuration

FIGURE 4.11 – *Stress intensity factors for the studied Class II dislocations on the unrelaxed configuration*

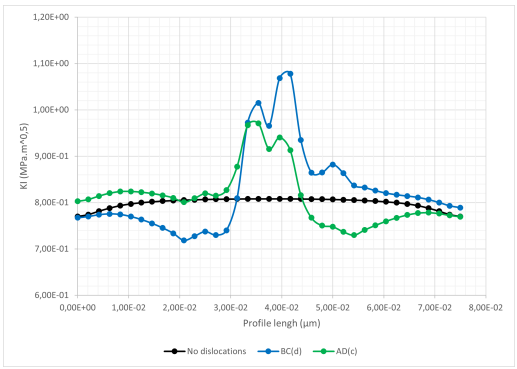

(a) Values of K_I along the crack front for Class II dislocations on the relaxed configuration

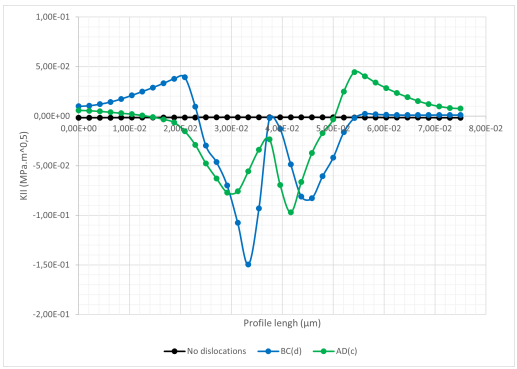

(b) Values of K_{II} along the crack front for Class II dislocations on the relaxed configuration

FIGURE 4.12 – *Stress intensity factors for the studied Class II dislocations on the relaxed configuration*

Relaxed configuration Once the dislocations reach the relaxed configuration, we obtain the results illustrated in Figure 4.12. The observed behavior is quite similar to the unrelaxed one. The predominant effect on the crack front energy is still the antishielding one though a small shielding zone does appear. The fact that the dislocations cross the crack front does not seem to affect the obtained results.

Unlike the unrelaxed configuration, K_{II} does show a mirror symmetry on its results. The dislocation effect zone is large enough to cover the whole crack length.

Conclusion

Overall, the studied Class II dislocations provide an antishielding effect to the crack. This effect does not change even after the dislocations crossed the crack front. The dislocations symmetry is translated to a symmetry of the results for the studied stress intensity factors. Independently of the dislocation relaxation, the whole crack is under the effects of the studied dislocations.

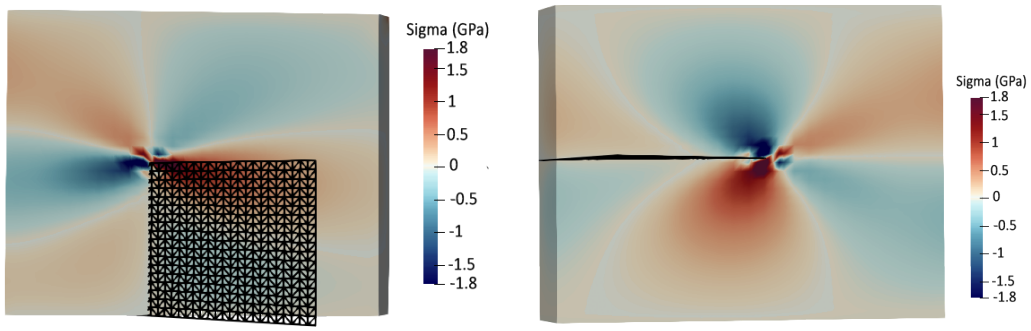

(a) AB(d) *(b) DC(a)*

FIGURE 4.13 – *Shear stress map induced by the solely presence of the crack and resolved on different slip systems*

Class III

Stress maps

Stress maps perceived by the Class III dislocations are illustrated in Figure **??**. Similarly to Class I dislocations, the stress sign perceived by these dislocations varies all along their glide plane. This sign variation can lead to a variety of dislocation behaviors. It is worth noting that the overall stress perceived by these dislocations is higher than for Class I dislocations.

Dislocation symmetry

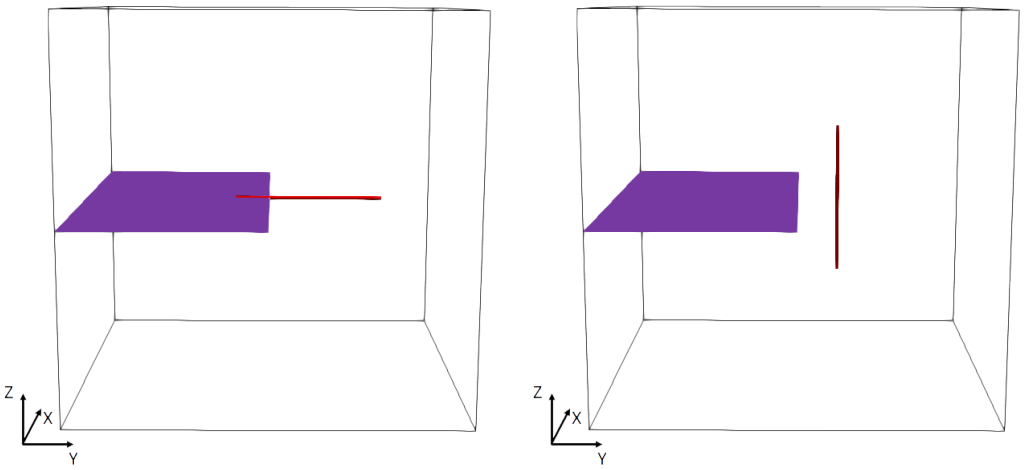

(a) AB(d) *(b) DC(a)*

FIGURE 4.14 – *Starting configuration of the two studied Class III dislocations*

Setting The starting configurations for the Class III dislocations illustrated in Figure 4.14 differ greatly from each other. Dislocation *AB(d)* is co-planar with the crack which, knowing the positioning of the dislocation, makes it cross the crack front. This leads us to believe that the results for this dislocation will be of much higher magnitude.

Once the dislocation relax, we obtain the configuration illustrated in Figure 4.15. Even if the *AB(d)* dislocation is much closer to the crack front since its glide plane is coincident with the crack plane, the two configurations are close in shape. Both dislocations do not need to propagate much in order to reach a stable configuration.

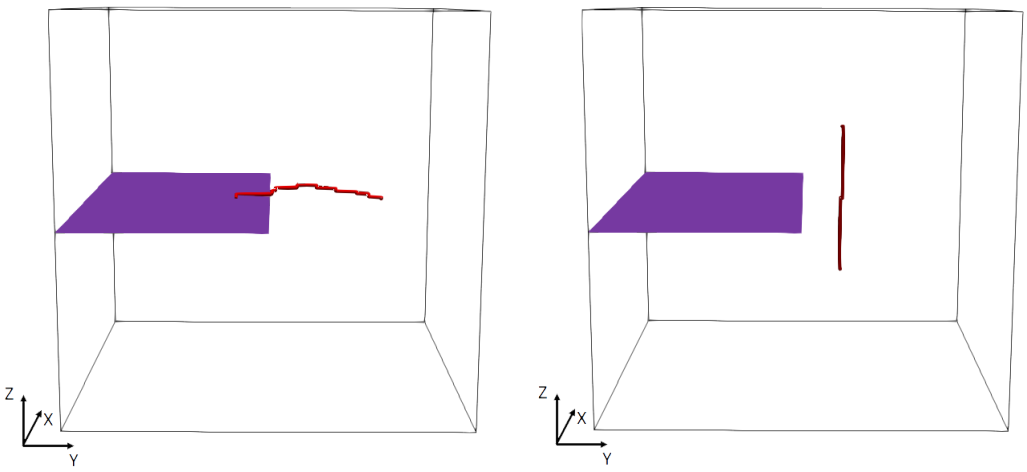

(a) AB(d) *(b) DC(a)*

FIGURE 4.15 – *Relaxed configuration of the two studied Class III dislocations*

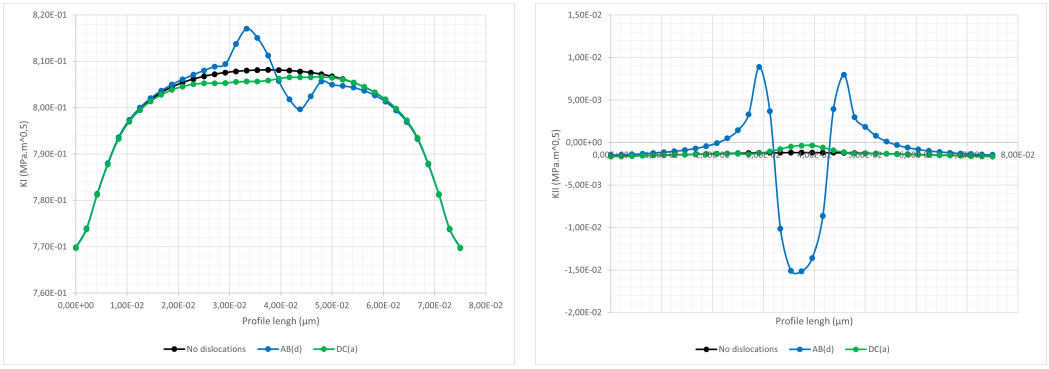

(a) Values of K_I along the crack front for Class III dislocations on the unrelaxed configuration *(b) Values of K_{II} along the crack front for Class III dislocations on the unrelaxed configuration*

FIGURE 4.16 – *Stress intensity factors for the studied Class III dislocations on the unrelaxed configuration*

Unrelaxed configuration As suspected, the results for the *AB(d)* dislocation (blue curve) illustrated in Figure 4.16 are of a much larger magnitude than those for the *DC(a)* dislocation (green curve). Both dislocations provide a very different effect on the crack. *AB(d)* provides both shielding and antishielding in equal measures while *DC(a)* only provides shielding. The values of K_{II} suggest a very drastic change of propagation angle, which is controlled by K_{II}, around the dislocation.

Relaxed configuration Once the dislocations relax, the same general behavior is observed. As illustrated in Figure 4.17, the values for K_I seem to be of a closer magnitude after relaxation. On the contrary, K_{II} still shows a difference of more than five times the absolute value between both dislocations. The dislocation effect on K_{II} is therefore more dependent on the crack-dislocation distance.

As for K_I, the values obtained could almost be considered a mirrored image of each other if the value of *DC(a)* was higher. Overall, the results are consistent with the ones obtained for the unrelaxed configuration.

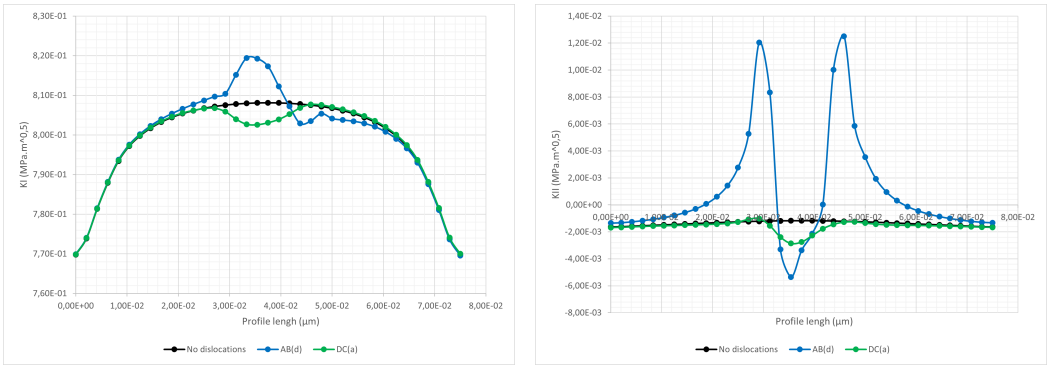

(a) Values of K_I along the crack front for Class III dislocations on the relaxed configuration

(b) Values of K_{II} along the crack front for Class III dislocations on the relaxed configuration

FIGURE 4.17 – *Stress intensity factors for the studied Class III dislocations on the relaxed configuration*

Conclusion The differences observed on this Class are mainly due to the dislocation position. Both dislocation stabilize close to their starting position. The dislocation effect varies from a dislocation to the other but there seems to be a slight symmetry on the dislocations effect that might be independent from the dislocation position.

Conclusion

We studied both the stress perceived by different dislocations as well as their effects on the crack front stress intensity factors. We aimed to compare our results with atomistic simulation results. Globally, the results obtained are what we expected. The stress fields perceived by the dislocations of the same Class are equivalent. The dislocation effect on the crack front energy is also equivalent, between dislocations of the same Class, except for Class III dislocations due to the crack-dislocation distance not being equivalent for both studied cases. More on crack dislocation distance will be discussed in Chapter 5.

4.3 Direct results comparative : Parameters

In order to further verify the accuracy of our simulations, we will now compare or DDD-XFEM calculations to an atomistic simulation. To have an accurate comparison, both simulations need to be done using the exact same parameters when possible. The atomistic simulation was carried out by Erik Bitzek [16]. The simulation parameters used for these simulations will be described next.

Mesh

The mesh used for both simulations corresponds to a cube of 75 nm of size. Both meshes are oriented as shown in Figure 4.18. In XFEM, cracks do not change of nature and are always considered as sharp. For atomistic simulations, as all atoms are studied, cracks can be not only simulated as sharp or blunt but the nature of the crack can change during the simulation. For this reason both simulations will be carried out with a mesh containing a sharp crack.

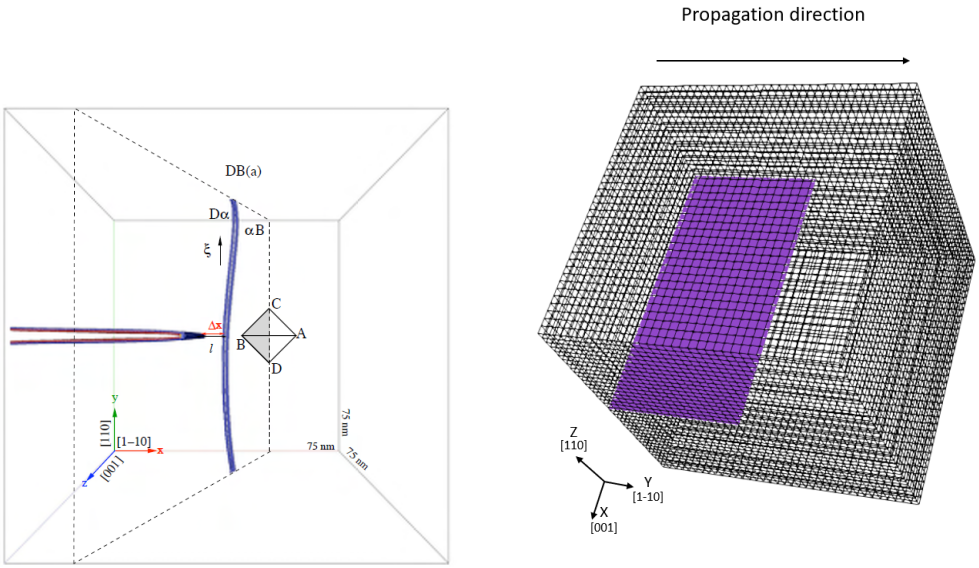

FIGURE 4.18 – ***(a)*** *Atomistic mesh, the dislocation displayed is just an illustration and does correspond to the studied dislocation [16].* ***(b)*** *XFEM mesh, the purple plane corresponds to the crack position*

Dislocation

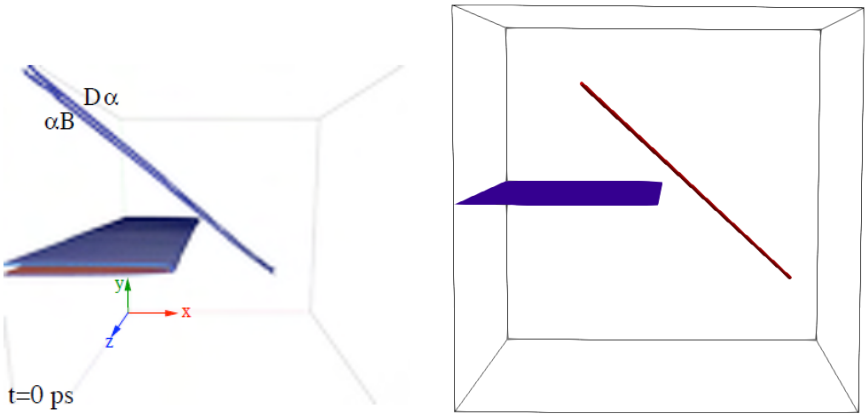

(a) Atomistic configuration [16] *(b) DDD configuration*

FIGURE 4.19 – *Dislocations configuration used on both simulations. In atomistic simulations, the dislocation lines split in partial segments. Both volumes share the same orientation*

For these comparative simulations, both will include a single screw dislocation of Class I, specifically of the *BD(a)* system. Both starting configurations are illustrated in Figure 4.19. The dislocation will be placed so it is at 8 nm of the crack front following the crack propagation direction.

Loading

The loading conditions used are those of plane strain. The strain applied on the mesh will correspond to $0.998\varepsilon_G$ with ε_G being the Griffith strain presented in Section 4.2. The loading will be opening the crack in mode I though no crack propagation occurs. It will be applied at the start of the simulation and will not change of value.

4.4 Direct results comparative : Results

Atomistic simulation results

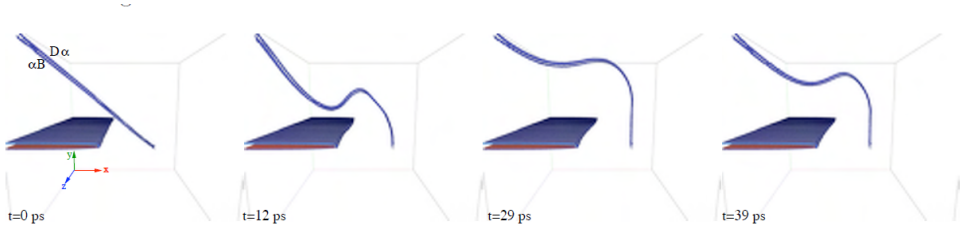

FIGURE 4.20 – *Snapshots of a screw dislocation interacting with a sharp crack. These results were obtained in an atomistic simulation [16]*

Figure 4.20 shows the stabilization of a dislocation and a crack in an atomistic simulation with the parameters described above. Compared to DDD simulations, in atomistic simulations dislocations have more freedom of movement while stabilizing. The simulated crack is a sharp crack, meaning that it can either close or open during the simulation due to the dislocation influence and the loading.

During this simulation the dislocations bows and oscillates while moving towards the crack surface. The stable configuration reached puts the dislocation so it is bowed towards the crack surface while remaining distant from the crack front.

Dislocation Dynamics results

This simulation was carried out to replicate the previous simulation using the DDD+XFEM model and the same parameters. Unlike the atomistic simulation, the crack will not advance in this simulation. This might cause some differences in the results as the crack stress field would vary. The focus will be on the dislocation movement.

The results for this simulations are represented in Figure 4.21. Globally, the dislocation moves away from the crack, though the center of the dislocation remains near the crack front, only slightly moving away at the end of the simulation when the dislocation reaches a stable configuration. This is most likely due to the effect of the image forces on the dislocation created by the crack surface.

Results comparison

Both simulation results share several similarities. First, neither dislocation crosses the crack front nor interacts directly with it. The lower part of both dislocations have moved away from the crack to reach a stable configuration, while the middle part of the dislocation remains close to the crack front.

As these simulations were carried out using different methods, there are of course differences in the results too. Firstly, the behavior of the upper part of the dislocation varies from one simulation to the other. For the atomistic simulation, the dislocations moves towards the crack while for the DDD simulation the dislocation moves away from it. Also, the dislocation movement is more pronounced in the atomistic simulations.

These differences find their origins in several factors. First, both methods define dislocation movement in different ways. Atomistic simulations is based on the movement of the atoms which in turn moves the dislocation while in DDD the dislocations are explicitly defined as well as their movement. It is worth noting that in atomistic simulations, dislocations are partial dislocations which is not the case in DDD. On the other hand, DDD defines a dislocation as edge and screw segments connected between each other. The crack on the atomistic simulation is allowed to freely

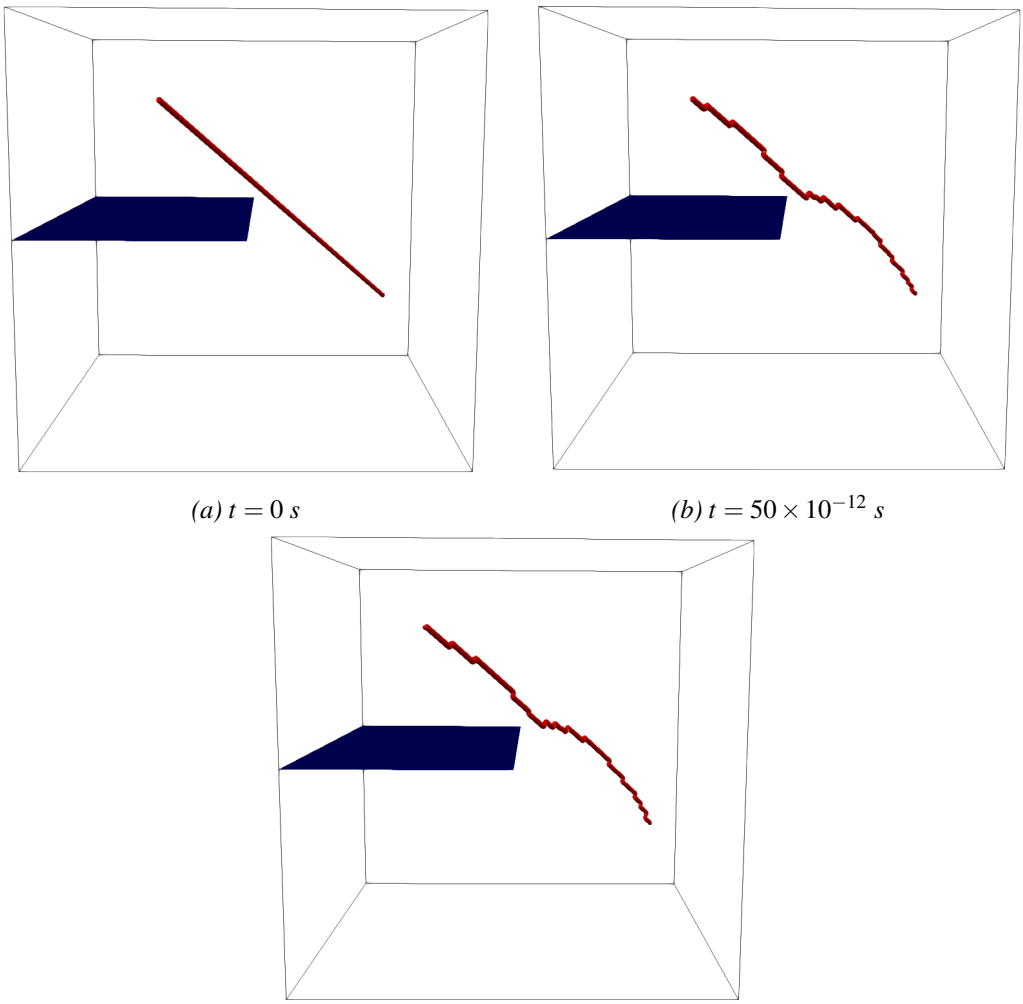

(a) $t = 0\ s$ *(b)* $t = 50 \times 10^{-12}\ s$

(c) $t = 100 \times 10^{-12}\ s$

FIGURE 4.21 – *Snapshots of a screw dislocation interacting with a sharp crack These results were obtained with a DDD simulation*

move which will inevitably influence the dislocation movement. The main difference behind the movement difference in the damping of the dislocation. DDD overdamps the dislocation which leads to its movements being limited compared to the atomistic simulation.

4.5 Conclusion

We compared to results obtained with atomistic simulations. First, we test several dislocations of different orientations to see their effects on the stress intensity factors. Dislocation orientation can be grouped by the effects they have on a crack. We tested if this classification still hold true within our model. As the results presented show, this classification stands for our model.

In order to further validate our model, a simulation aiming at replicating the results of an atomistic simulation was carried out. Both simulations used the same parameters. Overall, the same dislocation behavior is observed between both simulations though some differences are apparent. These differences are originated in the differences between both simulation methods. These first

simulations give self confidence to the DDD-XFEM method so that it can be further used for more detailed crack-dislocation investigations as presented in next Chapters.

5

Effect of dislocations on the stress intensity factors for the $O_{1\bar{1}0}$ orientation

Contents

5.1 Introduction

We seek to study the effect of dislocations, in particular their nature as well as their number on the stress intensity factors. Dislocations can cause both shielding and antishielding effects on the crack. Understanding what causes these effects is primordial to understand how cracks propagate and how the crack chooses a path to propagate on. Without dislocations present, the crack will propagate in plane, it is the addition of the dislocations that can potentially make the crack propagate out of plane.

The studied parameters will be the applied loading, the crack dislocation distance as well as the number of dislocations. Simulations will be carried out on pure screw dislocations. We will be using one dislocation of each Class described in Chapter 4.

5.2 Numerical parameters

Studied mesh parameters as well as discrete dislocation dynamics parameters are defined in Section 3.5.

Crystal orientation

A single crystal system will be studied here. This orientation is noted $O_{1\bar{1}0}$ and is the same orientation as used in Chapter 4 and recalled in Figure 5.1. $O_{1\bar{1}0}$ was chosen because it allowed comparisons of our DDD results with atomistic simulations results. The crack is defined with a crack plane (110), a crack front [001] and a propagation direction $\left[1\bar{1}0\right]$.

Dislocations

Dislocations used in the following simulations are all of the same length, $l = 30$ nm. They all are Frank-Read sources made of pinned screw segments that are able to create dislocation loops at high stress. Screw dislocations were chosen as the starting dislocations for their ability to cross slip if the conditions are met. Three dislocation orientations, described in Table 5.1, will be used. As described in Chapter 4, for the $O_{1\bar{1}0}$ orientation, dislocations can be divided in three classes depending on their interactions with a propagating crack. We decide to study one dislocation of each class to see their effects on the stress intensity factors. The same dislocations will be studied on the $O_{\bar{1}0\bar{1}}$ orientation.

	Class I	Class II	Class III
System	*CB(a)*	*CB(d)*	*AB(d)*
Burgers vector	$\left[10\bar{1}\right]$	$\left[10\bar{1}\right]$	$\left[\bar{1}10\right]$
Line vector	$\left[10\bar{1}\right]$	$\left[10\bar{1}\right]$	$\left[\bar{1}10\right]$
Slip plane	$(\bar{1}1\bar{1})$	(111)	(111)
Schmid-Boas notation	D4	B4	B5

TABLE 5.1 – *Dislocations used in the simulations*

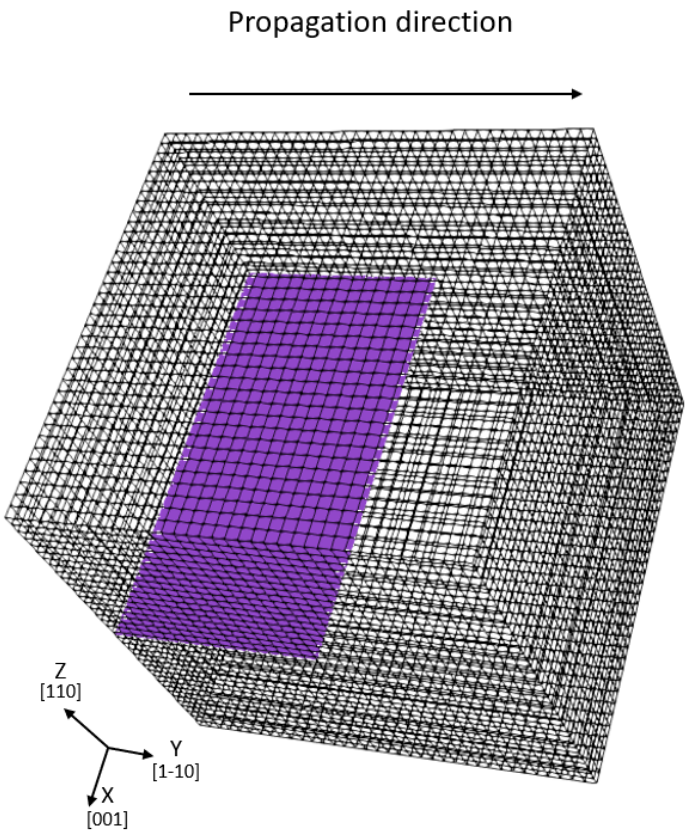

FIGURE 5.1 – *Studied crack orientation $O_{1\bar{1}0}$. The studied volume is a cube of 75 nm of size*

Dislocations are placed in front of the crack. The center of the dislocations are placed at 8 nm of the crack front following the propagation direction y. Dislocations are placed at the center of the crack length, if there is more than one dislocation, the remaining dislocations are spaced out at regular intervals in front of the crack tip. Simulations will be carried out with one, three or five dislocations in front of the crack.

Loading conditions

The simulations will be carried by imposing a displacement on the upper surface nodes which will induce a tensile strain on the upper surface of the volume following the z direction, opening the crack in mode I. This displacement, once imposed, will remain the same through the simulation. According to the Griffith concept of energy balance [74], a crack is thermodynamically stable when the energy released by the surface creation equals the reduction of strain energy by crack advance. For a sharp crack, we note ε_G the critical strain for which said crack is stable. We use the strain values calculated in [16] and referred in Equation 5.1 as critical strain. Our loading will be of $0.998\varepsilon_G$.

$$\varepsilon_G = 0.01896 \Rightarrow \varepsilon = 0.998\varepsilon_G \Rightarrow \varepsilon = 0.01892208 \tag{5.1}$$

In order to accurately compare the obtained results in this first investigation, the crack will not be allowed to propagate since this propagation would be entirely dependent on the dislocation configuration.

Dislocation configurations

Starting dislocations placed in the volume are Frank-Read sources. Since the length is fixed to $L = 30$nm, the theoretical critical stress for the Frank-Read mechanism is : $\tau = 2 \times 0.63 \frac{Gb}{L} = 836$MPa. We study two dislocation configurations, the first one, before any dislocation movement occurs that will be named from now on the unrelaxed configuration. The second one corresponds to the relaxed configuration obtained when the dislocations have reached an equilibrium state after propagation.

5.3 Studied results

Stress intensity factors

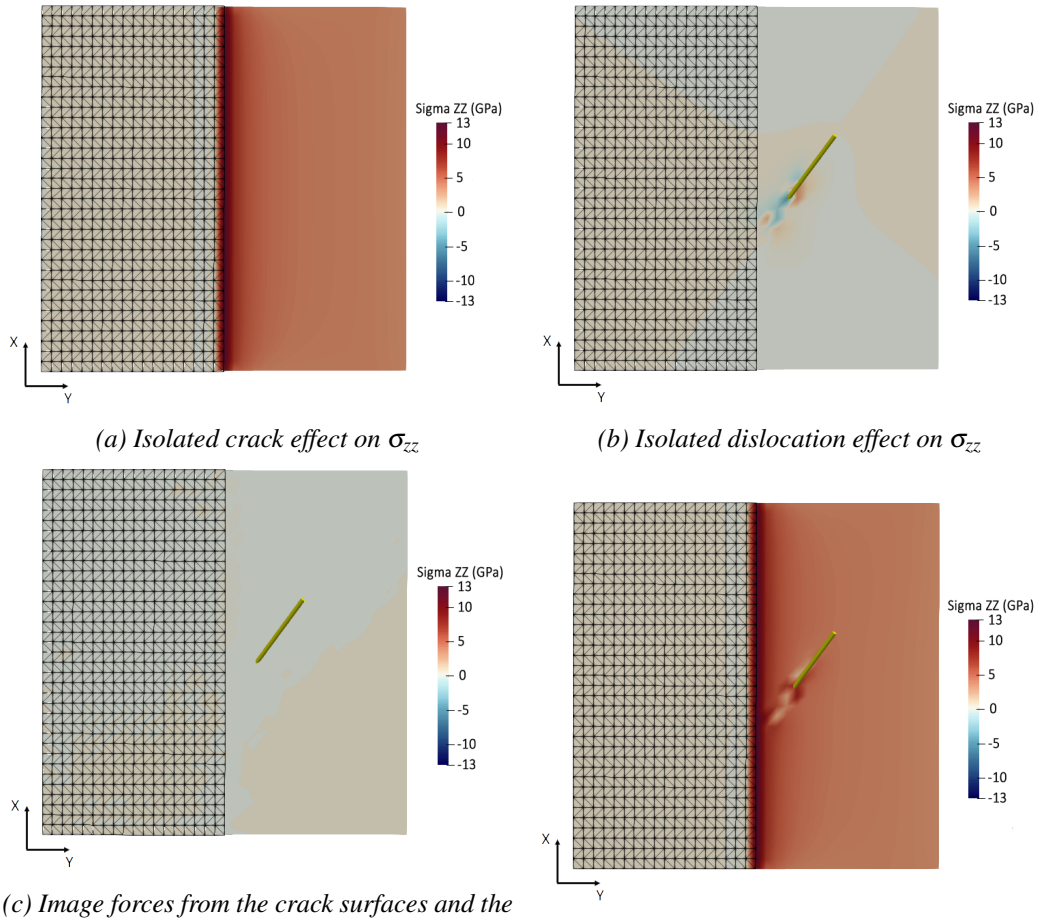

(a) Isolated crack effect on σ_{zz}

(b) Isolated dislocation effect on σ_{zz}

(c) Image forces from the crack surfaces and the volume front effect on σ_{zz}

(d) Global value of σ_{zz}

FIGURE 5.2 – *Decomposition of the stresses affecting K_I on the crack tip. Crack surface is represented by the black wireframe, and the dislocation(screw, Class I (CB(a)) with a Burgers vector of $b = \frac{1}{2}[10\bar{1}]$, line vector of $L = [10\bar{1}]$) by the yellow line- σ_{zz} corresponds to the stress on the direction of the applied force*

As defined above, the studied cracks are open in mode I, making K_I the only stress intensity factor that should have a non-zero value. K_I controls the crack advancement, hence why K_I will

be a studied parameter. Figure 5.2 illustrates the stress component σ_{zz} responsible for the crack opening. It can be observed how the stress is concentrated at the crack tip, which it is expected since the loading is applied in order to open the crack, and how the presence of the dislocation alters the value of σ_{zz} leading us to believe the dislocation will impact K_I. It is worth noticing that in this case, the dislocations both increases and decreases locally the stress.

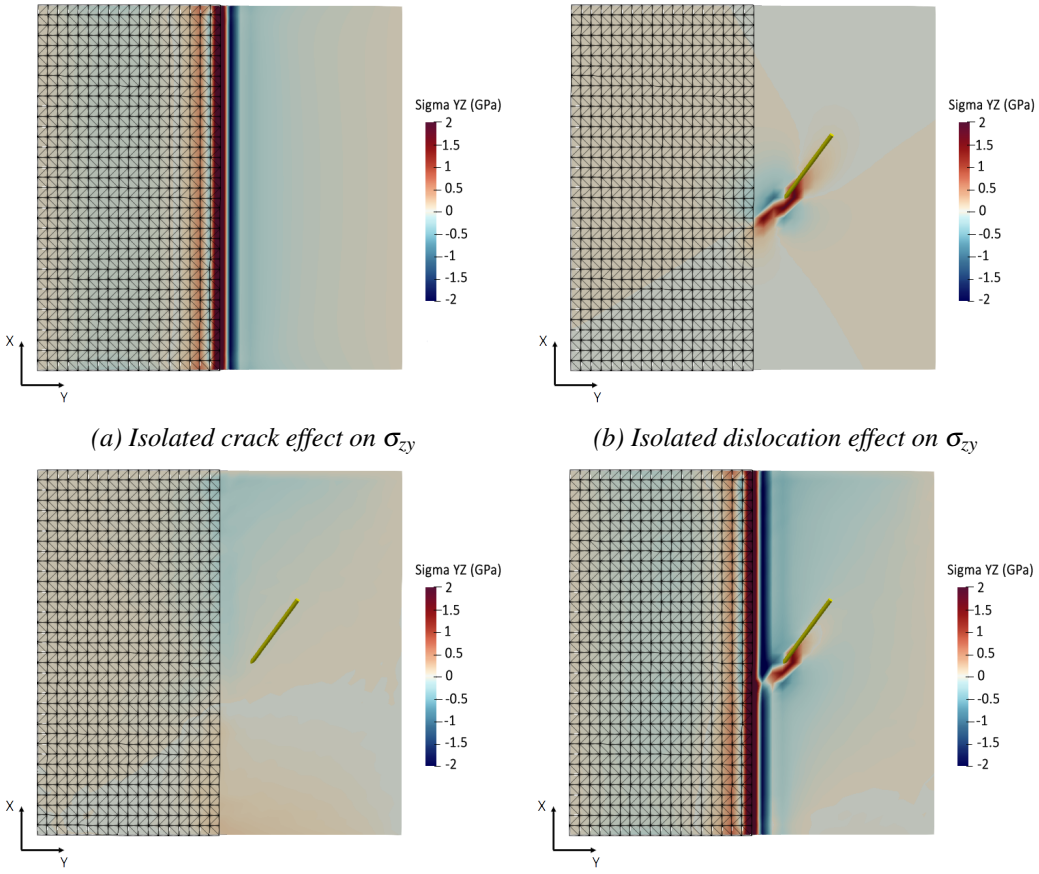

(a) Isolated crack effect on σ_{zy}

(b) Isolated dislocation effect on σ_{zy}

(c) Isolated image force effect on σ_{zy}

(d) Global value of σ_{zy}

FIGURE 5.3 – *Decomposition of the stresses affecting K_{II} on the crack tip. Crack surface is represented by the black wireframe, and the dislocation (Class I (CB(a)) with a Burgers vector of $b = \frac{1}{2}[10\bar{1}]$) by the yellow line $\varepsilon = 0.01892208$*

Figure 5.3 illustrates σ_{zy} which is the stress component responsible for K_{II}. Dislocation movement create shearing in the volume. This shearing can be observed in the variations that appear in σ_{zy}, the once null value at the crack tip varies greatly with the presence of a dislocation. It is also noted how the influence of the dislocation on σ_{zy} is far greater than its influence on σ_{zz} as dislocations create mainly shear.

K_{III} will not be studied as it remains zero as there is no out of plane shear.

While K_I controls the opening of the crack, K_{II} controls the angle of the crack propagation θ_c with respect to the horizontal (XY) plane following Equation 5.2. See also Figure 5.4 for the definition of θ_c. This equation implies that if K_{II} is negative the angle of propagation will be positive and if K_{II} is positive the angle will be negative.

$$\theta_c = 2\arctan\left(\frac{1}{4}\left[\frac{K_I}{K_{II}} - \text{sign}\,(K_{II})\sqrt{8+\left(\frac{K_I}{K_{II}}\right)^2}\right]\right) \tag{5.2}$$

To quantify more globally the variations observed, the average stress intensity factors will be

calculated as well as a percentile variation between the stress intensity factors with and without dislocations influence. We will consider a decrease in K_I a shielding effect and an increase an antishielding effect.

Isolated dislocation effect on the stress intensity factors

During the stress intensity factor calculations, two sets of values are calculated. The first one, only includes the effects of the crack itself and the applied strain. We will call these values from now on K(xfem). On the other hand, the second set of values include the dislocation stress field as well as the effect of the image forces created by the dislocations on the crack surfaces, giving the real values of the stress intensity factors, that we will note K(global). It is worth noting that for a same crack configuration, we always obtained the same values for K(xfem), validating that part of the model.

Since we wish to study the dislocation effects, we will isolate it by simply calculating the following :

$$K(\text{dislocation}) = K(\text{global}) - K(\text{xfem}) \tag{5.3}$$

K(dislocation) gives a clearer view of the dislocation effects on the crack propagation.

Propagation angle

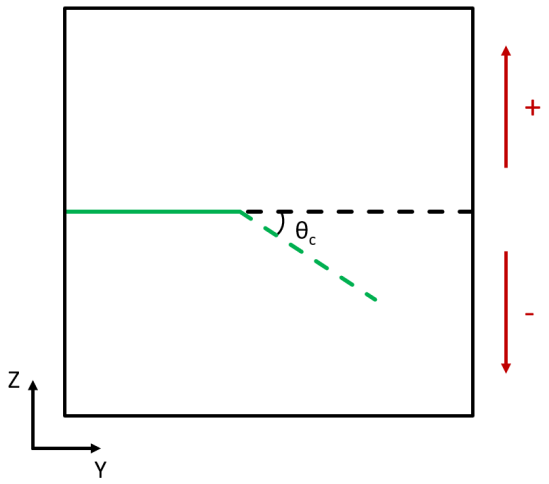

FIGURE 5.4 – *Definition of the propagation angle* θ_c

Using Equation 5.2 we will also calculate the propagation angle of the crack θ_c along the crack front. The angle sign determines the overall direction of the crack as illustrated in Figure 5.4. The variation of the propagation angle created by the dislocations will be one of the studied variables.

5.4 Initial strain variation

Parameters

Two initial tensile strains will be tested. The used strains are presented in Table 5.2. We seek to verify if the dislocations impact on the crack propagation is proportional to the applied strain.

ε_1	0.01892208
$\varepsilon_{0.5}$	0.00946104

TABLE 5.2 – *Strain amplitudes studied on the following simulations*

We will be studying the interactions between the crack and one screw dislocation of Class I (*CB(a)*) with a Burgers vector of $[10\bar{1}]$ and a length of 30 nm placed so its center is at 8 nm of the center of the crack front in the propagation direction.

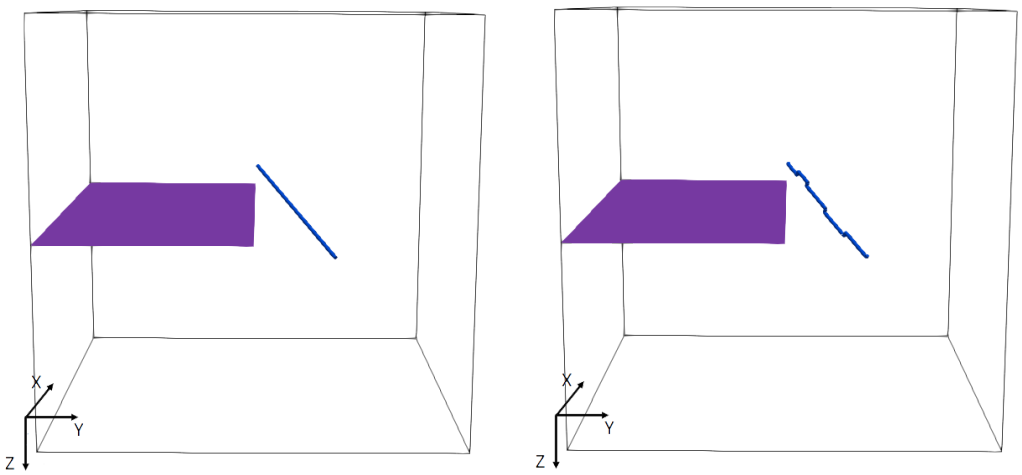

(a) Initial configuration *(b) Relaxed configuration*

FIGURE 5.5 – *Dislocation evolution under an applied strain of* $\varepsilon_{zz} = \varepsilon_{0.5}$

Figure 5.5 illustrates the unrelaxed and relaxed configuration of the dislocation studied. As can be noted in Figure 5.5b, $\varepsilon_{0.5}$ is not high enough to make the dislocation move, it only oscillates around its initial position. It is also worth noting that the dislocation does not interact directly with the crack. We can suppose that the dislocation effect on the crack will be similar for both the relaxed and unrelaxed configuration as the dislocation position remains nearly unchanged.

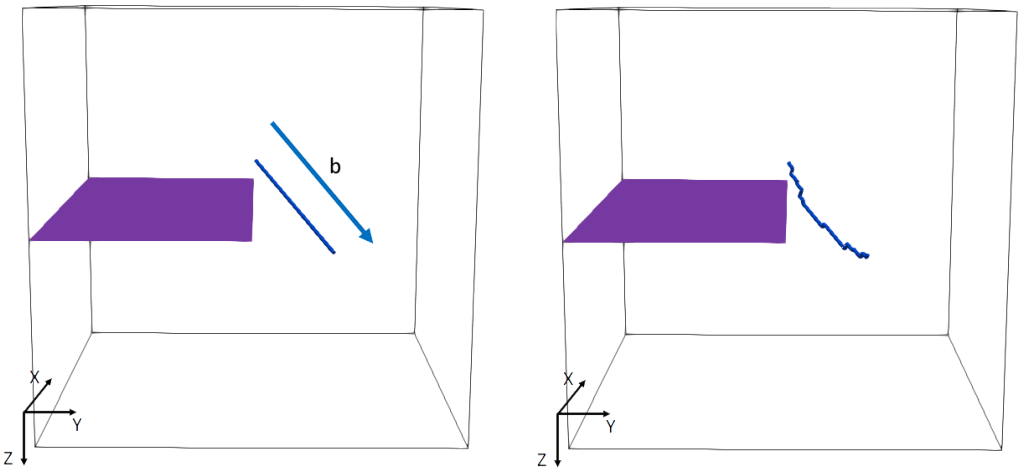

(a) Initial configuration *(b) Relaxed configuration*

FIGURE 5.6 – *Dislocation evolution under an applied strain of* $\varepsilon_{zz} = \varepsilon_1$

Dislocation movement for the second strain tested, ε_1, is illustrated in Figure 5.6. A higher

dislocation movement is observed, though there is no dislocation loop crated and neither a direct crack dislocation interaction. Since the dislocation moves towards the crack, we can suppose that there will be a notable difference between the relaxed and unrelaxed configurations. ε_1 is the strain used for future simulations.

Results

Unrelaxed configuration

We start this study with the unrelaxed configuration. We chose to study this configuration because the dislocations haven't moved yet, staying at the initial position which allows us to compare more precisely the results without having to consider a possible difference between the dislocation position.

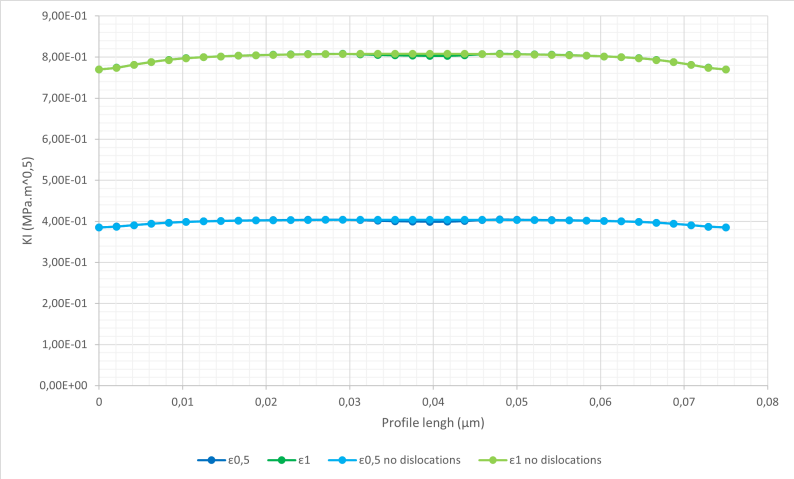

(a) K_I along the crack front

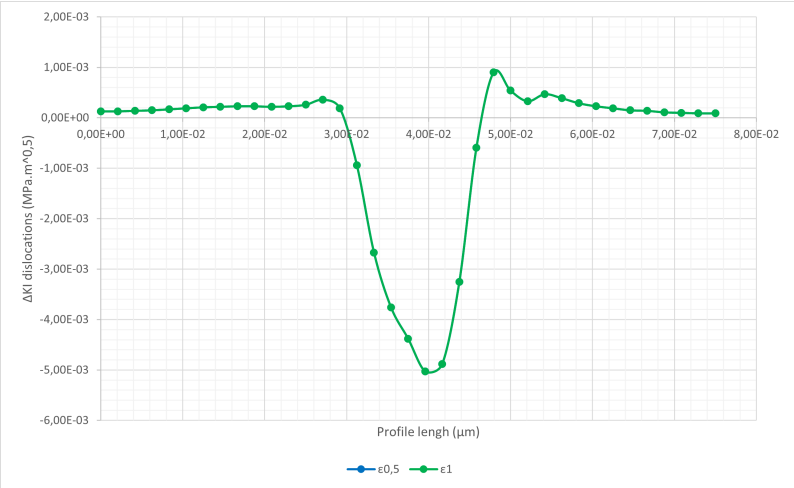

(b) Dislocation contribution to K_I

FIGURE 5.7 – *K_I along the crack front for the initial unrelaxed configuration and for the two applied strain amplitudes. Dislocation contribution to K_I has been isolated for clarity.*

K_I In Figure 5.7a, K_I doubles between strain $\varepsilon_{0.5}$ and ε_1. This was expected since stress intensity factors are inherently dependent on the loading conditions. Dislocation presence lowers K_I, it provides a shielding effect to the crack. It is worth mentioning that in Figure 5.7b, dislocations affects the same length of crack no matter the loading applied. The dislocation effect on the crack

is also shaped similarly, though the intensity of said effect does not seem to be proportional to the applied strain.

As expected, the initial loading not only affects the stress intensity factors, but also the dislocations effects on said factors. The dislocation effect is more than doubled. This results could be due to the impact of the image forces on the crack front as they are also taken into account when calculating the stress intensity factors. Note than when the dislocation is placed in front of the crack center, the center of the crack front is not the closest point between crack and dislocation. That is why the center of the valley for the dislocation effect on K_I is slightly off center as the point where the dislocation impact peaks does not correspond to the center of the crack but to the closest point between the crack front and the dislocation line.

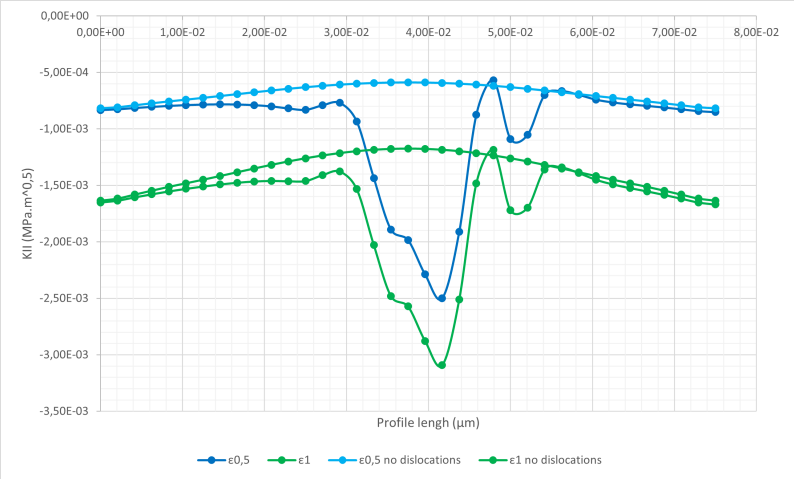

(a) K_{II} along the crack front

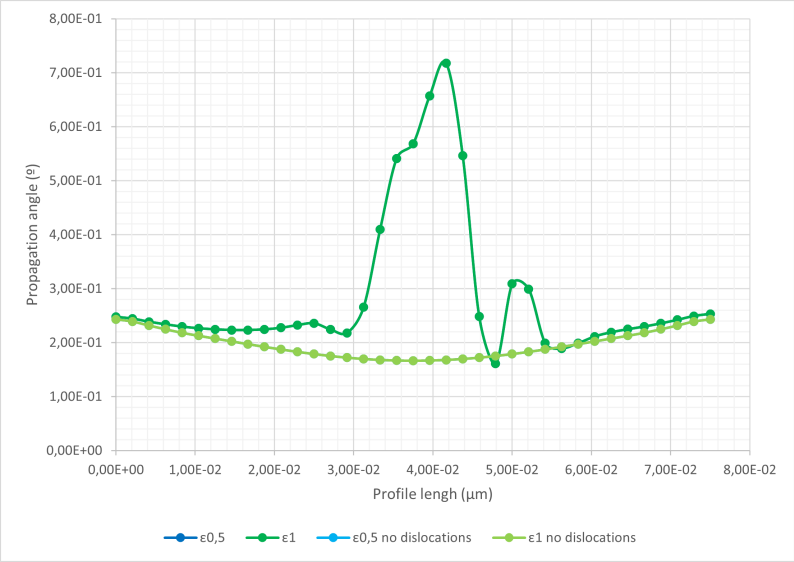

(b) Propagation angle of the crack front

FIGURE 5.8 – *K_{II} and propagation angle along the crack front for the initial unrelaxed configuration and for the two applied strain amplitudes.*

K_{II} First and foremost, in Figure 5.8, we observe a difference in the base values of K_{II}. Following the same trend as K_I, the value doubles when doubling the applied strain. As the applied strain opens the crack in mode I, K_{II} should be null, but there is a non-zero value. As mentioned in Chapter 3, the crack needs to be slightly off center to ensure the simulations can run. This slight

offset is responsible for the non null value of K_{II}. The dislocation presence in both cases accentuates the directional change of the crack. As for the propagation angle, it remains the same for both strain values and it is slightly positive to account for the crack offset on the volume.

We observe a shape variation between the two cases; for the strain $\varepsilon_{0.5}$, K_{II} shows some irregularities. These irregularities do not seem to come from a computation error as the rest of results extracted from the same simulation are coherent with other simulations. We can only assume that for this value of strain, the dislocation effect on the stress intensity factors changes. We do have the same behavior as presented before, where the dislocation effect is more than doubled when the applied loading doubles. The influence zone of the dislocations remains unchanged.

Relaxed configuration

Secondly, we study the dislocations in the relaxed configuration. As shown before, for a strain of $\varepsilon_{0.5}$ the initial dislocation does not propagate, so we expect the results for this strain to remain similar if not the same. On the other hand, for a strain of ε_1, we expect to see the stress intensity factors evolve further since the dislocation is able to propagate.

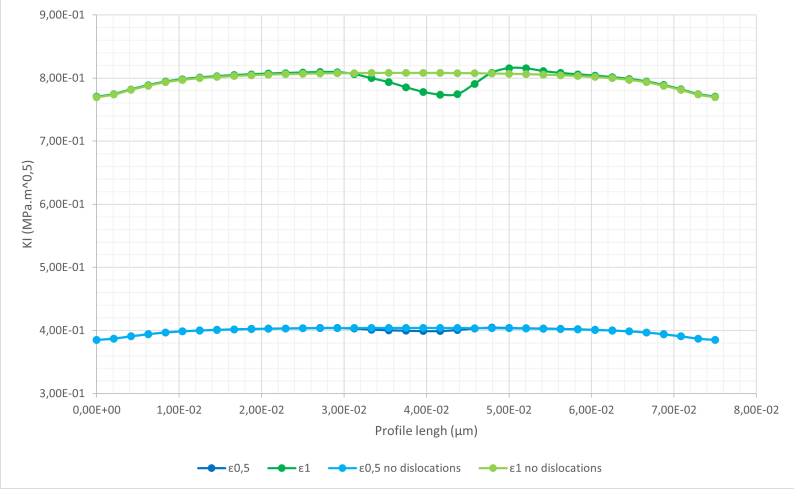

(a) K_I along the crack front

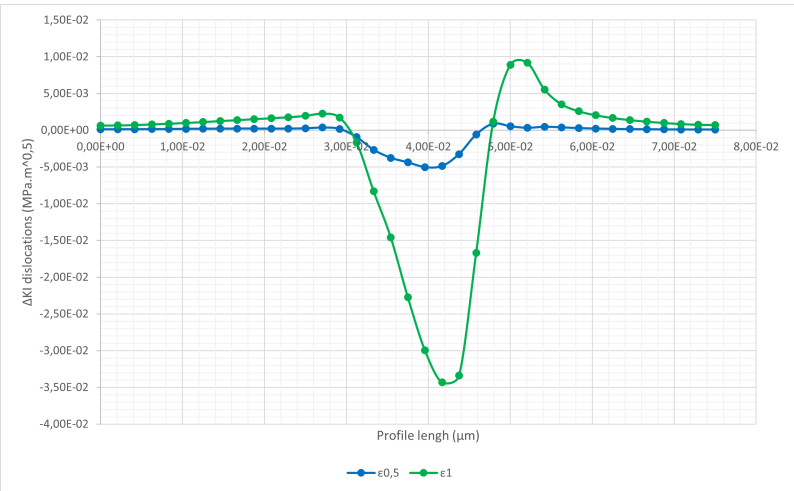

(b) Dislocation contribution to K_I

FIGURE 5.9 – *K_I along the crack front for the relaxed configuration and for the two applied strain amplitudes. Dislocation contribution to K_I has been isolated for clarity.*

K_I Since the stress intensity factors without the dislocation influence are only recalculated when the crack propagates, their values do not change between configurations. As it was hypothesized,K_I for $\varepsilon_{0.5}$ does not vary between configurations. On the other hand, for ε_1, as can be observed in Figure 5.9, the dislocation effect sharply increases due to the proximity of the dislocation to the crack.

While the length of the crack front affected by the dislocation remains unchanged, the intensity of said effect more than doubles for ε_1. Around the zone where the dislocation shields the crack, an increase in the value of K_I can be observed. While the dislocation seems to stop the crack propagation, the crack also seems to want to circumvent the obstacle. This effect can also be observed for $\varepsilon_{0.5}$ although in a minor way.

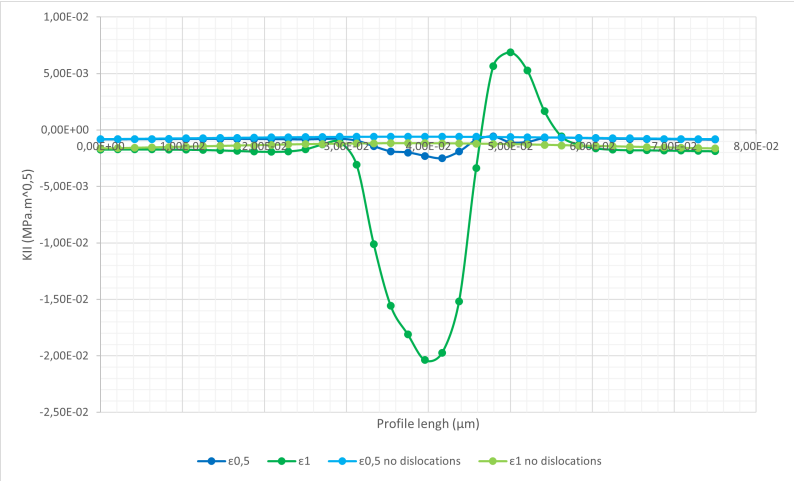

(a) K_{II} along the crack front

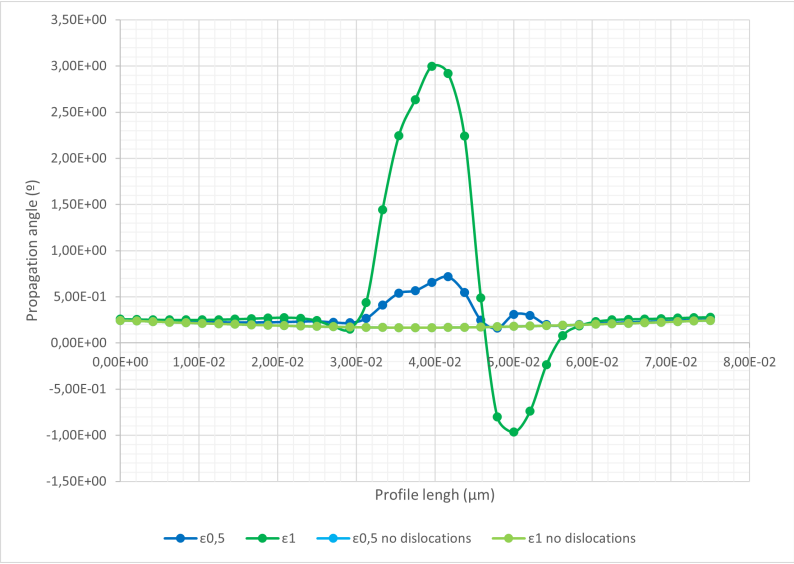

(b) Propagation angle of the crack front

FIGURE 5.10 – *K_{II} and propagation angle along the crack front for the relaxed configuration and for the two applied strain amplitudes.*

K_{II} As observed for K_I, there is the same increase on K_{II} for ε_1 as can be seen in Figure 5.10. Likewise, the values for $\varepsilon_{0.5}$ remain unchanged ; the smoother look of the curve is the result of the change of scale in the graphic.

The variation of K_{II} created by the dislocation results in an increase in the crack surface rough-

ness as shown in the crack propagation angle results. As K_{II} is positive and negative due to the dislocation, the propagation angle alongside the crack tip will be both positive and negative resulting in said surface roughness. We can hypothesize that, just like for K_I, the crack tends to try to avoid this kind of dislocation and tries to circumvent it. Since for $\varepsilon_{0.5}$ we do not observe this change of sign in K_{II}, we can suppose that there is a threshold strain for which a dislocation will create such an effect.

Average stress intensity factors

In order to quantify our results, we decide to calculate and compare the average stress intensity factors for each simulation. The values with and without dislocations will be calculated as well as a the percentile variation using the stress intensity factors without dislocations as a reference. Both the relaxed and unrelaxed configurations are studied.

	K_I		K_{II}	
	$\varepsilon_{0.5}$	ε_1	$\varepsilon_{0.5}$	ε_1
No dislocations (MPa.m$^{0.5}$)	0.39929	0.79858	-0.00069	-0.00138
Dislocations (MPa.m$^{0.5}$)	0.39879	0.79723	-0.00100	-0.00196
Variation (%)	-0.12	-0.17	45.48	42.76

TABLE 5.3 – *Average values of the strain intensity factors for the two initial strains studied at the unrelaxed configuration and quantification of the dislocation effects*

First and foremost, as shown in Table 5.3, the dislocation free stress intensity factors are perfectly doubled from $\varepsilon_{0.5}$ to ε_1 as was observed in the graphics above. Since dislocations move shearing the volume they are located in, the values of K_{II} are the most affected by the presence of dislocations in the volume. It is worth noting, that, before propagation, the percentile effect of dislocations on the stress intensity factors are similar for the two studied strains.

	K_I		K_{II}	
	$\varepsilon_{0.5}$	ε_1	$\varepsilon_{0.5}$	ε_1
No dislocations (MPa.m$^{0.5}$)	0.39929	0.79858	-0.00069	-0.00138
Dislocations (MPa.m$^{0.5}$)	0.39879	0.79583	-0.00100	-0.00345
Variation (%)	-0.12	-0.34	45.48	151.01

TABLE 5.4 – *Average values of the strain intensity factors for the two initial strains studied at the relaxed configuration and quantification of the dislocation effects*

Once the dislocation relaxes, we can see in Table 5.4 that the values for $\varepsilon_{0.5}$ remain the same while the values for ε_1 triple. It is the dislocation moving towards the crack that makes the stress intensity values vary so sharply, and not the applied strain which increases proportionally with the dislocation effect on them.

Conclusions

We studied the effect of the applied strain on the dislocation effect on the stress intensity factors. Two configurations of the dislocations were studied, the relaxed and the unrelaxed ones. For both configurations, the dislocation affected zone on the crack front remains the same, as well as the qualitative effect, shielding the crack locally and changing its angle of propagation.

But, what causes major impact on the stress intensity factors, is not the raw value of the applied strain, but the dislocation movement it can create. As we observed on the study of the average values of both K_I and K_{II}, the percentile variation remains the same for the unrelaxed configuration but a sharp variation is observed on the relaxed configuration that can only be explained by the difference in the dislocation position and the distance between crack and dislocation.

5.5 Dislocation crack distance

Dislocation crack distance is, as seen above, an important parameter to consider. That is why the impact of said distance will be studied in the following simulations.

Parameters

The following simulations will be carried out using one screw dislocation of Class I (*CB(a)*) with a Burgers vector of $[10\bar{1}]$ and a length of 30 nm. Three crack-dislocation distances will be studied; 8, 12 and 16 nm. These study cases are illustrated in Figure 5.11.

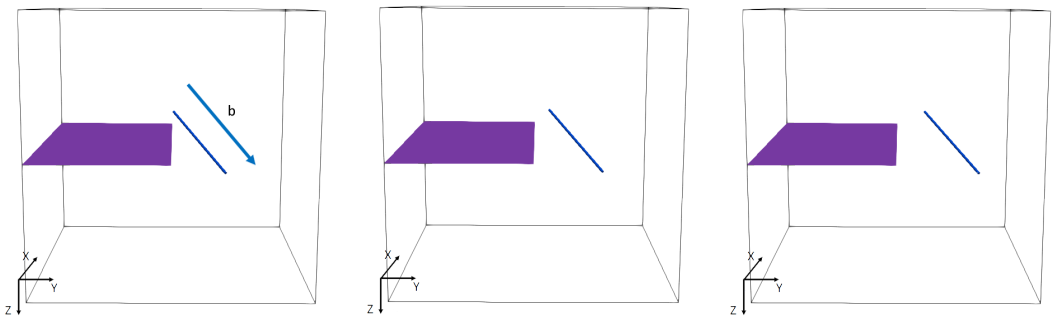

(a) $d = 8$ *nm* *(b)* $d = 12$ *nm* *(c)* $d = 16$ *nm*

FIGURE 5.11 – *Initial configurations of the three study cases for different dislocation crack distances*

The distances mentioned above are the distances between the center of the crack front and the dislocation center measured along the Y=$[10\bar{1}]$ direction. These dislocations making an angle with the crack, the actual minimal distance between them and the crack front does not correspond to the center of said dislocation but to one of its ends. Therefore, using Paraview, we measure the actual minimal distance between the crack front and the dislocation which is measured along the direction perlendicular to both lines. These results can be found in Table 5.5.

d_{ini} (nm)	8	12	16
d_{min} (nm)	7.3	8.8	11.5

TABLE 5.5 – *Placement distance and real minimal distance between the dislocation and the crack front. d_{ini} : distance dislocation center - crack, d_{min} : minimal distance measured between dislocation line and crack front*

The calculations will be performed for the initial unrelaxed configuration, i.e. when the crack-dislocation distance is accurately defined so that the solely effect of this distance can be estimated.

Results

K_I

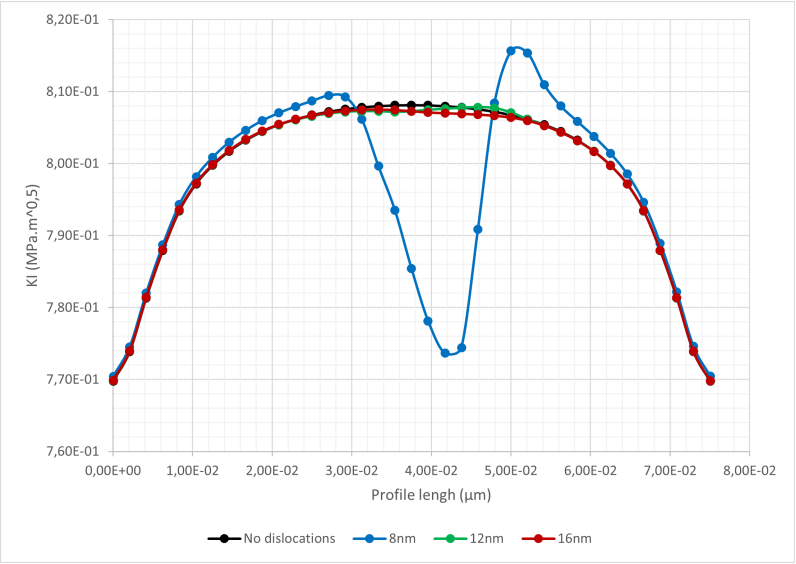

(a) K_I along the crack front

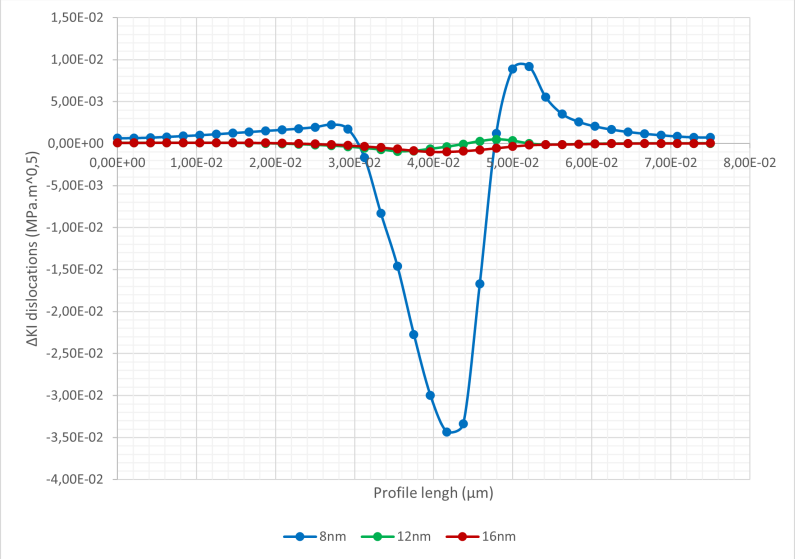

(b) Dislocation contribution to K_I

FIGURE 5.12 – *K_I along the crack front for various crack dislocation distances. Dislocation contribution to K_I has been isolated for clarity.*

Figure 5.12 shows the simulation results for K_I. As can be observed, only the simulation for 8 nm yields a noticeable change in K_I. Farther dislocations still have an effect on the crack, but it is negligible compared to a closer dislocation.

In real cases, for a higher dislocation density case, the added effects of the farther dislocations will have a much higher effect than a single dislocation would, making their cumulative effect non negligible. The dislocations placed far from the crack front only retain a light shielding effect compared to the dislocation placed near to the crack front.

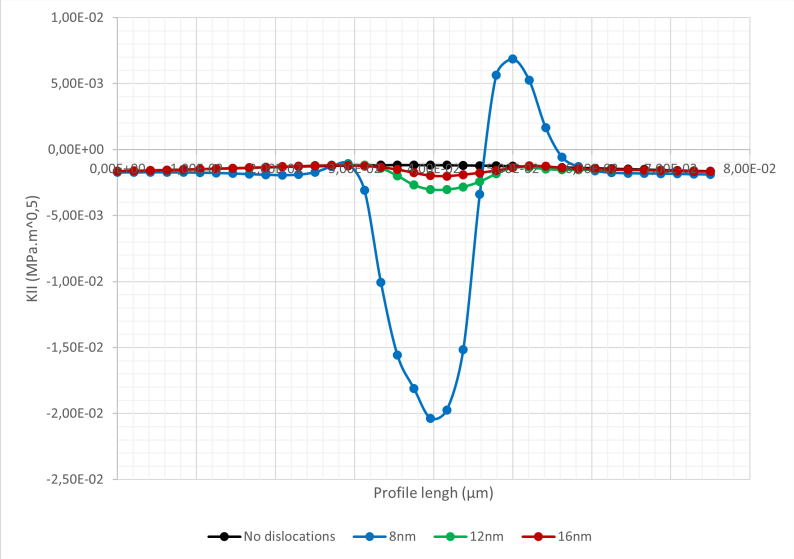

(a) K_{II} along the crack front

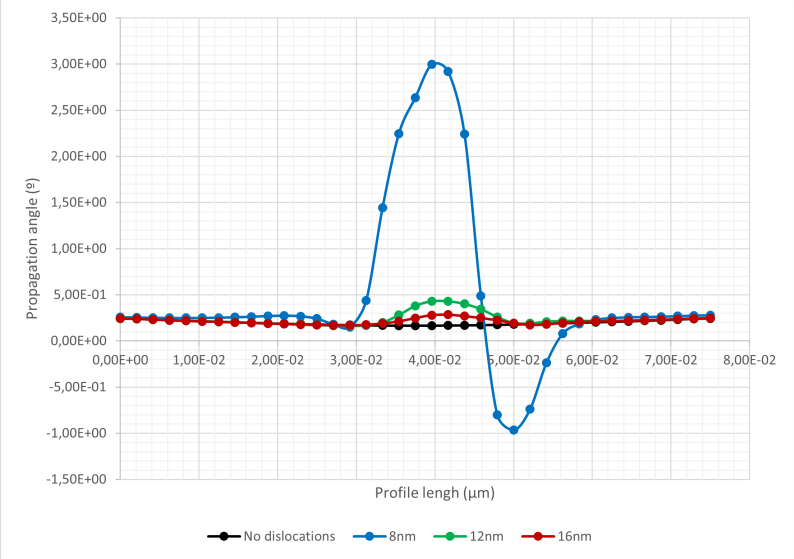

(b) Propagation angle of the crack front

FIGURE 5.13 – *K_{II} and propagation angle along the crack front for various crack dislocation distances. Dislocation contribution to K_{II} has been isolated for clarity.*

K_{II}

In the same vein as K_I, the results for K_{II}, illustrated in Figure 5.13, only shows a significant change for the 8 nm case. Farther dislocations show a lower effect and only change slightly the crack propagation angle in one direction contrary to the 8 nm case.

The relative effect is still important since dislocations shear the volume. It is worth mentioning that for a base value of zero, any relative change is more significant and noticeable than for a higher base value as it is the case for K_I.

Average stress intensity factors

In Table 5.6, the average value of the stress intensity factors are listed. As seen before, both K_I and K_{II} remain mostly unchanged for the farther studied dislocations. Since K_{II} without dislocations is close to zero, any relative variation created by the dislocations is very high. The impact of

	K_I			K_{II}		
	8 nm	12 nm	16 nm	8 nm	12 nm	16 nm
No dislocations (MPa.m$^{0.5}$)	0.79858	0.79858	0.79858	-0.00138	-0.00138	-0.00138
Dislocations (MPa.m$^{0.5}$)	0.79583	0.79849	0.79841	-0.00345	-0.00166	-0.00150
Variation (%)	-0.34	-0.01	-0.02	151.01	20.61	8.89

TABLE 5.6 – *Average values of the strain intensity factors for the studied crack dislocation distances*

the further dislocations is negligible compared to the closer dislocation.

Conclusions

In order to study the impact of the dislocation crack distance and at which point a dislocation does not affect the crack front energy we simulated a dislocation in front of the crack for different distances varying from 8 to 16 nm. Only the closest dislocation, situated at 8 nm in front of the crack, had a significant effect on the stress intensity factors, in both K_I and K_{II}. The further dislocations, at 12 and 16 nm from the crack, display a very minimal interaction with the crack front, though they do slightly shield the crack. For higher dislocation densities, their effect would be important enough to be taken into account. We will concentrate our simulation efforts in dislocations placed at 8 nm of the crack to maximize the crack dislocation interaction.

5.6 Effect of dislocation sign

Up until now, the dislocations we studied moved towards the crack. Knowing that the crack dislocation distance is an important factor on its impact on the stress intensity factors, we decide to study two dislocations of opposite Burgers vector. Since these dislocations will move in opposite directions, we can observe how this difference in propagation direction affects the crack energy and the effect of the dislocation itself.

Parameters

The studied dislocations will be screw dislocations of Class I (*CB(a)*) and a length of 30 nm. The first studied dislocation will have a Burgers vector of $[10\bar{1}]$, which corresponds to the previously studied line direction, while the second one will have the opposite Burgers vector $[\bar{1}01]$. This dislocation was chosen because the dislocation of positive Burgers vector will move towards the crack and the opposite dislocation will move away from it. We wish to see if the shielding effect that has been noted previously remains if the dislocation moves in the opposite direction.

Both dislocations will be studied in the relaxed and unrelaxed states. As mentioned previously, the dislocation with the [10-1] Burgers vector will move towards the crack as illustrated in Figure 5.14 while the dislocation with the $[\bar{1}01]$ Burgers vector will move away from the crack as can be observed in Figure 5.15.

Results

Unrelaxed state

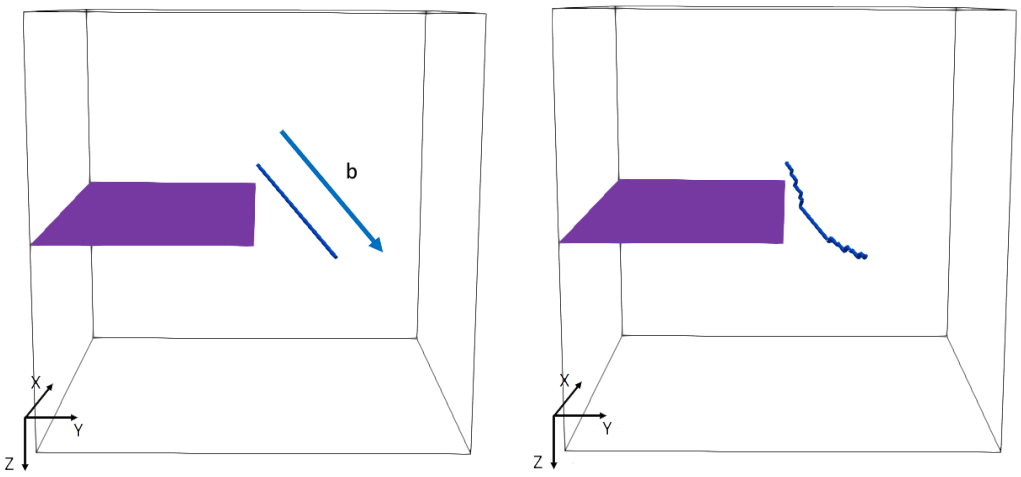

(a) Initial configuration *(b) Relaxed configuration*

FIGURE 5.14 – *Evolution of a dislocation with a* $[10\bar{1}]$ *Burgers vector*

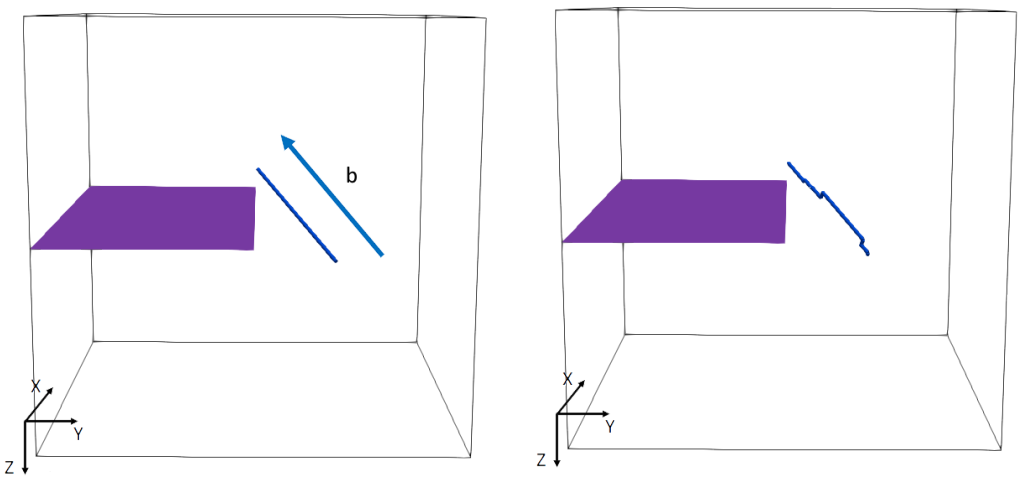

(a) Initial configuration *(b) Relaxed configuration*

FIGURE 5.15 – *Evolution of a dislocation with a* $[\bar{1}01]$ *Burgers vector*

K_I The unrelaxed results, illustrated in Figure 5.16 show a shielding effect created by both dislocations. The dislocation with a positive Burgers vector (blue curve) has an effect on the crack front energy roughly three times higher than the dislocation with a negative Burgers vector. The area of effect of both dislocations is roughly the same. The dislocation orientation has an effect on how much the dislocation will affect the crack front energy but the nature of the effect remains unchanged.

K_{II} As for K_{II}, the results are illustrated in Figure 5.17. Following the same trend as K_I, the dislocation with a positive Burgers vectors creates an effect three times higher than the dislocation with a negative Burgers vector. Both dislocations still influence the same portion of the crack front and both follow the same general shape.

Relaxed state

K_I The results for K_I for the relaxed configuration are illustrated in Figure 5.18. A clear value difference between the two dislocations can be observed. Both dislocations still provide shielding

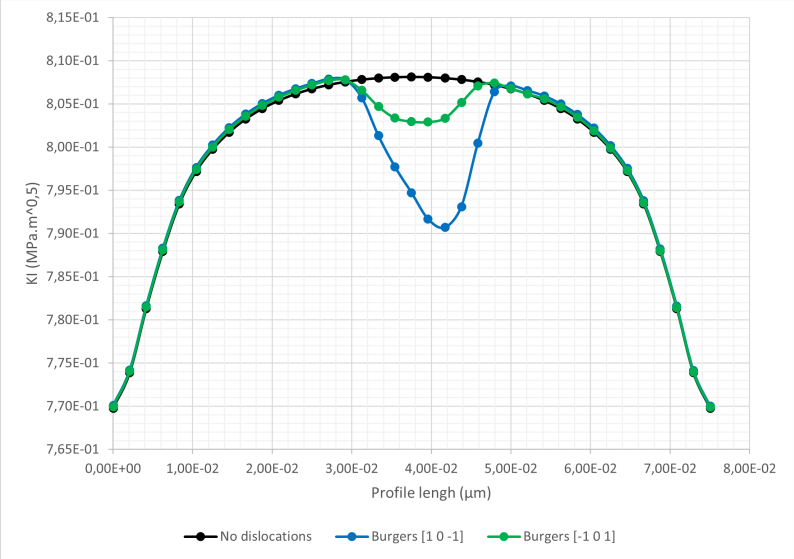

(a) K_I along the crack front

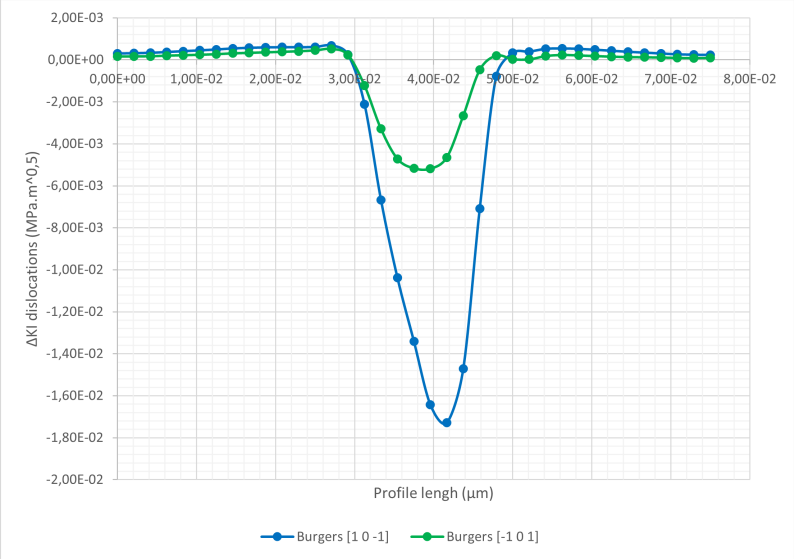

(b) Dislocation contribution to K_I

FIGURE 5.16 – *K_I along the crack front for dislocations of opposite Burgers vector for an unrelaxed configuration. Dislocation contribution to K_I has been isolated for clarity.*

to the crack front but the dislocation with a negative Burgers vector has a lower effect. It can also be observed that the positive Burgers vector dislocations created locally a small antishielding effect.

The dislocation propagation direction does not determine the dislocation effect on the crack front energy but it does greatly influence the magnitude of said effect. On the same note, the zones of local antishielding also seem to be dependent on the distance between the dislocation and the crack front.

K_{II} As for K_{II}, the results are illustrated in Figure 5.19. Both curves have a similar shape but the results of the negative Burgers vector dislocation are negligible compared to the other curve. Even if the nature of the effect remains unchanged, it seems that the intensity of said effect is greatly dependent on the distance between the dislocation and the crack front. The crack front affected length remains the same between the two studied cases.

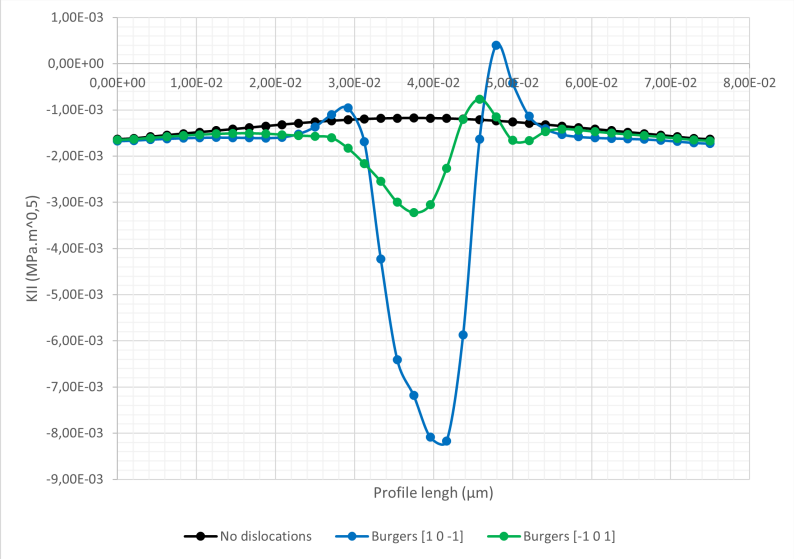

(a) K_{II} along the crack front

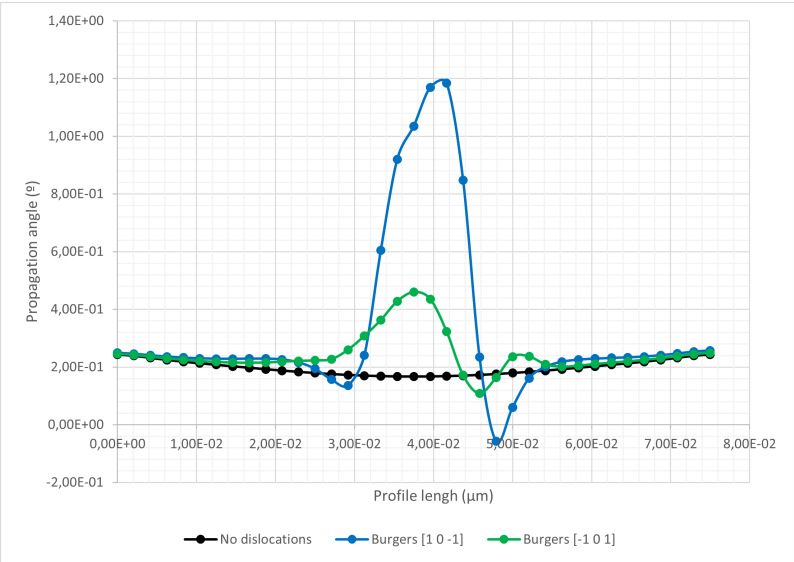

(b) Propagation angle of the crack front

FIGURE 5.17 – *K_{II} and propagation angle along the crack front for dislocations of opposite Burgers vector for an unrelaxed configuration.*

Average stress intensity factors

The average stress intensity factors for the unrelaxed configuration, compiled on Table 5.7, show the aforementioned shielding created by the dislocations. The effect of the dislocation with a negative Burgers vector is indeed less pronounced than the one with a positive Burgers vector.

Once the dislocation reaches the relaxed configuration, the average stress intensity factors, gathered in Table 5.8, show a significant change. The shielding seen on the K_I values is more prominent, though the change for the dislocation with a negative Burgers vector is negligible. The same can be said for the values of K_{II}.

The dislocation effect on K_{II} seems more dependent on distance between the crack front and the dislocation than the effect on K_I. The nature of the dislocation effect remains unchanged.

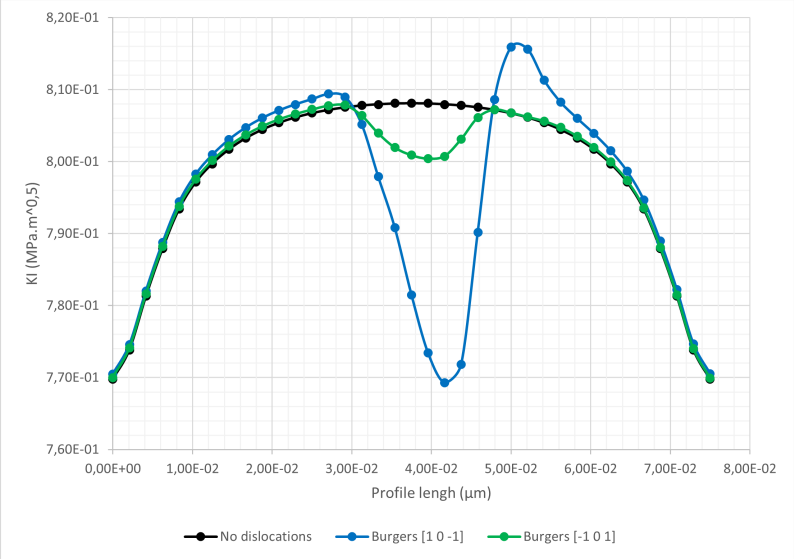

(a) K_I along the crack front

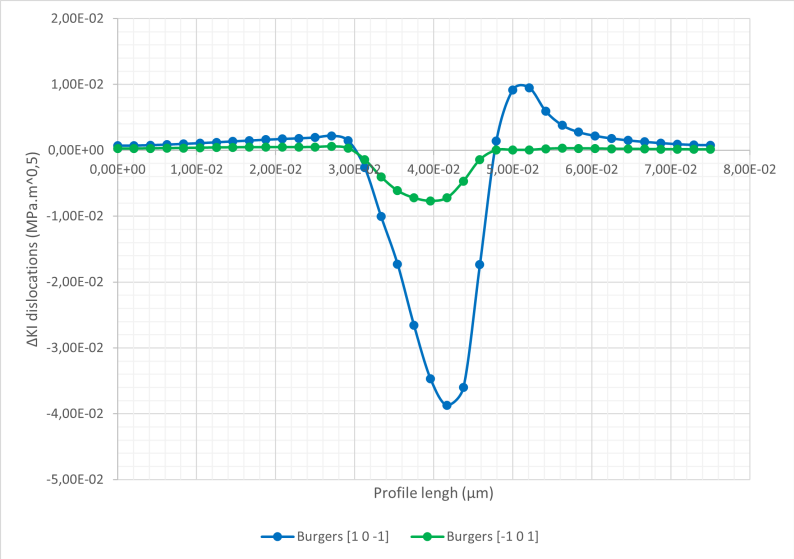

(b) Dislocation contribution to K_I

FIGURE 5.18 – *K_I along the crack front for dislocations of opposite Burgers vector for a relaxed configuration. Dislocation contribution to K_{II} has been isolated for clarity.*

Conclusions

The effect of the Burgers vector direction was studied here. Both studied dislocations show to have a shielding effect on the crack front energy. The dislocation propagation direction does not influence the nature of the dislocation effect on the crack front energy.

The effect magnitude is tied to the Burgers vector direction since the effects are thrice as important for the positive Burgers vector than for the negative one. It is also worth noting that K_{II} is more sensitive to the crack dislocation distance than K_I.

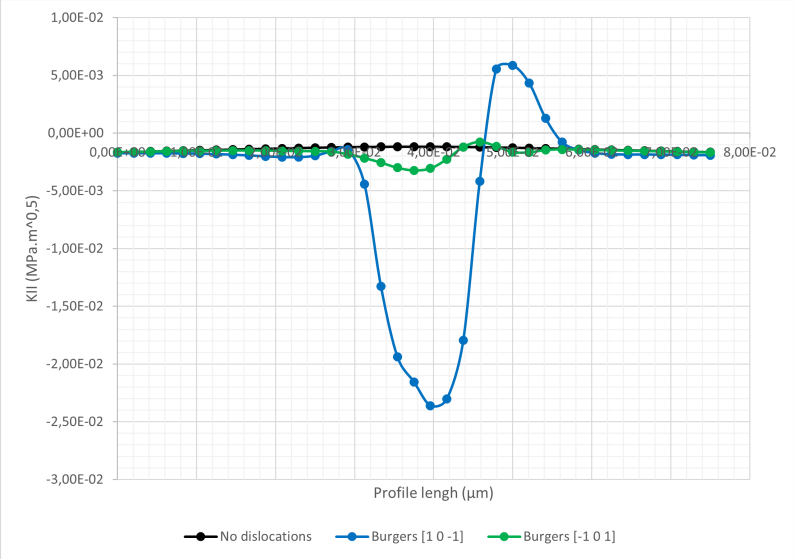

(a) K_{II} along the crack front

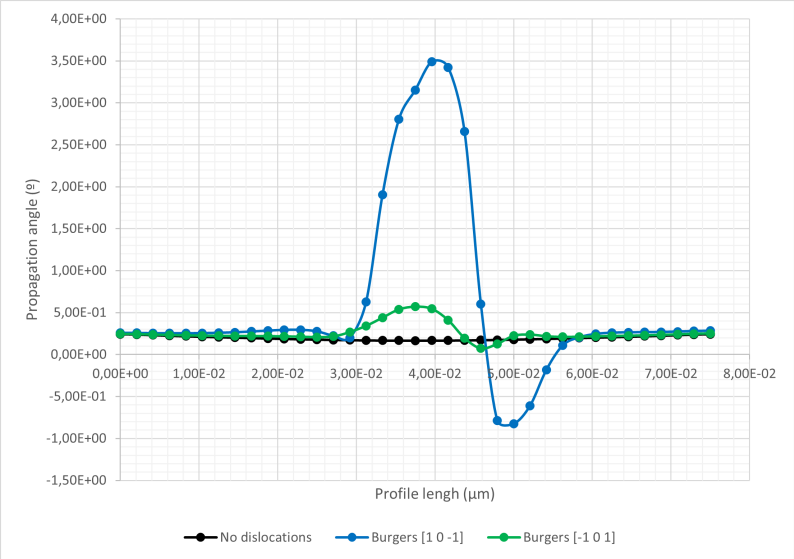

(b) Dislocation contribution to K_{II}

FIGURE 5.19 – *K_{II} and propagation angle along the crack front for dislocations of opposite Burgers vector for a relaxed configuration.*

5.7 Class I dislocations

After studying various parameters, now we will study the effect of the number of dislocations on the stress intensity factors. First we will study dislocations of Class I.

Parameters

The studied dislocations will be screw dislocations of Class I (*CB(a)*), Burgers vector of $[10\bar{1}]$ and a length of 30 nm. Three simulations, aside the dislocation free simulation, will be carried out. The loading applied for these simulations is : $\varepsilon_{zz} = \varepsilon_1 = 0.01892208$

These simulations illustrated in Figure 5.20, have one, three and five dislocations respectively. Dislocations are placed so the center of the dislocation group is located at 8 nm from the crack front in the propagation direction. The dislocations are positioned at equal distance from each

	KI		KII	
	$[10\bar{1}]$	$[\bar{1}01]$	$[10\bar{1}]$	$[\bar{1}01]$
K No dislocation (MPa.m$^{0.5}$)	0.79858	0.79858	-0.00138	-0.00138
K Dislocation (MPa.m$^{0.5}$)	0.79651	0.79801	-0.00230	-0.00171
Variation (%)	-0.26	-0.07	66.96	24.45

TABLE 5.7 – *Average values of the strain intensity factors for the studied Burgers vectors in an unrelaxed configuration*

	K_I		K_{II}	
	$[10\bar{1}]$	$[\bar{1}01]$	$[10\bar{1}]$	$[\bar{1}01]$
K No dislocation (MPa.m$^{0.5}$)	0.79858	0.79858	-0.00138	-0.00138
K Dislocation (MPa.m$^{0.5}$)	0.79533	0.79774	-0.00418	-0.00181
Variation (%)	-0.41	-0.11	203.53	31.80

TABLE 5.8 – *Average values of the strain intensity factors for the studied Burgers vectors in a relaxed configuration*

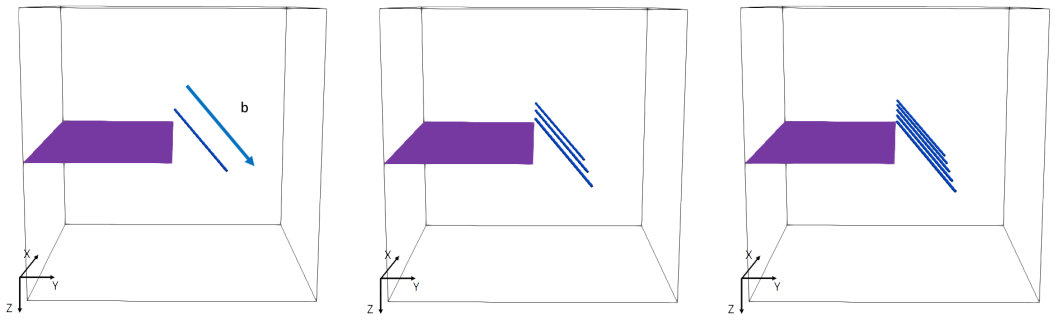

(a) $n = 1$ *(b)* $n = 3$ *(c)* $n = 5$

FIGURE 5.20 – *Initial configurations of the studied cases for different dislocation numbers*

other in front of the crack occupying the available space without exiting the volume. Both the relaxed and unrelaxed configurations will be considered.

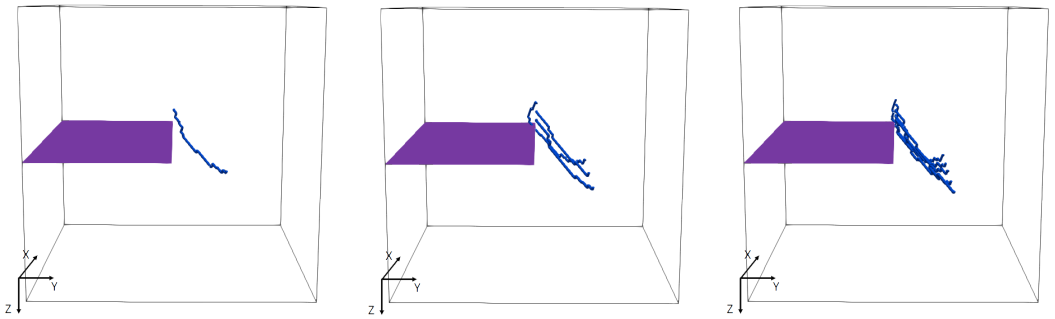

(a) $n = 1$ *(b)* $n = 3$ *(c)* $n = 5$

FIGURE 5.21 – *Final configurations of the study cases for different dislocation amounts*

The relaxed configuration is illustrated in Figure 5.21. We observe that some dislocations do

cross the crack surface in this case.

Results

Unrelaxed configuration

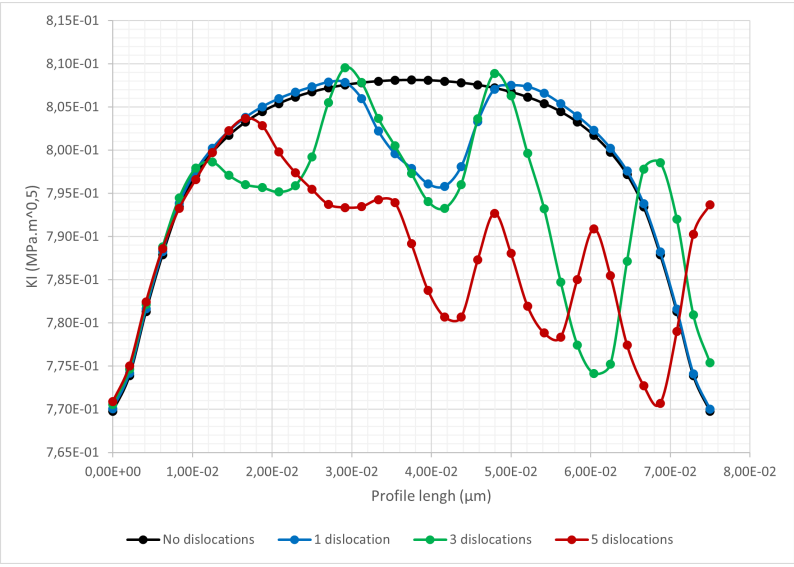

(a) K_I along the crack front

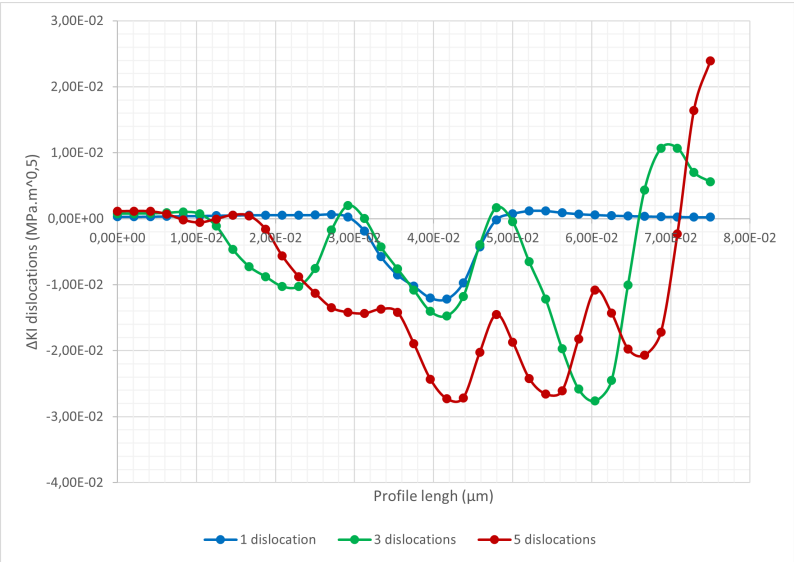

(b) Dislocation contribution to K_I

FIGURE 5.22 – *K_I along the crack front for various amounts of Class I dislocations for the unrelaxed configuration. Dislocation contribution to K_I has been isolated for clarity.*

K_I Figure 5.22 illustrates the results for K_I plotted along the crack front in the initial unrelaxed configuration. As can be noted, there is, at around 40 nm, a shared valley for one and three dislocations simulations. This valley coincides with the position of the dislocation center of both simulations. The same valley can be seen for the five dislocations configuration but for a lower value. A large antishielding effect can be observed to the right of the graphs. It corresponds to the accumulation of all the dislocations effects.

This accumulation effect can be observed for the three dislocations simulation but is specially marked for the five dislocations simulation. As can be seen, only four valleys corresponding to

the dislocations positions can be clearly observed. There is a small variation at around 10 nm that corresponds to the first dislocation. This is caused by the superposition of the dislocations affected zone.

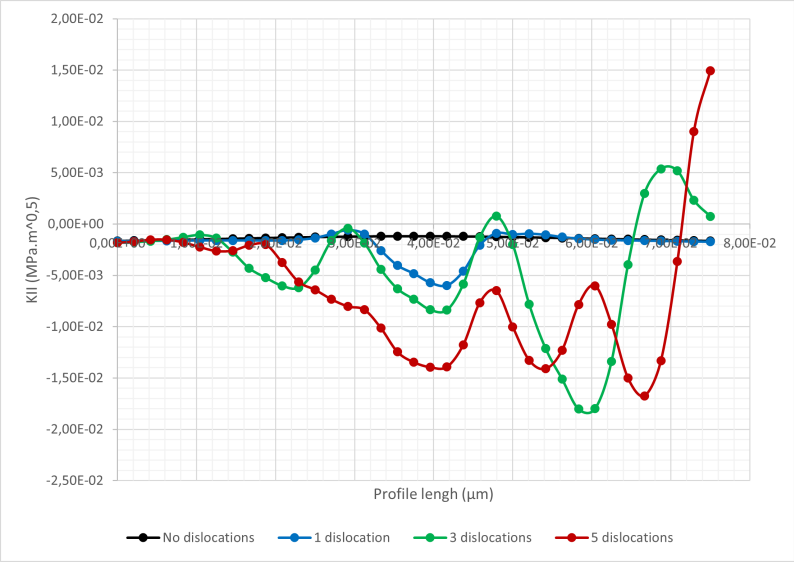

(a) K_{II} along the crack front

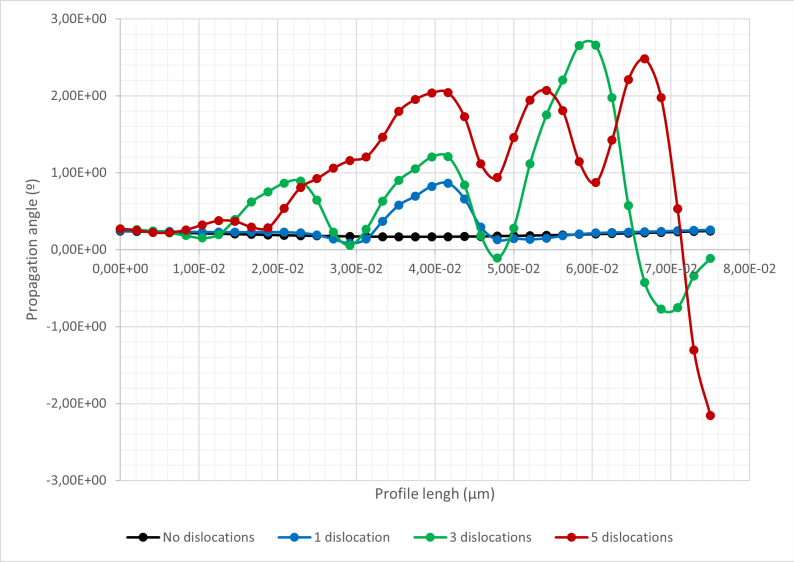

(b) Propagation angle of the crack front

FIGURE 5.23 – *K_{II} and propagation angle along the crack front for various amounts of Class I dislocations for the unrelaxed configuration.*

K_{II} The dislocation impact on K_{II}, illustrated in Figure 5.23 is very similar to the impact on K_I. Though the erasure of the valleys in K_{II} created by the farther left dislocation is less marked.

The propagation angle varies in a range of values making the crack front rapidly change its orientation increasing the crack surface roughness. There is also the end of the crack that instead of propagating downwards will go in the opposite direction due to the cumulative dislocation effects.

Relaxed configuration

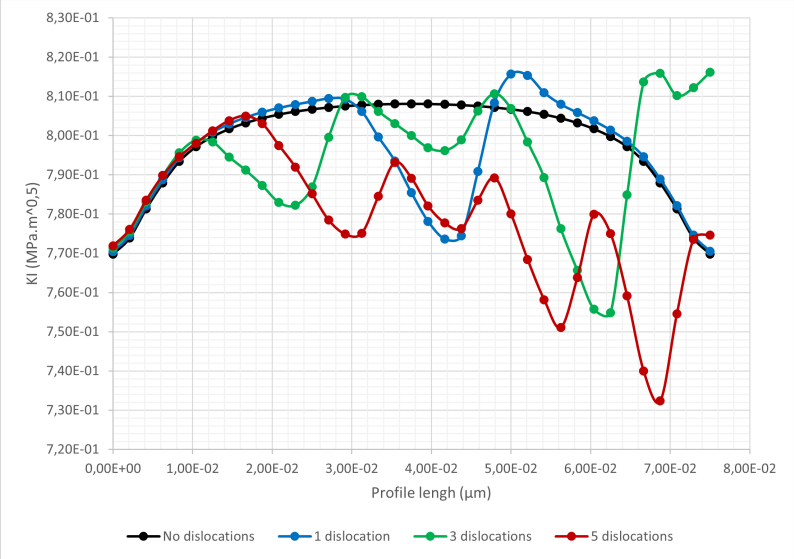

(a) K_I along the crack front

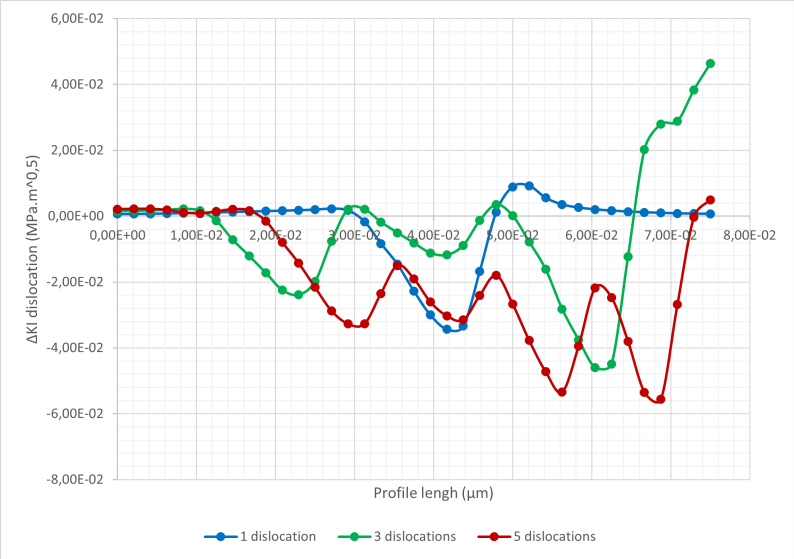

(b) Dislocation contribution to K_I along the crack front

FIGURE 5.24 – *K_I along the crack front for various amounts of Class I dislocations for the relaxed configuration. Dislocation contribution to K_I has been isolated for clarity.*

K_I In Figure 5.24 we observe, compared to the unrelaxed configuration, a decrease of the intensity of the antishielding zones. We thus obtain a general state of shielding on almost the whole crack length. Each dislocation individual effect is still visible on the graphs.

It is worth mentioning that the point where the antishielding effect is at his highest for the three dislocations simulation corresponds to the point where the dislocation crosses the crack. Since there is no actual interaction with the surfaces, this antishielding effect might be caused by the dislocation being behind the crack front. Globally, the behavior of multiple dislocations remains very similar to the behavior of only one dislocation, providing a general shielding effect in this case.

K_{II} In general, we observe in Figure 5.25 the same general shape for K_{II} as in the unrelaxed configuration. In the same way as K_I, there is a sharp increase in value on the right side of the crack front. While generally the curve shape is similar, the values are smoothed over compared

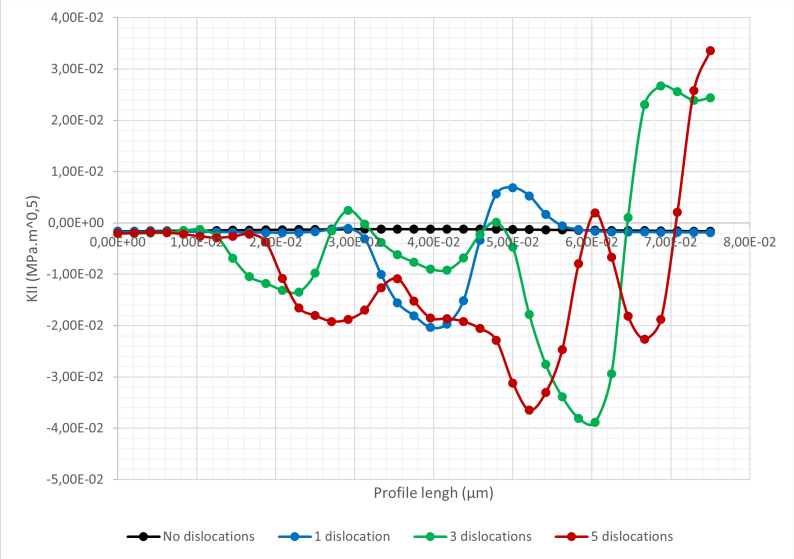

(a) K_{II} along the crack front

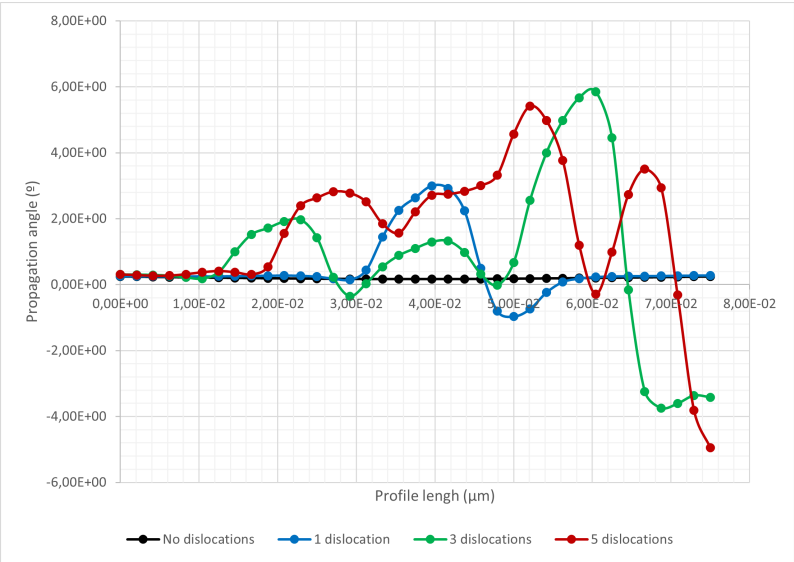

(b) Propagation angle of the crack front

FIGURE 5.25 – *K_{II} and propagation angle along the crack front for various amounts of Class I dislocations for the relaxed configuration.*

to the unrelaxed configuration. As a consequence, the crack will experience less changes of the propagation planes.

As for the propagation angle, it will be mostly positive, but some negative values appear after relaxation. Generally speaking, the relaxation seems to have smoothed the angle of the crack propagation.

Average stress intensity factors

The results provided in Table 5.9 show a consistent increase in average values for both K_I and K_{II}. There is a constant shielding created by the dislocations. It is interesting to point out that the variation created by the dislocations is not proportional to the number of dislocations present in the volume. The more dislocations there are, the strongest is the shielding effect and the propagation angle variation.

	K_I			K_{II}		
Number of dislocations	1	3	5	1	3	5
K No dislocation (MPa.m$^{0.5}$)	0.79858	0.79858	0.79858	-0.00138	-0.00138	-0.00138
K Dislocation (MPa.m$^{0.5}$)	0.79723	0.79322	0.78820	-0.00196	-0.00427	-0.00668
Variation (%)	-0.17	-0.67	-1.30	42.76	210.40	385.71

TABLE 5.9 – *Average values of the strain intensity factors for the studied Class I dislocations amounts in the initial unrelaxed configuration*

	K_I			K_{II}		
Number of dislocations	1	3	5	1	3	5
K No dislocation (MPa.m$^{0.5}$)	0.79858	0.79858	0.79858	-0.00138	-0.00138	-0.00138
K Dislocation (MPa.m$^{0.5}$)	0.79583	0.79393	0.77882	-0.00345	-0.00510	-0.01078
Variation (%)	-0.34	-0.58	-2.47	151.01	270.55	683.91

TABLE 5.10 – *Average values of the strain intensity factors for the studied Class I dislocations amounts in the relaxed configuration*

Once the dislocations relax, there is a general increase of their effect as shown in Table 5.10. This effect is absent for the three dislocation simulation as its K_I effect decreases. This is due to the antishielding effect that was created when one of the dislocations crossed the crack. In general, the dislocation effects are strengthened by the dislocation propagation, due mainly to the crack dislocation distance.

Conclusions

In this section we studied the effect of different numbers of Class I dislocations on the stress intensity factors. For these dislocations, we observed a general shielding effect, that is exacerbated when the number of dislocations increases. This increase is not proportional to the number of dislocations present in the volume. This suggest an interaction between the dislocation stress fields. We also observed an antishielding effect that appears when a dislocation crossed the crack. It is uncertain if this effect appears because the dislocation is behind the crack of because it crossed the crack. As observed before, the propagation increases the dislocation effect as they end up closer to the crack. It also seems that for the stabilized dislocations, the energy on the crack distribute itself more equally along the crack front, leading to a more stable configuration.

5.8 Class II dislocations

After studying Class I dislocations and their effect on the crack energy, we will now analyze Class II dislocations and their effects.

Parameters

The studied dislocations will be screw dislocations of Class II (*CB(d)*), Burgers vector of $[10\bar{1}]$ and a length of 30 nm. Three simulations, aside the dislocation free simulation, will be carried out.

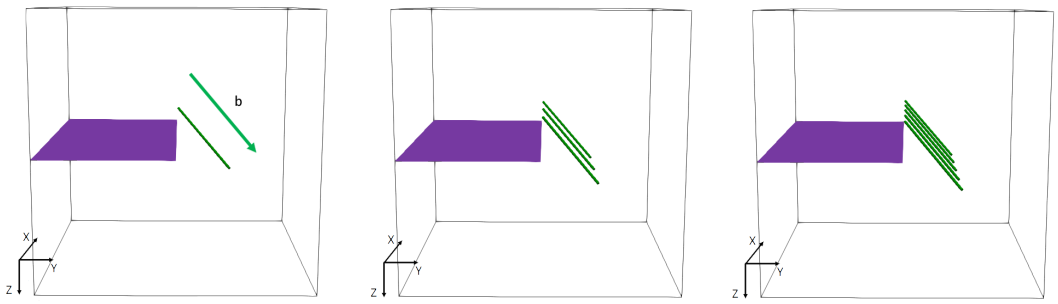

(a) $n = 1$ *(b)* $n = 3$ *(c)* $n = 5$

FIGURE 5.26 – *Initial configurations of the study cases for different number of dislocations*

The initial dislocation configurations are illustrated in Figure 5.26. As was done for Class I dislocations, these dislocations are placed so their centers are at 8 nm ahead of the crack front in the crack propagation direction. Both unrelaxed and relaxed configurations will be analyzed.

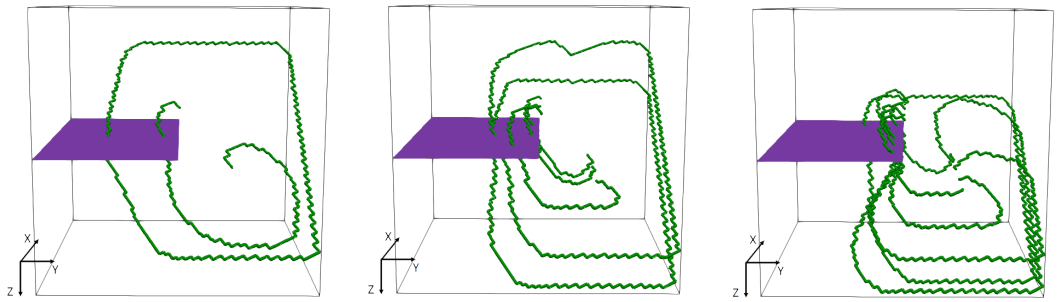

(a) $n = 1$ *(b)* $n = 3$ *(c)* $n = 5$

FIGURE 5.27 – *Final configurations of the study cases for different number of dislocations*

The dislocations relaxed configuration is illustrated in Figure 5.27. The starting dislocations, being Frank-Read sources, have emitted one complete a dislocation loop before stabilizing. These loops crossed the crack entirely. As said before, there is no specific interaction coded between the crack surfaces and the dislocations.

Results

Unrelaxed configuration

K_I Unrelaxed results for K_I are illustrated in Figure 5.29. A prominent antishielding effect can be observed. Unlike all the other studied cases, there is no shielding zone created by Class II dislocations, only a very strong antishielding effect. Individual dislocation effect can be observed in these results.

One single dislocation is able to influence the whole crack front as illustrated by the one dislocation simulation (blue curve). The dislocation itself might not globally slow down the crack, but, judging by the graph, it seems to accelerate it to go around said dislocation.

K_{II} The dislocation influence on K_{II}, illustrated in Figure 5.29, is also very high. The shortest distance between the crack front and the dislocation coincides with the point where K_{II} remains unchanged. Each dislocation creates two very marked propagation direction changes around it, making the crack go upwards.

Unlike the effect on K_I, dislocations do not affect the entirety of the crack front when it comes to K_{II}. The propagation angle will greatly vary due to the dislocation presence, making the crack

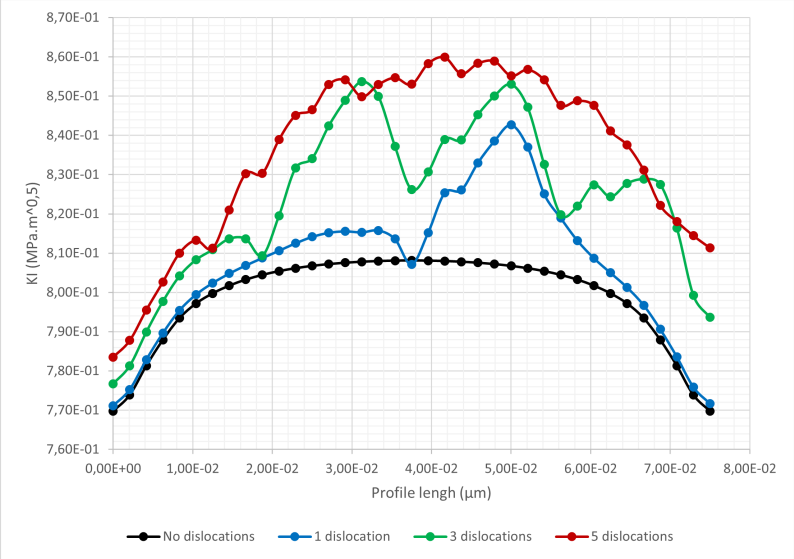

(a) K_I along the crack front

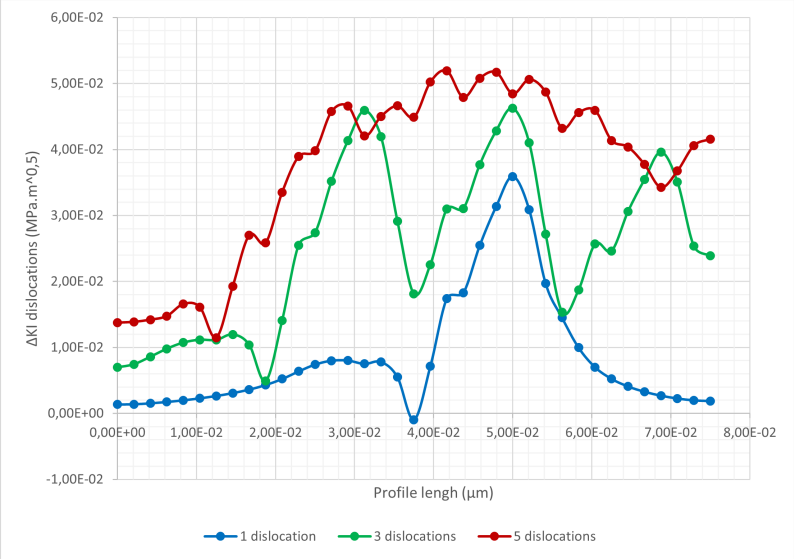

(b) Dislocation contribution to K_I along the crack front

FIGURE 5.28 – *K_I along the crack front for various amounts of Class II dislocations for the unrelaxed configuration. Dislocation contribution to K_I has been isolated for clarity.*

front wavy if it was to propagate with these values of K_{II}

Relaxed configuration

K_I Once dislocations relax, which is illustrated in Figure 5.30, we observe that although dislocations mainly provide antishielding to the crack, a shielding effect appears. As seen in Figure 5.27, dislocation loops cross the crack front. This could cause an increase in antishieling as seen for Class I dislocations.

Dislocation positions can still be determined using this results ; the lowest point between two peeks correspond to the dislocation position. This also means that locally, each dislocation slows down the crack even if globally they accelerate it.

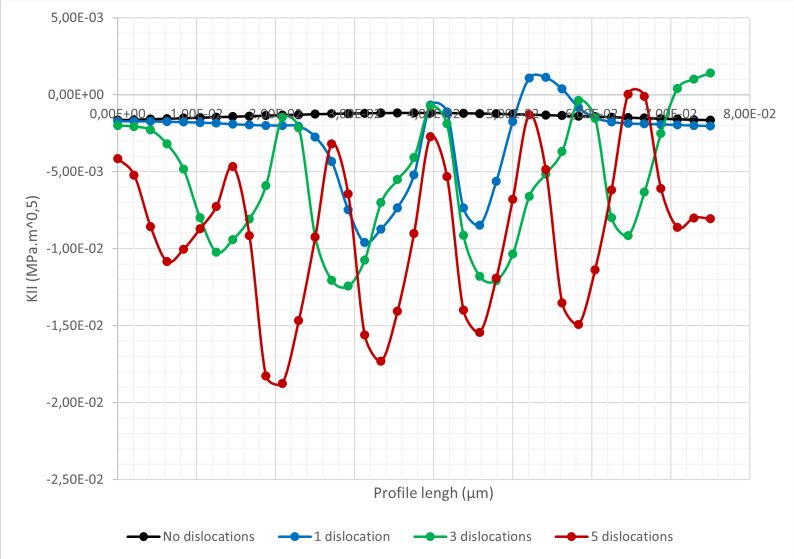

(a) K_{II} along the crack front

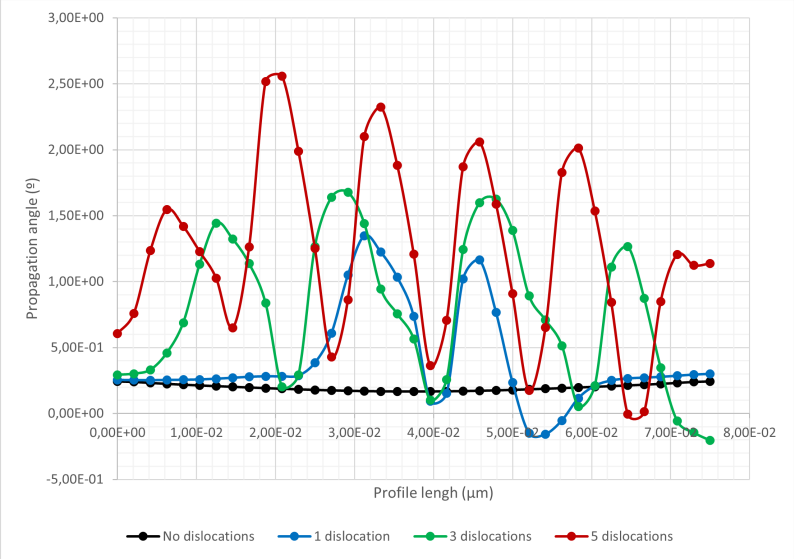

(b) Propagation angle of the crack front

FIGURE 5.29 – *K_{II} and propagation angle along the crack front for various amounts of Class II dislocations for the unrelaxed configuration. Dislocation contribution to K_{II} has been isolated for clarity.*

K_{II} Following a similar trend than the results for K_I, the results on K_{II} illustrated in 5.31, show a change of sign for K_{II}. Now the crack will partially go downward too instead of all of it going upwards.

Unlike the unrelaxed configuration, the crack front energy seems to be smoothed over; the crack front will still be wavy but less than it would have been with the unrelaxed configuration. The dislocation affected zone is larger than in the unrelaxed configuration, due to the new proximity between the crack and the dislocations.

Average stress intensity factors

The average values printed in Table 5.11 show the increase in both stress intensity factors previously discussed. The variation between values is not proportional to the number of dislocations

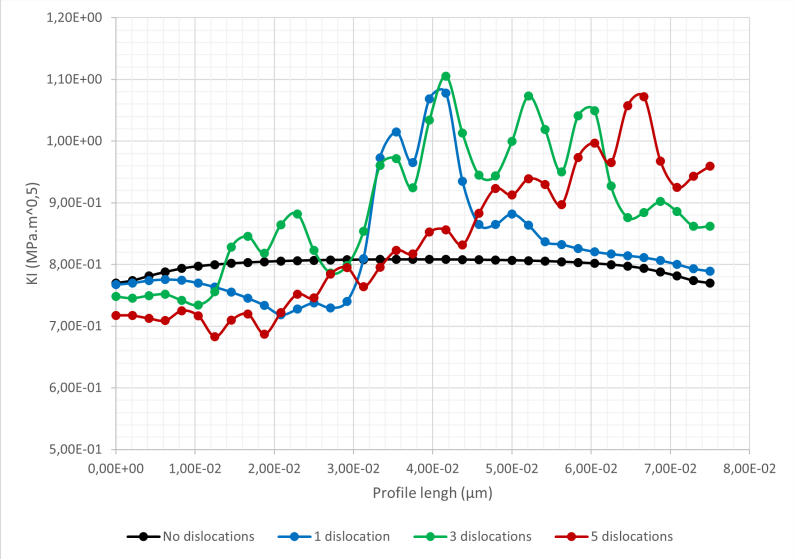

(a) K_I along the crack front

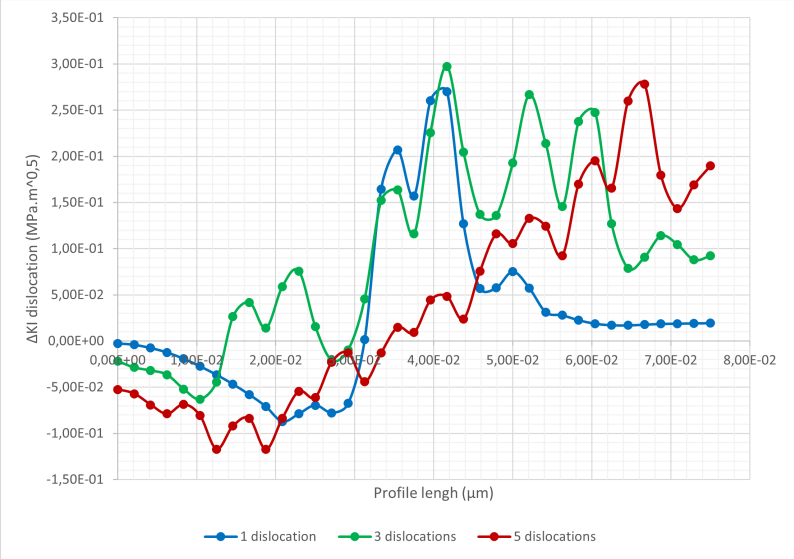

(b) Dislocation contribution to K_I along the crack front

FIGURE 5.30 – *K_I along the crack front for various amounts of Class II dislocations for the relaxed configuration. Dislocation contribution to K_I has been isolated for clarity.*

placed in the volume. The general antishielding effect is clearly illustrated here.

The antishielding trend continues on the results of Table 5.12 corresponding to the relaxed case. There is a sharp increase on the antishielding for the three dislocations simulation, it is probably due to a less extensive shielding zone created by the dislocations in comparison to the other two study cases. Even if the dislocation relaxation leads to the creation of some shielding zones on the crack front, globally, Class II dislocations create an antishielding effect.

Conclusions

We studied the effect of the amount of Class II dislocations on the stress intensity factors. It is shown that these dislocations create an antishielding effect on K_I. These dislocations, once they reach the relaxed configuration, create a dislocation loop that crosses the crack. We hypothesize that dislocations crossing the crack will create an antishielding effect, but in this case, a shielding

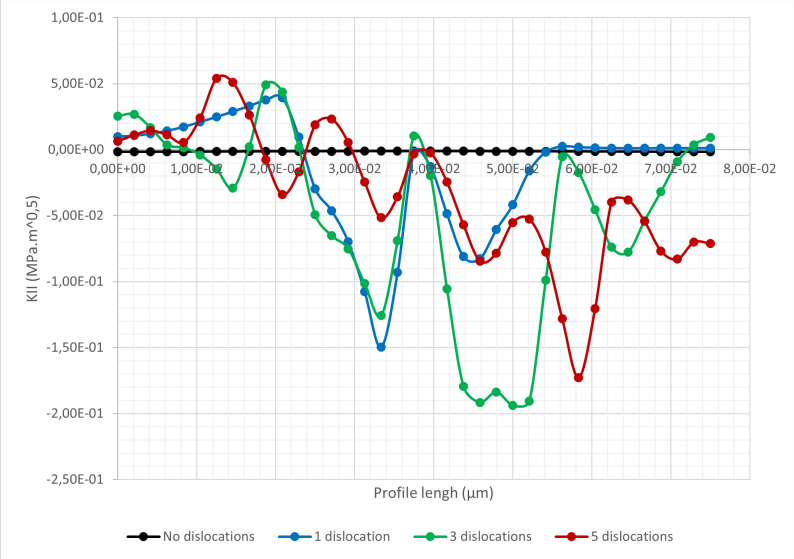

(a) K_{II} along the crack front

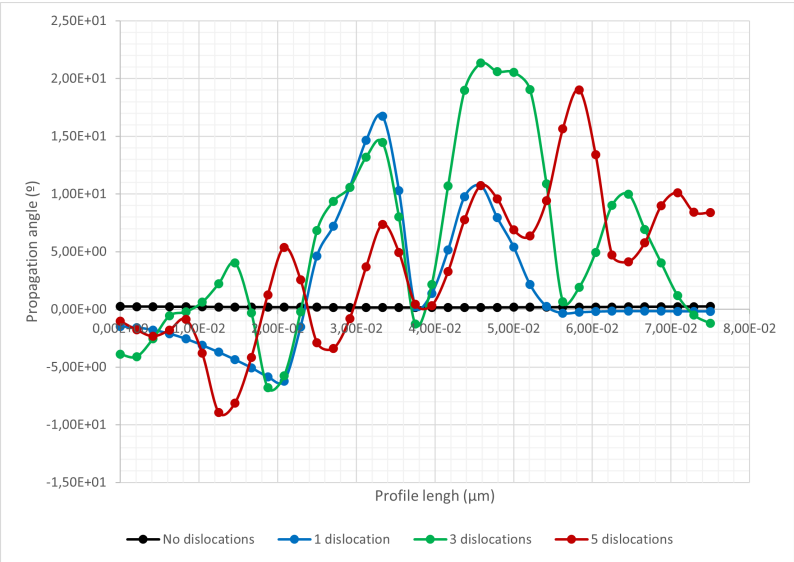

(b) Propagation angle of the crack front

FIGURE 5.31 – *K_{II} and propagation angle along the crack front for various amounts of Class II dislocations for the relaxed configuration. Dislocation contribution to K_{II} has been isolated for clarity.*

effect was observed once the dislocations attained the relaxed configuration. There is also a similar effect that happens for K_{II} where the relaxation of the dislocations create a change of sign on K_{II}. We hypothesize that the dislocations that end up on the other side of the crack front create the opposite effect on the crack front than the dislocations in the crack path. It remains to be determined how the crack will react after the dislocations crosses the crack surfaces.

	K_I			K_{II}		
Number of dislocations	1	3	5	1	3	5
K No dislocation (MPa.m$^{0.5}$)	0.79858	0.79858	0.79858	-0.00138	-0.00138	-0.00138
K Dislocation (MPa.m$^{0.5}$)	0.80718	0.82360	0.83544	-0.00285	-0.00559	-0.00903
Variation (%)	1.08	3.13	4.62	107.52	306.51	556.63

TABLE 5.11 – *Average values of the strain intensity factors for the studied Class II dislocations amounts in an unrelaxed configuration*

	K_I			K_{II}		
Number of dislocations	1	3	5	1	3	5
K No dislocation (MPa.m$^{0.5}$)	0.79858	0.79858	0.79858	-0.00138	-0.00138	-0.00138
K Dislocation (MPa.m$^{0.5}$)	0.82557	0.89061	0.83725	-0.01545	-0.04915	-0.03267
Variation (%)	3.38	11.52	4.84	1023.10	3472.93	2275.24

TABLE 5.12 – *Average values of the strain intensity factors for the studied Class II dislocations amounts in a relaxed configuration*

5.9 Class III dislocations

Let's finish our investigation with Class III dislocations.

Parameters

The studied dislocations will be screw dislocations of Class III (*AB(d)*), Burgers vector of $[\bar{1}10]$ and a length of 30 nm. Three simulations, aside the dislocation free simulation, will be carried out.

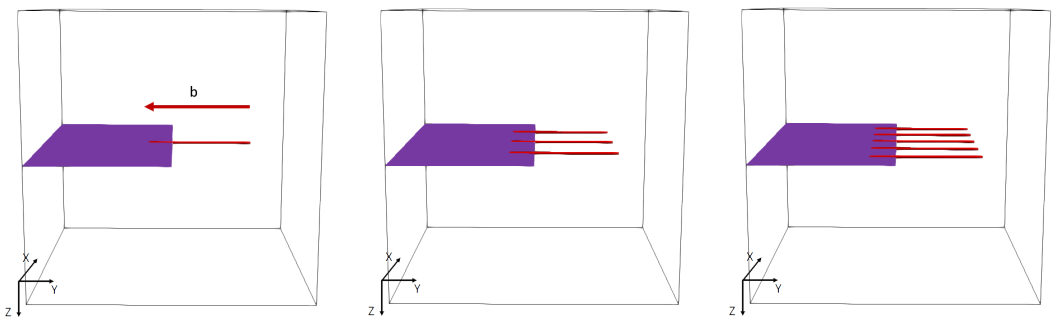

(a) $n = 1$ *(b)* $n = 3$ *(c)* $n = 5$

FIGURE 5.32 – *Initial configurations of the study cases for different number of dislocations*

Class III dislocations are coplanar with the crack in this orientation. Their center being placed at 8 nm ahead of the crack, they intersect with the crack for 7 nm.

Due to the dislocation position, the dislocation movements are restrained by the crack stress field. This causes the dislocations to stabilize without much propagation.

Results

Unrelaxed configuration

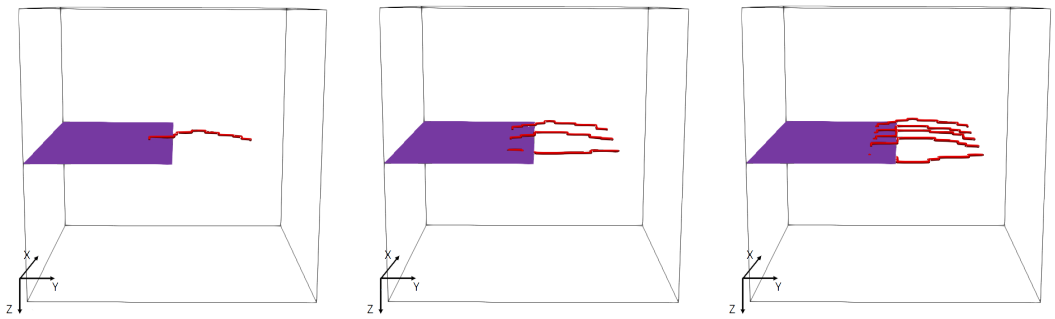

(a) $n = 1$ *(b)* $n = 3$ *(c)* $n = 5$

FIGURE 5.33 – *Final configurations of the study cases for different number of dislocations*

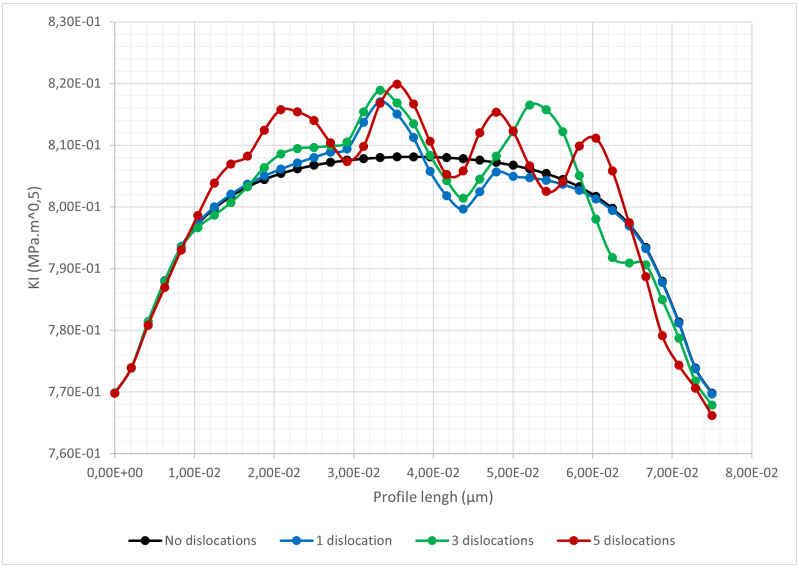

(a) K_I *along the crack front*

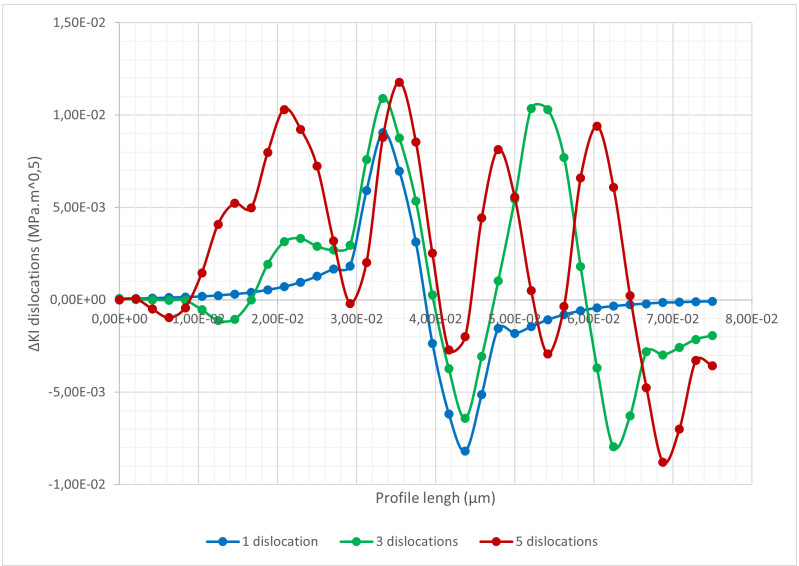

(b) Dislocation contribution to K_I *along the crack front*

FIGURE 5.34 – K_I *along the crack front for various amounts of Class III dislocations for the unrelaxed configuration. Dislocation contribution to* K_I *has been isolated for clarity.*

K_I K_I, illustrated in Figure 5.35, shows for all three cases a very similar effect as that created by the single centered dislocation. Each dislocation created a clear mark on the crack energy,evolution along the crack front making it easy to identify their position on the crack.

A single dislocation seems to be able to influence most of the crack length, most certainly due to the dislocation proximity to the crack. Class III dislocations create both a shielding and an antishielding effect on the crack, but the antishielding effect is more pronounced, making these dislocations have an average antishielding effect.

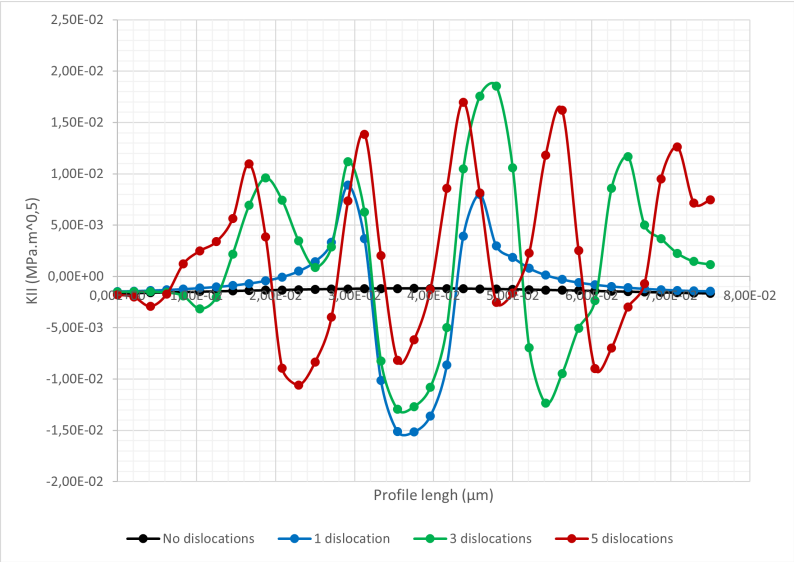

(a) K_{II} along the crack front

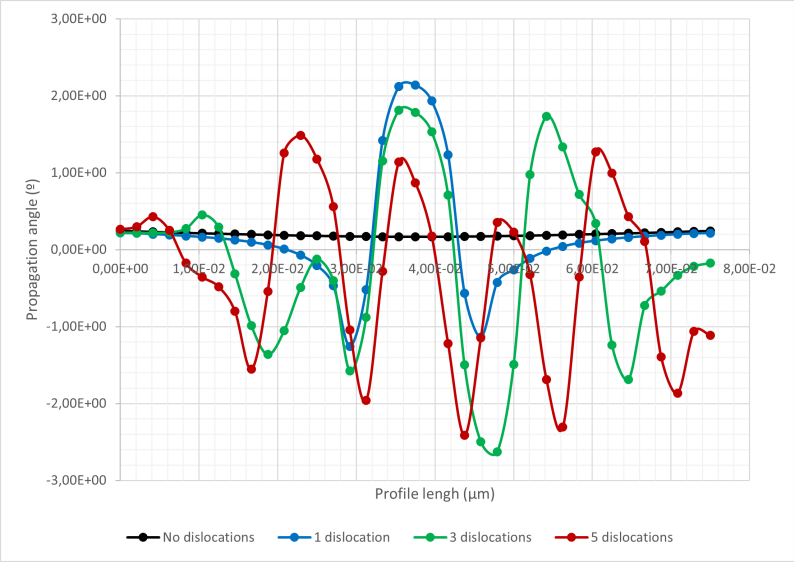

(b) Propagation angle of the crack front

FIGURE 5.35 – *K_{II} and propagation angle along the crack front for various amounts of Class III dislocations for the unrelaxed configuration. Dislocation contribution to K_{II} has been isolated for clarity.*

K_{II} Dislocations effect on K_{II}, as can be seen in Figure 5.35, is also evidenced as clear marks on the energy profile along the crack. The more dislocations present in the volume, the wavier the crack front will be when it propagates as shown by the propagation angle.

Driven by the observed energy, the crack will move as much as possible to avoid the disloca-

tions. It will move upwards to avoid the dislocations but it will also move along the opposite angle around the crack, creating a Λ shape where the dislocation is located.

Relaxed configuration

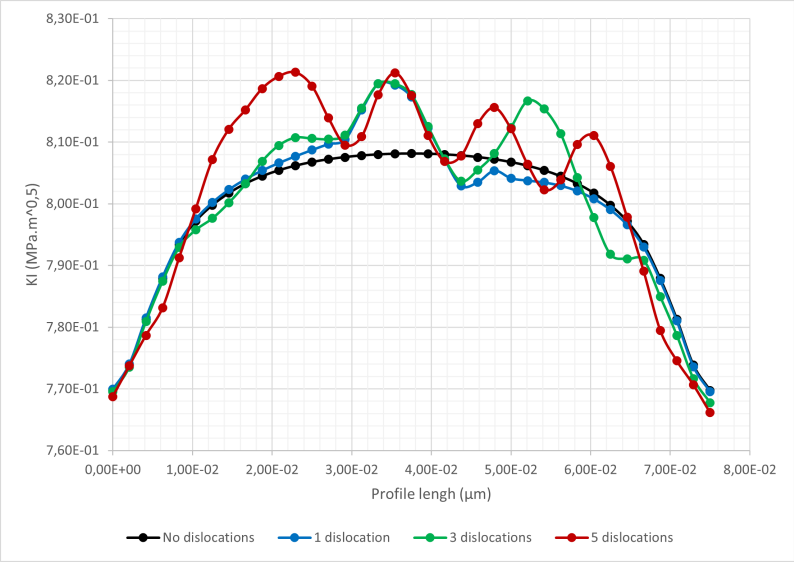

(a) K_I along the crack front

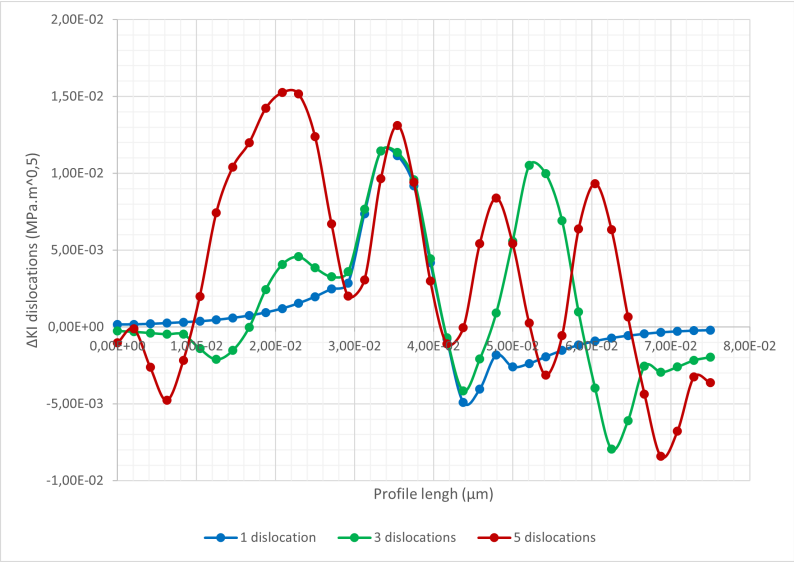

(b) Dislocation contribution to K_I along the crack front

FIGURE 5.36 – *K_I along the crack front for various amounts of Class III dislocations for the relaxed configuration. Dislocation contribution to K_I has been isolated for clarity.*

K_I Once the dislocations are relaxed, the results illustrated in Figure 5.36 show a very similar pattern as the unrelaxed ones. There is still a local shielding effect present, but it is less pronounced than before. On the other hand, the antishielding effect has increased. Since the dislocations reach a relaxed configuration without much propagation, it was expected for the results to remain similar to the unrelaxed ones.

K_{II} Similarly to K_I, K_{II} also remains close to its values in the unrelaxed configuration. In Figure 5.37 we observe that the most significant change is that the negative values or K_{II} increase in a

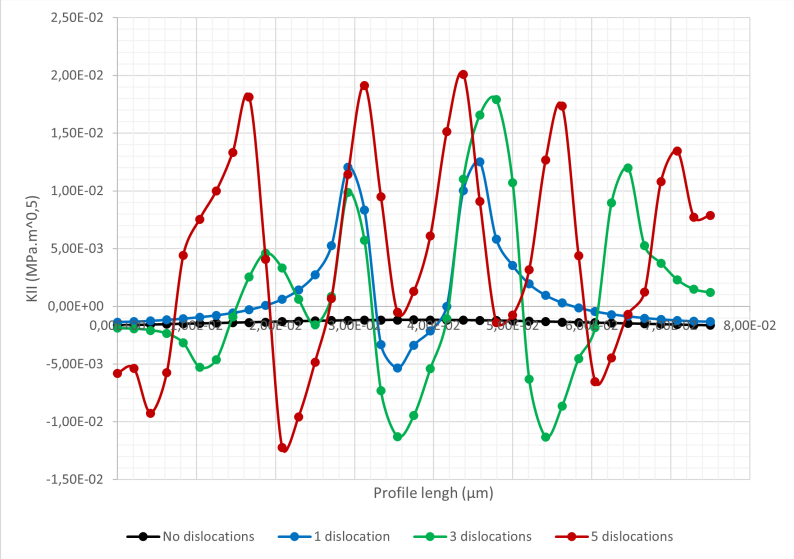

(a) K_{II} along the crack front

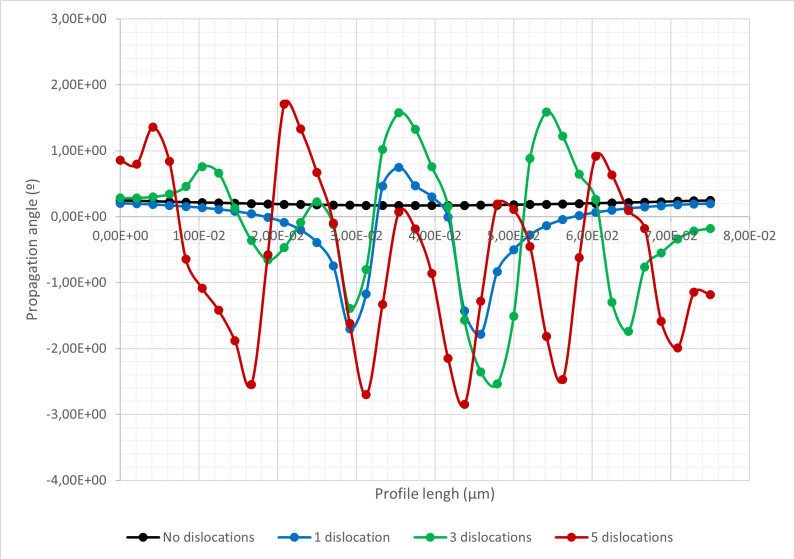

(b) Propagation angle of the crack front

FIGURE 5.37 – *K_{II} and propagation angle along the crack front for various amounts of Class III dislocations for the relaxed configuration. Dislocation contribution to K_{II} has been isolated for clarity.*

way that for some of the dislocations present in the five dislocation simulation there will be no angle changes on those points. The positive values increase slightly, but the general behavior of the crack will be unchanged compared to the unrelaxed configuration.

Average stress intensity factors

The average stress intensity factors calculated in Table 5.13 confirm what the graphics showed ; there is a global antishielding effect created by the Class III dislocations. Moreover, the values of K_{II} show that the cumulative effect of the dislocations create a stronger effect than a single dislocation could.

The simulation with one dislocation shows a minimal change in the global values as said dislocation creates both a positive and a negative effect. Once more dislocations are added, there

	K_I			K_{II}		
Number of dislocations	1	3	5	1	3	5
K No dislocation (MPa.m$^{0.5}$)	0.79858	0.79858	0.79858	-0.00138	-0.00138	-0.00138
K Dislocation (MPa.m$^{0.5}$)	0.79866	0.79967	0.80104	-0.00131	0.00116	0.00201
Variation (%)	0.01	0.14	0.31	-4.57	-184.30	-245.96

TABLE 5.13 – *Average values of the strain intensity factors for the studied Class III dislocations amounts in an unrelaxed configuration*

is a stronger global effect that is created.

	K_I			K_{II}		
Number of dislocations	1	3	5	1	3	5
K No dislocation (MPa.m$^{0.5}$)	0.79858	0.79858	0.79858	-0.00138	-0.00138	-0.00138
K Dislocation (MPa.m$^{0.5}$)	0.79946	0.80012	0.80226	0.00094	0.00075	0.00438
Variation (%)	0.11	0.19	0.46	-168.41	-154.69	-418.09

TABLE 5.14 – *Average values of the strain intensity factors for the studied Class III dislocations amounts in a relaxed configuration*

The relaxed configuration heightens the antishielding effect of the dislocations as well as the direction change of the crack. The dislocation effect remains non proportional to the number of dislocations present as shown in Table 5.14. K_{II} does increase dramatically and remains positive for all the case studied, but its raw values remain variable.

Conclusions

We studied the effect of Class III dislocations on the stress intensity factors. Generally speaking, they create an antishielding effect on the crack. As they are coplanar with the crack, their position can strongly affect the results. Both K_I and K_{II} vary greatly along the crack front. This will lead to a crack front that, once it propagates, will be wavy, increasing the global crack energy. Of course this is a hypothetical case as the simulated dislocation crosses the crack front and does not encounter a real surface.

5.10 Dislocation class comparison

We studied each dislocation class effect individually. Now we seek to compare their effect to each other.

Parameters

The studied dislocations are the same that were previously studied. We will only consider the cases with single dislocations present. As a reminder the dislocations studied, illustrated in Figure 5.38, are :

— Class I : (*CB(a)*), Burgers vector $[10\bar{1}]$

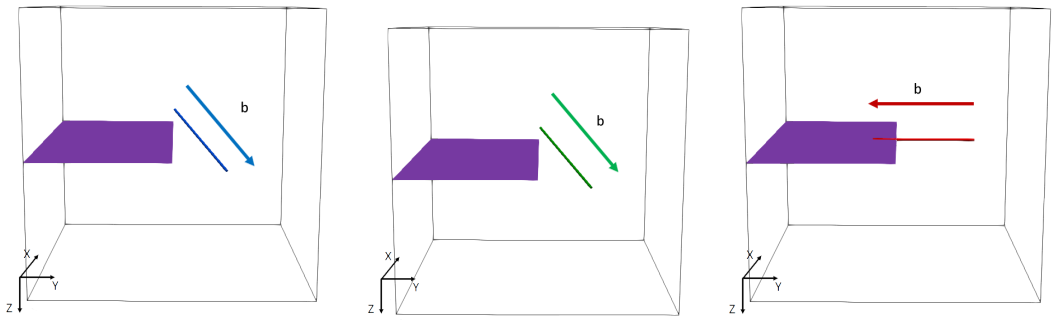

(a) Class I *(b) Class II* *(c) Class III*

FIGURE 5.38 – *Initial configurations of the study cases for different types of dislocation*

— Class II : $(CB(d))$, Burgers vector $[10\bar{1}]$

— Class III : $(AB(d))$, Burgers vector $[\bar{1}10]$

All dislocations are 30 nm long. The applied strain is so : $\varepsilon_{zz} = \varepsilon_1 = 0.01892208$

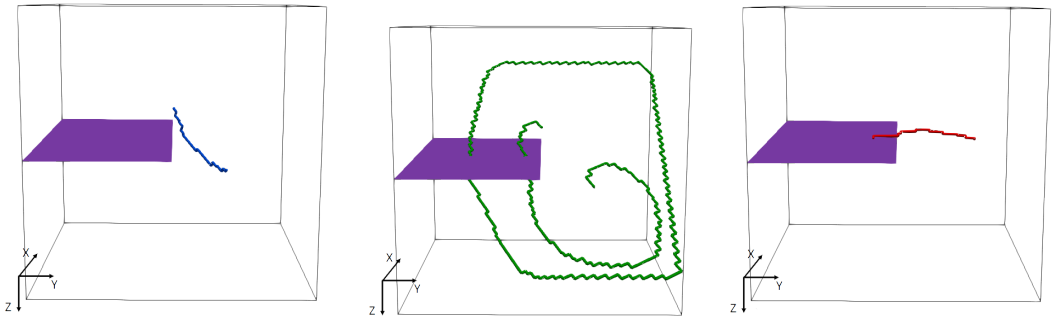

(a) Class I *(b) Class II* *(c) Class III*

FIGURE 5.39 – *Final configurations of the study cases for different types of dislocations*

We will also consider the relaxed configuration of the dislocations, illustrated in Figure 5.39. As these dislocations interact differently with the crack stress fields, their relaxed configurations vary greatly from one to another.

Results

Unrelaxed configuration

K_I First, we compare the unrelaxed results for K_I shown in Figure 5.40. Each dislocation has a different effect on the crack, be it shielding, for Class I, antishielding, for Class II, or a mix of both, for Class III. These results confirm the uniqueness of the different dislocation classes.

It is also worth noting that the dislocation with the highest effect on the crack, Class II, is the one that will propagate the most to the point of creating a dislocation loop. On the other hand, Class I, even if it has a Burgers vector that will lead the dislocation to cross the crack front, it stabilizes mostly before it happens. As Class III is already touching the crack, there is not much to say.

K_{II} As for K_{II}, illustrated in Figure 5.41, we also observe a very diverse energy variation created by the dislocations. The highest dislocation impact is created by the Class III dislocation. This dislocation is also the closest to the crack, thus increasing its effect on said crack.

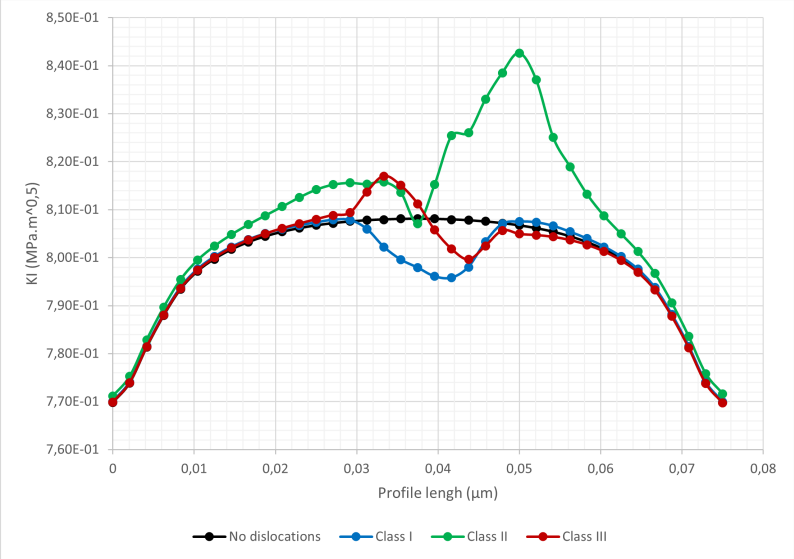

(a) K_I along the crack front

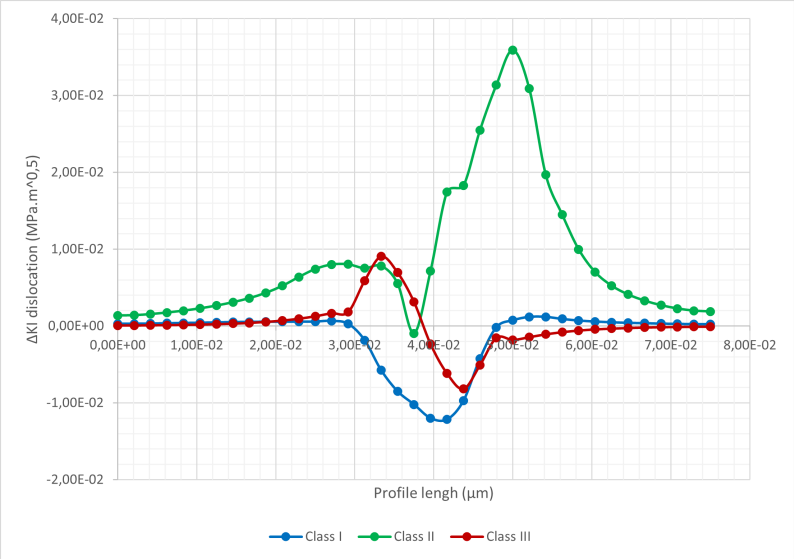

(b) Dislocation contribution to K_I along the crack front

FIGURE 5.40 – *K_I along the crack front for different dislocation classes in an unrelaxed configuration. Dislocation contribution to K_I has been isolated for clarity.*

Class I dislocation has a similar effect to Class III but in a smaller scale. When the crack front changes of angle in a direction, it will also partially change to the other direction in a lower scale. On the other hand, Class II dislocations only modify the propagation angle around the dislocation position.

Relaxed configuration

K_I Once the dislocations are relaxed, we obtain the results illustrated in Figure 5.42. We observe a dramatic increase of K_I for the Class II dislocation. It was expected since it is the dislocation that propagated the most. On the other hand, the Class III dislocation loses its shielding effect, now it only pushes the crack to advance farther. At last, the Class I dislocation retains its shielding effect and continues to affect the crack in the same way.

Regarding the dislocation affected zone, Class II dislocation is the one that has the most ex-

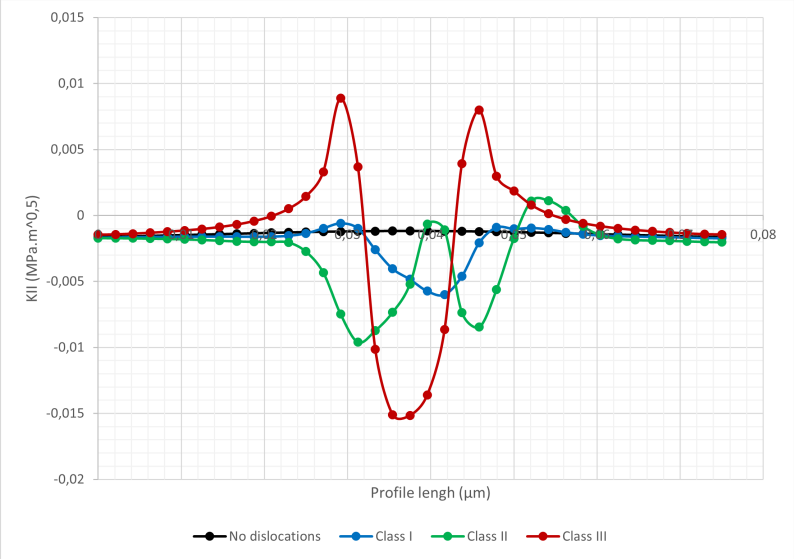

(a) K_{II} along the crack front

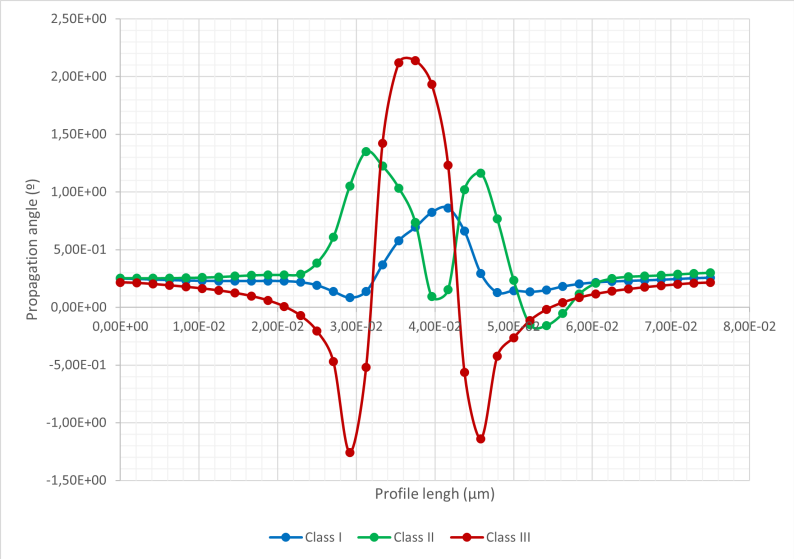

(b) Propagation angle of the crack front

FIGURE 5.41 – *K_{II} along the crack front for different dislocation classes for the unrelaxed configuration. Dislocation contribution to K_{II} has been isolated for clarity.*

tended effect on the crack front among the studied dislocations. It is possible that what affects the crack front energy is not only the dislocation crack distance, as the Class III dislocation is much closer than the Class II is, but also the shear created by the dislocations when they propagate. Since the crack front is sheared by at least one dislocation loop when the Class II dislocation stabilizes, this could be the reason of such a high value of K_I.

K_{II} For the relaxed configuration, illustrated in Figure 5.43, the general behavior of Class I and Class III dislocations remains unchanged. On the other hand, Class II dislocations have a change in their behavior. Aside from a general increase on K_{II} values, we observe an increase in the left side of the graph that only appeared on the relaxed configuration. As before, it is Class II which has the highest effect on the stress intensity factors. Furthermore, Class I dislocation effect becomes more pronounced than Class III dislocations. This shows that the dislocation distance is not a parameter of first order for the dislocation influence on the crack stress intensity factors.

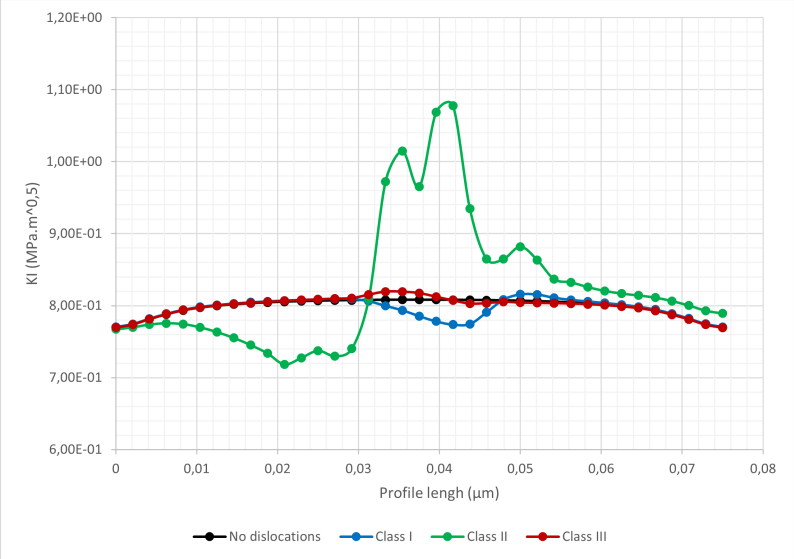

(a) K_I along the crack front

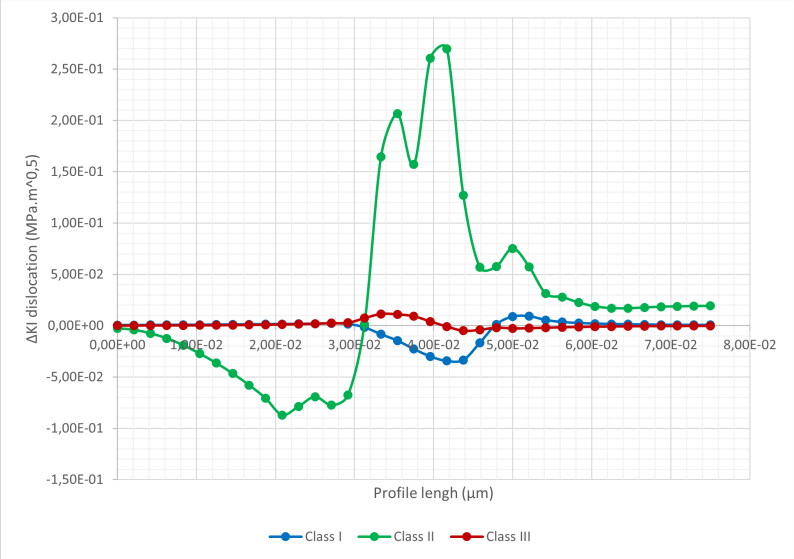

(b) Dislocation contribution to K_I along the crack front

FIGURE 5.42 – *K_I along the crack front for different dislocation classes for the relaxed configuration. Dislocation contribution to K_I has been isolated for clarity.*

Average stress intensity factors

As was expected from the previous results, Class II dislocation are shown to have the highest impact on the stress intensity factors as visible in Table 5.15. Class I dislocations are the only ones that provide shielding to the crack. On the other hand, the average values do not allow to determine the overall effect of Class III dislocations since the shielding and antishielding effects cancel each other out when calculating an average value.

Once the dislocations get to the relaxed configuration, the absolute average values, gathered in Table 5.16, have all increased in various ways. For Class I, relaxation doubles the dislocation effect while for Class II it triples it. As said before, Class III dislocations had both a shielding and an antishielding effect. The fact that there is a difference in the average value indicates that the antishielding effect took the upper hand and became the main effect created by this dislocation.

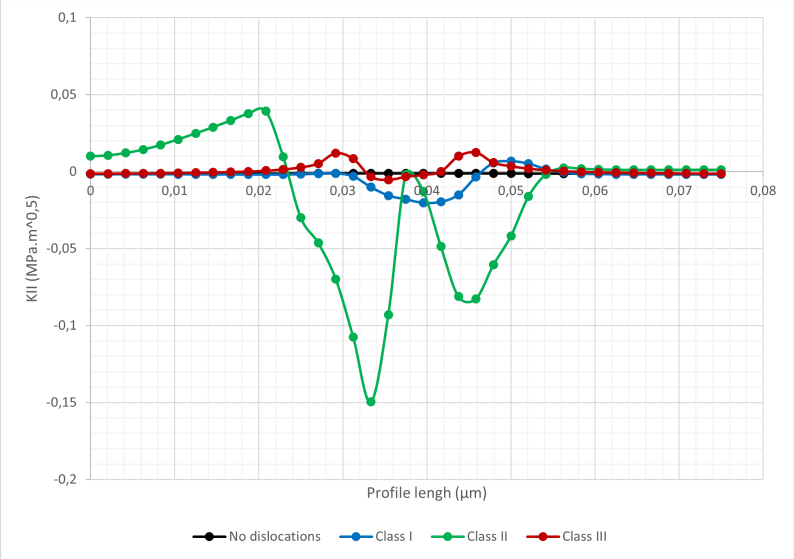

(a) K_{II} along the crack front

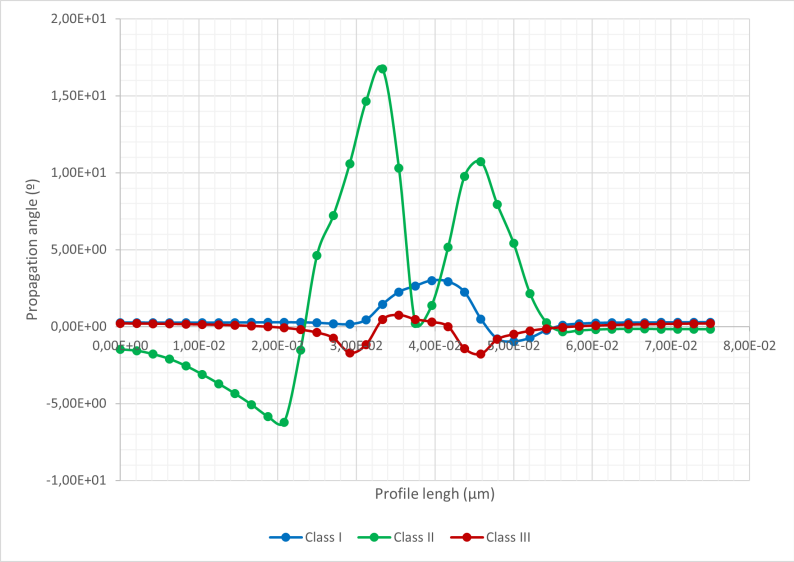

(b) Propagation angle of the crack front

FIGURE 5.43 – *K_{II} and propagation angle along the crack front for different dislocation classes for the relaxed configuration. Dislocation contribution to K_{II} has been isolated for clarity.*

Conclusions

We have studied three types of dislocations belonging to different classes and compare their effect on the stress intensity factors along the crack front. We observe how each dislocation Class has a different effect on the crack energy. Class I dislocation provides shielding to the crack while Class II provides antishielding and finally Class III provides both effects to the crack. It is worth mentioning how the dislocation with the largest effect on the crack front, Class II dislocation, is the only one that will propagate enough to create a dislocation loop that will cross the crack surface.

	K_I			K_{II}		
	Class I	Class II	Class III	Class I	Class II	Class III
K No dislocation (MPa.m$^{0.5}$)	0.79858	0.79858	0.79858	-0.00138	-0.00138	-0.00138
K Dislocation (MPa.m$^{0.5}$)	0.79723	0.80718	0.79866	-0.00196	-0.00285	-0.00131
Variation (%)	-0.17	1.08	0.01	42.76	107.52	-4.57

TABLE 5.15 – *Average values of the strain intensity factors for the studied dislocations in an unrelaxed configuration*

	K_I			K_{II}		
	Class I	Class II	Class III	Class I	Class II	Class III
K No dislocation (MPa.m$^{0.5}$)	0.79858	0.79858	0.79858	-0.00138	-0.00138	-0.00138
K Dislocation (MPa.m$^{0.5}$)	0.79583	0.82557	0.79946	-0.00345	-0.01545	0.00094
Variation (%)	-0.34	3.38	0.11	151.01	1023.10	-168.41

TABLE 5.16 – *Average values of the strain intensity factors for the studied dislocations in a relaxed configuration*

5.11 Conclusion

We have studied the stress intensity factors by plotting its evolution along the crack front and compute its average. Different parameters were considered. First, we studied the effect of the applied loading strain, from which we deduced that, even if the total influence of the dislocation increases with a higher strain, it is the fact that the dislocation propagates that increases the energy on the crack and not the strain itself. As for the crack dislocation distance, we deduced that dislocations need to be closer to 9 nm from the crack for it to be able to influence on the stress intensity factors. We lastly considered the dislocation sign, which affects the intensity of the dislocation effect on the crack front energy but not its nature.

Various number of initial dislocations were studied too. It leads to results that indicate that the effect on the stress intensity factors of the dislocations are not proportional to the number of dislocations, it looks rather like an exponential relationship. Lastly, several dislocation types were considered. Dislocations of Class I lead to a shielding of the crack, while Class II dislocations created the opposite effect ; antishielding. As for Class III dislocations, we obtained a mix of shielding and antishielding of the crack.

6

Effect of dislocations on the stress intensity factors for the $O_{\bar{1}01}$ orientation

Contents

6.1 Introduction

This chapters contains a study of the dislocations effect on the crack stress intensity factors for the orientation noted as $O_{\bar{1}0\bar{1}}$. This orientation corresponds to the one studied in [70]. The referred study deals with dislocation crack interactions using DDD with DCM and a static crack presented in 1.4. Therefore, the aim was to compare our results, however due to the differences in procedures, this comparison is impossible. This study will focus on the individual effect of a dislocation on the crack while the mentioned study tends to a more global approach.

Similarly to the study carried out in Chapter 5, we will study the effect of several dislocation orientations on the crack as well as different amounts of initial dislocations.

6.2 Simulation parameters

Volume orientation

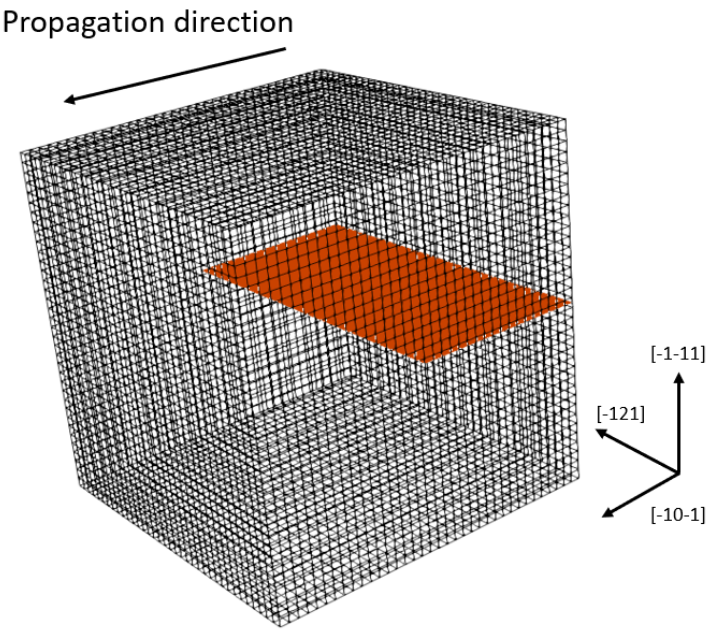

FIGURE 6.1 – *Studied crack orientation* $O_{\bar{1}0\bar{1}}$. *Volume of* $75 \times 75 \times 75nm$

The orientation noted $O_{\bar{1}0\bar{1}}$ and illustrated in Figure 6.1 will be studied in this chapter. This orientation places the crack plane on a dense $\{111\}$ atomic plane. It was chosen because studies of a similar crack interacting with dislocations already exist. The studied mesh corresponds to a cube of 75 nm of size.

Dislocations

The dislocations studied are the screw dislocations described in Table 6.1, and are the same as studied in Chapter 5. Even if these dislocations will be referred as dislocations belonging to classes for simplicity sake, this class distinction is not relevant for this crack configuration.. The

	Class I	Class II	Class III
System	*CB(a)*	*CB(d)*	*AB(d)*
Burgers vector	$[10\bar{1}]$	$[10\bar{1}]$	$[\bar{1}10]$
Line vector	$[10\bar{1}]$	$[10\bar{1}]$	$[\bar{1}10]$
Slip plane	$(\bar{1}1\bar{1})$	(111)	(111)
Schmid-Boas notation	D4	B4	B5

TABLE 6.1 – *Dislocations used for the simulations*

class definition was based on the strain perceived by the dislocations, with the orientation change, the strain distribution will change too. The dislocations will be placed so that their center is at 8 nm ahead of the crack front following the propagation direction of the crack.

Figure 6.2 illustrates the shear stress resolved on the dislocation slip system for each studied dislocation. The fields seen by the dislocations belonging to Class I and Class II are symmetrical, we can expect their behavior to be similar. As for Class III dislocations, they are subjected to a high shear stress on their whole length, which should lead to a higher influence on the stress intensity factors than the other dislocations.

Loading conditions

These simulations will be carried out under the same loading as in the simulations described in Chapter 5. The volume will be subjected to an imposed strain applied to the upper surface of the volume opening the crack in mode I. The applied strain will be of $\varepsilon = 0.01892208$ as it corresponds to $0.998\varepsilon_G$ as described in Section 4.2. This strain allows dislocation mobility without having a too large dislocation multiplication.

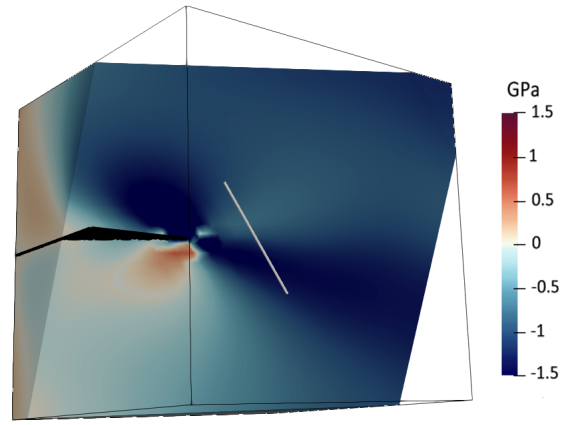

(a) $\tau_{CB(a)}$

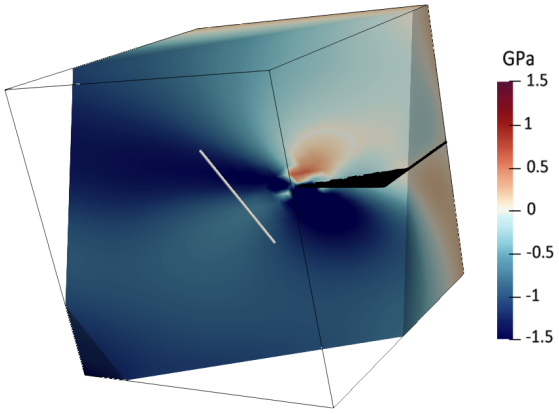

(b) $\tau_{CB(d)}$

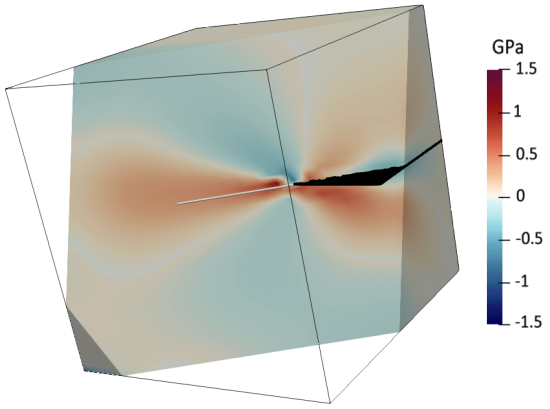

(c) $\tau_{AB(d)}$

FIGURE 6.2 – *Shear stress created by the crack on the mentioned dislocations slip planes*

6.3 Class I dislocations

First, we will study the effect of one or several class I dislocations on the stress intensity factors. The studied dislocations will be screw dislocations of Class I (*CB(a)*), Burgers vector of $\left[10\bar{1}\right]$, slip plane : $(\bar{1}1\bar{1})$ and a length of 30 nm.

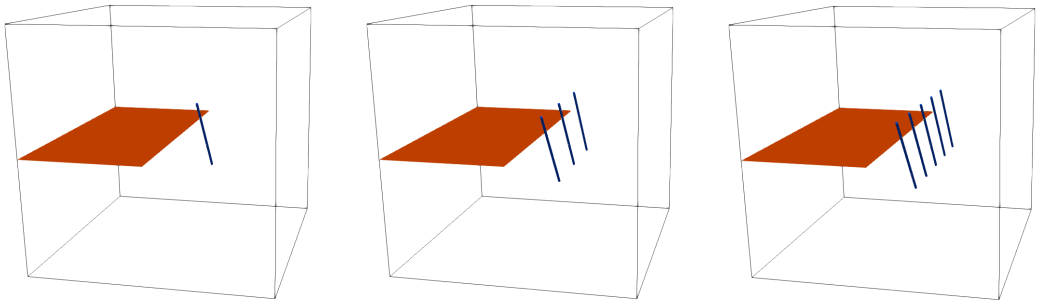

(a) $n = 1$ (b) $n = 3$ (c) $n = 5$

FIGURE 6.3 – *Initial configurations of the study cases for different number of Class I dislocations*

Parameters

Three simulations will be carried out. Their initial state is illustrated in Figure 6.3. In these simulations we vary the number of starting dislocations.

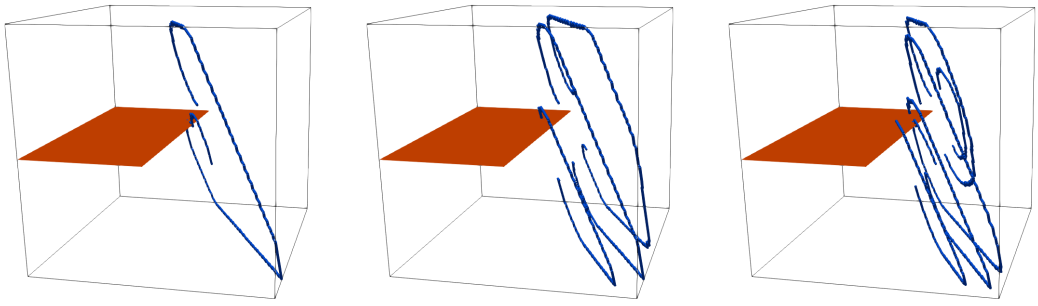

(a) $n = 1$ (b) $n = 3$ (c) $n = 5$

FIGURE 6.4 – *Final configurations of the study cases for different number of class I dislocations*

The relaxed state of these simulations, illustrated in Figure 6.4, will also be analyzed. The dislocations propagate away from the crack without creating a dislocation loop. Even if the dislocations propagate away from the crack there is some points where the dislocations cross the crack surface. This happens for the simulations containing one and five dislocations. These interactions will probably increase the dislocation effect on the crack energy.

Results

Unrelaxed state

K_I The results for K_I for an unrelaxed state plotted in Figure 6.5 show that the dislocation position can be easily evidened from the valleys created on the energy on the crack front. The curve corresponding to the one dislocation case shows how much a single dislocation is able to influence all the crack length. Is is found that class I dislocations present a high antishielding effect all along the crack front.

Even if globally these dislocations have an antishielding effect, we observe locally a small amount of shielding where the dislocation is closer to the crack front. Since K_I increases around the dislocation, the crack will want to surround the dislocation. The dislocations will not directly slow down the crack, but they will nonetheless redirect it around themselves.

K_{II} As shown in Figure 6.6, the effect of the dislocations on K_{II} is not as simple as its effet on K_I. Just as for K_I, one dislocation is enough to affect the entirety of the crack front.

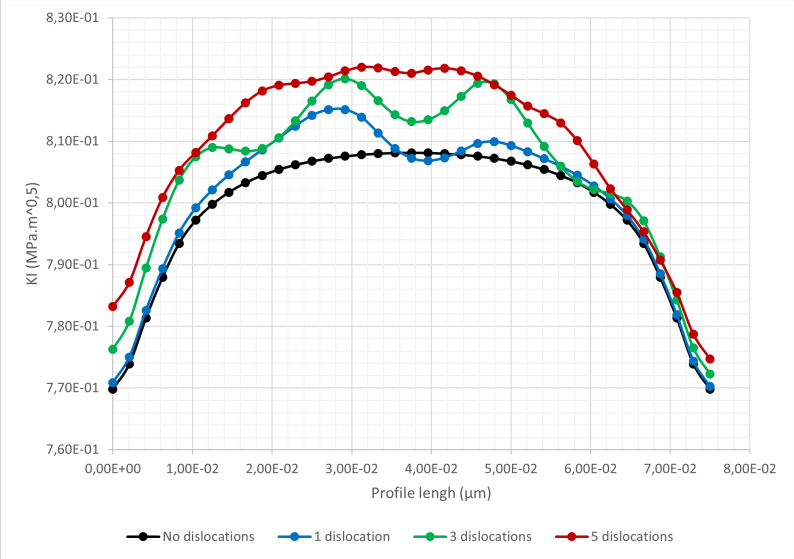

(a) K_I along the crack front

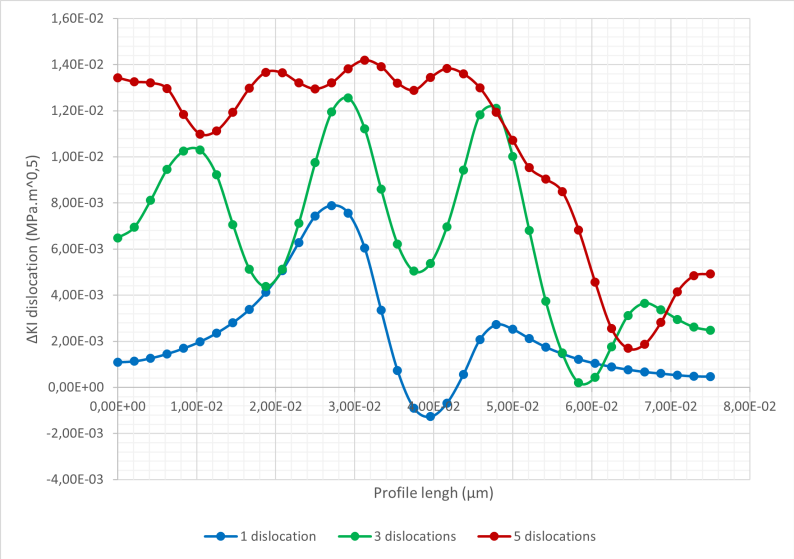

(b) Dislocation contribution to K_I

FIGURE 6.5 – *K_I along the crack front for different number of Class I dislocations in for the unrelaxed configuration. Dislocation contribution to K_I has been isolated for clarity.*

Unlike the other studied cases, the studied dislocations do not create a very clear mark on the energy values. Here, we observe a general increase on the crack energy on the whole crack. The zone surrounding the dislocations does seem to have an increase in energy in a lesser manner than for the rest of the crack front. The crack propagation angle will change all in the same direction ; downwards i.e. in the direction of $(11\bar{1})$.

Relaxed state

K_I Once the dislocations have reached their equilibrium position for the given applied strain, we obtain the values of K_I illustrated in Figure 6.7. There is still a very clear antishielding effect on the whole crack front. Unlike the unrelaxed state results, here it is impossible to identify the direct effect of each singular dislocation on the energy. The fact that the dislocations have moved away from the crack is probably the origin of the smoother results. The crack seems to be affected by

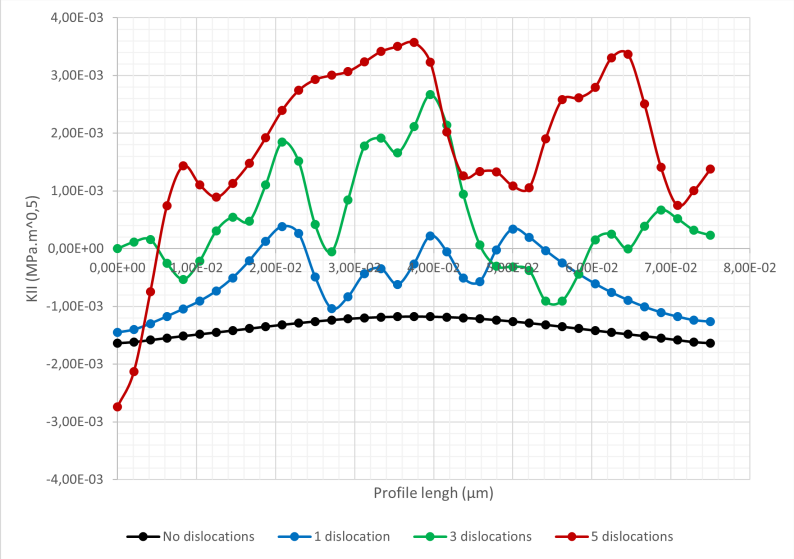

(a) K_{II} along the crack front

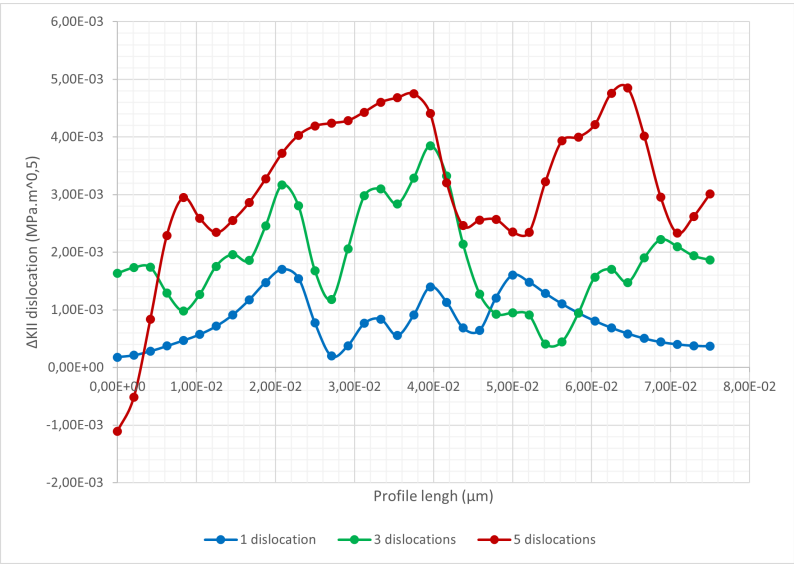

(b) Dislocation contribution to K_{II}

FIGURE 6.6 – *K_{II} along the crack front for different number of Class I dislocations for the unrelaxed configuration. Dislocation contribution to K_{II} has been isolated for clarity.*

the dislocations as a whole instead of each individual dislocations.

This is confirmed by the three dislocations case for which the dislocation lines never cross the crack surface and where the K_I profile is smoother.

K_{II} K_{II} profiles computed in the relaxed state in Figure 6.8 yield similar results than the ones obtained for K_I. There is no individual mark for each dislocation effect but there is a sharp increase in values where the dislocations intersected the crack front. This is also due to the dislocations moving away from the crack. The energy distribution is similar in all cases and it does not seem to be proportional to the starting dislocations placed in the volume. Knowing the dislocation propagation pattern, seen in Figure 6.4, the farther the dislocations are, the lower the energy is.

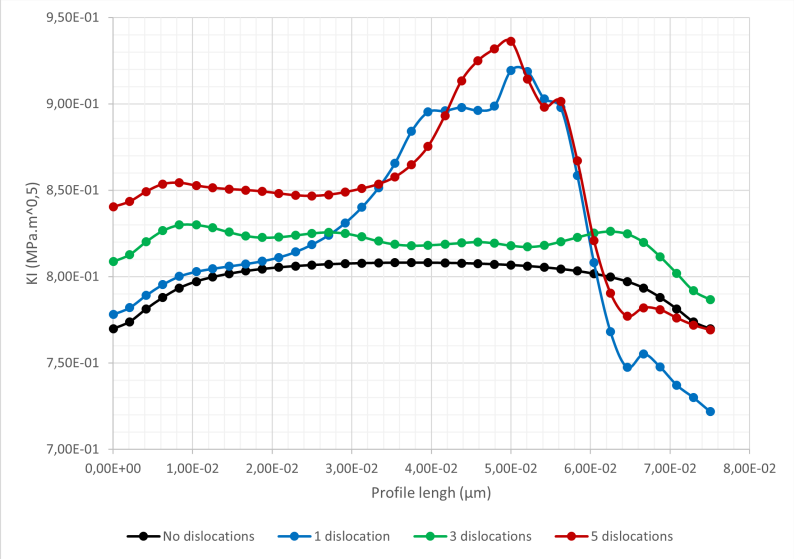

(a) K_I along the crack front

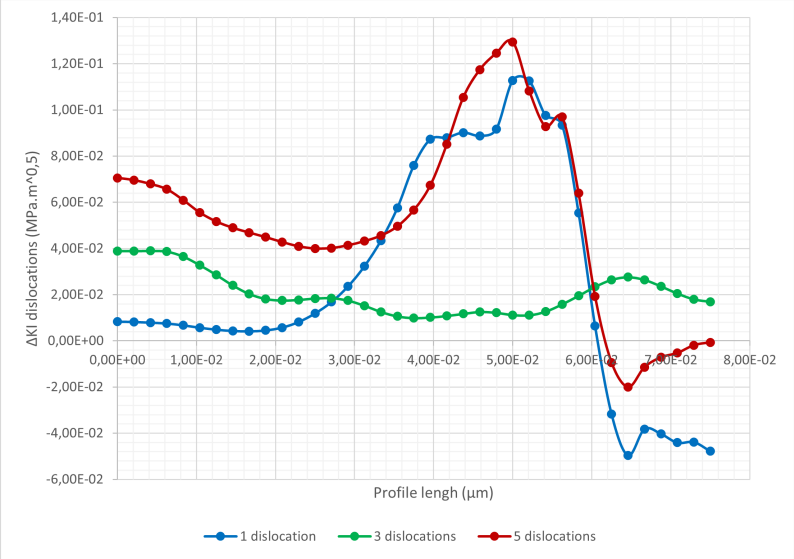

(b) Dislocation contribution to K_I

FIGURE 6.7 – *K_I along the crack front for different number of Class I dislocations for the relaxed configuration. Dislocation contribution to K_I has been isolated for clarity.*

Average stress intensity factors

The average stress intensity factors for the relaxed state compiled in Table 6.2 show how the values of K_I slightly increase with the number of dislocations present. The increase is proportional to the number of present dislocations. Even if there is an increase, the average values remain very close to the ones without dislocations present.

As for K_{II}, it also increases proportionally to the number of starting dislocations. The high variation is of course due to the shearing nature of the dislocations.

Once the dislocations have reached a stable state, the studied values in Table 6.3 show faint evolution for K_I. As was observed in the graphics, the three dislocation simulation has a lower value than the two others due to the fact that no dislocation in that simulation ever crosses the crack front. The energy increase is in accordance to the values previously seen in Chapter 5.

As for K_{II}, the high discordance on the values is due to the fact that the base value is almost null

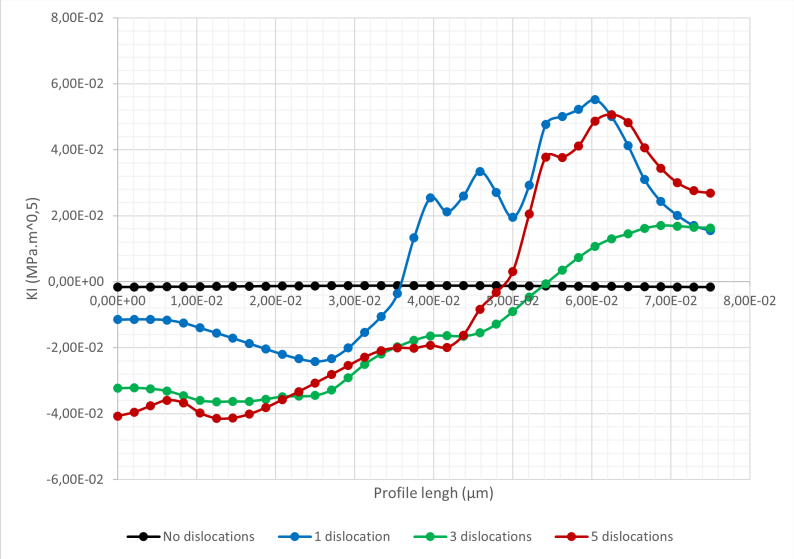

(a) K_{II} along the crack front

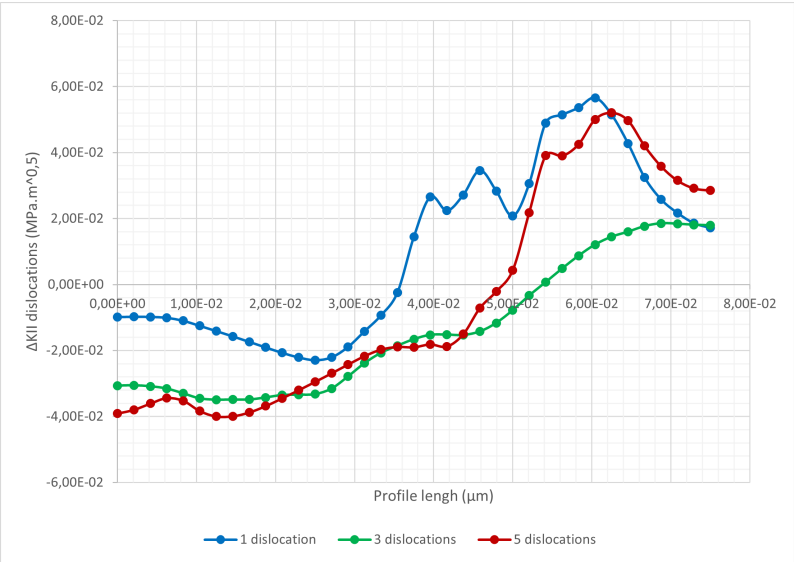

(b) Dislocation contribution to K_{II}

FIGURE 6.8 – *K_{II} along the crack front for different number of Class I dislocations for the relaxed configuration. Dislocation contribution to K_{II} has been isolated for clarity.*

and that along the crack front, K_{II} changes of sign. The highest impact, happens for the simulation with no direct crack dislocation interaction. Since we are looking at average values, they might not be accurate considering the raw results previously studied.

Conclusions

We observed in these simulations that the studied dislocations create an antishielding effect. Even with this antishielding, the crack still tended to have lower energies if a dislocation was right in front of it. The dislocation propagates away from the crack front.

Even when the dislocations have moved away from the crack, they still managed to influence its energy. The individual effect of each dislocation cannot be discerned once the dislocations get relaxed ; their combined effect widen the affected zone and smoothed the curve. There is still some dislocations crossing the crack surface in these simulations. These kind of interactions are shown

	KI			KII		
Number of dislocations	1	3	5	1	3	5
K No dislocation (MPa.m$^{0.5}$)	0.79858	0.79858	0.79858	-0.00138	-0.00138	-0.00138
K Dislocation (MPa.m$^{0.5}$)	0.80082	0.80516	0.80897	-0.00057	0.00051	0.00178
Variation (%)	100.280	100.823	101.300	41.589	-36.985	-129.466

TABLE 6.2 – *Average values of the stress intensity factors for the studied number of Class I dislocations for the initial unrelaxed configuration*

	KI			KII		
Number of dislocations	1	3	5	1	3	5
K No dislocation (MPa.m$^{0.5}$)	0.79858	0.79858	0.79858	-0.00138	-0.00138	-0.00138
K Dislocation (MPa.m$^{0.5}$)	0.82470	0.81925	0.85094	0.00846	-0.01502	-0.00673
Variation (%)	103.271	102.588	106.557	-615.108	1091.790	489.320

TABLE 6.3 – *Average values of the stress intensity factors for the studied number of Class I dislocations for the relaxed configuration*

to exacerbate the dislocation effect on the crack front energy.

6.4 Class II dislocations

The next studied dislocations will be Class II dislocations, i.e. the *CB(d)* case with one, three and five initial screw dislocations.

Parameters

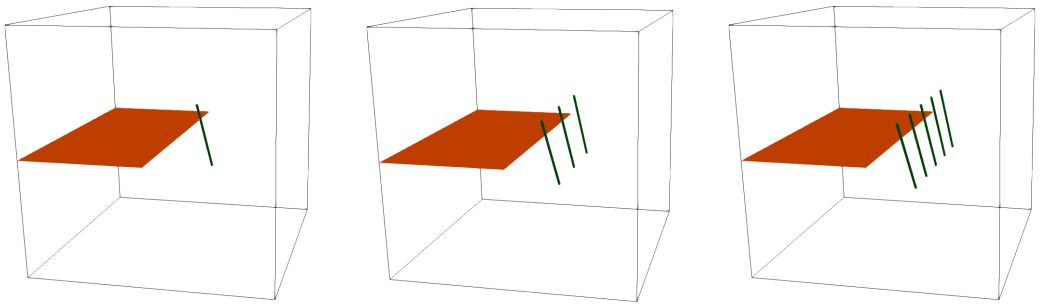

(a) $n = 1$ *(b)* $n = 3$ *(c)* $n = 5$

FIGURE 6.9 – *Initial configurations of the study cases for different number of Class II dislocation*

The studied dislocations will be screw dislocations of Class II (*CB(d)*), Burgers vector of $[10\bar{1}]$, slip plane of (111) and a length of 30 nm. Three simulations will be carried out each with a different number of starting dislocations. The initial dislocations, illustrated in Figure 6.9, are placed each at 8 nm ahead of the crack front following the y=$[10\bar{1}]$ direction.

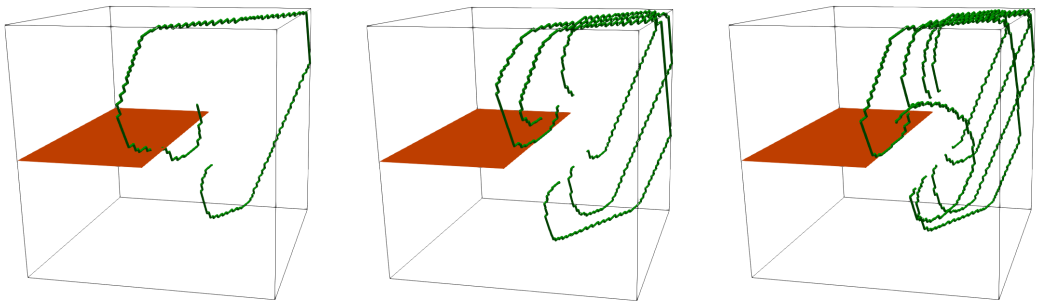

(a) $n = 1$ *(b)* $n = 3$ *(c)* $n = 5$

FIGURE 6.10 – *Final configurations of the study cases for different number of Class II dislocation*

Once the dislocations have reached the relaxed configuration, illustrated in Figure 6.10, we observe that they have moved away from the crack. It is worth noting that there is no dislocation loop created by the starting dislocations though there is a dislocation that crosses the crack surface for the one dislocation simulation case.

Results

Unrelaxed state

K_I The dislocations effects, shown in Figure 6.11, are mostly of an antishielding nature. A single dislocation is shown to affect a domain that includes the whole crack front.

The dislocations positions can be identified in the graphics by the valley created on the K_I values. There is, for the one dislocation simulation case, a small shielding zone where the dislocation is closer to the crack front. Therefore the crack front will try to surround the dislocation to move past it.

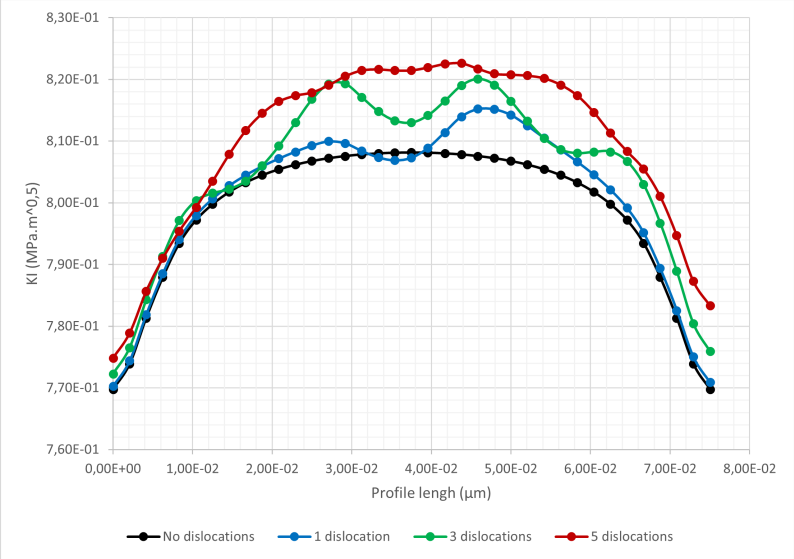

(a) K_I along the crack front

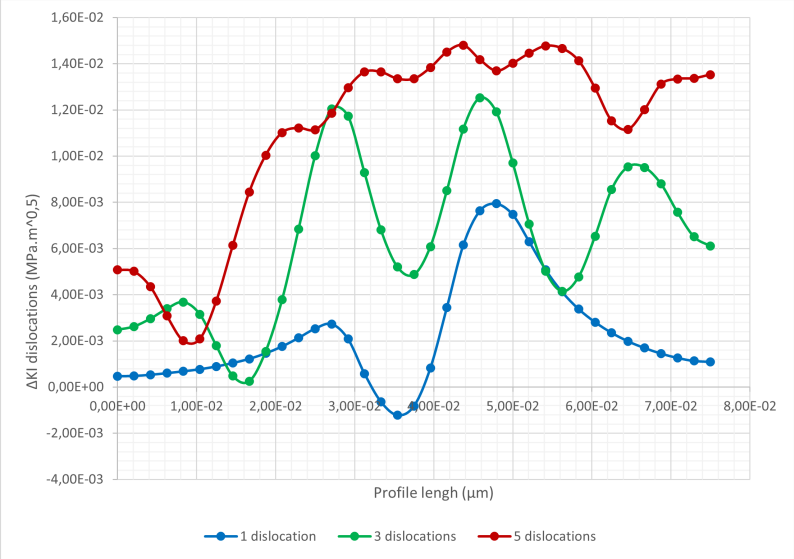

(b) Dislocation contribution to K_I

FIGURE 6.11 – *K_I along the crack front for different number of Class II dislocations for the unrelaxed configuration. Dislocation contribution to K_I has been isolated for clarity.*

K_{II} Dislocations effect lower the values of K_{II} as illustrated in Figure 6.12. Like for K_I, a single dislocation has a volume of influence that overlaps the whole crack front. The dislocation effect on the crack front creates a very distinct shape on the energy profile.

The way the dislocations affect the crack front energy varies with the dislocation position, it will become more wavy when advancing thus creating a less stable crack front. The crack front will move generally upwards to avoid the dislocations.

Relaxed state

K_I Once the dislocations have reached the relaxed configuration, they create a strong antishielding effect on the crack front energy as illustrated in Figure 6.13. Since the dislocations move away from the crack front, there is no longer any individual dislocation effect observed on the graphics. There is a small shielding effect on the single dislocation simulation (blue curve) which

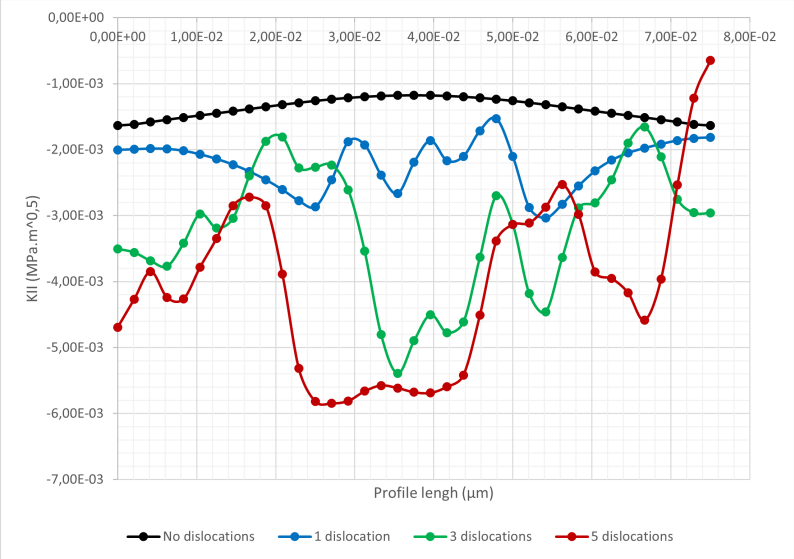

(a) K_{II} along the crack front

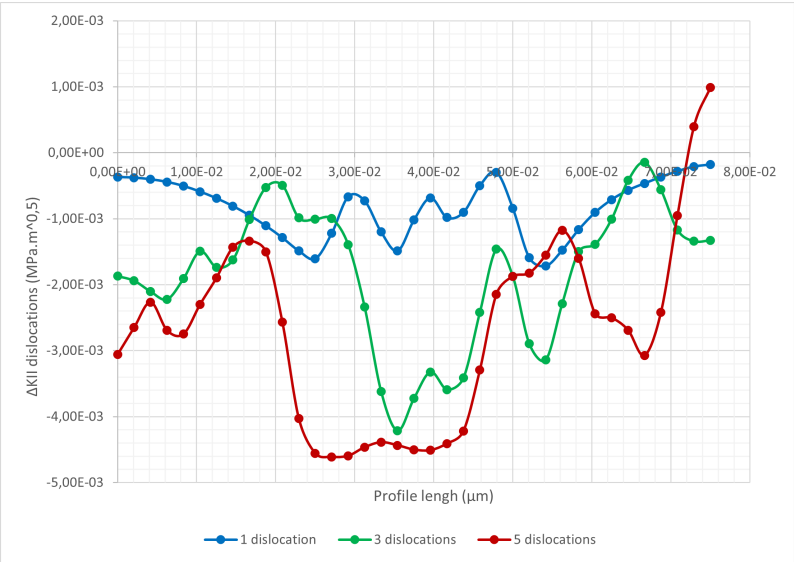

(b) Dislocation contribution to K_{II}

FIGURE 6.12 – *K_{II} along the crack front for different number of Class II dislocations for the unrelaxed configuration. Dislocation contribution to K_{II} has been isolated for clarity.*

is due to a dislocation crossing the crack front locally.

The three dislocations cccase displays a similar behavior which seems to indicate that K_I is independent from the number of initial dislocations. Even if the dislocations have moved away from the crack, they are still able to influence the whole crack front.

K_{II} The results for K_{II}, illustrated in Figure 6.14, display several similarities with those for K_I. There is no individual effect noticeable created by each dislocation, instead their effects combine and affect the whole crack length. The results are also independent from the number of starting dislocations. The crack front angle varies so the crack will change its habit plane to avoid the dislocations.

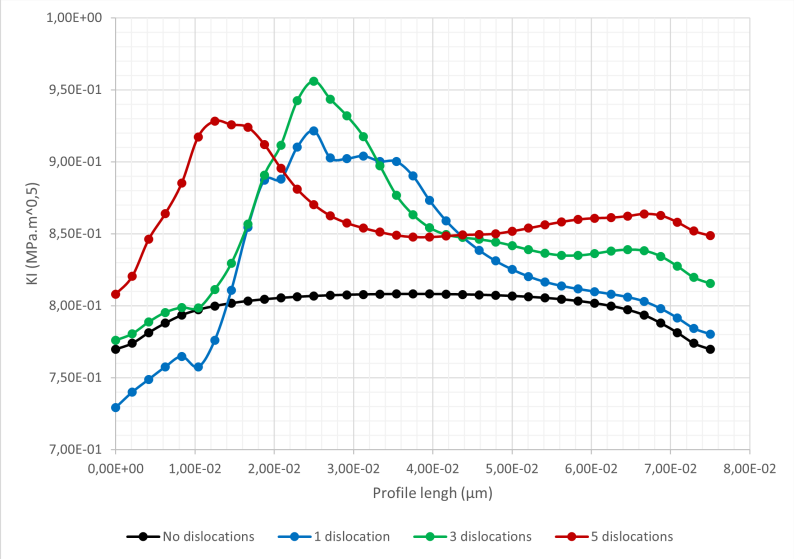

(a) K_I along the crack front

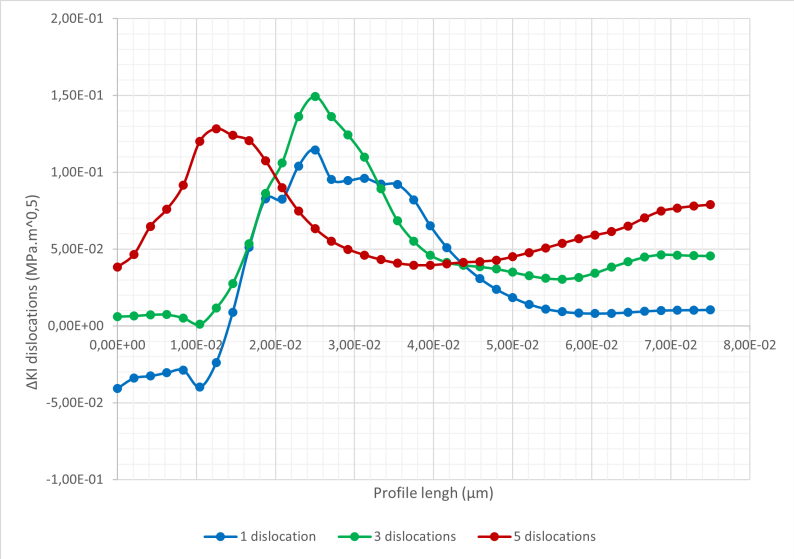

(b) Dislocation contribution to K_I

FIGURE 6.13 – *K_I along the crack front for different number of Class II dislocations for the relaxed configuration. Dislocation contribution to K_I has been isolated for clarity.*

Average stress intensity factors

The average stress intensity factors calculated in Table 6.4 for the unrelaxed configuration show a proportional increase for these average values depending on the starting dislocation number. The values of K_I show a global antishielding effect created by the dislocations. As for K_{II}, the dislocation effect makes it decrease further, the computed values are still proportional to the starting dislocation number.

Once the dislocations reach their relaxed configuration, the average intensity factors are recalculated and presented in Table 6.5. For K_I, the average values increase with the number of starting dislocations, increasing the antishielding provided by the dislocations. The resultant variation is even proportional to the starting dislocation number.

As for K_{II}, there is no clear trend for the average values. They do increase the more dislocations there are, but since K_{II} both includes positive and negative values, the average value just indicates

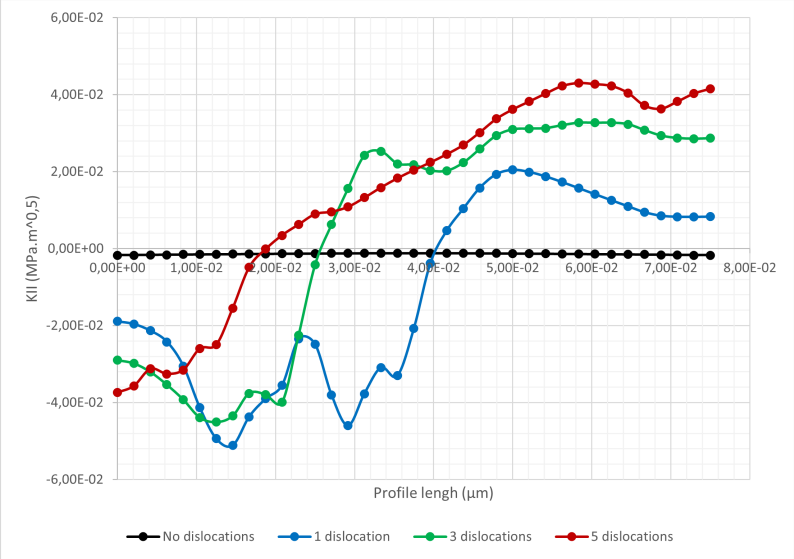

(a) K_{II} along the crack front

(b) Dislocation contribution to K_{II}

FIGURE 6.14 – *K_{II} along the crack front for different number of Class II dislocations for the relaxed configuration. Dislocation contribution to K_{II} has been isolated for clarity.*

towards which sign the values lean to. The great variation calculated was expected since it's mostly the dislocations that create the shear at the origin of K_{II}.

Conclusions

Class II dislocation results show great similarities to the Class I dislocations results. These similarities will be further studied in Section 6.6. Globally, K_I provides antishielding to the crack, with some localized zones of shielding created when the dislocations cross the crack front. For K_{II}, the energy both increases and decreases locally. The crack angle will adapt in order to avoid the dislocations as much as possible. As the dislocations move away from the crack, their individual effect on the crack front disappears and is replaced by a global effect that influences the crack much more regularly.

	KI			KII		
Number of dislocations	1	3	5	1	3	5
K No dislocation (MPa.m$^{0.5}$)	0.79858	0.79858	0.79858	-0.00138	-0.00138	-0.00138
K Dislocation (MPa.m$^{0.5}$)	0.80083	0.80498	0.80956	-0.00221	-0.00323	-0.00406
Variation (%)	100.282	100.802	101.375	160.504	234.493	295.170

TABLE 6.4 – *Average values of the stress intensity factors for the studied number of Class II dislocations for the initial unrelaxed configuration*

	KI			KII		
Number of dislocations	1	3	5	1	3	5
K No dislocation (MPa.m$^{0.5}$)	0.79858	0.79858	0.79858	-0.00138	-0.00138	-0.00138
K Dislocation (MPa.m$^{0.5}$)	0.82870	0.84977	0.86467	-0.01107	0.00530	0.01419
Variation (%)	103.771	106.410	108.276	804.788	-385.491	-1031.728

TABLE 6.5 – *Average values of the stress intensity factors for the studied number of Class II dislocations for the relaxed configuration*

6.5 Class III dislocations

Last dislocation configuration to be studied is the Class III case as described below.

Parameters

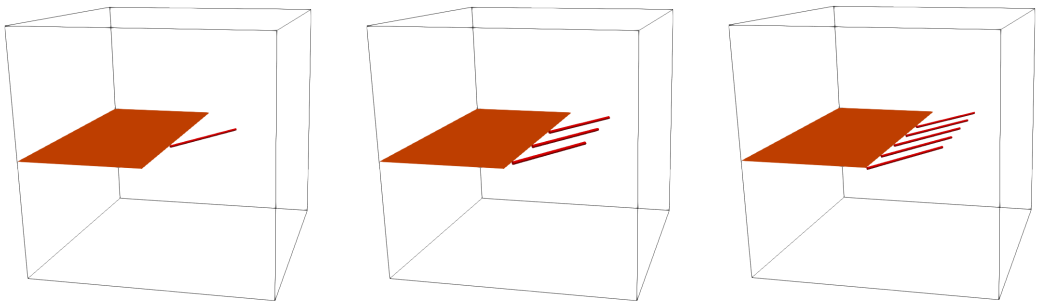

(a) $n = 1$ *(b)* $n = 3$ *(c)* $n = 5$

FIGURE 6.15 – *Initial configurations of the study cases for different number of Class III dislocations*

The studied dislocations will be screw dislocations of Class III (*AB(d)*), Burgers vector of $[\bar{1}10]$, slip plane (111) and a length of 30 nm. Three simulations will be carried out, their initial state is illustrated in Figure 6.15. The starting dislocations are all coplanar with the crack.

The other studied configuration, illustrated in Figure 6.16, corresponds to the relaxed configuration. These dislocations do not propagate away or towards the crack considering their starting position. The dislocations nearly touch the crack front. We suppose this will cause the dislocation effect on the crack front to be higher than for the other studied cases.

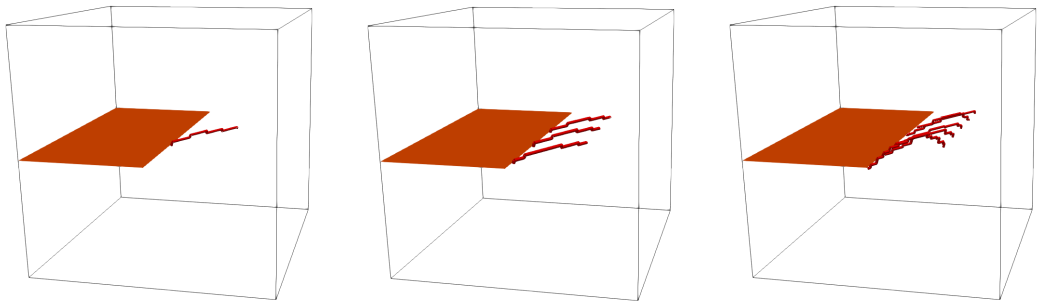

(a) $n = 1$ (b) $n = 3$ (c) $n = 5$

FIGURE 6.16 – *Final configurations of the study cases for different number of Class III dislocations*

Results

Unrelaxed state

K_I The results for K_I on the unrelaxed configuration are illustrated in Figure 6.17. We observe that the dislocations have a shielding effect on the crack front. Each dislocation creates a singular shielding effect that clearly marks the crack front energy.

It is worth noting that the highest shielding point does not correspond to the closest point between the crack and the dislocation. Actually, on that point there is a slight antishielding effect, though that is more likely due to it being the end point of the dislocation than because it is the closest point between crack and dislocation since there is also some antishielding cause by the other end of the dislocation. A single dislocation, even if it is very close to the crack, does not affect the whole crack front.

K_{II} As for K_{II}, the results correspond to Figure 6.18. The dislocation presence lowers the values of K_{II}. Contrary to K_I, the dislocation effect is exacerbated the closer the dislocation is to the crack front. The dislocations zone of effect is also reduced compared to K_I. This also causes K_{II} to have sharper variations.

Relaxed state

K_I Once the dislocations reach their equilibrium position, the results obtained, illustrated in Figure 6.19, are very similar to the ones for the unrelaxed configuration. With the exception of the five dislocation simulation (red curve), the obtained results retain the same geometry of the initial configuration. For the simulations of one and three dislocations, the individual dislocations marks are still visible. We also obtain the same result on both curves for the middle dislocation.

As for the five dislocations simulation case, the obtained results are probably due to the superposition of the individual dislocation effects which, as has been shown for other cases, can erase the singular dislocations marks. There is still some antishielding present in the curves, but it is negligible compared to the shielding provided by the dislocations.

K_{II} As for the K_{II} results, illustrated in Figure 6.20 we obtain the same energy distribution as for the unrelaxed configuration. The zone affected by the dislocations does not change in this configuration. The results obtained for the middle dislocation in the simulations for one and three dislocations are also very similar, meaning that the dislocations in the three dislocation simulation have minimal interactions between each other.

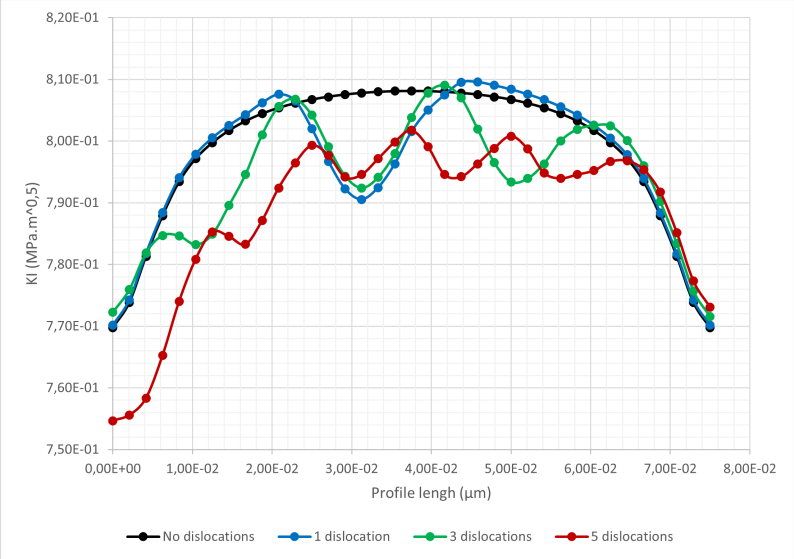

(a) K_I along the crack front

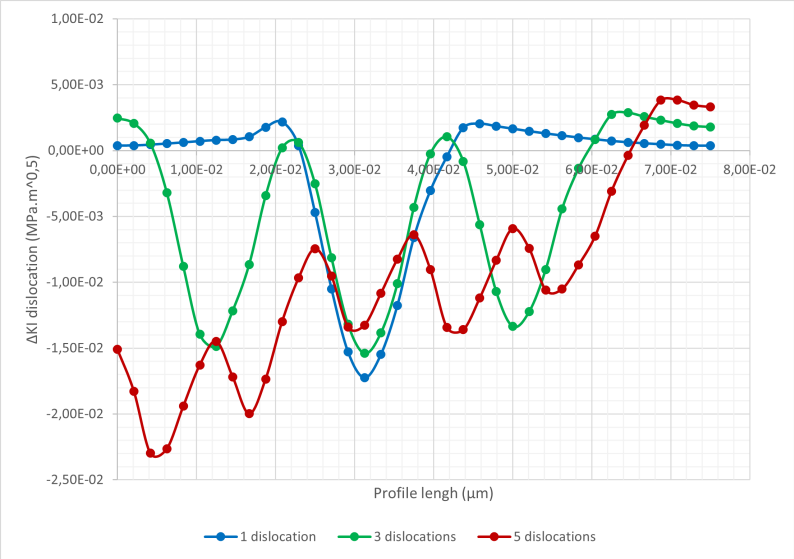

(b) Dislocation contribution to K_I

FIGURE 6.17 – *K_I along the crack front for different number of Class III dislocations for the unrelaxed configuration. Dislocation contribution to K_I has been isolated for clarity.*

The main changes occur for the five dislocations simulation case. The individual dislocation marks that could be observed for the unrelaxed configuration disappear here. It is most certainly the same phenomenon that also happens for the calculations of K_I.

Average stress intensity factors

The average stress intensity factors for the unrelaxed configuration, gathered in Table 6.6, show a non-proportional variation created by the dislocations. The dislocations effects previously mentionned are seen here too. There is an average shielding effect created by the dislocations, and the values of K_{II} decrease even further.

The average stress intensity factors for the relaxed configuration are compiled in Table 6.7. For K_I, we obtain the exact same results for the one and three dislocations simulations. This means that there has been no evolution in how the crack front perceives these dislocations. This holds

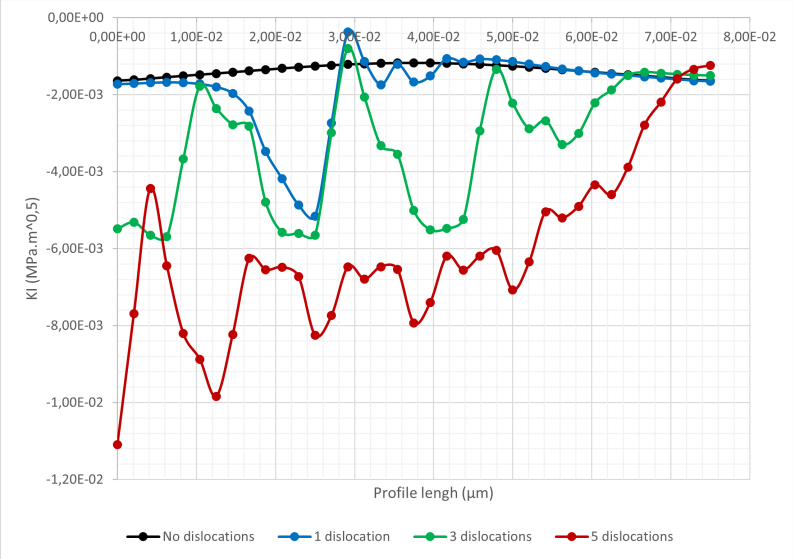

(a) K_{II} along the crack front

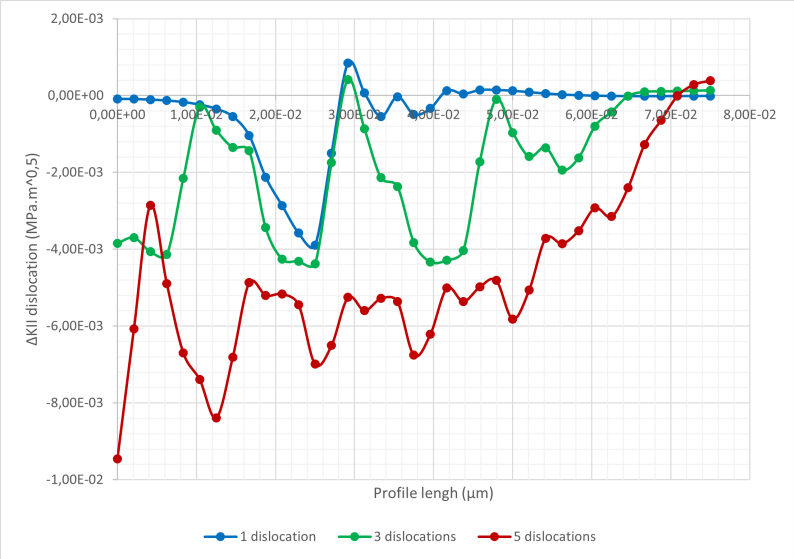

(b) Dislocation contribution to K_{II}

FIGURE 6.18 – *K_{II} along the crack front for different number of Class III dislocations for the unrelaxed configuration. Dislocation contribution to K_{II} has been isolated for clarity.*

true for K_{II} too. As for the five dislocations simulation, the dislocations effects are exacerbated as was observed previously. These results are probably due to the fact that for this last simulations, the dislocations interact with each other as they are close to one another, thus multiplying their effects on the crack front.

Conclusions

The studied Class III dislocations are parallel to the crack surface, thus placing the dislocations nearly at the crack front. Though dislocations are very close to the crack, it is not the closer point of the dislocation to the crack front that creates the highest effect on K_I. Class III dislocations provide shielding to the crack front. It is worth noting that the extremities of the dislocations create a small antishielding effect on the crack that is easily overpowered by the shielding. The zone of effect of these dislocations is small enough that only the five dislocations simulations has some dislocation-

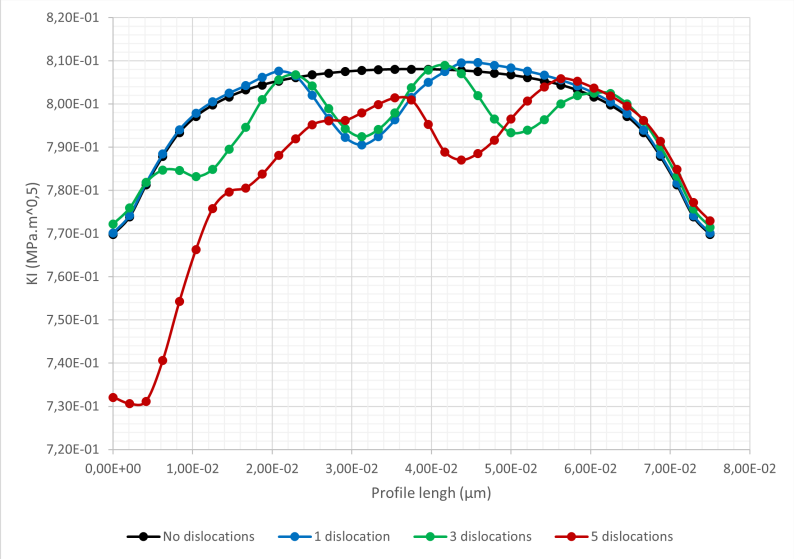

(a) K_I along the crack front

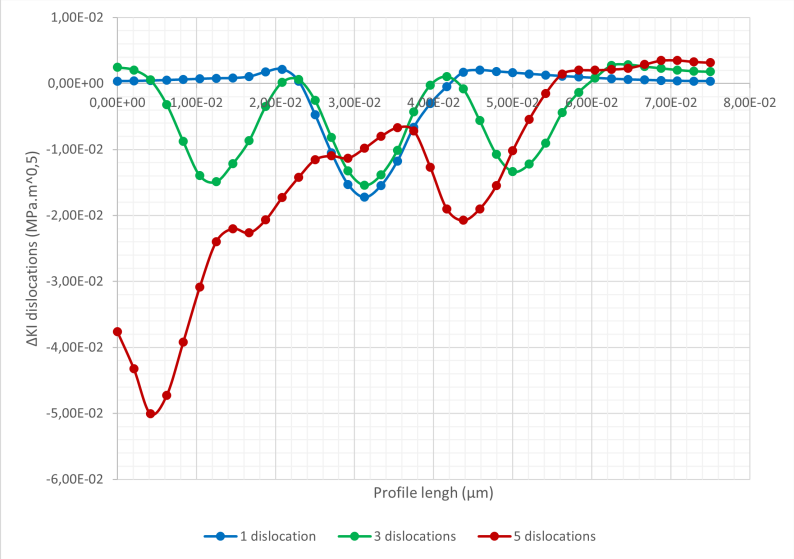

(b) Dislocation contribution to K_I

FIGURE 6.19 – *K_I along the crack front for different number of Class III dislocations for the relaxed configuration. Dislocation contribution to K_I has been isolated for clarity.*

dislocation interactions. These interactions lead to a stronger shielding effect on the crack front. As no dislocation crosses the crack, we do not know if said crossing could create an antishielding effect on the crack.

K_{II} yields very similar results to K_I as there is no difference between the relaxed and unrelaxed configurations for the one and three dislocations simulations but there is an increase in the dislocations effect for the five dislocations simulation. The main difference between the two stress intensity factors is that for K_{II}, the point with the highest effect on the crack front energy corresponds to the dislocation point that is closer to the crack front.

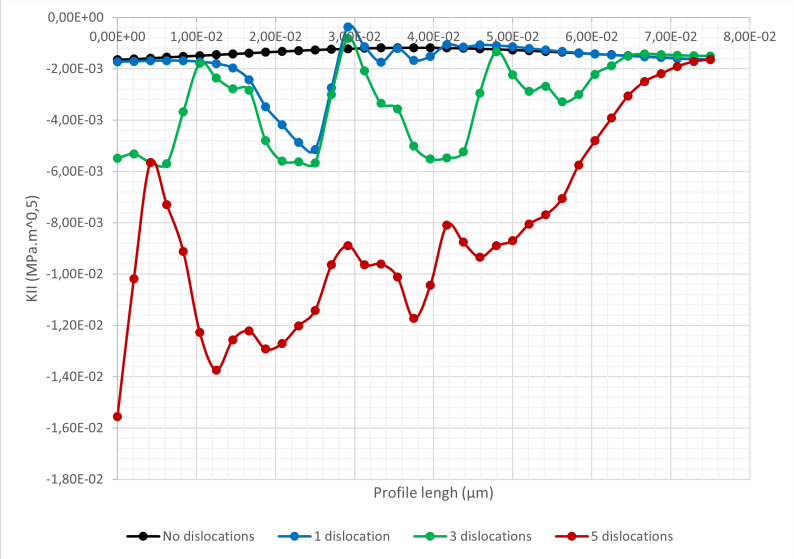

(a) K_{II} along the crack front

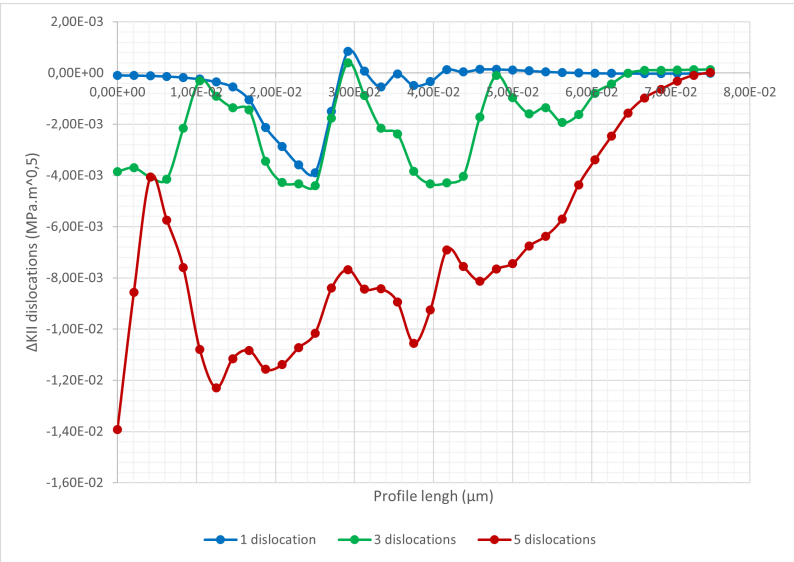

(b) Dislocation contribution to K_{II}

FIGURE 6.20 – *K_{II} along the crack front for different number of Class III dislocations for the relaxed configuration. Dislocation contribution to K_{II} has been isolated for clarity.*

6.6 Dislocation class comparison

Following our investigation of each dislocation class, we now seek to compare their effects.

Parameters

In order to compare the effect of the previously studied dislocations, we will study the effect of a single dislocation of each class on the crack front. As a reminder the dislocations studied, illustrated in Figure 6.21, are :

— Class I : (*CB(a)*), Burgers vector of $\left[10\bar{1}\right]$, slip plane $(\bar{1}1\bar{1})$

— Class II : (*CB(d)*), Burgers vector of $\left[10\bar{1}\right]$, slip plane (111)

— Class III : (*AB(d)*), Burgers vector of $\left[\bar{1}10\right]$, slip plane (111)

	KI			KII		
Number of dislocations	1	3	5	1	3	5
K No dislocation (MPa.m$^{0.5}$)	0.79858	0.79858	0.79858	-0.00138	-0.00138	-0.00138
K Dislocation (MPa.m$^{0.5}$)	0.79700	0.79409	0.78865	-0.00182	-0.00331	-0.00605
Variation (%)	99.801	99.437	98.756	132.554	240.378	439.954

TABLE 6.6 – *Average values of the stress intensity factors for the studied number of Class III dislocations for the initial unrelaxed configuration*

	KI			KII		
Number of dislocations	1	3	5	1	3	5
K No dislocation (MPa.m$^{0.5}$)	0.79858	0.79858	0.79858	-0.00138	-0.00138	-0.00138
K Dislocation (MPa.m$^{0.5}$)	0.79700	0.79408	0.78474	-0.00182	-0.00331	-0.00842
Variation (%)	99.801	99.437	98.267	132.554	240.711	612.428

TABLE 6.7 – *Average values of the stress intensity factors for the studied number of Class III dislocations for the relaxed configuration*

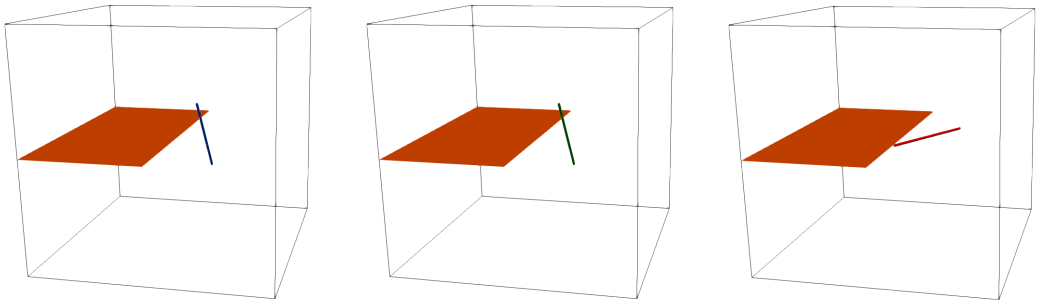

(a) Class I *(b) Class II* *(c) Class III*

FIGURE 6.21 – *Initial configurations of the study cases for different types of dislocation*

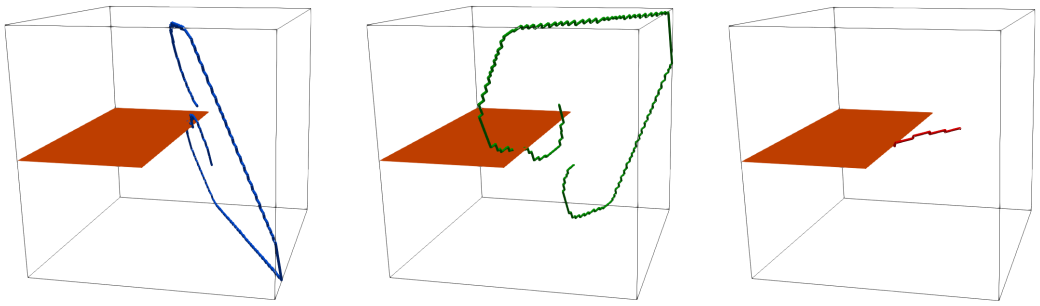

(a) Class I *(b) Class II* *(c) Class III*

FIGURE 6.22 – *Final configurations of the study cases for different types of dislocations*

The studied dislocations are 30 nm long, and the applied loading is so : $\varepsilon_{zz} = \varepsilon_1 = 0.01892208$

The relaxed configuration, illustrated in Figure 6.22 will also be studied. It is worth noting how similarly dislocations from Classes I and II behave.

Results

Unrelaxed state

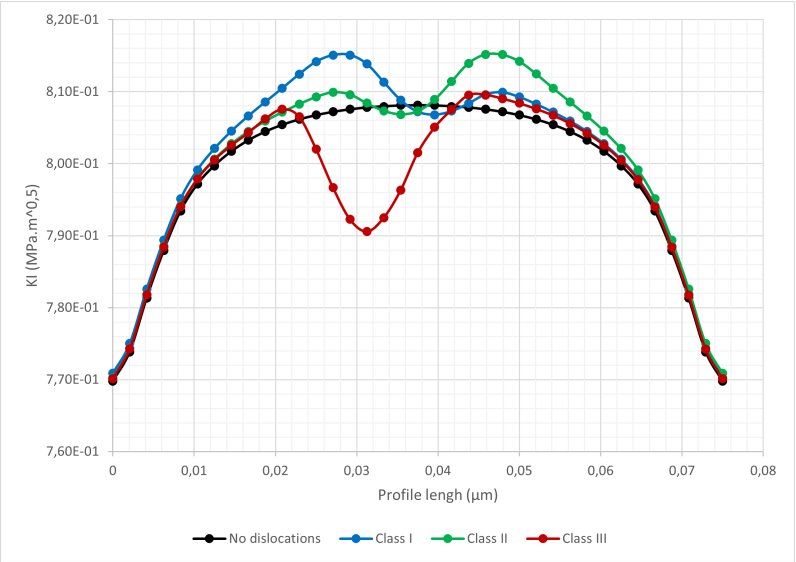

(a) K_I along the crack front

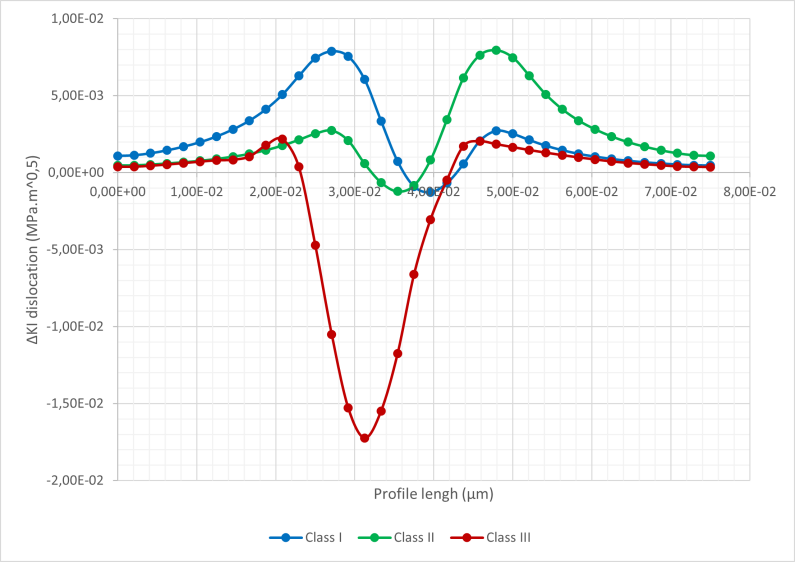

(b) Dislocation contribution to K_I

FIGURE 6.23 – *K_I along the crack front for different dislocation classes for the unrelaxed configuration and for a single dislocation. Dislocation contribution to K_I has been isolated for clarity.*

K_I First, we compare the values for K_I for the unrelaxed configuration illustrated on Figure 6.23. The dislocation class with the highest impact on the crack front energy is Class III. It is also the only class that provides a significant amount of shielding to the crack. On the other hand, Class I and Class II provide an antishielding effect to the crack front. These two classes have effects on the crack that create a symmetry on the energy profiles. This symmetry corresponds to a glide reflection symmetry. This is due to the fact that the crack is on the c plane, so these two dislocations, that share a line vector, are placed on the same place but move in different directions.

It is also worth noting that even if Class III dislocations are the closest to the crack front, it is Class I and II dislocations that have the larger zone of effect on the crack front. The Class III results is also not aligned with the other two results because of the angle the dislocation is at.

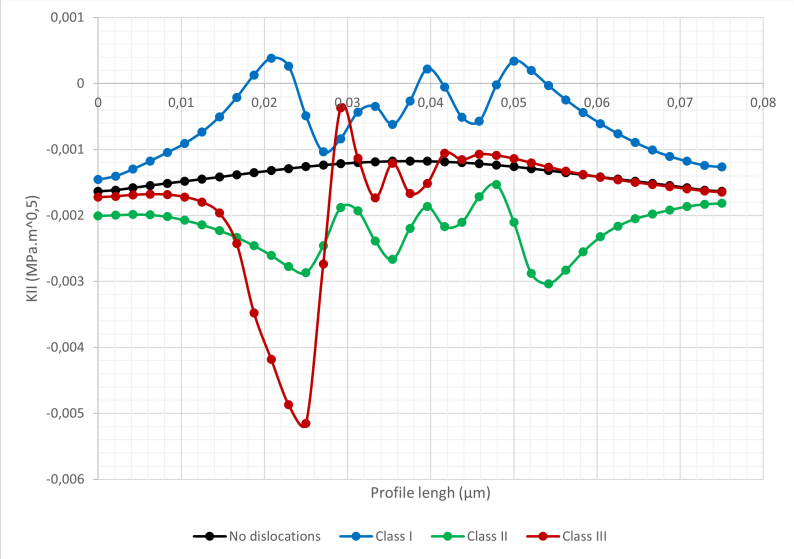

(a) K_{II} along the crack front

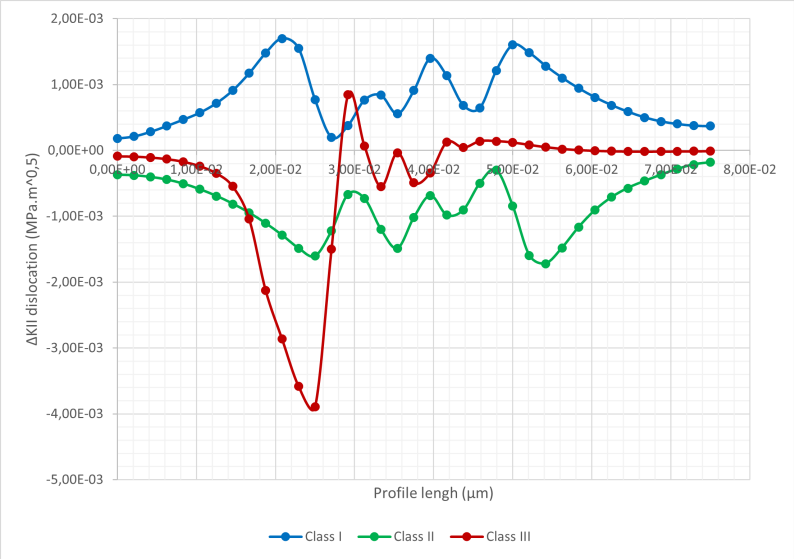

(b) Dislocation contribution to K_{II}

FIGURE 6.24 – *K_{II} along the crack front for different dislocation classes for the unrelaxed configuration and for a single dislocation. Dislocation contribution to K_{II} has been isolated for clarity.*

K_{II} As for K_{II} the results for the unrelaxed configuration are illustrated on Figure 6.24. Class III dislocation has the highest localized effect on the crack front, lowering sharply K_{II}. The effect of this dislocation is situated on the closest point of the dislocation to the crack tip and affects a smaller zone than the other two studied dislocations.

Class I and II dislocations have very similar results here too. But this time, the relative curves are a point reflection of each other. It is worth noting that while at first glance, the results between classes are quite different, they are actually quite close to each other in shape. Each dislocation creates an imprint on the energy that has four energy low points. This pattern is also present on Class III dislocations. The reason it is different is probably because most of the dislocation influence is concentrated in one point of the crack due to the dislocation proximity instead of being equally distributed along the crack front.

Relaxed state

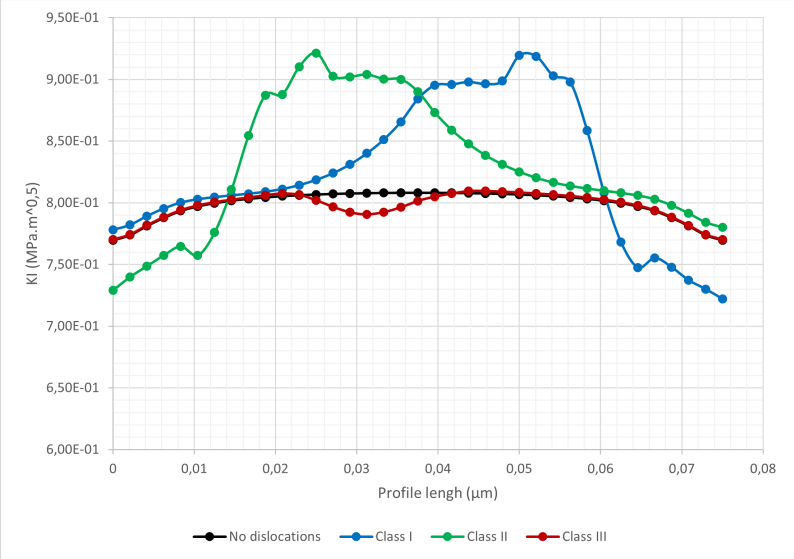

(a) K_I along the crack front

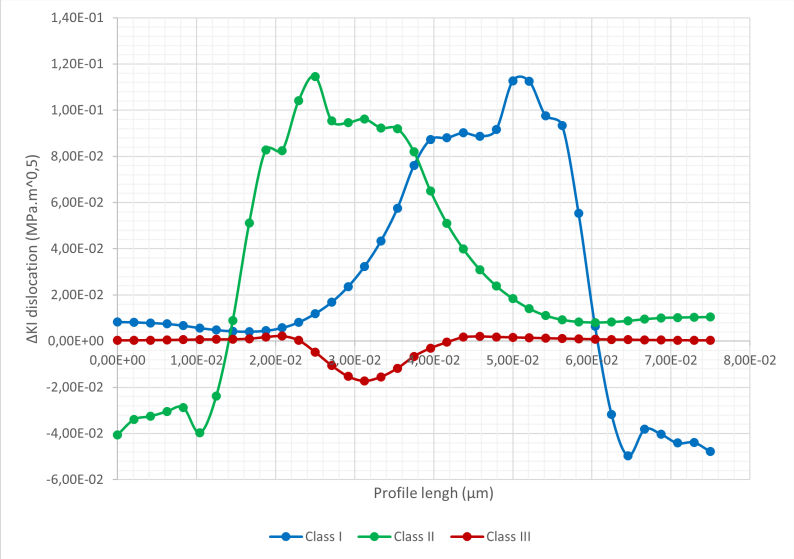

(b) Dislocation contribution to K_I

FIGURE 6.25 – *K_I along the crack front for different dislocation classes for the relaxed configuration and for a single dislocation. Dislocation contribution to K_I has been isolated for clarity.*

K_I Once the dislocations reach the relaxed configuration, we obtain the results for K_I illustrated in Figure 6.25. The symmetry observed between Class I and II still remains in this configuration. Their antishielding effect has vastly increased. There is some shielding that appears too due to the dislocations crossing the crack front.

On the other hand, Class III effect hasn't evolved between the two configurations. This it probably due to the fact that Class III dislocations have a very low propagation distance compared to the other two Classes.

K_{II} The results for K_{II} for the relaxed configuration are shown in Figure 6.26. The values for the Class III dislocation remain unchanged with the dislocation propagation, the propagation does not influence this dislocation behavior. On the other hand, the effect of the other two classes has vastly increased. Class I and II dislocation effect are still the point reflection symmetry of each other but there is some minor differences between Class I and II results that are due to the difference on

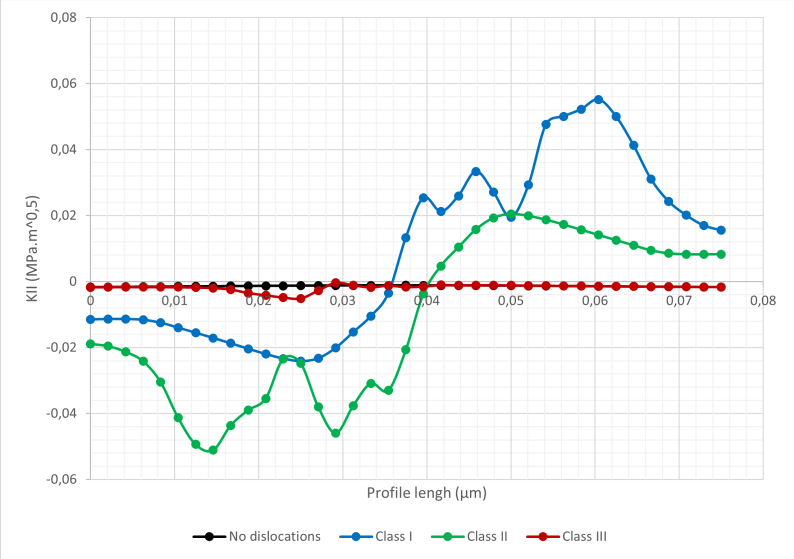

(a) K_{II} along the crack front

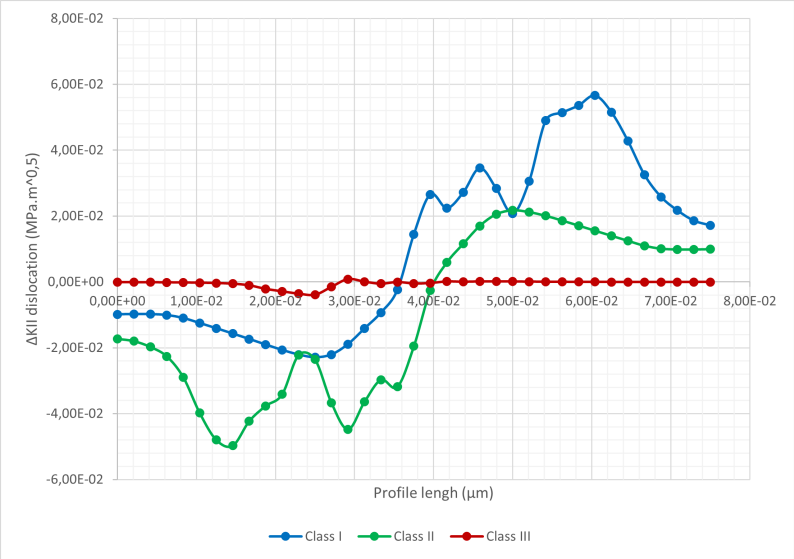

(b) Dislocation contribution to K_{II}

FIGURE 6.26 – *K_{II} along the crack front for different dislocation classes for the relaxed configuration and for a single dislocation. Dislocation contribution to K_{II} has been isolated for clarity.*

propagation of these two dislocations. It is possible that the differences we observe between Class III and the two other classes are also due to the differences in dislocation propagation.

Average stress intensity factors

The average stress intensity factors for the unrelaxed configuration are gathered in Table 6.8. For K_I, Class I and II have the same value and show a global antishielding effect. Whereas for Class III, there is a clear shielding effect that appears to be, if considering the absolute values, weaker than the antishielding effect created by the two other studied dislocation configurations.

Concerning K_{II}, the values for Class I and Class II are both equidistant from the non dislocation value. It confirms what was observed in the graphics. As for Class III, even if it had a minimal value lower than the one for the other classes, Class II still has more impact globally on K_{II}. Class III effect zone is smaller than for the other dislocation configurations.

	KI			KII		
	Class I	Class II	Class III	Class I	Class II	Class III
K No dislocation (MPa.m$^{0.5}$)	0.79858	0,79858	0.79858	-0.00138	-0.00138	-0.00138
K Dislocation (MPa.m$^{0.5}$)	0.80082	0.80083	0.79700	-0.00057	-0.00221	-0.00182
Variation (%)	100.280	100.282	99.801	41.589	160.504	132.553

TABLE 6.8 – *Average values of the strain intensity factors for the studied dislocations for the initial unrelaxed configuration*

	KI			KII		
	Class I	Class II	Class III	Class I	Class II	Class III
K No dislocation (MPa.m$^{0.5}$)	0.79858	0.79858	0.79858	-0.00138	-0.00138	-0.00138
K Dislocation (MPa.m$^{0.5}$)	0.82470	0.82870	0.79700	0.00846	-0.01107	-0.00182
Variation (%)	103.271	103.771	99.801	-615.108	804.788	132.554

TABLE 6.9 – *Average values of the strain intensity factors for the studied dislocations for the relaxed configuration*

Once the dislocations have relaxed, the average intensity factors are calculated and gathered in Table 6.9. The values for Class III remain unchanged for both stress intensity factors confirming what was said before about their lack of evolution after dislocation propagation.

On the other hand, there is an evolution for the two other classes. The antishielding present for Class I and Class II for K_I is still present, and is stronger than before. The values obtained for both cases are very close. As for K_{II}, the values are also equidistant from the non dislocation value. Class I and Class II dislocations have also increased their effect on the crack front energy.

Conclusions

In this section we have compared the effects of the three studied dislocation classes and one single dislocation for both the unrelaxed and relaxed configuration. For the Class III case, the energy of this dislocation does not evolve from one configuration to the other. Furthermore, even if the absolute maximum for Class III is higher than for the other cases, the global value is still lower due to the dislocation effect zone being smaller. The dislocations marks on the energy profiles are similar between the three cases though.

For Class I and Class II, we have observed a symmetry between the curves of the stress intensity factors plotted along the crack front. This symmetry is reflectional for K_I and point reflexional for K_{II}. Both stress intensity factors evolve with the relaxation of the dislocations and both results remain almost identical through all the simulation.

In conclusion, for the same propagation of the studied dislocations, it seems that the distance is the factor that weights more on the effect of the dislocations on the stress intensity factors. But, it is the dislocation movement that seems to be the key factor influencing the stress intensity factors.

6.7 Conclusion

Three dislocations classes have been simulated for this study. The first part of the study consisted in the study of the effect of the dislocation number on the stress intensity factor for dislocations of different nature. We observed that the dislocation effects are additive unless the size of the affected zone overlap one another. When the overlay occurs, the dislocations effect on the crack front energy grow larger.

Of the three studied classes, Class III dislocations are the ones that propagate the least. Their effect on both initial and relaxed configurations remain unchanged unless there is dislocation-dislocation interactions within the volume. For the unrelaxed state, Class III dislocations have the highest impact on the crack front as they are closer to it. Once the dislocations relax, it is Class I and Class II dislocations that have the highest effect as they propagate more, creating a stronger stress field around the crack front.

It is worth mentioning that Class III dislocations provide shielding to the crack while Class I and Class II dislocations provide antishielding unless the dislocations cross the crack front which creates locally a shielding zone.

The different class dislocations where also compared to one another. We observed a symmetry between the results of Class I and Class II. This symmetry is due to the fact that the crack plane corresponds to the c plane, and since Class I and Class II dislocations share a line vector, they start at the same point and move in two other faces of the Thompson tetrahedron, namely, the a and the d planes respectively. This symmetry manifests differently for K_I and K_{II}. The symmetry is reflectional for K_I and point reflexional for K_{II}.

Conclusions

This study aimed at creating a model to simulate the interactions between dislocations and a propagating crack. Once the model created, it was also tested to verify its accuracy and then used to study the effect of dislocation on the stress intensity factors.

Two existing simulations methods were coupled in order to be able to model the interactions between a crack and dislocations. The methods coupled were the eXtended Finite Element Method (XFEM) and the Discrete Dislocations Dynamics (DDD). The softwares used for these simulations were Cast3M, for the XFEM, and TriDis, for the DDD. The coupling created allowed these softwares to communicate between each other.

Once the coupling was functional, the first simulations carried out quantified the impact of the mesh parameters on the stress intensity factors of the volume. These simulations also allowed the mesh and overall simulations parameters to be adjusted. With the mesh parameters established, the simulations carried out aimed at understanding the effect of different dislocation parameters on their effect on the stress intensity factors of the crack front. The studied parameters include the dislocations slip system, their number, their distance to the crack front, their Burgers vector direction and the strain applied to the volume. There were also simulations aiming at comparing our results with similar simulation results from either atomistic simulations or discrete dislocation dynamics simulations which led us to using two different crack orientations to be able to reproduce the existing simulations.

The first crack orientation studied corresponded to the orientation used on atomistic simulations of a crack interacting with a dislocation. The first simulation carried out used the same parameters as the ones used on the atomistic simulation in order to replicate its results. The results obtained showed a very similar dislocation behavior even if the stabilization process of the dislocation differed. Stress maps for the different slip system were also calculate for comparison. The geometry of the stress maps allows the dislocations to be separated in categories depending on its symmetry. The effects of dislocations belonging to the same category were compared as it had been observed that dislocations of the same category behaved in a similar fashion towards the crack. Our results showed a similar trending of behavior among dislocations of the same class though the intensity of the observed behavior changed from one dislocation to the other.

After the preliminary studies, several dislocation parameters were studied to qualify their effect on the crack front stress intensity factors. Our observations concluded that the nature of the dislocation slip system controls the dislocation behavior towards the crack, it being shielding, anti-shielding or a mix of both. The intensity of the dislocation effect is influenced by other parameters such as the distance between the crack and the dislocation or the dislocation line direction. The number of dislocations present was also considered. It seemed that the dislocations effect was somewhat further amplified by the number of dislocations present than what would be justified by a simple addition of the singular dislocations effects.

The second crack orientation studied corresponds to one of the orientations studied for a discrete dislocation dynamics model with a static crack. The results comparison can only be qualitative as our volume is considerably smaller as it was made to be compared with atomistic simulations results. Globally, the dislocations behavior seems to be the same we observed. We also studied the same dislocations studied previously, but as the crack orientation was different, the stress perceived by the dislocations does not allow the dislocations to be separated into different categories. Which is why these results cannot be generalized. Each studied dislocation created a different effect on the crack front stress intensity factors, and, as previously observed, the more dislocations, the higher in magnitude is the effect independently of the dislocation number.

While not being overly mentioned, the main accomplishment of this study is the implementation of a crack propagation model that takes into account the internal stresses generated by the dislocations. Figure 6.27 is an example of this implementation. In this simulation, the crack propagation direction changes locally due to the presence of dislocations. Locally, the crack is also

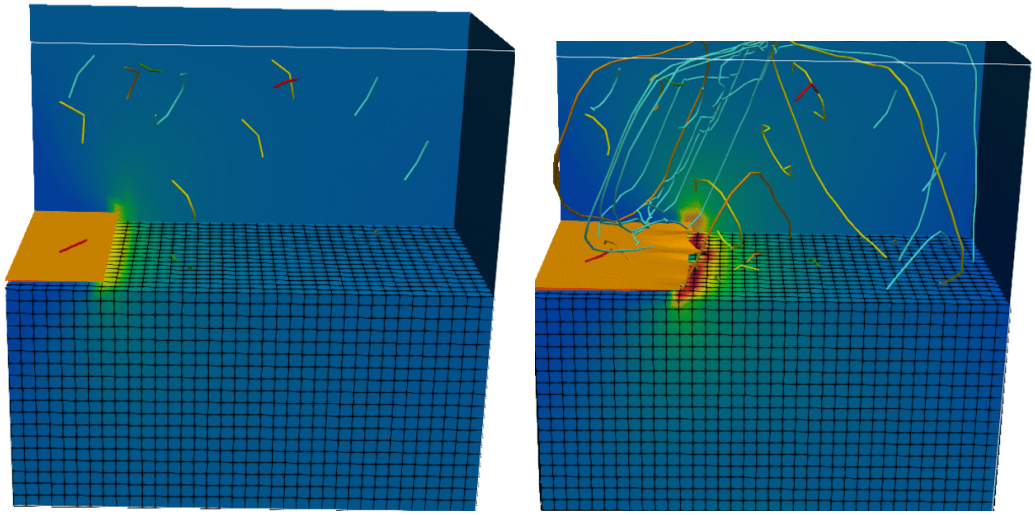

(a) Initial configuration *(b) Final configuration*

FIGURE 6.27 – *Example of a crack (orange surface) propagation influenced by the presence of surrounding dislocations (lines)*

both slowed and accelerated by the dislocations which leads to a complex 3D shape of the crack front.

We created a coupling that allows us to simulate the interactions between a propagating crack front and dislocations in a three dimensional environment. Our results were compared to other preexisting simulations results. We also were able to study the effect of several parameters on the stress intensity factors of a crack front, and to influence the crack propagation with the presence of one or several dislocations.

Perspectives

There are still a number of improvements that can be implemented in the simulation code used for this thesis. First, the crack surfaces could be exported to TriDis so the dislocations present in the simulation volume can interact with them. Dislocations should be able to exit the volume by going through the crack surfaces. The main complication presented here is that both crack surfaces are represented by the same surface so it needs to behave as a free surface from both sides or be duplicated to be able to represent two surfaces. The dislocations crossing these surfaces should not be able to interact with the dislocations remaining on the volume as they are now outside said volume. On the same vein, TriDis would also need to be able to update the surfaces conforming the volume to accommodate the crack propagation. Not only the surfaces will need to be modified, but also the dislocations placed where the crack will propagate need to be identified and accordingly modified. One way to achieve this will be to calculate the level set functions for the dislocations ends to verify if it is crossing the crack and be able to act accordingly. The code includes an implementation of a nucleation of dislocations function on the crack front but there is no clear nucleation criteria used. An in-depth study of dislocation nucleation at crack tips should

be carried out in order to have an accurate nucleation criteria.

The simulations were carried out using an FCC material. Initially, it was planned for a BCC material to be used, but the dislocation behavior laws for TriDis are still been worked on at the moment. It will be simple to adapt the current work for BCC materials once the behavior of dislocations in BCC materials have been updated in TriDis.

This work centers around interactions with dislocations, but this model could also be implemented with voids or inclusions that could interact with the crack front. These simulations will broaden the understanding of the origins of fracture toughness and crack behavior.

In order to physically simulate a crack propagation, a value for K_{IC} is needed since when $K_I > K_{IC}$, the crack is able to advance. K_{IC} can be obtained either experimentally, by recreating the simulated volume and study its crack propagation, or by using results obtained by atomistic simulations where the propagation of a crack is also studied.

Aside from TriDis, SIMaP also works on another DDD software called numodis. This software, while requiring higher computation times than TriDis, allows for the simulation of partial dislocations. It would be interesting to implement a similar model than the one presented here for numodis in order to study the effects of partial dislocations on the crack front energy.

Bibliography

[1] R. Abedi, R. B. Haber, S. Thite, and J. Erickson. An h-adaptive spacetime-discontinuous galerkin method for linear elastodynamics. *European Journal of Computational Mechanics*, 15(6) :619–642, 2006.

[2] P. M. Anderson, J. P. Hirth, and J. Lothe. *Theory of dislocations*. Cambridge University Press, 2017.

[3] S. S. Antman and J. E. Osborn. The principle of virtual work and integral laws of motion. *Archive for Rational Mechanics and Analysis*, 69(3) :231–262, 1979.

[4] P. M. Areias and T. Belytschko. A comment on the article "a finite element method for simulation of strong and weak discontinuities in solid mechanics" by a. hansbo and p. hansbo [comput. methods appl. mech. engrg. 193 (2004) 3523–3540]. *Computer Methods in Applied Mechanics and Engineering*, 195(9) :1275–1276, 2006.

[5] J. H. Argyris. Energy theorems and structural analysis : A generalized discourse with applications on energy principles of structural analysis including the effects of temperature and non-linear stress-strain relations. *Aircraft Engineering and Aerospace Technology*, 1954.

[6] M. F. Ashby and D. R. H. Jones. *Engineering materials 1 : an introduction to properties, applications, and design*. Butterworth-Heinemann, Amsterdam ; Boston, 4th ed edition, 2012.

[7] I. Babuška and J. Melenk. The partition of unity method. 40 :727–758, 1997.

[8] H. Bao and A. McEvily. On plane stress–plane strain interactions in fatigue crack growth. *International Journal of Fatigue*, 20(6) :441–448, 1998.

[9] D. Barnett. The displacement field of a triangular dislocation loop. *Philosophical Magazine A*, 51(3) :383–387, 1985.

[10] K.-J. Bathe. Finite element method. *Wiley encyclopedia of computer science and engineering*, pages 1–12, 2007.

[11] E. Béchet, H. Minnebo, N. Moës, and B. Burgardt. Improved implementation and robustness study of the x-FEM for stress analysis around cracks. *International Journal for Numerical Methods in Engineering*, 64(8) :1033–1056, 2005.

[12] T. Belytschko and T. Black. Elastic crack growth in finite elements with minimal remeshing. *International Journal for Numerical Methods in Engineering*, 45 :601–620, 1999.

[13] E. Benvenuti. Mesh-size-objective xfem for regularized continuous–discontinuous transition. *Finite elements in analysis and design*, 47(12) :1326–1336, 2011.

[14] S. E. Benzley. Representation of singularities with isoparametric finite elements. *International Journal for Numerical Methods in Engineering*, 8(3) :537–545, 1974.

[15] B. A. Bilby, A. H. Cottrell, and K. Swinden. The spread of plastic yield from a notch. *Proceedings of the Royal Society of London. Series A. Mathematical and Physical Sciences*, 272(1350) :304–314, 1963.

[16] E. Bitzek. *Atomistic Simulation of Dislocation Motion and Interaction with Crack Tips and Voids*. Theses, Universität Kalrsuhe, Oct. 2006.

[17] E. Bitzek and P. Gumbsch. Mechanisms of dislocation multiplication at crack tips. *Acta Materialia*, 61(4) :1394–1403, Feb. 2013.

[18] J. Bonneville, B. Escaig, and J. Martin. A study of cross-slip activation parameters in pure copper. *Acta Metallurgica*, 36(8) :1989–2002, 1988.

[19] P. Bouchard, F. Bay, and Y. Chastel. Numerical modelling of crack propagation : automatic remeshing and comparison of different criteria. *Computer Methods in Applied Mechanics and Engineering*, 192(35) :3887–3908, 2003.

[20] P. Bouchard, F. Bay, Y. Chastel, and I. Tovena. Crack propagation modelling using an advanced remeshing technique. *Computer Methods in Applied Mechanics and Engineering*, 189(3) :723–742, 2000.

[21] B. Bourdin, G. Francfort, and J.-J. Marigo. Numerical experiments in revisited brittle fracture. *Journal of the Mechanics and Physics of Solids*, 48(4) :797–826, 2000.

[22] R. Brighenti, A. Carpinteri, A. Spagnoli, and D. Scorza. Crack path dependence on inhomogeneities of material microstructure. *Frattura ed Integrità Strutturale*, 6(20) :6–16, Mar. 2012.

[23] P. Burchard, L.-T. Cheng, B. Merriman, and S. Osher. Motion of curves in three spatial dimensions using a level set approach. *Journal of Computational Physics*, 170(2) :720–741, 2001.

[24] W. Cai, V. V. Bulatov, J. Chang, J. Li, and S. Yip. Dislocation core effects on mobility. *Dislocations in solids*, 12(1), 2004.

[25] G. Camacho and M. Ortiz. Computational modelling of impact damage in brittle materials. *International Journal of Solids and Structures*, 33(20) :2899–2938, 1996.

[26] CEA. Cast3m. [Online ; accessed October 30, 2021].

[27] C. . CEA. anumodis. [Online ; accessed January 3, 2022].

[28] K. S. Chan. Roles of microstructure in fatigue crack initiation. *International Journal of Fatigue*, 32(9) :1428–1447, Sept. 2010.

[29] L.-T. Cheng, P. Burchard, B. Merriman, and S. Osher. Motion of curves constrained on surfaces using a level-set approach. *Journal of Computational Physics*, 175(2) :604–644, 2002.

[30] J. Chessa and T. Belytschko. An enriched finite element method and level sets for axisymmetric two-phase flow with surface tension. *International Journal for Numerical Methods in Engineering*, 58(13) :2041–2064, 2003.

[31] J. Chessa and T. Belytschko. An extended finite element method for two-phase fluids. *Journal of Applied Mechanics*, 70(1) :10–17, 2003.

[32] J. Chessa, P. Smolinski, and T. Belytschko. The extended finite element method (XFEM) for solidification problems. *International Journal for Numerical Methods in Engineering*, 53(8) :1959–1977, 2002.

[33] K. Y. Chia and S. J. Burns. Crack tip deformation in lif single crystals. *Scripta Metallurgica*, 18(5) :467–472, 1984.

[34] R. W. Clough. The finite element method in plane stress analysis. In *Proceedings of 2nd ASCE Conference on Electronic Computation, Pittsburgh Pa., Sept. 8 and 9, 1960*, 1960.

[35] CNRS-ONERA. micromegas. [Online ; accessed January 20, 2022].

[36] A. H. Cottrell. Theory of dislocations. *Progress in Metal Physics*, 4 :205–264, 1953.

[37] R. De Borst, J. Remmers, and A. Needleman. Computational aspect of cohesive zone models, 2004.

[38] V. Deshpande, A. Needleman, and E. Van der Giessen. Discrete dislocation plasticity modeling of short cracks in single crystals. *Acta Materialia*, 51(1) :1–15, 2003.

[39] P. Destuynder, M. Djaoua, and S. Lescure. Quelques remarques sur la mécanique de la rupture élastique (some remarks on elastic fracture mechanics). *Journal de Mécanique Théorique et Appliquée*, 2 :113–135, 1983.

[40] B. Devincre and M. Condat. Model validation of a 3d simulation of dislocation dynamics : discretization and line tension effects. *Acta metallurgica et materialia*, 40(10) :2629–2637, 1992.

[41] B. Devincre and L. P. Kubin. Mesoscopic simulations of dislocations and plasticity. *Materials Science and Engineering : A*, 234 :8–14, 1997.

[42] C. Déprés. Modélisation physique des stades précurseurs de l'endommagement en fatigue dans l'acier inoxydable austénitique 316l, 2004.

[43] J. Drouet, L. Dupuy, F. Onimus, F. Mompiou, S. Perusin, and A. Ambard. Dislocation dynamics simulations of interactions between gliding dislocations and radiation induced prismatic loops in zirconium. *Journal of Nuclear Materials*, 449(1-3) :252–262, 2014.

[44] M. Duflot. A study of the representation of cracks with level sets. *International Journal for Numerical Methods in Engineering*, 70(11) :1261–1302, 2007.

[45] A. A. El-Azab and M. Fivel. Linking continuum mechanics and 3D discrete dislocation simulations. Oct. 1998.

[46] T. Elguedj, A. Gravouil, and A. Combescure. Appropriate extended functions for x-FEM simulation of plastic fracture mechanics. *Computer Methods in Applied Mechanics and Engineering*, 195(7) :501–515, 2006.

[47] U. Essmann and H. Mughrabi. Annihilation of dislocations during tensile and cyclic deformation and limits of dislocation densities. *Philosophical Magazine A*, 40(6) :731–756, 1979.

[48] M. Fivel. Dislocation concept : Burgers vector, class support, 2022.

[49] M. C. Fivel, T. J. Gosling, and G. R. Canova. Implementing image stresses in a 3d dislocation simulation. *Modelling and Simulation in Materials Science and Engineering*, 4(6) :581–596, nov 1996.

[50] M. Fleming, Y. Chu, B. Moran, and T. Belytschko. Enriched element-free galerkin methods for crack tip fields. *International journal for numerical methods in engineering*, 40(8) :1483–1504, 1997.

[51] P. L. Freddolino, A. S. Arkhipov, S. B. Larson, A. McPherson, and K. Schulten. Molecular dynamics simulations of the complete satellite tobacco mosaic virus. *Structure*, 14(3) :437–449, 2006.

[52] D. Frenkel and B. Smit. *Understanding molecular simulation : from algorithms to applications*. Number 1 in Computational science series. Acad. Press, 2. ed., [nachdr.] edition, 2001. OCLC : 554151822.

[53] J. Friedel. *Dislocations : international series of monographs on solid state physics*, volume 3. Elsevier, 2013.

[54] A. George and G. Michot. Dislocation loops at crack tips : nucleation and growth— an experimental study in silicon. *Materials Science and Engineering : A*, 164(1-2) :118–134, May 1993.

[55] A. Gravouil, N. Moës, and T. Belytschko. Non-planar 3d crack growth by the extended finite element and level sets-part II : Level set update : Non-planar 3d crack growth - part II. *International Journal for Numerical Methods in Engineering*, 53(11) :2569–2586, 2002.

[56] A. Griffith. The phenomena of rupture and flow in solids. *Philosophical Transactions of the Royal Society of London*, 221 :163–198, 1921.

[57] S. Groh, B. Devincre, F. Feyel, L. Kubin, A. Roos, and J.-L. Chaboche. Discrete-continuum modeling of metal matrix composites plasticity. In *IUTAM Symposium on Mesoscopic Dynamics of Fracture Process and Materials Strength*, pages 235–244. Springer, 2004.

[58] S.-I. Gustafsson. Furniture design by use of the finite element method. *Holz als Roh-und Werkstoff*, 53(4) :257–260, 1995.

[59] A. Hansbo and P. Hansbo. An unfitted finite element method, based on nitsche's method, for elliptic interface problems. *Computer Methods in Applied Mechanics and Engineering*, 191(47) :5537–5552, 2002.

[60] A. Haslam, S. Phillpot, D. Wolf, D. Moldovan, and H. Gleiter. Mechanisms of grain growth in nanocrystalline fcc metals by molecular-dynamics simulation. *Materials Science and Engineering : A*, 318(1-2) :293–312, 2001.

[61] A. Hmelo, J. Bilello, S. Davies, and D. Bowen. Synchrotron x-ray fractography : a novel technique for fracture-surface analysis. *Materials Letters*, 2(1) :6–11, 1983.

[62] J. Horton and S. Ohr. Tem observations of dislocation emission at crack tips in aluminium. *Journal of Materials Science*, 17(11) :3140–3148, 1982.

[63] H. Huang and F. Costanzo. On the use of space-time finite elements in the solution of elasto-dynamic fracture problems. *International Journal of Fracture*, 127(2) :119–146, 2004.

[64] D. Hull and D. J. Bacon. *Introduction to dislocations*. Elsevier/Butterworth-Heinemann, 5. ed edition, 2011. OCLC : 704891549.

[65] G. Irwin. Analysis of stresses and strains near the end of a crack traversing a plate. *Journal of Applied Mechanics*, 24 :361–364, 1957.

[66] O. Jamond, R. Gatti, A. Roos, and B. Devincre. Consistent formulation for the discrete-continuous model : Improving complex dislocation dynamics simulations. *International Journal of Plasticity*, 80 :19–37, 2016.

[67] H. Jiang and D. Meng. 3d numerical modelling of rock fracture with a hybrid finite and cohesive element method. *Engineering Fracture Mechanics*, 199 :280–293, 2018.

[68] H. JP and J. Lothe. Theory of dislocations', 355, 1968.

[69] A. Keyhani, M. Goudarzi, S. Mohammadi, and R. Roumina. Xfem–dislocation dynamics multi-scale modeling of plasticity and fracture. *Computational Materials Science*, 104 :98–107, 2015.

[70] L. Korzeczek. *Modélisation mésoscopique en 3D par le modèle Discret-Continu de la stabilité des fissures courtes dans les métaux CFC*. Theses, Université Paris-Saclay, July 2017.

[71] S. Kumar and W. A. Curtin. Crack interaction with microstructure. *Materials Today*, 10(9) :34–44, Sept. 2007.

[72] L. L. N. Laboratory. Paradis. [Online ; accessed January 3, 2022].

[73] R. W. Lardner. *Mathematical theory of dislocations and fracture*. University of Toronto Press, 2019.

[74] B. Lawn. *Fracture of Brittle Solids - Second Edition*. University Press, 1993.

[75] H. C. Lee, J. S. Choi, K. Jung, and Y. Im. Application of element deletion method for numerical analyses of cracking. *Journal of Achievements in Materials and Manufacturing Engineering*, 35(2) :154–161, 2009.

[76] C. Lemarchand, B. Devincre, and L. Kubin. Homogenization method for a discrete-continuum simulation of dislocation dynamics. *Journal of the Mechanics and Physics of Solids*, 49(9) :1969–1982, 2001.

[77] J. C. Li. Stress field of a dislocation segment. *Philosophical Magazine*, 10(108) :1097–1098, 1964.

[78] M. Li and J. Gilman. Dislocation mobility. 2016.

[79] S. Liang, Y. Zhu, M. Huang, and Z. Li. Simulation on crack propagation vs. crack-tip dislocation emission by xfem-based ddd scheme. *International Journal of Plasticity*, 114 :87–105, 2019.

[80] X. Lu, M. Ridha, B. Chen, V. Tan, and T. Tay. On cohesive element parameters and delamination modelling. *Engineering Fracture Mechanics*, 206 :278–296, 2019.

[81] H. L. Luk, J. Feist, J. J. Toppari, and G. Groenhof. Multiscale molecular dynamics simulations of polaritonic chemistry. *Journal of chemical theory and computation*, 13(9) :4324–4335, 2017.

[82] B. Majumdar and S. Burns. Crack tip shielding—an elastic theory of dislocations and dislocation arrays near a sharp crack. *Acta Metallurgica*, 29(4) :579–588, 1981.

[83] B. Majumdar and S. Burns. A griffith crack shielded by a dislocation pile-up. *International Journal of Fracture*, 21(3) :229–240, 1983.

[84] R. Malladi and J. Sethian. Image processing : Flows under min/max curvature and mean curvature. *Graphical Models and Image Processing*, 58(2) :127–141, 1996.

[85] E. Martinez, J. Marian, A. Arsenlis, M. Victoria, and J. M. Perlado. Atomistically informed dislocation dynamics in fcc crystals. *Journal of the Mechanics and Physics of Solids*, 56(3) :869–895, 2008.

[86] R. McClung and H. Sehitoglu. On the finite element analysis of fatigue crack closure—1. basic modeling issues. *Engineering Fracture Mechanics*, 33(2) :237–252, 1989.

[87] R. McClung and H. Sehitoglu. On the finite element analysis of fatigue crack closure—2. numerical results. *Engineering Fracture Mechanics*, 33(2) :253–272, 1989.

[88] J. Melenk and I. Babuška. The partition of unity finite element method : Basic theory and applications. *Computer Methods in Applied Mechanics and Engineering*, 139(1) :289–314, 1996.

[89] T. Menouillard, J. Réthoré, A. Combescure, and H. Bung. Efficient explicit time stepping for the eXtended finite element method (x-FEM) : Explicit dynamics for x-FEM. *International Journal for Numerical Methods in Engineering*, 68(9) :911–939, 2006.

[90] R. Merle and J. Dolbow. Solving thermal and phase change problems with the eXtended finite element method. *Computational Mechanics*, 28(5) :339–350, 2002.

[91] G. Michot and A. George. Dislocation emission from cracks-observations by x-ray topography in silicon. *Scripta metallurgica*, 20(11) :1495–1500, 1986.

[92] N. Moës and T. Belytschko. Extended finite element method for cohesive crack growth. *Engineering Fracture Mechanics*, 69(7) :813–833, 2002.

[93] N. Moës, J. Dolbow, and T. Belytschko. A finite element method for crack growth without remeshing. *International Journal for Numerical Methods in Engineering*, 48 :131–150, 1999.

[94] N. Moës, A. Gravouil, and T. Belytschko. Non-planar 3d crack growth by the extended finite element and level sets-part i : Mechanical model : Non-planar 3D crack growth - part i. *International Journal for Numerical Methods in Engineering*, 53(11) :2549–2568, 2002.

[95] T. Mura. General theory of eigenstrains. In *Micromechanics of defects in solids*, pages 1–62. Springer, 1982.

[96] J. Newman. A finite-element analysis of fatigue crack closure. In J. Rice and P. Paris, editors, *Mechanics of Crack Growth*, pages 281–281–21. ASTM International, 1976.

[97] T. Nishioka and S. N. Atluri. Numerical modeling of dynamic crack propagation in finite bodies, by moving singular elements—part 1 : Formulation. *Journal of Applied Mechanics*, 47(3) :570–576, 1980.

[98] S. Ohr. Dislocation-crack interaction. *Journal of Physics and Chemistry of Solids*, 48(11) :1007–1014, Jan. 1987.

[99] S. Ohr. Dislocation-crack interaction. *Journal of Physics and Chemistry of Solids*, 48(11) :1007–1014, 1987.

[100] S. Ohr And and J. Narayan. Electron microscope observation of shear cracks in stainless steel single crystals. *Philosophical Magazine A*, 41(1) :81–89, 1980.

[101] E. Orowan. Zur Kristallplastizitt. I : Tieftemperaturplastizitt und Beckersche Formel. *Zeitschrift fr Physik*, 89(9-10) :605–613, Sept. 1934.

[102] S. Osher and J. A. Sethian. Fronts propagating with curvature-dependent speed : Algorithms based on hamilton-jacobi formulations. *Journal of Computational Physics*, 79(1) :12–49, 1988.

[103] A. Pandolfi, P. Guduru, M. Ortiz, and A. Rosakis. Three dimensional cohesive-element analysis and experiments of dynamic fracture in c300 steel. *International Journal of Solids and Structures*, 37(27) :3733–3760, 2000.

[104] E. Pena, B. Calvo, M. Martinez, and M. Doblare. A three-dimensional finite element analysis of the combined behavior of ligaments and menisci in the healthy human knee joint. *Journal of biomechanics*, 39(9) :1686–1701, 2006.

[105] J. Philibert. Dislocations et déformation plastique. *Les éditions de la physique*, 101, 1979.

[106] S. Pommier, A. Gravouil, N. Moës, and A. Combescure. *La simulation numérique de la propagation des fissures milieux tridimensionnels, fonctions de niveau, éléments finis étendus et critères énergétiques*. Hermès Science : Lavoisier, 2009. OCLC : 690354664.

[107] B. Prabel. *Modélisation avec la méthode X-FEM de la propagation dynamique et de l'arrêt de fissure de clivage dans un acier de cuve REP*. Theses, Institut National des Sciences Appliquées de Lyon, Sept. 2007.

[108] W. T. Read. *Dislocations in crystals*, volume 10. McGraw-Hill, 1953.

[109] J. N. Reddy and D. K. Gartling. *The finite element method in heat transfer and fluid dynamics*. CRC press, 2010.

[110] J. Réthoré, A. Gravouil, and A. Combescure. A stable numerical scheme for the finite element simulation of dynamic crack propagation with remeshing. *Computer Methods in Applied Mechanics and Engineering*, 193(42) :4493–4510, 2004.

[111] J. Réthore. Méthode éléments finis étendus en espaces et en temps : application à la propagation dynamique des fissures, 2005.

[112] M. Sander and H. Richard. Finite element analysis of fatigue crack growth with interspersed mode i and mixed mode overloads. *International Journal of Fatigue*, 27(8) :905–913, 2005.

[113] M. Sander and H. Richard. Experimental and numerical investigations on the influence of the loading direction on the fatigue crack growth. *International Journal of Fatigue*, 28(5) :583–591, 2006.

[114] C. Scandian, H. Azzouzi, N. Maloufi, G. Michot, and A. George. Dislocation Nucleation and Multiplication at Crack Tips in Silicon. *physica status solidi (a)*, 171(1) :67–82, Jan. 1999.

[115] C. Scandian, H. Azzouzi, N. Maloufi, G. Michot, and A. George. Dislocation nucleation and multiplication at crack tips in silicon. *physica status solidi (a)*, 171(1) :67–82, 1999.

[116] J. A. Sethian. *Level set methods and fast marching methods : evolving interfaces in computational geometry, fluid mechanics, computer vision, and materials science*. Number 3 in Cambridge monographs on applied and computational mathematics. Cambridge Univ. Press, 2. ed., 9. print edition, 2008. OCLC : 316142500.

[117] J. A. Sethian and J. Straint. Crystal growth and dendritic solidification. *Journal of Computational Physics*, 98(2) :231–253, 1992.

[118] A. Shahani and M. Amini Fasakhodi. Finite element analysis of dynamic crack propagation using remeshing technique. *Materials & Design*, 30(4) :1032–1041, 2009.

[119] SIMaP. Tridis. [Online ; accessed January 3, 2022].

[120] K. Solanki, S. Daniewicz, and J. Newman. Finite element modeling of plasticity-induced crack closure with emphasis on geometry and mesh refinement effects. *Engineering Fracture Mechanics*, 70(12) :1475–1489, 2003.

[121] K. Solanki, S. Daniewicz, and J. Newman. Finite element analysis of plasticity-induced fatigue crack closure : an overview. *Engineering Fracture Mechanics*, 71(2) :149–171, 2004.

[122] J.-H. Song, H. Wang, and T. Belytschko. A comparative study on finite element methods for dynamic fracture. *Computational Mechanics*, 42(2) :239–250, 2008.

[123] M. Stolarska, D. L. Chopp, N. Moës, and T. Belytschko. Modelling crack growth by level sets in the extended finite element method. *International Journal for Numerical Methods in Engineering*, 51(8) :943–960, 2001.

[124] T. Strouboulis, I. Babuška, and K. Copps. The design and analysis of the generalized finite element method. *Computer Methods in Applied Mechanics and Engineering*, 181(1) :43–69, 2000.

[125] N. Sukumar, D. Chopp, N. Moës, and T. Belytschko. Modeling holes and inclusions by level sets in the extended finite-element method. *Computer Methods in Applied Mechanics and Engineering*, 190(46) :6183–6200, 2001.

[126] N. Sukumar, N. Moës, B. Moran, and T. Belytschko. Extended finite element method for three-dimensional crack modelling. *International Journal for Numerical Methods in Engineering*, 48(11) :1549–1570, Aug. 2000.

[127] S. Suresh. *Fatigue of materials*. Cambridge university press, 1998.

[128] M. Sussman, E. Fatemi, P. Smereka, and S. Osher. An improved level set method for incompressible two-phase flows. *Computers & Fluids*, 27(5) :663–680, 1998.

[129] D. Tanguy, M. Razafindrazaka, and D. Delafosse. Multiscale simulation of crack tip shielding by a dislocation. *Acta Materialia*, 56(11) :2441–2449, June 2008.

[130] P. Theocaris and E. Gdoutos. The modified dugdale-barenblatt model adapted to various fracture configurations in metals. *International Journal of Fracture*, 10(4) :549–564, 1974.

[131] R. Thomson. Brittle fracture in a ductile material with application to hydrogen embrittlement. *Journal of Materials Science*, 13(1) :128–142, 1978.

[132] R. Thomson. Physics of fracture. volume 39 of *Solid State Physics*, pages 1–129. Academic Press, 1986.

[133] M. J. Turner, R. W. Clough, H. C. Martin, and L. Topp. Stiffness and deflection analysis of complex structures. *journal of the Aeronautical Sciences*, 23(9) :805–823, 1956.

[134] E. Van der Giessen and A. Needleman. Discrete dislocation plasticity : a simple planar model. *Modelling and Simulation in Materials Science and Engineering*, 3(5) :689, 1995.

[135] A. Vattré, B. Devincre, F. Feyel, R. Gatti, S. Groh, O. Jamond, and A. Roos. Modelling crystal plasticity by 3d dislocation dynamics and the finite element method : the discrete-continuous model revisited. *Journal of the Mechanics and Physics of Solids*, 63 :491–505, 2014.

[136] G. Ventura, J. X. Xu, and T. Belytschko. A vector level set method and new discontinuity approximations for crack growth by EFG. *International Journal for Numerical Methods in Engineering*, 54(6) :923–944, 2002.

[137] M. Verdier, M. Fivel, and I. Groma. Mesoscopic scale simulation of dislocation dynamics in fcc metals : Principles and applications. *Modelling and Simulation in Materials Science and Engineering*, 6(6) :755–770, Nov. 1998.

[138] V. Volterra. Sur l'équilibre des corps élastiques multiplement connexes. In *Annales scientifiques de l'École normale supérieure*, volume 24, pages 401–517, 1907.

[139] G. J. Wagner, S. Ghosal, and W. K. Liu. Particulate flow simulations using lubrication theory solution enrichment. *International Journal for Numerical Methods in Engineering*, 56(9) :1261–1289, 2003.

[140] G. J. Wagner, N. Moës, W. K. Liu, and T. Belytschko. The extended finite element method for rigid particles in stokes flow. *International Journal for Numerical Methods in Engineering*, 51(3) :293–313, 2001.

[141] J. Weertman. Fracture mechanics : A unified view for griffith-irwin-orowan cracks. *Acta Metallurgica*, 26(11) :1731–1738, 1978.

[142] J. Weertman. Crack tip blunting by dislocation pair creation and separation. *Philosophical Magazine A*, 43(5) :1103–1123, 1981.

[143] Wikipedia, the free encyclopedia. Three fracture modes, 2008. [Online ; accessed October 19, 2020].

[144] Wikipedia, the free encyclopedia. Fracture toughness, 2020. [Online ; accessed November 14, 2021].

[145] Z. Wu, X. Xu, Q. Liu, and Y. Yang. A zero-thickness cohesive element-based numerical manifold method for rock mechanical behavior with micro-voronoi grains. *Engineering Analysis with Boundary Elements*, 96 :94–108, 2018.

[146] X.-P. Xu and A. Needleman. Numerical simulations of fast crack growth in brittle solids. *Journal of the Mechanics and Physics of Solids*, 42(9) :1397–1434, 1994.

[147] A. Zehnder. Fracture mechanics. Number 62 in Lecture notes in applied and computational mechanics. Springer, 2012. OCLC : 755698387.

[148] F. Zhou and J. F. Molinari. Dynamic crack propagation with cohesive elements : a methodology to address mesh dependency. *International Journal for Numerical Methods in Engineering*, 59(1) :1–24, 2004.

[149] G. Zi and T. Belytschko. New crack-tip elements for XFEM and applications to cohesive cracks. *International Journal for Numerical Methods in Engineering*, 57(15) :2221–2240, 2003.

List of Figures

List of Tables

Simulation 3D des interactions entre fissure et dislocations

3D simulations of the interactions between crack and dislocations

Résumé

Mots-clés :

Abstract

Keywords :